



**NAVAL
POSTGRADUATE
SCHOOL**

MONTEREY, CALIFORNIA

DISSERTATION

**A MULTI-SCALE ANALYSIS OF TROPICAL
CYCLOGENESIS WITHIN THE CRITICAL LAYER OF
TROPICAL EASTERLY WAVES IN THE ATLANTIC AND
WESTERN NORTH PACIFIC SECTORS**

by

Louis L. Lussier III

September 2010

Dissertation Supervisor:

Michael T. Montgomery

Approved for public release; distribution is unlimited

THIS PAGE INTENTIONALLY LEFT BLANK

REPORT DOCUMENTATION PAGE

Form Approved OMB No. 0704-0188

Public reporting burden for this collection of information is estimated to average 1 hour per response, including the time for reviewing instruction, searching existing data sources, gathering and maintaining the data needed, and completing and reviewing the collection of information. Send comments regarding this burden estimate or any other aspect of this collection of information, including suggestions for reducing this burden, to Washington headquarters Services, Directorate for Information Operations and Reports, 1215 Jefferson Davis Highway, Suite 1204, Arlington, VA 22202-4302, and to the Office of Management and Budget, Paperwork Reduction Project (0704-0188) Washington DC 20503.

1. AGENCY USE ONLY (Leave blank)	2. REPORT DATE September 2010	3. REPORT TYPE AND DATES COVERED Dissertation	
4. TITLE AND SUBTITLE: A Multi-Scale Analysis of Tropical Cyclogenesis Within the Critical Layer of Tropical Easterly Waves in the Atlantic and Western North Pacific Sectors		5. FUNDING NUMBERS	
6. AUTHOR(S) Louis L. Lussier III			
7. PERFORMING ORGANIZATION NAME(S) AND ADDRESS(ES) Naval Postgraduate School Monterey, CA 93943-5000		8. PERFORMING ORGANIZATION REPORT NUMBER	
9. SPONSORING / MONITORING AGENCY NAME(S) AND ADDRESS(ES) N/A		10. SPONSORING / MONITORING AGENCY REPORT NUMBER	
11. SUPPLEMENTARY NOTES The views expressed in this thesis are those of the author and do not reflect the official policy or position of the Department of Defense or the U.S. Government. IRB Protocol Number: _____ N/A _____.			
12a. DISTRIBUTION / AVAILABILITY STATEMENT Approved for public release; distribution is unlimited	12b. DISTRIBUTION CODE		
13. ABSTRACT (maximum 200 words) A newly proposed tropical cyclogenesis sequence that describes the transition of a tropical wave's critical layer to a tropical cyclone is used to examine two formation cases in the western North Pacific basin. Typhoon Nuri (2008), formed from a precursor easterly wave during the Tropical Cyclone Structure 2008 field experiment, and Typhoon Man-yi (2007), formed within an equatorial Rossby wave as it interacted with a monsoon trough. In each case, i) the critical layer of the parent wave protects a proto-vortex from an external hostile environment and allows it to strengthen until it becomes a self-sustained entity and ii) the intersection between the wave trough and critical latitude, within the Kelvin cat's eye, is the preferred location for tropical cyclogenesis. Numerical simulations suggest that the so-called "bottom-up" pathway to tropical cyclogenesis is favored within Typhoon Man-yi's critical layer. Additionally, Tropical Rainfall Measurement Mission (TRMM) composite analyses of 55 developing easterly waves indicate that as genesis approaches, i) convection is favored in the Kelvin cat's eye circulation, ii) the convective contribution to total rain rate becomes dominant, iii) the radius of maximum convection decreases, and iv) a convective-type heating profile is present. These findings support the "bottom-up" development model within easterly wave critical layers.			
14. SUBJECT TERMS tropical cyclone, tropical cyclogenesis, tropical cyclone formation, TRMM		15. NUMBER OF PAGES 247	
			16. PRICE CODE
17. SECURITY CLASSIFICATION OF REPORT Unclassified	18. SECURITY CLASSIFICATION OF THIS PAGE Unclassified	19. SECURITY CLASSIFICATION OF ABSTRACT Unclassified	20. LIMITATION OF ABSTRACT UU

NSN 7540-01-280-5500

Standard Form 298 (Rev. 2-89)
Prescribed by ANSI Std. Z39-18

THIS PAGE INTENTIONALLY LEFT BLANK

Approved for public release; distribution is unlimited

**A MULTI-SCALE ANALYSIS OF TROPICAL CYCLOGENESIS WITHIN THE
CRITICAL LAYER OF TROPICAL EASTERLY WAVES IN THE ATLANTIC
AND WESTERN NORTH PACIFIC SECTORS**

Louis L. Lussier III
Major, United States Air Force
B.S., Lyndon State College, 1995
M.S., Air Force Institute of Technology, 2004

Submitted in partial fulfillment of the
requirements for the degree of

DOCTOR OF PHILOSOPHY IN METEOROLOGY

from the

NAVAL POSTGRADUATE SCHOOL
September 2010

Author:

Louis L. Lussier III

Approved by:

Michael Montgomery
Professor of Meteorology
Dissertation Supervisor/
Dissertation Committee Chair

Patrick Harr
Professor of Meteorology

Richard Moore
Assistant Professor of Meteorology

Francis Giraldo
Associate Professor of
Mathematics

Zhuo Wang
Assistant Professor of Meteorology
University of Illinois

Approved by:

Phillip Durkee, Chairman, Department of Meteorology

Approved by:

Douglas Moses, Vice Provost for Academic Affairs

THIS PAGE INTENTIONALLY LEFT BLANK

ABSTRACT

A newly proposed tropical cyclogenesis sequence that describes the transition of a tropical wave's critical layer to a tropical cyclone is used to examine two formation cases in the western North Pacific basin. Typhoon Nuri (2008), formed from a precursor easterly wave during the Tropical Cyclone Structure 2008 field experiment, and Typhoon Man-yi (2007), formed within an equatorial Rossby wave as it interacted with a monsoon trough. In each case, i) the critical layer of the parent wave protects a proto-vortex from an external hostile environment and allows it to strengthen until it becomes a self-sustained entity and ii) the intersection between the wave trough and critical latitude, within the Kelvin cat's eye, is the preferred location for tropical cyclogenesis. Numerical simulations suggest that the so-called "bottom-up" pathway to tropical cyclogenesis is favored within Typhoon Man-yi's critical layer.

Additionally, Tropical Rainfall Measurement Mission (TRMM) composite analyses of 55 developing easterly waves indicate that as genesis approaches, i) convection is favored in the Kelvin cat's eye circulation, ii) the convective contribution to total rain rate becomes dominant, iii) the radius of maximum convection decreases, and iv) a convective-type heating profile is present. These findings support the "bottom-up" development model within easterly wave critical layers.

THIS PAGE INTENTIONALLY LEFT BLANK

TABLE OF CONTENTS

I.	INTRODUCTION.....	1
II.	OVERVIEW OF SYNOPTIC AND MESO- α SCALE ASPECTS OF THE TROPICAL CYCLOGENESIS SEQUENCE WITHIN THE CRITICAL LAYER OF TROPICAL EASTERLY WAVES.....	7
A.	THEORETICAL CONSIDERATIONS REVISITED	7
B.	ECMWF ERA-40 COMPOSITE ANALYSES	11
III.	THE EVOLUTION OF PRECIPITATION WITHIN THE CRITICAL LAYER OF 55 DEVELOPING EASTERLY WAVES AS SEEN BY THE TRMM TMI	21
A.	INTRODUCTION.....	21
B.	DATA AND METHODOLOGY	22
C.	RESULTS	24
1.	Radial Averages	24
2.	Spatial Distribution.....	27
D.	SUMMARY AND DISCUSSION	31
IV.	THE GENESIS OF TYPHOON NURI AS OBSERVED DURING THE TCS-08 FIELD EXPERIMENT: THE ROLE OF THE EASTERLY WAVE CRITICAL LAYER.....	35
A.	INTRODUCTION.....	35
B.	DATA AND METHODOLOGY	37
1.	Data	37
2.	Summary of Aircraft Missions	38
3.	Analysis Methodology.....	41
a.	<i>GFS FNL</i>	41
b.	<i>Real-Time Marsupial Forecasts</i>	41
C.	RESULTS	43
1.	Evolution of the Easterly Wave Precursor (12Z 7 August–00Z 10 August)	43
2.	Maintenance of the Pouch Through a Hostile Environment (12Z 10 August–00Z 15 August)	47
3.	Reinvigoration of Convection and Initiation of the Genesis Sequence (12Z 15 August–12Z 17 August)	53
4.	Consideration of Other Possible Factors in the Formation of Typhoon Nuri	61
a.	<i>The Possible Role of a Monsoon Trough</i>	61
b.	<i>The Possible Role of a TUTT</i>	67
5.	Evaluation of Real-time Forecasts (00Z 11 August–12Z 17 August)	67
D.	INTERPRETIVE DISCUSSION.....	70
E.	CONCLUSIONS AND FUTURE WORK.....	76

V.	TESTING THE HYPOTHEZIZED ROLE OF AN EQUATORIAL ROSSBY WAVE CRITICAL LAYER IN THE GENESIS OF SUPER TYPHOON MAN-YI—PART I: SYNOPTIC-SCALE OBSERVATIONS AND ANALYSES	79
A.	INTRODUCTION.....	79
1.	Paradigms of Tropical Cyclogenesis in the Western North Pacific Sector	79
2.	Theoretical and Observed Characteristics of n=1 ER Waves	81
3.	Synoptic-scale Background Relevant to the Formation of Typhoon Man-yi (2007)	82
B.	DATA AND METHODOLOGY	85
1.	Observational and Analyses Data.....	85
2.	Wave Tracking	85
C.	GFS FNL SYNOPTIC AND MESO- α SCALE EVOLUTION	86
1.	GFS FNL Solution.....	86
2.	The Origin of Typhoon Man-yi's Proto-vortex.....	98
D.	OBSERVATIONS OF SYNOPTIC-SCALE FEATURES	105
1.	QuikSCAT Observations.....	105
2.	MTSAT IR and TRMM Observations.....	110
E.	DISCUSSION	114
1.	Prevailing Paradigms of Tropical Cyclogenesis in the Western North Pacific Sector	114
2.	Marsupial Analysis	118
VI.	TESTING THE HYPOTHEZIZED ROLE OF AN EQUATORIAL ROSSBY WAVE CRITICAL LAYER IN THE GENESIS OF TYPHOON MAN-YI PART II: MESOSCALE OBSERVATIONS AND NUMERICAL SIMULATIONS	119
A.	INTRODUCTION.....	119
1.	Background	119
2.	Numerical Simulations	121
B.	DESCRIPTION OF NUMERICAL SIMULATIONS.....	122
1.	Model Configuration	122
2.	Model Initial Conditions.....	123
C.	ANALYSIS OF THE NUMERICAL SIMULATIONS.....	124
1.	Wave Tracking	124
2.	The Marsupial Sequence on the Synoptic and Meso- α Scales.....	125
3.	The Tropical Cyclogenesis Model on the Meso- β /Meso- γ Scales.....	129
a.	<i>Evaluation of “Bottom-up” vs. “Top-down”</i>	129
b.	<i>The Evolution of Precipitation and VHTs</i>	132
4.	Differences in Cyclone Evolution Between the Three Numerical Simulations	141
D.	SUMMARY	146
VII.	CONCLUSIONS AND FUTURE WORK.....	149
A.	CONCLUSIONS	149

B. FUTURE WORK	152
APPENDIX A: GLOSSARY.....	155
APPENDIX B: ADDITIONAL FINDINGS FROM THE TRMM DATA DISTRIBUTION AND INITIAL RESULTS FROM THE TRMM PR PRECIPITATION OBSERVATIONS	157
A. THE DISTRIBUTION OF TRMM 2A12 DATA.....	157
B. ADDITIONAL ANALYSIS OF TRMM PRECIPITATION AND LATENT HEATING PROFILES	163
1. Analysis of Areal Coverage of Precipitation	165
2. Additional Analysis of TRMM Rain Rate Data	172
3. Preliminary Analysis of TRMM PR Vertical Latent Heating Profiles	175
APPENDIX C: ADDITIONAL CONSIDERATION ON THE TROPICAL CYLCOGENESIS OF TYPHOON NURI.....	181
A. SUPPLEMENTARY COMMENTS ON THE ORIGIN AND EVOLUTION OF THE PRECURSOR WAVE.....	181
B. DISCUSSION OF OTHER POSSIBLE FACTORS IN TYPHOON NURI'S GENESIS	185
APPENDIX D: TRMM PR OBSERVATIONS OF TYPHOON MAN-YI	191
A. BACKGROUND	191
B. TRMM PR PRECIPITATION DISTRIBUTION AND LATENT HEATING PROFILES.....	192
C. DISCUSSION	205
LIST OF REFERENCES	207
INITIAL DISTRIBUTION LIST	217

THIS PAGE INTENTIONALLY LEFT BLANK

LIST OF FIGURES

Figure 1.	Schematic of the evolution of a nonlinear critical layer over time (adapted from Andrews et al. 1987). The thin black lines are streamlines and the purple line is the critical line (or critical latitude) of linear wave theory. This is the location where the wave's intrinsic frequency vanishes or where the wave's phase speed coincides with the zonal mean flow. Cyclonic vorticity is represented by white area in the stable case and the shading in the unstable case. The red oval indicates the Kelvin cat's eye circulation.	8
Figure 2.	Flow schematic of an idealized tropical easterly wave. The green dashed streamlines represent an idealized easterly wave in background easterly flow in the resting frame. The purple line is the critical latitude in linear theory and the thick black line is the wave trough axis. The thick black streamlines represent the Kelvin cat's eye of this small, but finite amplitude easterly wave. Pink scalloping represents convection within the wave pouch (adapted from Wang et al. 2010a).	11
Figure 3.	Composite analyses of 700 hPa low-pass filtered ERA-40 data for the 55 storms studied by DMW09. The black lines are streamlines in the resting (left) and co-moving (right) frames. In the co-moving frame, the thick black line is the wave trough and the purple line is the critical latitude, defined as $u = \bar{c}_p$. The shading is OW ($\times 10^{-10} \text{ s}^{-2}$). The abscissa is longitude and the ordinate latitude.....	16
Figure 4.	ERA-40 composite analyses for the 55 storms presented in DMW09 plotted by basin, with the Atlantic on the left and the eastern Pacific on the right. For each basin the black lines indicate streamlines in the resting (left column) and co-moving (right columns) frames. In the co-moving frame, the thick black line is the wave trough and the purple line is the critical latitude, defined as $u = \bar{c}_p$. The shading is OW ($\times 10^{-10} \text{ s}^{-2}$). The abscissa is longitude and the ordinate latitude.....	17
Figure 5.	Time height cross sections of key meteorological variables averaged within a $3^\circ \times 3^\circ$ box moving with the center of the sweet spot. The abscissa is time (h) prior to genesis declaration by NHC and the ordinate is pressure (hPa). The variables plotted are OW ($\times 10^{-10} \text{ s}^{-2}$), divergence ($\times 10^{-5} \text{ s}^{-1}$), relative circulation ($\text{km}^2 \text{ k s}^{-1}$), and relative vorticity ($\times 10^{-5} \text{ s}^{-1}$).....	18
Figure 6.	Latitudinal cross-sections through the center of the sweet spot at 12-hour intervals prior to tropical cyclogenesis from the low-pass filtered ERA-40 data. The left column is relative vorticity ($\times 10^{-5} \text{ s}^{-1}$) and the right column is divergence ($\times 10^{-5} \text{ s}^{-1}$). The abscissa is latitude and spans the 31 ERA-40 grid points and the ordinate is pressure 1000–200 hPa.....	19
Figure 7.	Radial plots of TRMM TMI precipitation: CRR (+) and STRR (o), normalized by annulus area ($\text{mm h}^{-1} \text{ km}^{-2}$) plotted as radial distance from	

the sweet spot position. Green lines represent the T3 time, red is the T2 time, and blue is the T1 time.....	25
Figure 8. Scatter plots of TRMM 2A12 convective (red) and stratiform (green) rain rates (mm h^{-1}) by radius for each time period.	26
Figure 9. Radial plots of number of convectively dominated heavy precipitation pixels ($\# \text{ km}^{-2}$) for the three time periods.	27
Figure 10. Contour plots of TRMM TMI normalized rain rate data ($\text{mm h}^{-1} \text{ pixel}^{-1}$) within the composite pouches plotted by precipitation type (rows) and time (columns). The composite pouches are oriented geographically with the top being north.	29
Figure 11. Sensitivity test of the TRMM 2A12 normalized rain rate data ($\text{mm h}^{-1} \text{ pixel}^{-1}$) within the composite pouches. The position of the sweet spot at each pouch/TRMM satellite intersection is recalculated by randomly adding phase speed errors within ± 1 standard deviation to the original wave propagation speed. Layout is as in Figure 10.	31
Figure 12. Timeline of key events during the observational period of Typhoon Nuri during the TCS08 field experiment between 12Z 15 August and 12Z 19 August 2008.	39
Figure 13. Schematic of original flight plans for the USAF C130 flights centered on 00Z 16 August (top) and 00Z 17 August (bottom). The green lines are 850 hPa streamlines in the resting frame and the shading is relative vorticity ($\times 10^5 \text{ s}^{-1}$) derived from ECMWF forecast data. The large blue circles indicates Guam, the smaller gray circles highlight the predicted sweet spot position, and the red circles indicate locations where dropwindsondes were planned to be released. The streamline analysis clearly depicts the presence of an open wave (top) approaching Guam. The red lines highlight the ‘lawn-mover’ pattern that is centered along the wave trough (top). In the bottom panel, the ‘square spiral’ pattern used during the second mission has the USAF C130 spiraling inward toward the forecasted sweet spot position.....	40
Figure 14. CIMMS Morphed TPW time series valid at 12-hour intervals beginning at 12Z 6 August. The red oval highlights the ITCZ roll-up event that is proposed to be the origin of the pre-Nuri disturbance.	45
Figure 15. Latitudinally-averaged (9–17N) GFS FNL TPW Hovmoeller diagram valid 00Z 6 August–12Z 17 August (the time when the precursor Nuri disturbance is upgraded to a TS). The black oval highlights the higher moisture content observed in the pouch of the pre-Nuri disturbance versus its surrounding environment.	46
Figure 16. GFS FNL location of the sweet spot (blue triangles) valid at 12-hour intervals from 12Z 7 August–12Z 17 August. The thick black line delineates the time of the change in phase speeds used to calculate the sweet spot location. JTWC Best Track positions are indicated (red) at 12-hour intervals beginning at 00Z 16 August. An open circle designates an invest and a closed circle a TD. TS and typhoon symbols are shown when storm upgrades occurred.	47

Figure 17.	Four-day time series of CIMMS Morphed TPW valid at 12Z each day. Red arrows point to the location of the pouch, which is hypothesized by DMW09 to be an area of increased moisture in the low to mid-troposphere. The wave pouch protects the proto-vortex from lateral intrusions of dry air.....	49
Figure 18.	NRL Stennis oceanic HHC analysis valid 12Z 15 August overlaid with the track of the sweet spot from the GFS FNL analyses (solid blue triangles). The red oval indicates the area of higher HHC that the pouch passes over from the time convection is reinvigorated (12Z 15 August) until a TS is declared.....	50
Figure 19.	GFS FNL 850–200 hPa shear (kt, shaded), 925 hPa streamlines in the co-moving frame, and sweet spot location (solid blue triangles) valid at 12Z each day.	52
Figure 20.	Time series of depth of areally-averaged positive OW (shaded) over time from the GFS FNL. The OW is areally-averaged within a $3^\circ \times 3^\circ$ box centered on and moving with the sweet spot at the 925 hPa level. The depth of positive OW is considered an estimate of the vertical depth of the pouch. The thick black lines delimit key time periods in pre-Typhoon Nuri's evolution as described in this study. TD and TS indicate JTWC upgrades of the storm.....	53
Figure 21.	Time series of GFS FNL 925 hPa streamlines in the resting frame overlaid with MTSAT IR brightness temperature valid every 12 hours from 12Z 15 August to 12Z 17 August.....	55
Figure 22.	Time series of GFS FNL 925 hPa streamlines in the co-moving frame overlaid with MTSAT IR brightness temperature valid every 12 hours from 12Z 15 August to 12Z 17 August. The black line represents the wave trough axis and the purple line the critical latitude as seen by the wave plus sub-synoptic scale flow. The thick black line indicates the approximate propagation of the sweet spot	56
Figure 23.	Combined USAF C130 and NRL P3 850 hPa dropwindsonde observations from the genesis flight centered on 00Z 16 August overlaid with MTSAT IR data. Wind barbs are in the resting (top) and co-moving (bottom) frames. Wind speeds are in knots with a full barb representing 10 kt. Magenta barbs indicate winds with a westerly component in the earth-relative frame. The red cross represents the location of Guam and the blue triangle represents the location of the low-level cyclonic circulation center in the co-moving frame. The C130 flight was centered along the wave trough axis and collected data throughout the pouch.....	57
Figure 24.	GFS FNL 925 hPa streamlines in the resting (left) and co-moving (right) frames overlaid with MTSAT IR brightness temperature valid 12Z 16 August. In the co-moving frame, the black line represents the wave trough axis and the purple line the critical latitude. The red arrows indicate the convective bands spiraling cyclonically inward towards the sweet spot in the co-moving frame. The black dot represents the JTWC Best Track position.....	59

Figure 25.	Combined USAF C130 and NRL P3 850 hPa dropwindsonde observations from the second genesis flight centered on 00Z 17 August in the resting (top) and co-moving frames (bottom). Wind speeds are in knots with a full barb representing 10 kt.....	60
Figure 26.	CIMMS low-level cloud drift winds (top) valid 06Z 15 August and QuikSCAT Level-3 retrieved wind vectors and wind speed (shaded) valid 15 August (bottom). The blue wind barbs in the CIMMS product are retrievals between the levels of 950–851 hPa and the yellow are retrievals between 850–700 hPa. The red circle highlights the easterly wave that is the precursor to Typhoon Nuri and the red line indicates the easternmost extent of large-scale organized westerly flow. Note that westerly winds are more than 10 degrees from the pre-Nuri disturbance in both analyses.....	65
Figure 27.	Six-panel time series of AAMF ($\times 10^7 \text{ m}^3 \text{ s}^{-2}$) from the GFS FNL. The AAMF are calculated at radial distances from the sweet spot. The abscissa is radial distance ($\times 100\text{km}$) from the sweet spot and the ordinate is pressure.....	66
Figure 28.	Real-time 72-hr NOGAPS forecast for the potential genesis of Typhoon Nuri. Model initialization time is 12Z 14 August and is valid at 12Z 17 August (time of TS declaration by JTWC). The left panel is 925 hPa streamlines in the co-moving frame with OW (shaded), the wave trough (black line), critical latitude (purple line), and location of Guam (red plus). The right panels are area-averaged diagnostics calculated within a $3^\circ \times 3^\circ$ box moving with the pouch so as to quantify the dynamic features within the pouch. The top depicts average relative vorticity (green trace) and the average square root of OW (red trace). The bottom is detrained volume flux. Unplotted data in the vertical profile are due to missing model data at that level.....	69
Figure 29.	Thirty-six hour (00Z 16 August–12Z 17 August) GFS FNL time series encapsulating the genesis phase of Typhoon Nuri. Thin black line are 925 hPa streamlines in the co-moving frame, OW is shaded, the thick black line is the wave trough axis, and the purple line the critical latitude. The black dot indicates the JTWC Best Track position. The OW increases in intensity and centers on the sweet spot as genesis nears.	72
Figure 30.	Summary of idealized numerical simulation of the spatial and temporal evolution of precipitation within the critical layer of a developing easterly wave (Montgomery et al. 2010a). The time series depicts surface rain rate (mm h^{-1}), 850 hPa streamlines in the co-moving frame, the wave trough (thick black line), and critical latitude (purple line) at 12-hour intervals beginning 120 hours into the model run. The abscissa is longitude and the ordinate is latitude. The simulated evolution of precipitation is consistent with the observed data in the pre-Nuri case.....	75
Figure 31.	Idealized solution of Matsuno's (1966) $n=1$ ER wave, negative contours are dashed. Shading represents areas of convergence and hatching is divergence. From Kiladis and Wheeler (1995).....	82

Figure 32.	Track of Typhoon Man-yi from 8–23 July (Digital Typhoon 2010). The colored circles indicate storm intensity, with blue a TD, green a TS, red a typhoon, and purple denoting the transition to an extratropical system.	83
Figure 33.	GFS FNL streamlines (resting) and relative vorticity (shaded $\times 10^{-5} \text{ s}^{-1}$) at the 850 hPa level, valid every six hours from 00Z 3 July–18Z 7 July. The red line denotes the equator.	91
Figure 34.	Two-panel Hovmoeller diagram of AAMF ($\times 10^7 \text{ m}^3 \text{ s}^{-2}$) from the GFS FNL for the tropical cyclogenesis sequence of Typhoon Man-yi. The abscissa is radial distance ($\times 100\text{km}$) from the sweet spot and the ordinate is time.....	95
Figure 35.	Six-panel time series of symmetric RAM fluxes ($\times 10^6 \text{ m}^3 \text{ s}^{-2}$) in the vertical from the GFS FNL. The fluxes are calculated at radial distances from the sweet spot. The abscissa is radial distance ($\times 100\text{km}$) from the sweet spot and the ordinate is pressure. Warm colors are negative symmetric RAM fluxes and cool colors are positive symmetric RAM fluxes.....	96
Figure 36.	Six-panel time series of symmetric RAM fluxes ($\times 10^6 \text{ m}^3 \text{ s}^{-2}$) in the vertical from the GFS FNL. The fluxes are calculated at radial distances from the sweet spot. The abscissa is radial distance ($\times 100\text{km}$) from the sweet spot and the ordinate is pressure. Warm colors are negative symmetric RAM fluxes and cool colors are positive symmetric RAM fluxes.....	97
Figure 37.	Time series of GFS FNL 850 hPa relative vorticity ($\times 10^{-5} \text{ s}^{-1}$) valid 00Z 3 July–12Z 7 July. Latitudinal range is 0–10N. The circles/arrows highlight key features in Typhoon Man-yi’s tropical cyclogenesis sequence. Purple represents the ER wave, blue is Typhoon Man-yi’s proto-vortex, red is the monsoon trough, and orange are easterly waves.	100
Figure 38.	Hovmoeller diagram of GFS FNL latitudinal-averaged (2–10N) meridional wind and relative vorticity ($\times 10^{-5} \text{ s}^{-1}$). The dashed red line is used to derive the phase speed of the ER wave.	101
Figure 39.	850 hPa GFS FNL streamlines in the co-moving frame and relative vorticity ($\times 10^{-5} \text{ s}^{-1}$, shaded) valid at 12 hour intervals from 06Z 3 July–18Z 6 July. The purple cross indicates the location of the sweet spot.	102
Figure 40.	GFS FNL 1000 hPa streamlines in the earth-relative frame and divergence ($\times 10^{-5} \text{ s}^{-1}$, shaded). Note the strong area of low-level convergence ahead of the ER wave’s twin cyclones.....	103
Figure 41.	850 hPa GFS FNL streamlines in the co-moving frame and relative vorticity ($\times 10^{-5} \text{ s}^{-1}$, shaded) valid at 6-hour intervals from 00Z 8 July–18Z 8 July. The purple cross indicates the location of the sweet spot.	104
Figure 42.	QuikSCAT surface wind vectors (m s^{-1}) and GFS FNL 1000 hPa streamlines (blue) valid 06Z 3 July.....	106
Figure 43.	As in Figure 42, except valid 18Z 3 July.....	107
Figure 44.	QuikSCAT Level-3 surface wind vectors (m s^{-1}) plotted every 0.5° overlaid with the position of the monsoon trough in QuikSCAT observations (black) and GFS FNL (blue). The position of the monsoon	

trough is defined as the location where $u=0$ and there is cyclonic relative vorticity in the Northern Hemisphere.	108
Figure 45. As in Figure 42, except valid 06Z 6 July.	109
Figure 46. QuikSCAT (top) and GFS FNL (bottom) low-level streamline analysis valid 18Z 7 July (left) and 06Z 8 July (right). The blue dots represent the position of the GFS FNL low-level cyclonic circulation center.	110
Figure 47. Hovmoeller diagram of MTSAT latitudinally-averaged (0–10N) IR brightness temperature ($^{\circ}$ C). The horizontal white lines indicate missing data. Key features are highlighted. The blue box highlights the suppressed convection as the ER wave propagated westward.....	111
Figure 48. TRMM 3B42 24-hour accumulated surface rain (mm) with 850 hPa streamlines in the resting frame from the GFS FNL valid 18Z 4 July–18Z 6 July. Figure courtesy of Dr. Zhuo Wang.	113
Figure 49. TRMM 3B42 24-hour accumulated surface rain (mm) with 850 hPa streamlines in the resting frame from the GFS FNL valid 06Z 7 July. Figure courtesy of Dr. Zhuo Wang.	114
Figure 50. Schematic of the hypothesized tropical cyclogenesis sequence of Typhoon Man-yi on the synoptic and meso- α scales in the lower-levels of the troposphere. The red hatching are areas of cyclonic relative vorticity, the dashed line depicts the monsoon trough, the solid line indicates the location of the equator, and the circles with arrows indicate closed low-level circulations.	117
Figure 51. Initial conditions for the WRF numerical simulations. The black lines are streamlines in the resting frame and the shading is relative vorticity (s^{-1}). The boxes indicate the approximate location/size of inner three domains (d02–d04) of the numerical simulations.	123
Figure 52. Hovmoeller diagram of latitudinally-averaged (0–12N) SF (%), shaded and meridional wind ($m s^{-1}$, contours) for the outer domain (d01) of the KF1 WRF simulation. The red dashed line is used to derive the phase speed based on the moisture gradient and the blue dashed line is used to derive the phase speed based on the location of wave trough ($\bar{v} = 0$).	125
Figure 53. Eight panel plot of 850 hPa streamlines in the co-moving (left) and resting frames (right) from the KF1 d01 simulation valid every 12 hours from 06Z 7 July. The shading indicates relative vorticity (s^{-1}) and the purple plus sign in the co-moving frame indicates the location of the sweet spot.	127
Figure 54. As in Figure 53, except for SF (%), shaded)....	128
Figure 55. Time-height cross-section relative vorticity (s^{-1} , top), divergence (s^{-1} , middle), and relative humidity (%), bottom) averaged in a $3^{\circ} \times 3^{\circ}$ box centered on the sweet spot and moving with the parent wave.	131
Figure 56. Three-hour accumulated precipitation (mm) from the KF1 d04 simulation overlaid with 850 hPa streamlines in the co-moving frame. The thick black line is the wave trough and the purple line is the critical latitude. The panels are valid at three-hour intervals beginning at 00Z 8 July.....	133
Figure 57. Precipitation type time series from the KF1 d04 simulation laid out as in Figure 56. Green shading represents stratiform pixels and red convective..	135

Figure 58.	Percent coverage of stratiform (left) and convective (right) rain types plotted by radial distance from the sweet spot. The data are from the KF d04 simulation and are plotted with a five point running mean.	136
Figure 59.	Time series of KF1 d04 850 hPa relative vorticity (s^{-1} , shaded) and upward vertical motion ($m s^{-1}$, black contours) are shown in the left column. Surface θ_e ($^{\circ}\text{K}$) is in the right column. Both columns are overlaid with streamlines in the co-moving frame. The thick black line is the wave trough and the purple line is the critical latitude. The time series is valid at 12 minute intervals from 13:48Z–15:12Z 8 July. Areas of interest are labeled A–C.....	138
Figure 60.	As in Figure 59 except valid 17:24Z–18:00Z 8 July.	140
Figure 61.	Time evolution of key meteorological variables for d01 of each simulation.....	142
Figure 62.	850 hPa streamlines (co-moving) and relative vorticity ($\times 10^5 s^{-1}$, shaded) from the BMJ d01 simulation valid at 12-hour intervals beginning at 06Z 7 July. The purple plus sign indicates the location of the sweet spot.	144
Figure 63.	Cross-sections of relative vorticity ($\times 10^{-4} s^{-1}$) from the BMJ d03 simulation centered on the latitude of the building vorticity monolith. Plots are every three hours beginning at 15Z 7 July.....	145
Figure 64.	Contour plot of number of TRMM TMI retrievals in each bin for the composite pouches by time (columns) and type (rows).....	158
Figure 65.	Deviation from the mean number of area normalized pixel counts for the TRMM 2A12 data. Layout as in Figure 64.....	160
Figure 66.	Number of standard deviations from the mean for the area normalized pixel count TRMM 2A12 data. Layout as in Figure 64.....	161
Figure 67.	Radial distribution of TRMM 2A12 retrievals in each annulus by time: total pixel counts (top); and pixel counts normalized by annulus area (# km^{-2} , bottom).	162
Figure 68.	Schematic illustrating idealized latent heating profiles for different precipitation distributions. (a) Observed by Houze (1982, 1989, 1997); (b) hypothesized by Montgomery et al. (2010a) and Wang et al. (2010b); and (c) hypothesized in Section III. The red line indicates the addition latent heating expected during vigorous convective events (i.e., Olson et al. 1999).	165
Figure 69.	Percent contribution of each rain type, stratiform (o) and convective (+), to total rain rate by radius and time.....	167
Figure 70.	As in Figure 67, except for the TRMM PR data.....	170
Figure 71.	Boxplots for the area normalized pixels distribution (# km^{-2}) within each annulus for the TRMM 2B31 data.	171
Figure 72.	Percent contribution to total rain coverage by each rain type (CRR, STRR, anvil rain [ARR], and shallow rain [SHRR]), within the composite pouches derived from the TRMM PR 2A25 data. These data are plotted as a six-hour running mean to reduce high frequency fluctuations arising from the limited sample size.....	172

Figure 73.	Hovmoeller diagrams of area-normalized rain rates (mm km^{-2}) from the TRMM TMI 2A12 data. These data are plotted by precipitation type with STRR on the left and CRR on the right. The abscissa is time and the ordinate is radial distance from the sweet spot. These data are plotted as six-hour running totals to eliminate high frequency variations.	174
Figure 74.	As in Figure 73 except for the TRMM PR data.....	175
Figure 75.	TRMM 2B31 retrieved latent heating profiles for the T3 composite pouch. These data are average heating per pixel ($^{\circ}\text{K h}^{-1}$), which retrieved a latent heating value. The top panel is a radial height cross-section of latent heating per pixel within each annulus and the bottom is latent heating per pixel within the 1° and 3° radii. The dotted lines represent the error bounds of the retrievals.....	178
Figure 76.	As in Figure 75, except for T2.....	179
Figure 77.	As in Figure 75, except for T1.....	180
Figure 78.	Time series of 850 hPa GFS FNL relative vorticity ($\times 10^{-5} \text{ s}^{-1}$, left) and OW ($\times 10^{-9} \text{ s}^{-2}$, right) beginning at 00Z 9 August. The location of Typhoon Nuri's initial vorticity seedling at this time is 172W. The vorticity/OW maxima entering the domain from the east at 06Z 11 August is Tropical Storm Kika. The abscissa longitude and the ordinate latitude ranging from 5–20N.....	182
Figure 79.	Time series of NRL stitched IR imagery. Images are valid at 00Z and 12Z from 8–10 August. The red oval highlights the cloud features associated with the pre-Nuri wave pouch.....	183
Figure 80.	Time series of IR imagery valid at 00Z (right) and 12Z (left) for the time period between 11–14 August. The red oval highlights the cloud features associated with the pre-Nuri wave pouch.....	184
Figure 81.	GFS FNL 1000–500 hPa steering flow. The magnitude (m s^{-1}) of the average flow from 12Z 7 August–12Z 17 August (contours) and direction (vectors) are plotted. The thick black line represents the point at which the average phase speed of the wave decreased. The symbols are positions of the sweet spot as in Figure 16.....	185
Figure 82.	Skew-T plots from Koror, Palau showing the low-level westerly flow (left) and the cessation of this flow (right).....	186
Figure 83.	Skew-T diagrams from Guam. The time evolution of the low-mid level wind field in these plots shows the pre-Nuri easterly wave passing over the island.....	187
Figure 84.	GFS FNL 1000 hPa wind field valid at six-hour intervals beginning 06Z 15 August. The black lines are streamlines in the resting frame and the red shading indicates areas with a westerly wind component. The blue circle is Guam and the blue square is Palau.....	188
Figure 85.	CIMMS upper-level cloud drift wind plots valid: 12Z 14 August (top), 15Z 15 August, and 00Z 16 August. The red circles highlight potential TUTT activity. The red arrows point to the pre-Nuri disturbance. The cyan barbs are winds at 100–250 hPa level, the yellow barbs are winds at 251–350 hPa level, and the green barbs are winds at 351–500 hPa level.	189

Figure 86.	Percent coverage of the TRMM PR within each 0.25° radius annulus for the four cases used in this study. The blue line represents the total number of retrievals and the red line is the number of latent heating retrievals.....	194
Figure 87.	Two panel plot of TRMM PR pass (top), valid 4 July 2024Z and MTSAT IR image (bottom) with a BD enhancement, valid 2030Z. The TRMM image depicts 2A25 rain type. Purple colors are stratiform precipitation, green pixels are convective precipitation, orange is shallow convective precipitation, and red is anvil precipitation. The light blue coloring indicates no rain observed at that location. The dark blue and yellow pixels represent uncertain retrievals of stratiform and convective precipitation. The yellow line on the IR image represents the approximate center of the TRMM PR pass. The plus signs indicate the approximate position of the GFS FNL derived sweet spot and the red circles indicate the 5° radius circles used as an approximation of the wave pouch.....	197
Figure 88.	TRMM 2B31 retrieved latent heating profiles for the 2024Z 4 July pass through the wave pouch of the pre-Man-yi disturbance. The plot depicts average heating per pixel within the 3° (blue) and 5° (green) radii. The dotted lines represent the error bounds of the retrievals.....	198
Figure 89.	As in Figure 87, except valid 21Z 6 July (TRMM) and 2130Z (MTSAT IR).	199
Figure 90.	TRMM 2B31 retrieved latent heating profiles for the 21Z 6 July pass through the wave pouch of the pre-Man-yi disturbance. Both plots are average heating per pixel ($^\circ\text{K h}^{-1}$). The top is a radial height cross-section of heating and the bottom is latent heating per pixel within the 1° (red), 3° (blue), and 5° (green) radii. The dotted lines represent the error bounds of the retrievals.....	200
Figure 91.	As in Figure 87, except valid 06Z 7 July (TRMM) and 0630Z (MTSAT IR).	201
Figure 92.	As in Figure 90, except valid 06Z 7 July. The red line indicates heating within the 1° radius.....	202
Figure 93.	As in Figure 87, except valid 20Z 8 July (TRMM) and 2030Z (MTSAT IR).	203
Figure 94.	As in Figure 90, except valid 20Z 8 July.....	204
Figure 95.	Percent contribution of each precipitation type to total precipitation coverage from the TRMM PR for the four passes used in this study. The blue line is convective coverage, the red is stratiform coverage, the green is anvil coverage, and the yellow is shallow convective coverage.....	206

THIS PAGE INTENTIONALLY LEFT BLANK

LIST OF TABLES

Table 1.	Summary of WRF numerical simulations.....	124
----------	---	-----

THIS PAGE INTENTIONALLY LEFT BLANK

LIST OF ACRONYMS AND ABBREVIATIONS

AEW	African Easterly Wave
AAM	Absolute Angular Momentum
AAMF	Absolute Angular Momentum Flux
ANOVA	Analysis of Variance
ARR	Anvil Rain Rate
ATOLL	Analysis of the Tropical Oceanic Lower Level
AXBT	Airborne Expendable Bathometry Thermograph
BMJ	Betts-Miller-Janjic
CAPE	Convective Available Potential Energy
CIMMS	Cooperative Institute for Meteorological Satellite Services, University of Wisconsin
CIN	Convective Inhibition
CRR	Convective Rain Rate
CSH	Convective Stratiform Heating Algorithm
DB	Depression Beginning
ELDORA	Electra Doppler Radar
ECMWF	European Center for Medium-range Weather Prediction Forecasts
ER	Equatorial Rossby
ERA-40	ECMWF Reanalysis Data
ESMR	Electrically Scanning Microwave Radiometer
EW	Easterly Wave
GFS FNL	Global Forecast System Final Analysis
HHC	Oceanic Hurricane Heat Content
IFS	International Forecast System
IR	Infrared
ITCZ	Inter-tropical Convergence Zone
JAXA	Japan Aerospace Exploration Agency
JTWC	Joint Typhoon Warning Center
KF	Kain-Fristch
MTSAT	Multi-Functional Transport Satellite

MCS	Mesoscale Convective System
MCV	Mesoscale Convective Vortex
MRG	Mixed Rossby Gravity Wave
NASA	National Aeronautics and Space Administration
NCEP	National Center for Environmental Prediction
NHC	National Hurricane Center
NOGAPS	Naval Operational Global Atmospheric Prediction System
NRL	Naval Research Laboratory
OW	Okubo-Weiss Parameter
PR	Precipitation Radar
PV	Potential Vorticity
RAM	Relative Angular Momentum
RH	Relative Humidity
RRTM	Rapid Radiative Transfer Model
SF	Saturation Fraction
SLH	Spectral Latent Heating Algorithm
SFMR	Stepped Frequency Microwave Radiometer
SHRR	Shallow Rain Rate
SRR	Surface Rain Rate
STD	Standard Deviation
STRR	Stratiform Rain Rate
TC	Tropical Cyclone
TCM-93	Tropical Cyclone Motion 1993
TCS-08	Tropical Cyclone Structure 2008
TD	Tropical Depression
TMI	Microwave Imager
TPW	Total Precipitable Water
TRMM	Tropical Rainfall Measurement Mission
TS	Tropical Storm
TUTT	Tropical Upper Tropospheric Trough
UKMO	United Kingdom Meteorological Office
UM	Unified Model

USAF	United States Air Force
VHT	Vortical Hot Tower
WRF	Weather Research and Forecasting Model

THIS PAGE INTENTIONALLY LEFT BLANK

ACKNOWLEDGMENTS

I would like to thank my dissertation committee: Professor Pat Harr, who memorably uttered, “because it’s the only game in town, Lou” as I questioned why I had to get up at 0100L to fly through TCS025 (i.e., “that crap to the north”) again. Persistence paid off, though, as I was able to fly four missions through Typhoon Nuri and examine its life cycle from easterly wave to typhoon. Professor Rich Moore, who actually likes TCS025 and still owes a climatology of formation cases in the western North Pacific basin. Professor Frank Giraldo, the first instructor I had at NPS and who stuck around to the end. A special thanks to Dr. Zhuo Wang, who was always there to provide help/knowledge/insight throughout this entire process. Thanks to my dissertation advisor, Professor Mike Montgomery, who made it possible for me to achieve many of these experiences. His undying enthusiasm and support are infectious and it motivated me to learn, investigate, and advance the understanding of the tropical cyclogenesis problem.

A special thanks to Bob Creasy, who always seemed to have a solution to my problems. Additional thanks go to all of the other PhD students that passed through NPS with me; especially Mark Allen, my office mate with whom I spent more time over the last three years than anyone else. Additionally, I would like to thank everyone I spent time with on Guam (including Jeff Hawkins, with whom I spent too many hours in the back of a C130). The opportunity to participate in a field campaign and fly through typhoon was a once in a lifetime opportunity. Thanks to Tim Dunkerton for his advice and knowledge throughout the process and Michael Riemer for everything, except his knowledge on ER waves.

Finally, I would like to thank my family: my son, Alexander, who ensured that I was unable to sleep while trying to finish this dissertation. My best friend Charlotte, who could always bring a smile to my face. Finally, to my wife, Jennifer, who likely sacrificed the most as I went through this process. I cannot possibly thank her enough.

THIS PAGE INTENTIONALLY LEFT BLANK

I. INTRODUCTION

Although some aspects of the transformation of atmospheric disturbances into tropical cyclones are relatively well understood, the general problem of tropical cyclogenesis remains in large measure, one of the greatest mysteries of the tropical atmosphere.

– Kerry Emanuel, *The Divine Wind* (2005)

Although advances in the understanding and prediction of some aspects of mature tropical cyclones have improved over recent years (AMS 2007), there remain significant barriers to understanding the problem of tropical cyclogenesis. First, there is no generally agreed upon definition of when tropical cyclogenesis occurs. The *Glossary of Meteorology* (Glickman 2000) defines cyclogenesis as “any development or strengthening of cyclonic circulation in the atmosphere.” This broad definition leads some (e.g., Ooyama 1982; Elsberry 2009) to argue that the term “tropical cyclogenesis” is entirely miscast. Since all tropical cyclone formations occur from a pre-existing disturbance, it can be argued that there is, in fact, no true point at which tropical cyclogenesis occurs. In this work, the sequence of events that leads to tropical cyclone formation is examined, rather than a focusing on a single point in time. Second, in areas where seedling disturbances for tropical cyclones originate and intensify, in-situ observations are almost non-existent. Although satellite coverage has greatly improved observational capability in recent years, there remain spatial and temporal gaps in coverage. Additionally, while there are numerous recognized synoptic-scale flow patterns favorable to tropical cyclogenesis (e.g., tropical waves, monsoon trough, tropical transition), a complete understanding of the complex multi-scale interactions during the transition to a mesoscale vortex is lacking. Finally, field campaigns are few and far between and rarely focus on the genesis stage.¹ A recent field campaign that took place in the western North Pacific basin, Tropical Cyclone Structure 2008 (TCS-08), collected

¹ See Appendix B of Montgomery et al. (2010a) for a summary of recent field campaigns.

data during the tropical cyclogenesis stage. A portion of this data is analyzed in this research to examine the synoptic and mesoscale aspects of tropical cyclogenesis.

In an attempt to address these issues, Dunkerton, Montgomery, and Wang (2009; hereafter DMW09) have proposed a new overarching framework for describing the transition sequence from synoptic-scale easterly wave (EW) to tropical depression (TD). Using the National Hurricane Center (NHC) best track data, National Aeronautics and Space Administration (NASA) Tropical Rainfall Measurement Mission (TRMM) data, and European Center for Medium-range Weather Prediction Forecasts (ECMWF) Reanalysis (ERA-40) data during August and September (1998–2001), they examine tropical cyclone formation from quasi-monochromatic easterly waves in the Atlantic and eastern Pacific basins and propose a dynamical pathway to genesis that holds true in 53/55 cases.²

Montgomery et al. (2010a) concisely summarize the three hypotheses that make up this proposed tropical cyclogenesis sequence. These hypotheses (hereafter H1-H3) describe the flow dynamics, moist thermodynamics, and wave/vortex interactions in which the Kelvin cat's eye within the critical layer³ of a tropical easterly wave is shown to be the location of storm formation. In these cases, formation is observed near the intersection of the wave's critical latitude and trough axis (i.e., the sweet spot). The cat's eye is hypothesized to be important to tropical storm formation because: H1) wave breaking or roll-up of the cyclonic vorticity near the critical surface in the lower troposphere provides a favorable environment for the aggregation of diabatic vortices and their vortical remnants, conditions favorable for tropical cyclone formation, H2) the cat's eye is a region of approximately closed Lagrangian circulation, and air is repeatedly moistened by convection and protected to some degree from dry air intrusion, which favors a predominantly convective type heating profile, and H3) the parent wave is maintained and possibly enhanced by diabatically amplified mesoscale vortices within

² Wang et al. (2010) note that the two remaining storms form in an area of closed circulation when the meridional component of the wave propagation is taken into account.

³ The critical layer is defined in DMW09 as the region surrounding a nonlinear wave's critical latitude in sheared flow. See the Glossary in DMW09 for a definition of all technical terms in reference to the new cyclogenesis model.

the cat's eye. The entire sequence has been referred to as the marsupial paradigm because DMW09 liken it to the development of a marsupial infant in its mother's pouch. In this sequence, the juvenile proto-vortex⁴ is carried along by the mother wave until it is strengthened into a self-sustaining entity.

The first goal of the research presented herein is to advance the ideas put forth by DMW09. The author hypothesizes that this new tropical cyclogenesis model is applicable to tropical cyclogenesis cases: i) in other tropical cyclone basins (specifically the western North Pacific), and ii) for different types of tropical waves.

Although DMW09 focus initially on the Atlantic and eastern Pacific sectors,⁵ the author hypothesizes that the *origin* and *type* of the precursor wave is of secondary importance to their proposed tropical cyclogenesis sequence. Rather, the essential dynamical mechanisms are the ability of the wave's critical layer to provide a focal point for vorticity aggregation and organization, and the wave's ability to provide a protective pouch⁶ for the proto-vortex. If one accepts the premise of the new cyclogenesis model, it seems quite plausible that this new model could be applied to other tropical cyclone basins and for different wave types. Observations and analyses data from two cyclogenesis cases are examined in this dissertation as a way of testing the applicability of the new model in the western North Pacific basin within easterly trade-wind regimes. The specific formations events to be examined are Typhoon Man-yi (2007), which is suggested to have formed from an n=1 equatorial Rossby (ER) wave precursor, and Typhoon Nuri (2008), which is suggested here to have formed from an easterly wave that was observed during the TCS-08 field campaign.

Additionally, it has been suggested (Wang et al. 2010a; Karyampudi and Pierce 2002) that tropical cyclogenesis can be viewed as a two-stage process, with the first stage being a preconditioning of the environment at the synoptic-scale and the second stage consisting of a mesoscale organization into a tropical cyclone strength vortex. There are

⁴ Defined in DMW09 as the initial mesoscale vortical structure within a hybrid diabatic Rossby wave-vortex.

⁵ In DMW09 54/55 cases they examine are from the Atlantic or eastern Pacific basins. The one exception is Hurricane Shangshang, a central Pacific formation case.

⁶ The wave pouch is defined in DMW09 as the flow bounded by the closed streamline that passes through the stagnation point closest to the sweet spot. The region of recirculating quasi-horizontal flow located within is the so-called Kelvin cat's eye circulation.

two competing theories that describe the mesoscale transformation of a tropical disturbance into a tropical cyclone prevalent in the literature today. One theory focuses on the presence of a mid-level positive potential vorticity (PV) anomaly that builds downward to the surface to form the tropical cyclone. The downward building of vorticity is hypothesized to result from a net downward transport of cyclonic vertical vorticity either through the merger of mesoscale convective vortices in the stratiform region of distinct but interacting mesoscale convective systems (Ritchie and Holland 1997) or in association with the downward movement of a stratiform precipitation/evaporation boundary (Bister and Emanuel 1997). Another theory focuses on the collective effects of deep convective clouds forming in vorticity-rich environments. These vortical clouds generate intense cyclonic vorticity in their cores and are generally termed “Vortical Hot Towers” (VHTs). From the buoyancy-induced convergence in the lower troposphere, these clouds generate small-scale positive vorticity anomalies in the lower troposphere, which serve as building blocks of the tropical cyclone vortex. The VHTs, and their vortical remnants, are hypothesized to undergo vortex merger and axisymmetrization with neighboring towers in close proximity. The diabatically-induced secondary circulation that these clouds produce acts in conjunction with the vorticity aggregation processes; together these processes enhance the near-surface positive vorticity and effectively build the tropical cyclone vortex from the “bottom-up” (e.g., Montgomery and Enagonio 1998; Montgomery et al. 2006).

The second hypothesis the author tests is that the “bottom-up” pathway to tropical cyclogenesis is the favored mechanism to transition a synoptic-scale easterly wave to a tropical cyclone within the wave’s critical layer.

Two sources of data are used to examine the applicability of the “bottom-up” formation mechanism within the critical layer of a developing tropical cyclone. First, TRMM observations are used to evaluate the precipitation distribution and the vertical profile of latent heat release within the critical layer of easterly waves. Second, numerical simulations are examined to attempt to understand the mesoscale aspects of the genesis sequence of Typhoon Man-yi. These simulations use the Weather Research and Forecasting (WRF) model and are run at near cloud resolving (3 km horizontal spacing) scales.

This dissertation is presented as follows. Chapter II offers an introduction to this new cyclogenesis model and presents composite analyses from the 55 storms examined in DMW09. Chapter III provides observational evidence of the precipitation distribution within the critical layer of easterly waves and discusses the implications to tropical cyclogenesis. Chapter IV uses analyses and in-situ observations to examine the tropical cyclogenesis sequence of Typhoon Nuri at the synoptic and meso- α scales. Chapter V focuses on the synoptic-scale environment within which Typhoon Man-yi emerges. Chapter VI examines the mesoscale transition of Typhoon Man-yi's critical layer. Chapter VII summarizes the work presented herein and offers pathways for future research.

THIS PAGE INTENTIONALLY LEFT BLANK

II. OVERVIEW OF SYNOPTIC AND MESO- α SCALE ASPECTS OF THE TROPICAL CYCLOGENESIS SEQUENCE WITHIN THE CRITICAL LAYER OF TROPICAL EASTERLY WAVES

A. THEORETICAL CONSIDERATIONS REVISITED

To optimally visualize this newly proposed tropical cyclogenesis sequence, it is necessary to view the system in a Lagrangian frame of reference moving westward at the phase speed of the parent easterly wave. In this frame, flow streamlines are an approximate representation of parcel trajectories as the flow becomes quasi-stationary (DMW09). This fact is important when considering parcel trajectories within a nonlinear critical layer in sheared background flow as it evolves over time (Figure 1, Andrews et al. 1987). In this representation, the purple line is the critical latitude⁷ the thin black lines are streamlines, and the red oval highlights the Kelvin cat's eye circulation. If the wave is acting on a stable zonal PV gradient with the vorticity maximum north of the critical latitude, the cyclonic vorticity within the Kelvin cat's eye circulation is represented in white (DMW09). Conversely, for the unstable case, the overturning of cyclonic vorticity is from below the critical latitude and is represented by the gray shading (DMW09). It has been argued (DMW09) that the Kelvin cat's eye circulation is favorable for vorticity aggregation. This is evident in the schematic (Figure 1) as cyclonic vorticity (in either the stable or unstable case) is observed rolling-up within the Kelvin cat's eye circulation over time. Additionally, since streamlines in the co-moving frame of reference are an approximate representation of parcel trajectories, parcels embedded in the westerly flow north of the Kelvin cat's eye circulation and easterly flow to the south are separated from the parcels within the Kelvin cat's eye circulation by a dividing streamline.⁸ This model suggests, then, that potential dry air from outside of this region is unable to enter the Kelvin cat's eye circulation if the flow does not have a divergent component (DMW09). Despite DMW09's original focus on wave propagation associated with the African

⁷ In linear wave theory, if one considers a wave propagating in a background sheared flow, the critical line (or latitude) is the locus of points where the phase speed of the wave is equal to the background flow.

⁸ In steady 2D flow, the streamline that runs through a nearby saddle point (DMW09).

Easterly Jet, the fluid dynamical concepts of the evolution of wave critical layers in sheared flow are thought to be applicable to different types of waves and different wave generation methods. As stated in DMW09:

Whether hydrodynamic instability plays an immediate role in TC [tropical cyclone] genesis (as sometimes observed in the eastern Pacific and mid-Atlantic) or excites waves that later become instrumental in genesis downstream (as in the African/Atlantic sector) there is a fluid dynamical situation arising in both scenarios that is relevant to genesis.

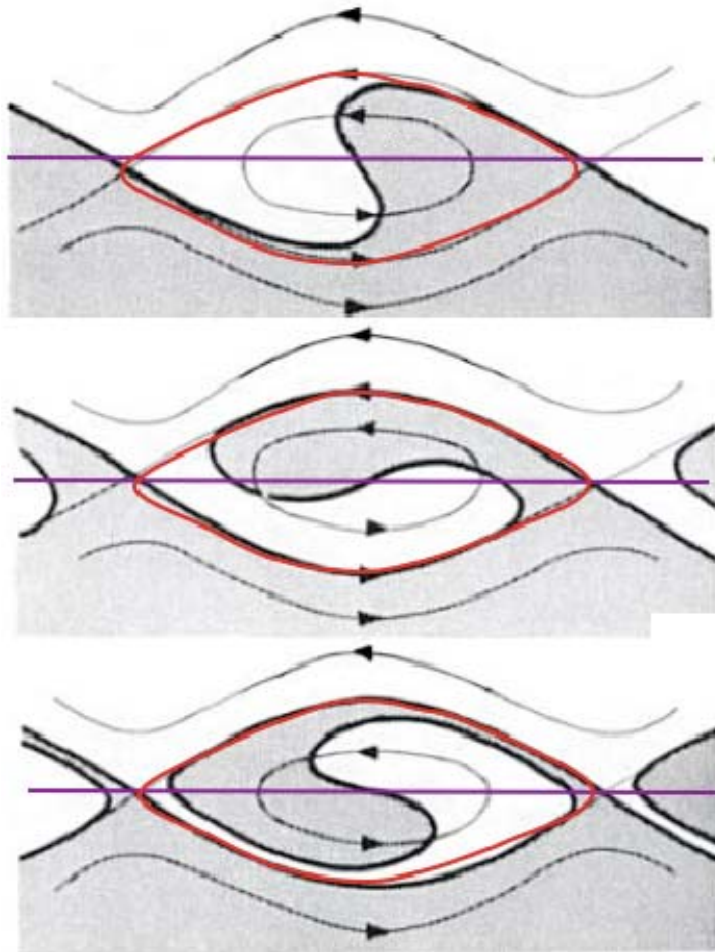


Figure 1. Schematic of the evolution of a nonlinear critical layer over time (adapted from Andrews et al. 1987). The thin black lines are streamlines and the purple line is the critical line (or critical latitude) of linear wave theory. This is the location where the wave's intrinsic frequency vanishes or where the wave's phase speed coincides with the zonal mean flow. Cyclonic vorticity is represented by white area in the stable case and the shading in the unstable case. The red oval indicates the Kelvin cat's eye circulation.

Figure 2 is a useful schematic because it offers a simple illustration of how the critical layer of a developing tropical wave may be applicable to the problem of tropical cyclogenesis. One can imagine that it is a representation of an idealized easterly wave embedded in a mean easterly background flow. The green streamlines depict the open wave in the earth relative (or resting) frame and illustrate the familiar “Inverted-V” pattern associated with tropical easterly waves noted as far back as Riehl (1955). In the co-moving frame of reference,⁹ an approximately closed Lagrangian circulation (black lines) exists. This closed circulation lies within the nonlinear critical layer of the easterly wave. The structure of streamlines in the two reference frames will differ nontrivially, assuming of course that the velocity of the parent wave does not equal zero. When compared to its outside environment, the cat’s eye circulation is relatively moist and these considerations led DMW09 to hypothesize that within the cat’s eye, air is repeatedly moistened by convection. Additionally, the intersection of the critical latitude (purple line) with the wave trough (thick black line) is defined by DMW09 as the sweet spot¹⁰ (indicated by the black dot). DMW09 suggest that this location is the favored region for upscale aggregation of vorticity and eventually, tropical cyclogenesis. By definition, the dividing streamline is quasi-closed in nature (as indicated by the opening to the southwest in Figure 2). Therefore, the opening of the streamline boundary offers the potential for entrainment of additional sources of moisture or dry air from the surrounding environment.

Because the generation and advection of vorticity is central to the problem of tropical cyclogenesis, it is useful to review the equation governing vertical vorticity. In cartesian coordinates on an f-plane, the vorticity equation may be written in material form as follows (see Holton 1992, 103–108 for a complete description):

⁹ Defined in DMW09 as a frame of reference translating horizontally at the velocity of the parent wave or proto-vortex.

¹⁰ Mathematically, the sweet spot is defined as the location where the wave trough ($\bar{v} = 0$) intersects the critical latitude ($\bar{u} = C_p$).

$$\frac{D\eta}{Dt} = -\eta \left(\frac{\partial u}{\partial x} + \frac{\partial v}{\partial y} \right) - \left(\frac{\partial w}{\partial x} \frac{\partial v}{\partial z} - \frac{\partial w}{\partial y} \frac{\partial u}{\partial z} \right) + \frac{1}{\rho^2} \left(\frac{\partial \rho}{\partial x} \frac{\partial p}{\partial y} - \frac{\partial \rho}{\partial y} \frac{\partial p}{\partial x} \right)$$

(2.1)

where η is the absolute vorticity, u is the zonal wind, v is the meridional wind, ρ is density, and p is pressure. The material derivative on the left hand side of Equation 2.1 is the rate of change of absolute vorticity following the motion of a fluid parcel, and can be broken into an advective and local time derivative component. The three groups of terms on the right side of Equation 2.1 indicate ways to change the absolute vorticity. They are the divergence term, the tilting or twisting term, and the solenoidal term. Therefore, absolute vorticity, following the motion of a fluid particle, is changed through: i) convergence, typically most important in synoptic-scale disturbances; ii) tilting or twisting, which generates vorticity by tilting the horizontal vorticity in the vertical through shear in the vertical velocity (Glickman 2000); and iii) the solenoidal term, which generates vorticity when surfaces of equal density are not coincident with surfaces of equal pressure.

To further illustrate the role of an easterly wave's critical layer in tropical cyclogenesis, ERA-40 composite analyses of the 55 storms studied by DMW09 are presented in the next section. This serves as both an introduction to the new cyclogenesis model and illustrates the usefulness of viewing tropical cyclogenesis in the co-moving frame.

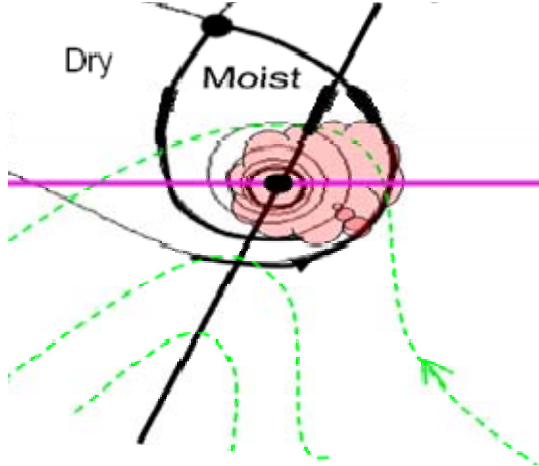


Figure 2. Flow schematic of an idealized tropical easterly wave. The green dashed streamlines represent an idealized easterly wave in background easterly flow in the resting frame. The purple line is the critical latitude in linear theory and the thick black line is the wave trough axis. The thick black streamlines represent the Kelvin cat's eye of this small, but finite amplitude easterly wave. Pink scalloping represents convection within the wave pouch (adapted from Wang et al. 2010a).

B. ECMWF ERA-40 COMPOSITE ANALYSES

Bracken and Bosart (2000) use 18 years' worth of NHC tropical cyclogenesis cases to develop composite analyses of the upper and lower tropospheric flow at the time of tropical cyclogenesis. They note the presence of an open easterly wave at the center of each of their composites, allowing them to postulate: “it seems probable that most of the Analysis of the Tropical Oceanic Lower Level (ATOLL) disturbances in the Bahamas and Cape Verde composites are EWs, likely of African origin.” They note also that maxima in low-level convergence, cyclonic relative vorticity, and upward vertical motion, conditions that are favorable to tropical cyclogenesis, are all located at the northern edge of the open easterly wave. This location is coincident with the location where tropical depression formation is eventually declared. While their findings focus mainly on the synoptic-scale flow characteristics, these features are re-examined in the context of the new tropical cyclogenesis model.

To illustrate the usefulness of this cyclogenesis model, composite analyses are created for the 55 storms evaluated by DMW09 using low-pass filtered ERA-40 analyses (DMW09).¹¹ Composite analyses at six-hour intervals out to 72 hours prior to genesis are created to view the evolution of the wave pouch. The easterly waves selected for analysis in DMW09 propagate nearly zonally throughout the pre-genesis stage and it is shown that effects of meridional propagation are negligible (DMW09). Therefore, an acceptable approximation for the location of the sweet spot at every time prior to genesis for this data set can be determined by extrapolating backwards from the genesis location (defined as the location where TD was declared by NHC). This is determined by using the phase speed of each easterly wave: $x = x_o - ct$ where x is the location at time t prior to genesis, x_o is the location where the disturbance is first declared a TD by NHC, and c is the zonal phase speed of the parent wave (obtained from DMW09). After the location of the sweet spot is established, data in a 31° longitude square is used to create the composite analyses.

Limitations to the composite analyses include: i) the broadening of the resultant synoptic-scale features in the latitude/longitude dimensions. This is due to the linear extrapolation methodology that results in variations of the true sweet spot position for individual storms versus the ERA-40 extrapolated position. ii) Potential position errors arising from zonal phase speed errors, or iii) a meridional component of translation. DMW09 show these to be negligible and are therefore neglected in this composite analysis.

Figure 3 is a time series of ERA-40 composite analyses at 700 hPa. These plots show Okubo-Weiss (OW)¹² and streamlines in the resting (left) and co-moving (right) frames for the 72 hours preceding genesis. At T-72, the resting frame streamline composite depicts an easterly wave as signified by the Inverted-V pattern. The OW

¹¹ The data quality and analysis methodology is documented thoroughly in DMW09. This data set was provided to the author by Dr Zhuo Wang.

¹² Superscript number Okubo-Weiss is defined in DMW09 as: $O W = \zeta^2 - S_1^2 - S_2^2$; where ζ is relative vorticity, S_1 is the stretching deformation, and S_2 is the shearing deformation. It is considered a more robust indicator of genesis potential than simply vorticity because it removes the contributions of shearing deformation that destroy potential genesis regions (DMW09).

maximum is located on the northern portion of the wave crest (consistent with Bracken and Bosart 2000). In the co-moving frame, a closed circulation is already evident and the largest values of OW lie within the Kelvin cat's eye circulation. At T-48, the easterly wave signal has amplified in the composite streamline analysis and the intensity of the OW maximum has increased over the previous 24 hours. However, a closed circulation is not evident in the resting frame. In the co-moving frame, the OW maximum remains centered within the closed cyclonic circulation. At T-24, the streamlines in the resting frame exhibit a closed cyclonic circulation and the OW maximum has intensified further. This closed cyclonic circulation in the resting frame persists until genesis. However, the OW maximum remains north of the circulation center, consistent with the low-level relative vorticity pattern in Bracken and Bosart (2000). In the co-moving frame, the closed cyclonic circulation is evident at T-72 and persists until genesis. Furthermore, the OW maximum remains coincident with this closed Kelvin cat's eye circulation and is concentrated around the sweet spot for the entire time period. In the resting frame, a persistent closed cyclonic circulation does not emerge in the composite analyses until T-24. This suggests that viewing the tropical cyclogenesis sequence in a frame of reference moving with the parent wave is a superior analysis/forecast tool.

To further illustrate this point, the composite analysis is constructed for each basin. Figure 4 is akin to Figure 3, but the composites are separated by geographic origin (Atlantic and eastern Pacific storms).¹³ As in the overall composite, there is a closed cyclonic circulation in the co-moving frame at all time periods from 72 hours until genesis for both basins. In the Atlantic composite, the Inverted-V pattern in the streamline analysis indicates the presence of an easterly wave in the resting frame from T-72 to T-12. A closed cyclonic circulation does not appear in the resting frame until genesis time and it remains south of the OW maximum. More interesting is the eastern Pacific composite. Note the presence of a northwest-southeast oriented wave at T-72 in the resting frame. In the resting frame, a closed cyclonic circulation develops at T-60 and persists until genesis is declared. This is likely due to the weaker low-level mean flow

¹³ Bracken and Bosart (2000) divide the Atlantic sector into Cape Verde formations and Bahamas formation. However, the smaller sample size used in the present study makes that delineation unwise.

and the slower wave speed over the eastern Pacific. The eastern Pacific composite also displays an initial OW pattern that is weak and disorganized. While a plausible explanation for the differences among the basin composites is suggested above, the differences need to be examined more thoroughly.

Time-height cross sections of meteorological variables averaged in a $3^{\circ}\times 3^{\circ}$ box centered on the sweet spot and moving the pouch are presented in Figure 5.¹⁴ The $3^{\circ}\times 3^{\circ}$ is used as an attempt to approximate the size of the cat's eye circulation around the sweet spot. At T-72, there is evidence of a weak cyclonic relative vorticity maximum centered at 600 hPa. This is consistent with the observed structure of AEWs, which display a relative vorticity maximum at 600 hPa (e.g., Reed et al. 1977).

The level of this mid-level cyclonic vorticity maximum appears to lower over the next 24 hours. At T-48, an area of low-level cyclonic relative vorticity accompanies this mid-level maximum. However, there is also strong surface convergence at T-48, whether this is evidence of surface convergence generating the near surface spin-up or a mid-level positive vorticity anomaly being advected downward cannot be fully determined given the resolution of this data set. After T-30 the spin-up at low and mid-levels intensifies and the low-level spin-up is again coincident with strong low-level convergence (Figure 5, middle). The strongest spin-up occurs in the low to mid-troposphere within the 12 hours immediately preceding tropical cyclogenesis and is coincident with strongest low-level convergence (Figure 5).

Latitude-height cross-sections of relative vorticity and divergence created north-south through the center of the pouch are presented in Figure 6. The vorticity time series shows weak cyclonic relative vorticity stretching from the surface to the mid-levels of the troposphere at T-72. These data suggest that the mid-level vorticity maximum observed in Figure 5 at the initial time period may have been present from the mid-levels down to

¹⁴ Composite analyses of the moisture evolution within the pouch are attempted using ERA-40 relative humidity (RH) and saturation fraction (SF) data. Several problems prevent this analysis from being meaningful. First, in translating the composite pouches backwards over time, many remain over the African continent. The RH over the desert is low to begin with, and questionable ERA-40 data made these data totally unreliable. Second, the ITCZ becomes the dominant moisture feature in the analysis over time. These factors lead to a representation that is not representative of individual cases and thus the moisture evolution is not presented herein.

the surface. The analysis presented in Figure 5 and Figure 6 is useful to view the evolution of wave pouch dynamics on the synoptic and meso- α scales. However, the resolution of the ERA-40 data makes it impossible to discern the sub-meso- α scale transition of a wave pouch to a tropical cyclone (i.e., “bottom-up” vs. “top-down”).

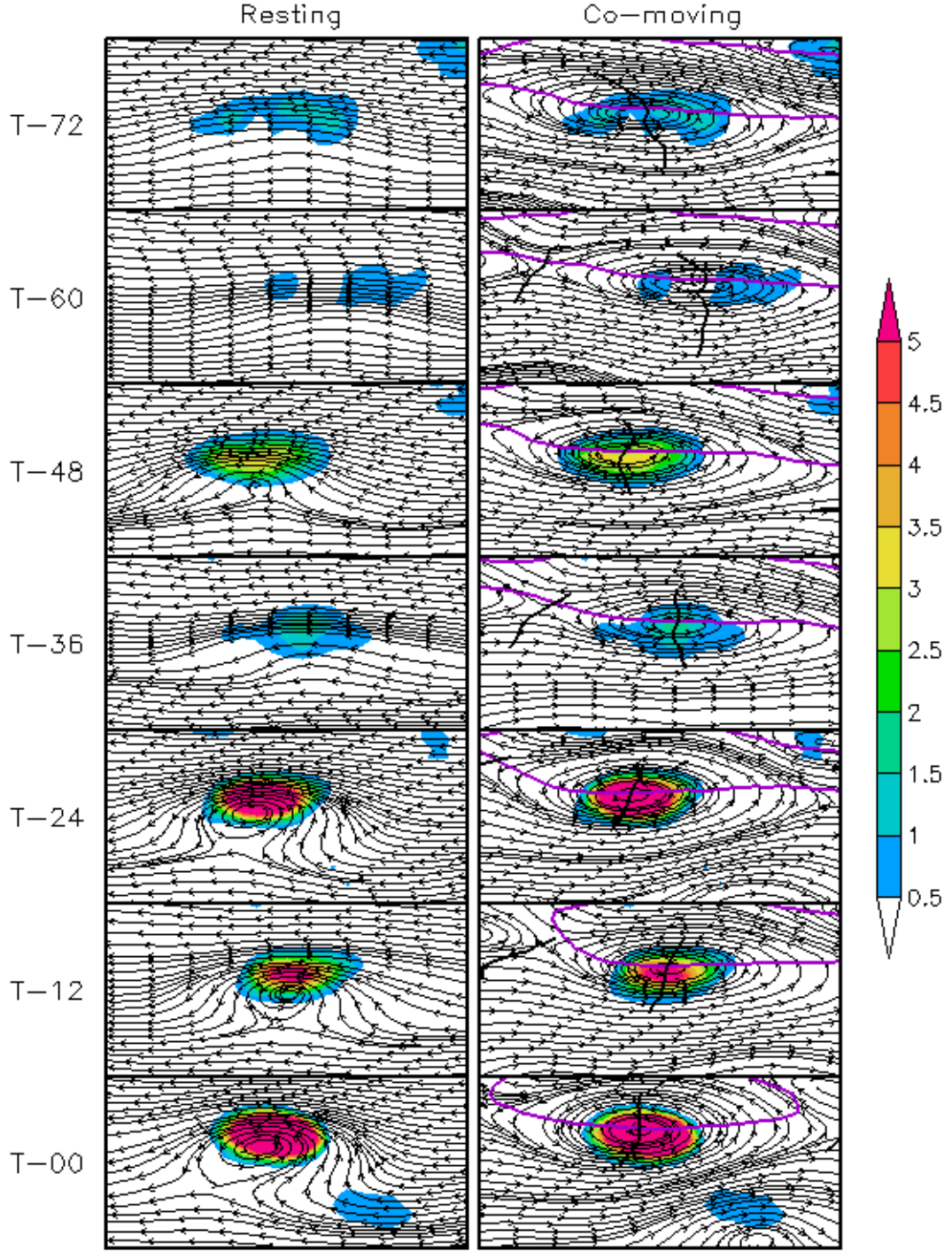


Figure 3. Composite analyses of 700 hPa low-pass filtered ERA-40 data for the 55 storms studied by DMW09. The black lines are streamlines in the resting (left) and co-moving (right) frames. In the co-moving frame, the thick black line is the wave trough and the purple line is the critical latitude, defined as $u = \bar{c}_p$. The shading is OW ($\times 10^{-10} \text{ s}^{-2}$). The abscissa is longitude and the ordinate latitude.

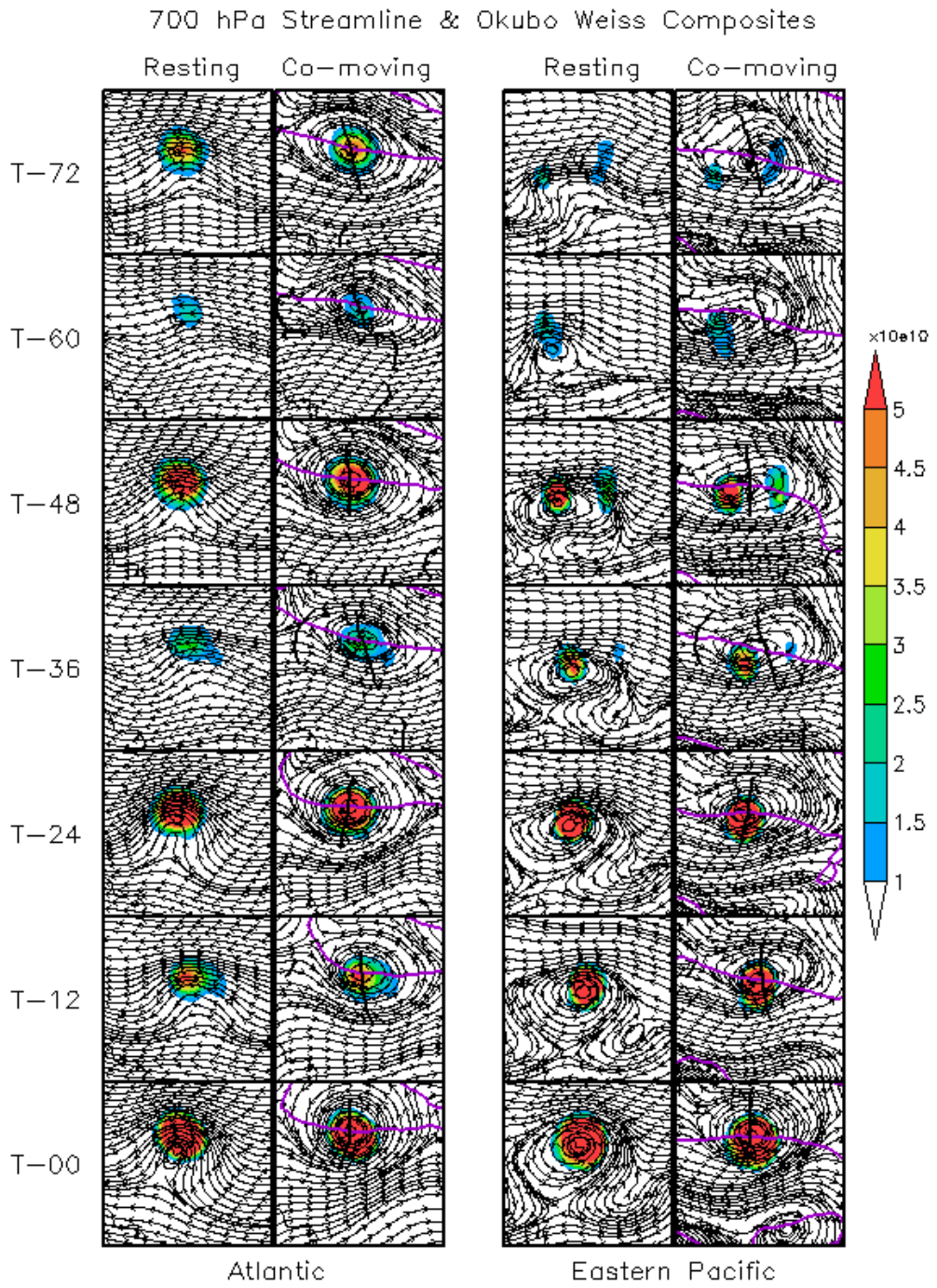


Figure 4. ERA-40 composite analyses for the 55 storms presented in DMW09 plotted by basin, with the Atlantic on the left and the eastern Pacific on the right. For each basin the black lines indicate streamlines in the resting (left column) and co-moving (right columns) frames. In the co-moving frame, the thick black line is the wave trough and the purple line is the critical latitude, defined as $u = \bar{c}_p$. The shading is OW ($\times 10^{-10} \text{ s}^{-2}$). The abscissa is longitude and the ordinate latitude.

ERA-40 Composite Area Averages

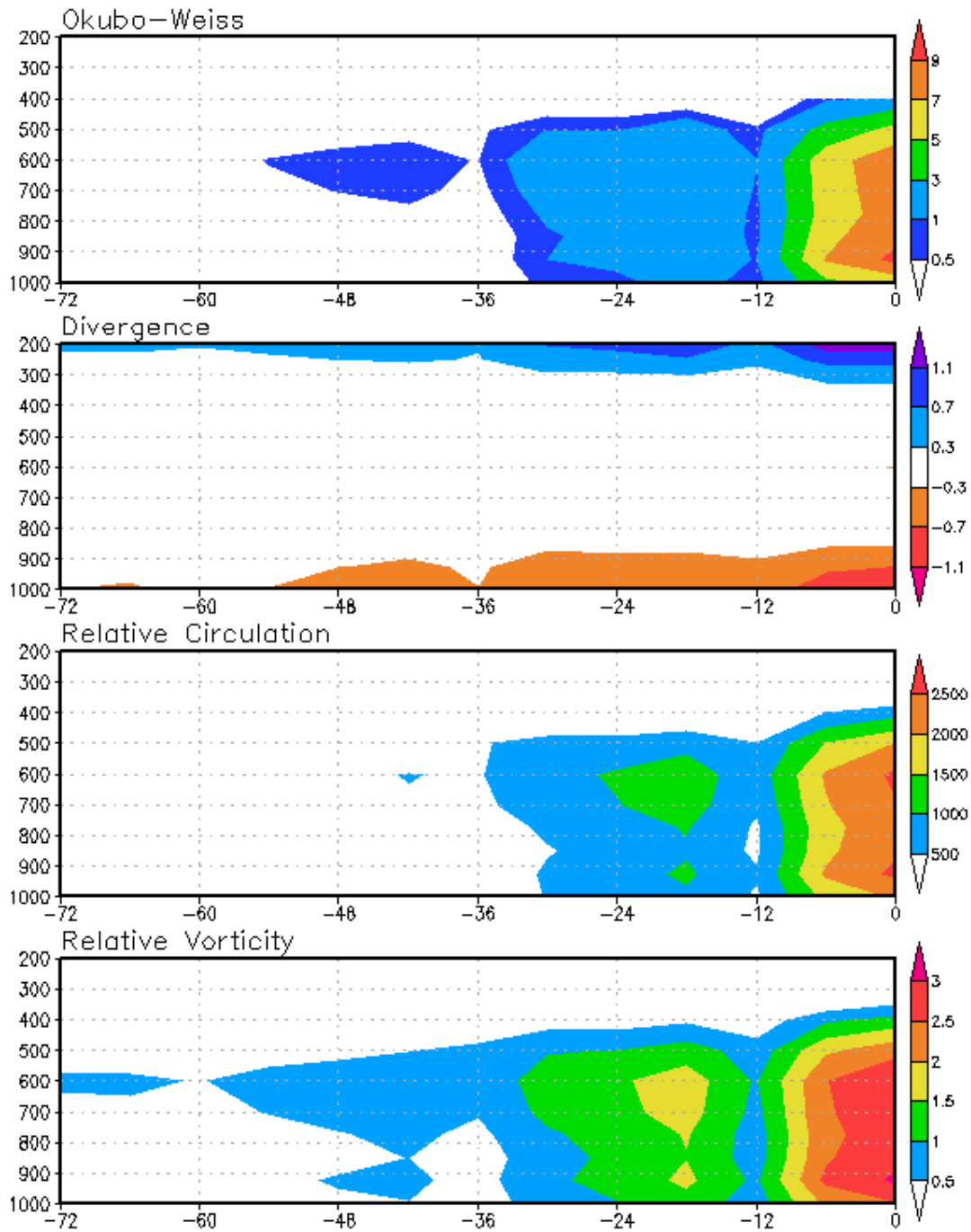


Figure 5. Time height cross sections of key meteorological variables averaged within a $3^\circ \times 3^\circ$ box moving with the center of the sweet spot. The abscissa is time (h) prior to genesis declaration by NHC and the ordinate is pressure (hPa). The variables plotted are OW ($\times 10^{-10} \text{ s}^{-2}$), divergence ($\times 10^{-5} \text{ s}^{-1}$), relative circulation ($\text{km}^2 \text{ k s}^{-1}$), and relative vorticity ($\times 10^{-5} \text{ s}^{-1}$).

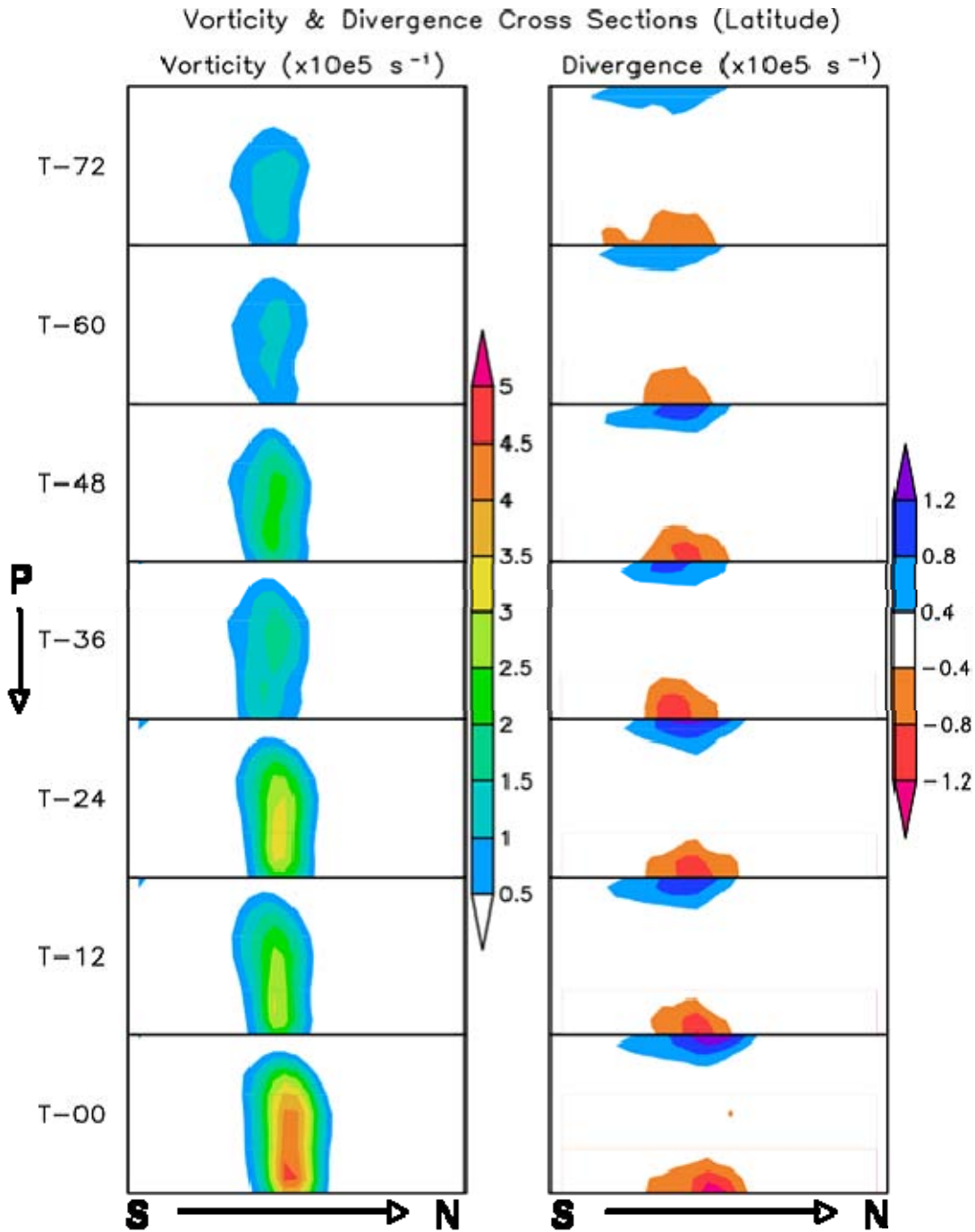


Figure 6. Latitudinal cross-sections through the center of the sweet spot at 12-hour intervals prior to tropical cyclogenesis from the low-pass filtered ERA-40 data. The left column is relative vorticity ($\times 10^{-5} \text{ s}^{-1}$) and the right column is divergence ($\times 10^{-5} \text{ s}^{-1}$). The abscissa is latitude and spans the 31 ERA-40 grid points and the ordinate is pressure 1000–200 hPa.

THIS PAGE INTENTIONALLY LEFT BLANK

III. THE EVOLUTION OF PRECIPITATION WITHIN THE CRITICAL LAYER OF 55 DEVELOPING EASTERLY WAVES AS SEEN BY THE TRMM TMI

A. INTRODUCTION

This chapter uses observations to evaluate the evolution of precipitation within the critical layer of an easterly wave. In their idealized high-resolution numerical simulations of the transition of an EW critical layer into a tropical depression Montgomery et al. (2010a) show that: i) sustained deep convection is favored in (but not limited to) the Kelvin cat's eye cyclonic circulation. ii) Deep convection organizes around the sweet spot as genesis nears. iii) Convective contributions to the total precipitation become increasingly dominant as genesis nears. The goal of this chapter is to use observations to verify these findings by examining the spatial and temporal distribution of precipitation within the protective pouch of precursor EW disturbances.

Observational studies documenting the evolution of precipitation and convection during the tropical cyclogenesis stage are limited. Lee et al. (2006) use hourly geostationary infrared (IR) satellite data to document the occurrence of mesoscale convective systems (MCSs) during the formation stage of 124 tropical cyclones in the western North Pacific basin. While their results identify a maximum in convection occurring north of the EW center, their study is limited by a small number of genesis cases in the EW regime (10). Rodgers and Adler (1981) use the Electrically Scanning Microwave Radiometer (ESMR) to study the distribution and intensity of rainfall within tropical disturbances at all stages of development, ranging from the pre-cyclone stage to fully developed typhoons. They show that storm intensification is related to an increase in heavy rain rates. The main limitation to their study arises from using curvature in rain bands from satellite data as the primary tool to identify the low-level cyclonic circulation center in the pre-genesis stage. This approach likely misrepresents the true center (as convection is disorganized at this early stage and it is unlikely that rain bands have formed).

DMW09 use gridded TRMM 3B42 data to document the spatial and temporal evolution of surface rain rate (SRR). They identify the preference for convection within the critical layer of an EW, an increase in the intensity of the convection, and its preference to organize around the sweet spot as genesis nears. These data have limitations as they are interpolated to a $0.25^\circ \times 0.25^\circ$ grid, represent three-hourly average precipitation, and combine TRMM with other satellite data (i.e., geostationary IR) to derive SRR. A different technique is used by Lonfat et al. (2004), who create composites of TRMM Microwave Imager (TMI) data to assess the spatial distribution of precipitation within 260 tropical cyclones. In this present study, TRMM orbital data is used in a complimentary way, focusing on the pre-genesis stage, and creating composite analyses viewed in a frame of reference moving with the parent wave, as advocated by DMW09. The use of TRMM TMI or TRMM Precipitation Radar (PR) data in this type of analysis allows for exploitation of the high spatial resolution TRMM orbital data, differentiation between rain types, and provides more accurate rain rate retrievals.

B. DATA AND METHODOLOGY

TRMM is a joint NASA/Japan Aerospace Exploration Agency (JAXA) remote sensing program designed to measure tropical rainfall amounts from space (Lonfat et al. 2004). The present study uses TRMM 2A12 TMI hydrometer profile data, that has a horizontal resolution of 4.4 km at 85 GHz with a swath width of 760 km pre-boost (before 7 August 2001) and a horizontal resolution 5.1 km with a swath width 878 km post-boost (after 24 August 2001). The 2A12 retrieval algorithm (Olson et al. 2006) uses a cloud-resolving model coupled with radiative transfer information to create a database of rainfall profiles that correspond to observed microwave radiances. The observed radiances from the TRMM TMI are then compared against this database to derive SRR and convective rain rates (CRR). For this study, the stratiform rain rate (STRR) is considered to be the difference between the SRR and CRR. Only retrievals over ocean are used as precipitation and hydrometer retrievals obtained over land are contaminated by the surface emissivity properties. Yang et al. (2006) use Dual Doppler radar and rain gauge data to evaluate the performance of the TRMM TMI V6 rainfall algorithm. They

conclude that: “In general, V6 TMI estimates of surface rain rate are consistent with estimates from ground-based or space-borne radar, both in terms of instantaneous structure and quantitative precipitation amounts.” Yang et al. (2006) note that the convective partitioning is the most significant challenge to the algorithm because of the difficulties in distinguishing among convective and stratiform signatures in radiance structures and polarization data.

This chapter examines all TRMM passes that intersect the pouch of the 55 tropical cyclones identified by DMW09 during the tropical cyclogenesis stage, which is defined here as the 72 hours prior to TD declaration in the NHC Best Track Data. The horizontal extent of the pouch is approximated as a three degree radius circle surrounding the sweet spot. The approximate location of the sweet spot, at every time prior to genesis, is determined by extrapolating backwards from the genesis location, using the phase speed of each EW: $x = x_o - ct$, where x is the location at time t prior to genesis, x_o is the location where the disturbance is first declared a TD by NHC, and c is the zonal phase speed of the parent wave. Once these positions are established, they are cross-referenced with the time and geolocation data from each TRMM pass during the three days prior to genesis. Any TRMM retrievals within a three degrees radius of this location are used to create composite pouches. These data are binned by radius (0.25° longitude intervals) and azimuth (10° intervals) to evaluate the spatial evolution of the rainfall. Finally, these data are separated into three time periods: 72–48 h prior to genesis (T3), 48–24 h prior to genesis (T2), and 24–0 h prior to genesis (T1). There are 355 TRMM passes within three degrees of the individual storm centers that are used in this study. The passes are distributed into the three time bins as follows: 122 passes in T3, 115 in T2, and 118 in T1.

Due to the limited coverage of the TRMM swath and the relatively small number of storms used in this study, there are sampling biases within the composite pouches worth noting: i) the T3 time period exhibits the fewest observations due to the exclusion of over-land retrievals. Many of the pre-genesis disturbances evaluated in this study remain over Africa or the Mexico/Central America landmass at this early stage of the genesis sequence. This bias is minimized in the next two time periods. ii) A slight high

sampling bias in the south-southwest and low sampling bias to the northeast through east of the composite pouch is observed in the T3 data. iii) A low sampling bias stretching from the north-northeast to southeast in the T2 time period. iv) An under-sampling to the east of the sweet spot in the T1 composite pouch. Although not perfect, the author believes that this data set is adequate to present a “first look” at the evolution of precipitation within the critical layer of an EW.

C. RESULTS

1. Radial Averages

Figure 7 shows CRR (+) and STRR (o) normalized by annulus area and plotted as a function of radial distance from the EW sweet spot. The green lines represent T3, red represent T2, and blue represent T1. During the T3 time period, there is little credible evidence of a CRR maximum. The T2 time period exhibits a broad convective maximum stretching from 1.25° to 0.75° , with the highest CRR at 1.25° . The T1 bin exhibits a broad CRR maximum similar to T2. However, it has moved closer to the sweet spot (1.0° - 0.5°). The inward migration of the convective maximum as genesis nears is consistent with the hypotheses put forth by DMW09. The STRR is less intense and follows a similar distribution as the convective precipitation. Of particular interest is the large increase in absolute difference between the two rain rate types as genesis nears. There is a spike in the CRR across the broad maxima seen in the T2 and T1 time periods (especially at the T1 time period). Conversely, the T1 STRR appears to level off and the T2 STRR amounts decrease across the broad CRR maximum.

These data are also plotted as a scatter plot of rain rates for each retrieval by time period, radial distance from the sweet spot, and rain type (Figure 8): convective (red) and stratiform (green). These data exhibit the same pattern of that seen in Figure 7, and further illustrate the dominance of the CRR, especially at the T1 time period.

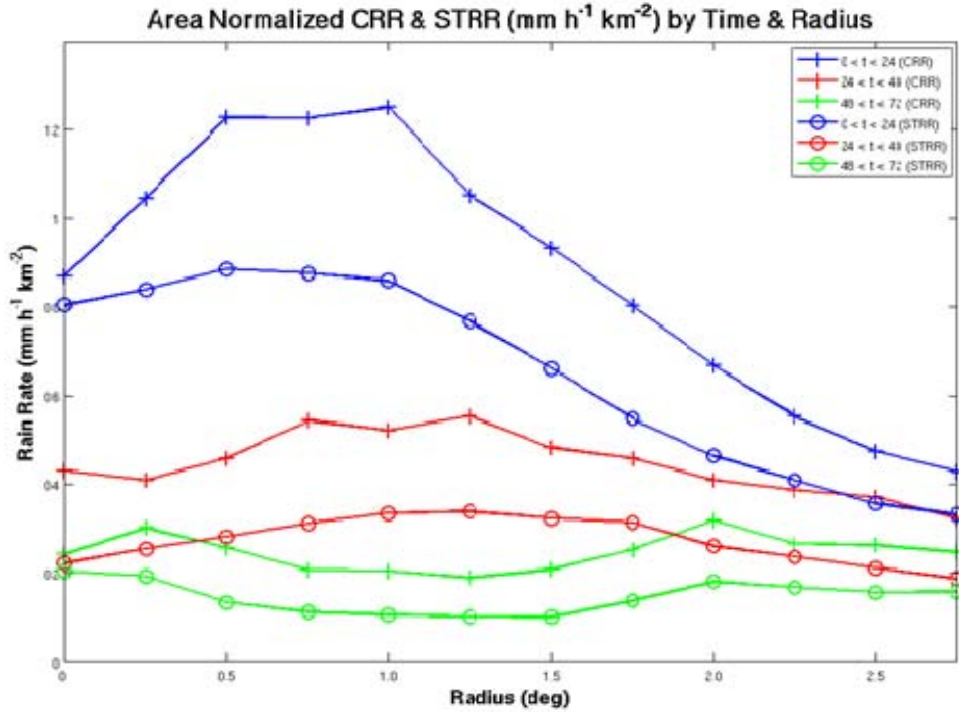


Figure 7. Radial plots of TRMM TMI precipitation: CRR (+) and STRR (o), normalized by annulus area ($\text{mm h}^{-1} \text{km}^{-2}$) plotted as radial distance from the sweet spot position. Green lines represent the T3 time, red is the T2 time, and blue is the T1 time.

Recent high-resolution cloud representing numerical simulations of the formation of Hurricane Felix (2007) (Wang et al. 2010b) suggest that the precipitation maximum is closer to the sweet spot (approximately 40 km versus the 100+ km observed in this study) at genesis time. These discrepancies could be due to: i) the inability of the numerical model to accurately represent the true atmospheric state, or ii) the fact that Hurricane Felix is akin to a midget typhoon. There are, however, potential errors in the TRMM 2A12 composite analysis that are noted. i) The T1 composites are representative of conditions from 24–0 h prior to genesis rather than at the genesis time. The radius of maximum rain rates is expected to continue to decrease with time as genesis nears. ii) The small sample size (~2500 samples in the innermost radius) near the pouch center is potential the reason for near equal CRR and STRR at the innermost radii in T1. Finally, iii) potential errors in pouch location could occur due to the linear extrapolation of the sweet spot (examined further below).

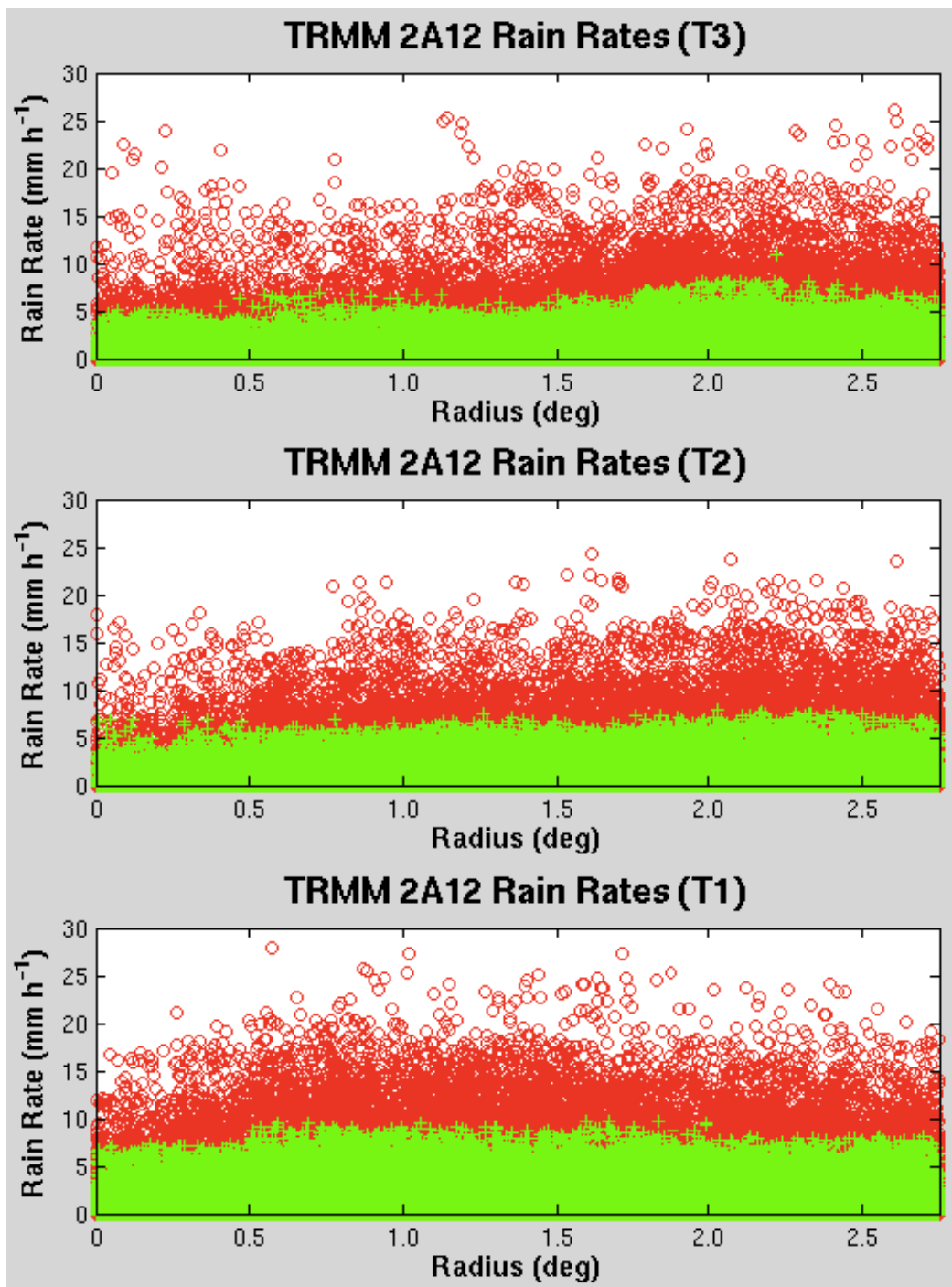


Figure 8. Scatter plots of TRMM 2A12 convective (red) and stratiform (green) rain rates (mm h^{-1}) by radius for each time period.

Rodgers and Adler (1981) observe that increases in the number of heavy convective elements are an indicator of storm intensification. Figure 9 displays the number of convectively dominated high precipitation pixels (defined as in Olsen et al. 1999: SRR >10 mm hr⁻¹ with >65% of SRR being convective) normalized by annulus area and plotted by radii for each time period. In these data the heavy convective activity moves closer to the sweet spot as genesis nears. Of particular importance is the approximate 300% increase in the number of heavy convective pixels at the 0.75° radius between the T2 and T1 time periods. These findings potentially provide new insight into the structure and evolution of the vertical latent heating profile within the pouch of a developing tropical cyclone (discussed in Section D).

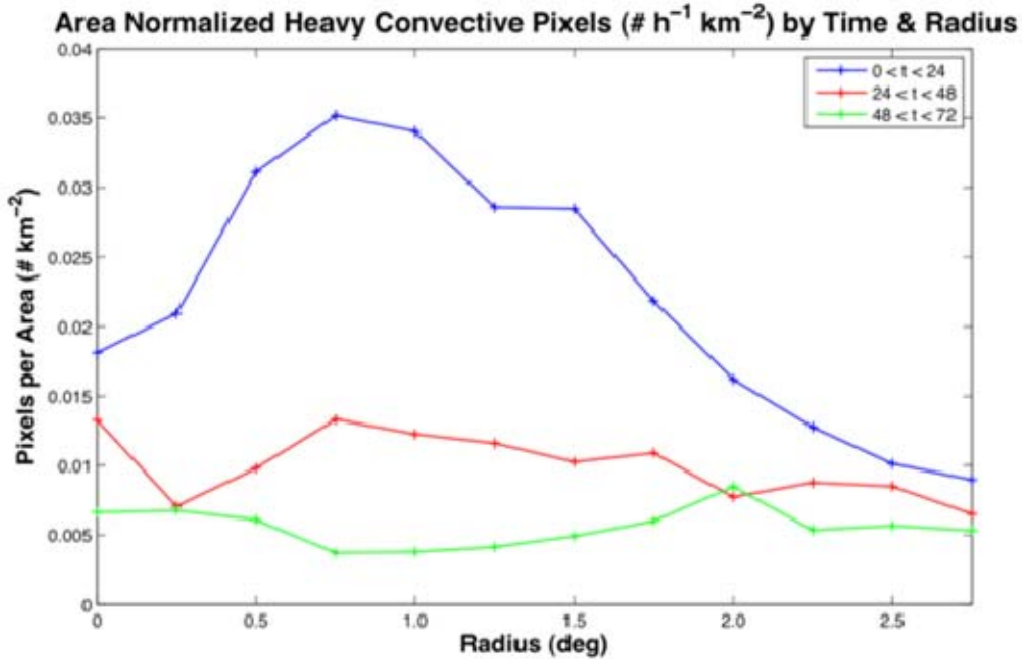


Figure 9. Radial plots of number of convectively dominated heavy precipitation pixels ($\# \text{ km}^{-2}$) for the three time periods.

2. Spatial Distribution

Initial results of the spatial distribution of TRMM 2A12 rain rate data within the critical layer of an EW are presented as a 9-panel composite pouch diagram (Figure 10).

Each row represents a precipitation type: the top is SRR, the middle CRR, and the bottom STRR. The columns are temporal periods prior to genesis: the left column is T3, the middle T2, and the right T1. The composite pouches are oriented geographically, with the top pointed north. Each bin is normalized by the total pixel count within the bin so as to derive an average rain rate per pixel ($\text{mm h}^{-1} \text{ pixel}^{-1}$). The T3 time period exhibits a minimum in the SRR intensity, with the relative SRR maxima at the farthest radii. Two distinct geographical regions are favored for higher SRR within the pouch: the south through west and east. The total precipitation pattern and intensity, while generally a mix of the CRR and STRR, suggests that the most intense convective elements ($>0.75 \text{ mm h}^{-1}$) dominate the distribution of SRR.

During the T2 time period, the spatial coverage of higher SRR values has increased and encompasses the lower three quarters of the pouch. Two distinct SRR maximum occur to the west and southeast at radii 1.25° - 1.75° from the center. The most intense area of convective precipitation is a banded-type feature located to the southeast of the sweet spot. A secondary convective maximum is located to the south-southwest of the sweet spot and is observed at the farthest radii. The STRR is less intense than the CRR and the heaviest stratiform precipitation regions are concurrent with the heaviest convective areas.

The T1 period indicates that higher SRR values have encompassed almost the entire pouch. The heaviest SRR have moved closer to and organized around the sweet spot as genesis nears. Strong asymmetries exist in these data with a SRR maximum ($>3 \text{ mm hr}^{-1} \text{ pixel}^{-1}$) located west-southwest of the sweet spot and a secondary SRR maximum located to the northeast ($2.5 \text{ mm hr}^{-1} \text{ pixel}^{-1}$). These SRR asymmetries are driven by the location of the convection, where the maximum exists to the west-southwest ($>2 \text{ mm hr}^{-1} \text{ pixel}^{-1}$) and is centered at the 1.25° radius. The secondary SRR maximum to the northeast of the sweet spot is also evident in the CRR composite at approximately 0.75° radius. The stratiform portion of the precipitation is less intense than the CRR and, and is co-located with the convective maximum.

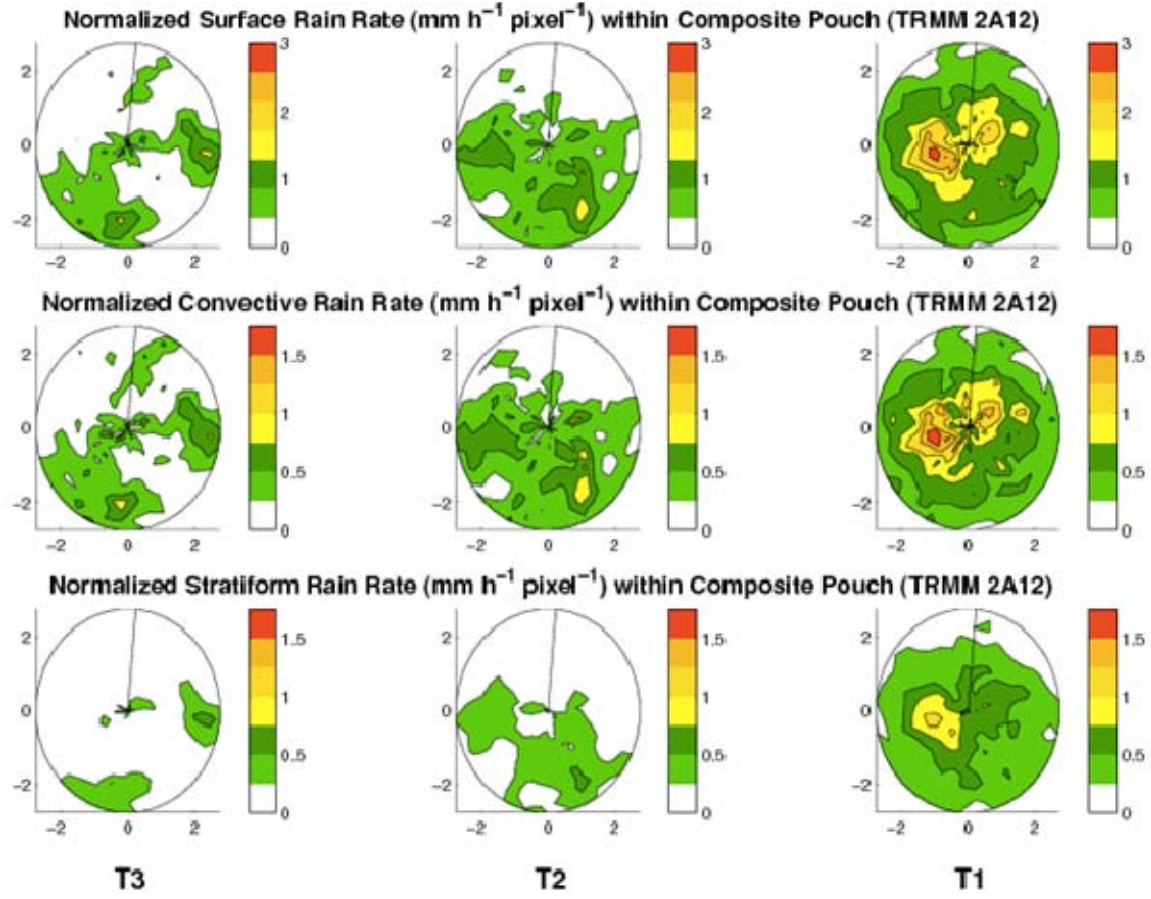


Figure 10. Contour plots of TRMM TMI normalized rain rate data ($\text{mm h}^{-1} \text{pixel}^{-1}$) within the composite pouches plotted by precipitation type (rows) and time (columns). The composite pouches are oriented geographically with the top being north.

Potential sources of error in the extrapolated pouch position used in this study can occur through errors in the meridional translation of the parent EW or errors in zonal phase speed calculation. DMW09 found that effects of meridional translation in the pre-genesis stage are negligible for the EW studied. More problematic are potential errors in the estimation of the parent wave's zonal phase speed. Although DMW09 show that the location of the pouch is relatively insensitive to $1\text{--}2 \text{ m s}^{-1}$ error in the translation speed, errors may accumulate as the sweet spot is traced backwards in time. For this reason, sensitivity tests of the TRMM 2A12 precipitation distribution to changes in pouch location created by potential phase speed errors are performed.

Using the potential phase speed errors derived in DMW09, randomly added values within ± 1 standard deviation (1STD) of the original phase speed are added to c to derive a new position (x) at time (t) of each TRMM/pouch intersection while the same values of x_0 are used from DMW09. These results illustrate: i) the coherent SRR and CRR maxima west-southwest and secondary maxima northeast of the pouch center observed at T1 are also evident in the 1STD data. ii) The relative SRR maximum and overall precipitation patterns in the T2 and T3 periods appear as coherent structures in similar locations to those observed in Figure 10. iii) SRR, CRR, and STRR increase from T3-T1. However, CRR still becomes increasingly dominant as genesis nears. These results suggest that potential position errors created by uncertainty in zonal phase speed estimates within one standard deviation do not qualitatively affect the TRMM 2A12 precipitation distribution within the pouch.

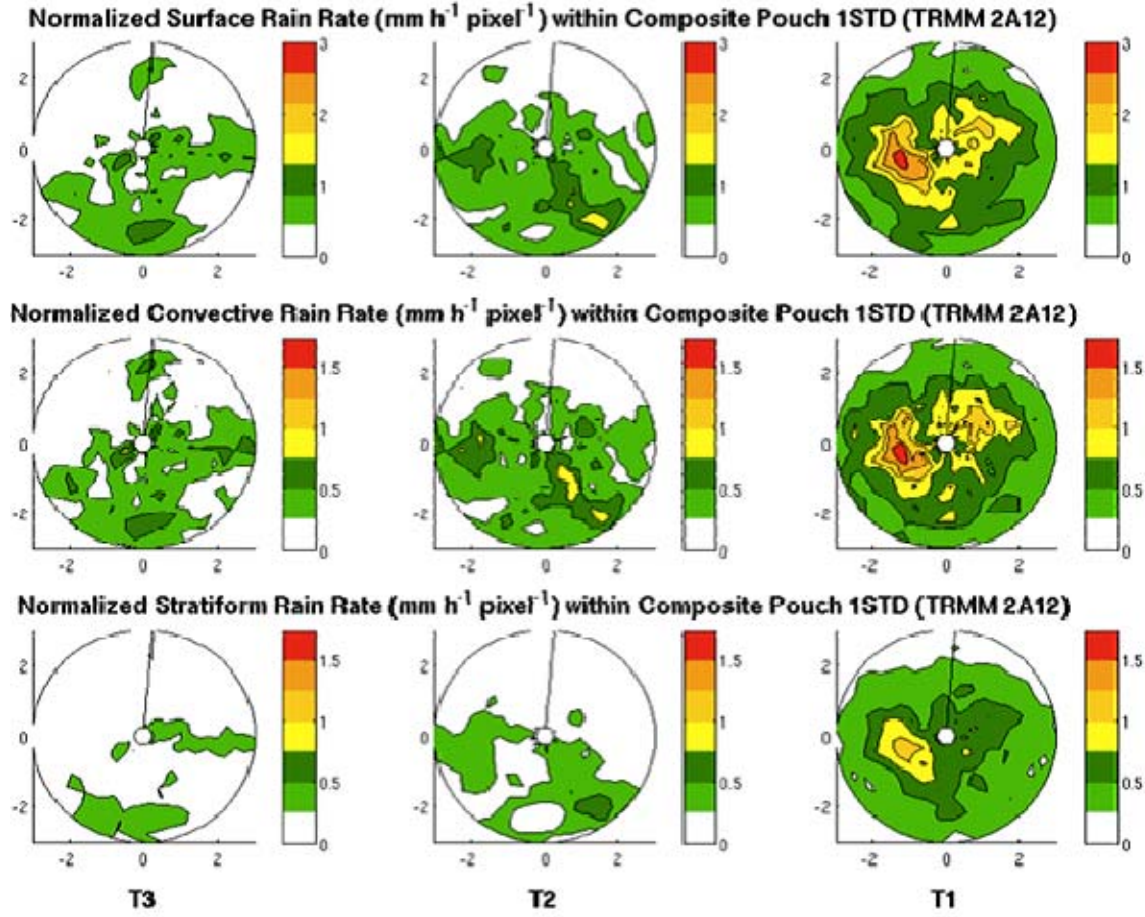


Figure 11. Sensitivity test of the TRMM 2A12 normalized rain rate data ($\text{mm h}^{-1} \text{ pixel}^{-1}$) within the composite pouches. The position of the sweet spot at each pouch/TRMM satellite intersection is recalculated by randomly adding phase speed errors within ± 1 standard deviation to the original wave propagation speed. Layout is as in Figure 10.

D. SUMMARY AND DISCUSSION

An initial evaluation of the temporal and spatial evolution of precipitation within the pouch of 55 developing tropical cyclones is presented using TRMM 2A12 TMI data in the Atlantic and eastern Pacific sectors for four seasons (1998-2001) during August and September. Data from 355 TRMM passes are used to create composite pouches in 24-hour intervals for three days leading up to tropical cyclogenesis. The composite pouch CRR data show that convection is favored near the center of the Kelvin cat's eye circulation and that the intensity and areal extent of the convection increases with time

and organizes around the sweet spot as genesis nears. While both CRR and STRR increase from T3 to T1, CRR becomes increasingly dominant and is the major contributor to SRR.

Initial results reveal asymmetries in the SRR and CRR maxima at the T1 time period in the west-southwest and northeast quadrants of the pouch. Tests of the sensitivity of these organized precipitation structures to errors in pouch location arising from zonal phase speed estimation errors confirm the robustness of these organized structures near the sweet spot as genesis nears. It is noted that the spatial patterns of the rain rate distribution may be subject to errors due to the small and non-uniformly distributed sample size. A more extensive study using TRMM PR data is underway in order to examine this problem more comprehensively.

These results have implications on both the organization of precipitation as genesis approaches, and on storm intensification. The number of convectively dominated high precipitation pixels increases 300% at the 0.75° radius between the T2 and T1 time periods. This is consistent with the increase in heavy convection leading to intensification observed by Rodgers and Adler (1981).

These findings point to new insight into the structure of the latent heating profile during the mesoscale transformation of the EW precursor. DMW09 hypothesize that developing tropical cloud clusters favor a convective type heating profile with a heating maximum in the low-mid troposphere within the cat's eye region (as opposed to the more widely accepted 'top heavy' heating profile of typical tropical MCSs (e.g., Houze 1989). DMW09 contend: "Bottom-up development is inextricably linked to column moistening, which favors convective over stratiform heating as the leading contribution to the vertical heating profile."

Although the TRMM 2A12 latent heat profile data is considered experimental, the SRR data nevertheless offers a hint into what the vertical heating profile may look like (e.g., Yanai et al. 1973) and how it evolves with time. To wit, consider the following:

- It has been shown that the CRR are the dominant contributor to the SRR at all time periods and that CRR becomes more dominant as genesis nears. For tropical MCSs, Houze (1989) notes: "The consistency of the

stratiform [heating] profiles from case to case indicates that the variability of net (convective plus stratiform) heating profiles ... lies primarily in the variation of convective regime profiles.” As genesis nears, the inner radii show a rapid increase in CRR that is not matched by the STRR, observations that would favor a convective heating profile.

- The relationship between SRR and latent heating derived by Yanai et al. (1973) assumes a saturated atmosphere in which all liquid immediately condenses from clouds. Olson et al. (1999) illustrate that this relationship does not hold true during periods of vigorous convection when the condensation of water vapor exceeds the precipitation fallout. In this situation, the convectively generated low-mid level heating maximum is enhanced. This is especially important during the T1 time period where the 300% increase in the number of heavy convective pixels (at the 0.75° radius) over the previous 24 hours acts to provide an additional source of low to mid-level tropospheric latent heat release within the cat’s eye circulation.

The dominant contribution of CRR to SRR during the genesis stage therefore suggests a convective divergence profile, and favors “bottom-up” type development. However, vertical latent heating profiles need to be examined comprehensively to confirm/falsify these claims. The TRMM PR directly measures 3D hydrometer profiles and is able to derive a vertical latent heating profile. Initial composites from the PR indicate the presence of this lower-mid troposphere heating maximum. However, the narrow swath width of the PR leads to a large under-sampling of the composite pouches. Work is currently underway to add more cases to this data set so as to achieve statistically robust results from the TRMM PR latent heating profiles and to assess also these initial results of the spatial and temporal distribution of precipitation presented herein.

THIS PAGE INTENTIONALLY LEFT BLANK

IV. THE GENESIS OF TYPHOON NURI AS OBSERVED DURING THE TCS-08 FIELD EXPERIMENT: THE ROLE OF THE EASTERLY WAVE CRITICAL LAYER

A. INTRODUCTION

The western North Pacific region is the most active tropical cyclone basin on the earth, responsible for, on average, 26 of the 84 named storms annually (Neumann 1993). Numerous synoptic-scale patterns have been identified as favorable to tropical cyclogenesis over the years, including, but not limited to: Tropical Upper Tropospheric Troughs (TUTT) (e.g., Sadler 1976, 1978), formation within a monsoon trough regime (e.g., Holland 1995) including the special cases of monsoon depression formation (Harr et al. 1996) and monsoon gyre formation (Lander 1994), wave energy dispersion from pre-existing depressions (Carr and Elsberry 1995; Holland 1995), filamentary intrusions from the subtropics (Deleon 2008), mixed Rossby-gravity (MRG) waves (Dickinson and Molinari 2002), and easterly waves (Ritchie and Holland 1999; Fu et al. 2007). Ritchie and Holland (1999) present a climatology of formation mechanisms in this basin and document five synoptic-scale regimes favorable to tropical cyclogenesis.¹⁵ Using eight years of data from the Australian Bureau of Meteorology tropical analysis scheme, they attribute 42% of the western North Pacific tropical cyclogenesis cases to monsoon shear lines, 29% to monsoon confluent regions, 18% to easterly wave disturbances, 8% to wave energy dispersion, and 3% to monsoon gyre formation. Ritchie and Holland (1999) note that these data most likely underestimate the true number of easterly wave type formations: “development may also occur entirely in the easterly wave (18% of cases examined here) although the sample for this pattern most probably has a low bias due to the exclusion of genesis cases near the date line.” Additionally, they note: “It is difficult to distinguish between genesis in the confluence region and genesis directly from an easterly wave because of the uncertainty of when genesis processes have finished.” It is possible that the easterly wave pathway to genesis is more prominent in the western

¹⁵ Ritchie and Holland (1999) define genesis as “the series of physical processes by which a warm-core, tropical cyclone-scale vortex with maximum amplitude near the surface forms.”

North Pacific basin than Ritchie and Holland (1999) suggest. Molinari (2004) examines genesis cases in the western North Pacific basin and he “believe[s] that a significant fraction, and likely the majority, of western-Pacific tropical cyclones form in association with westward moving disturbances.” Chen et al. (2008), for example, have proposed that 80% of the tropical cyclone formations in this basin are due to easterly wave influences either directly or indirectly (through wave-gyre interactions).¹⁶

Although easterly waves are ubiquitous in the trade wind region of the tropics, typically only a small percentage of these waves develop into tropical cyclones (Frank 1970; Ritchie and Holland 1999). While DMW09 focus on tropical waves over the Atlantic and eastern Pacific sectors, the data collected during TCS-08, a field campaign that took place from August-September 2008 over the western North Pacific, provides a unique opportunity to test the new tropical cyclogenesis model for easterly wave scenarios in a different basin. The overall objectives of TCS-08 are to develop a better understanding of storm-scale processes in the western North Pacific associated with tropical cyclones and to further the understanding of interactions between convective processes and tropical cyclone genesis, structure/evolution, intensity, and predictability (Elsberry and Harr 2008). To accomplish these objectives, a multi-platform observing strategy was implemented. Both United States Air Force (USAF) C130 Hurricane Hunter aircraft [providing dropwindsondes, flight-level data, Stepped Frequency Microwave Radiometer (SFMR) data, and the ability to drop both Airborne Expendable Bathometry Thermographs (AXBT) and ocean buoys] and the Naval Research Laboratory (NRL) P3 aircraft [fitted with the Electra Doppler Radar (ELDORA), dropwindsonde capability, a Doppler wind lidar, and the ability to collect flight-level data] flew aircraft research missions originating from Guam, a U.S.A. territory. For further information on the observing strategies and scientific objectives of TCS-08, see Elsberry and Harr (2008).

¹⁶Chen et al. (2008) specifically use the phrase: “*monsoon gyres develop through a monsoon trough-easterly wave interaction.*” However, their monsoon gyre definition is not consistent with the definition provided in the Glossary of Meteorology (Glickman 2000). Despite this non-standard terminology, the wave-gyre interaction concepts that Chen et al. (2008) present may offer useful insight into the formation process in association with easterly waves in the western North Pacific basin and the author would be remiss not to mention it.

Typhoon Nuri was the first tropical cyclogenesis event occurring within aircraft observational range (\sim 3000 km) during TCS-08. The storm was flown on four consecutive days (16–19 August) by the USAF C130 to allow for the documentation of the evolution from easterly wave through Category 2 typhoon. The NRL P3 flew concurrently with the C130 on three days (16–18 August) to enable a documentation of the mesoscale and convective structure during the transition from easterly wave to tropical storm (TS) intensity.

The goal of this chapter is to examine the genesis of Typhoon Nuri from the easterly wave precursor and provide a first test of the new tropical cyclogenesis model in the western North Pacific basin. This test is comprised of two parts: a post-analysis of a portion of the data collected during TCS-08 and an evaluation of the real-time marsupial forecasts for Typhoon Nuri that were produced and used as guidance for operational decisions during the TCS-08 field program.

The outline of this chapter is as follows. Section B describes the data and methodology used. Section C examines the results obtained from analysis of the observational and forecast data. Section D discusses the genesis of Typhoon Nuri in the context of real-time forecasting. Section E summarizes the results presented in this chapter and outlines my planned next steps for analysis of this storm.

B. DATA AND METHODOLOGY

1. Data

Multiple datasets are used in this research: 1) The National Center for Environmental Prediction (NCEP) Global Forecast Model Final Analyses (GFS FNL) and forecast data, projected onto a one degree grid at six hour intervals, 2) Multi-Functional Transport Satellite (MTSAT) half-hourly IR satellite data at 4-km resolution, 3) Joint Typhoon Warning Center (JTWC) Best Track Data, 4) USAF C130 and NRL P3 dropwindsonde data, 5) The US Navy’s global forecast model (Naval Operational Global Atmospheric Prediction System [NOGAPS]) and ECWMF analyses and forecast data, 6) QuikSCAT surface wind data, and 7) Cooperative Institute for Meteorological Satellite

Services (CIMSS) satellite products. Not all of these data are independent. Specifically, the JTWC Best Track Data rely heavily on the MTSAT satellite imagery and aircraft observations for position fixes, and all numerical models assimilate the in-situ aircraft observations and satellite observations into their analyses.

2. Summary of Aircraft Missions

Aircraft dropwindsonde data from the USAF C-130 and NRL P3 over two days (16–17 August) prior to TS declaration are evaluated herein. Figure 12 provides a summary of the key events in the genesis sequence of Typhoon Nuri. In the pre-Typhoon stage, the USAF C130 operated at 31,000 ft to provide extensive vertical profiles of the atmosphere. Its primary missions are to provide synoptic and mesoscale analysis of the developing system, locate a developing circulation center, and direct the NRL P3 to mesoscale areas of interest. The primary mission of the NRL P3 is to use the ELDORA to sample the convection within the marsupial pouch of the parent wave disturbance, with secondary missions of providing dropwindsonde and flight-level data coverage. While on station, the NRL P3 typically flew at altitudes of 8,000–12,000 ft.

During the 16 August flight, the USAF C130 flew in a so-called “lawn-mower” pattern (Figure 13, top) centered on 147E, and oriented along the axis of the easterly wave trough. Deviations were made to the pattern during flight to better sample the western edge of the wave as it was propagating faster than forecast and to the southern edge of the wave where the convection was most vigorous. The second C130 mission (17 August) flew a so-called “square spiral” pattern (Figure 13, bottom) centered at 14N, 142E, the sweet spot position as derived from NOGAPS model forecast data. In-flight deviations were made to this pattern as a low-level circulation was identified by dropwindsonde data in the southwestern corner of the pattern.

The first NRL P3 flight (16 August) focused on the convective process occurring near the potential sweet spot as identified by the NOGAPS forecast. Toward the end of its mission, the aircraft climbed to flight levels greater than 20,000 ft to provide dropwindsonde coverage on the extreme western edge of the wave, which was not covered by the C130. The second NRL P3 flight (17 August) began as a rectangular

pattern within the square spiral of the USAF C130 pattern. Its mission was to provide a statistical sample of the convection within the wave's pouch, therefore, multiple passes on convective cells were not made in order to obtain an unbiased sample.

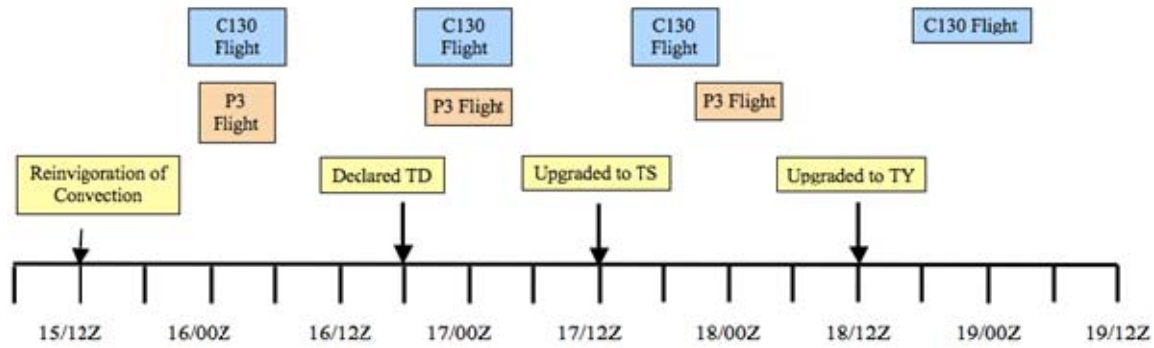


Figure 12. Timeline of key events during the observational period of Typhoon Nuri during the TCS08 field experiment between 12Z 15 August and 12Z 19 August 2008.

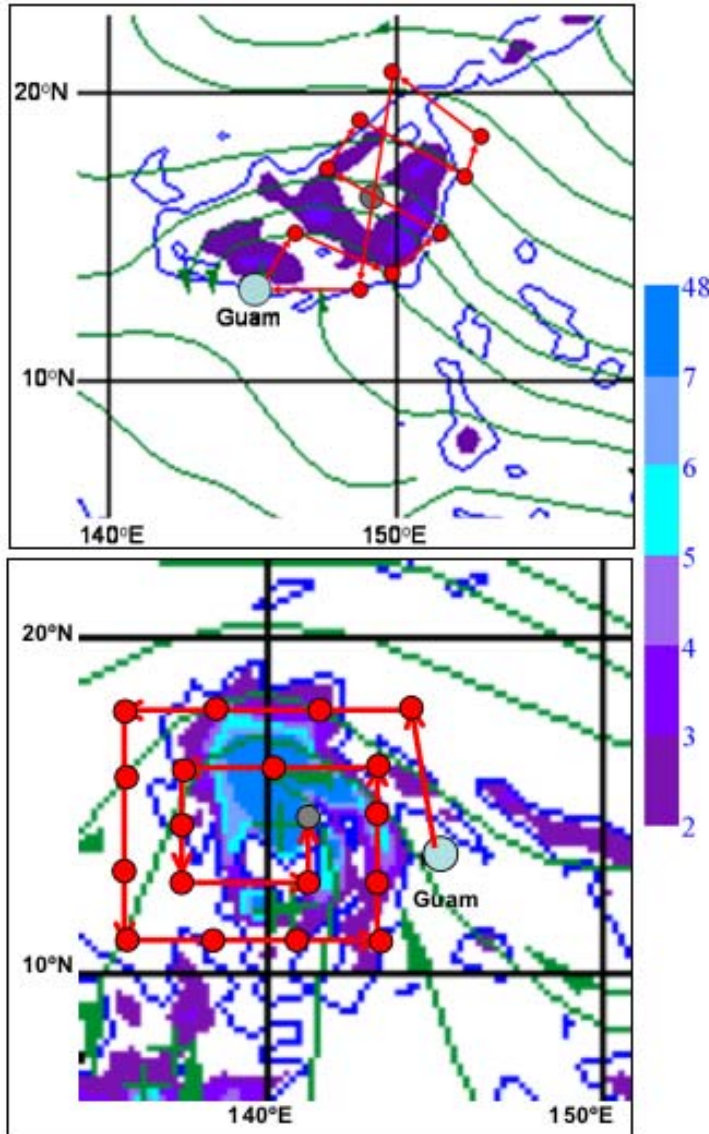


Figure 13. Schematic of original flight plans for the USAF C130 flights centered on 00Z 16 August (top) and 00Z 17 August (bottom). The green lines are 850 hPa streamlines in the resting frame and the shading is relative vorticity ($\times 10^5 \text{ s}^{-1}$) derived from ECMWF forecast data. The large blue circles indicates Guam, the smaller gray circles highlight the predicted sweet spot position, and the red circles indicate locations where dropwindsondes were planned to be released. The streamline analysis clearly depicts the presence of an open wave (top) approaching Guam. The red lines highlight the ‘lawn-mover’ pattern that is centered along the wave trough (top). In the bottom panel, the ‘square spiral’ pattern used during the second mission has the USAF C130 spiraling inward toward the forecasted sweet spot position.

3. Analysis Methodology

Marsupial analysis and forecast products are produced using the following methodology:

a. GFS FNL

For GFS FNL analyses, the maximum latitudinally-averaged (9–17N) total precipitable water (TPW) is used for both wave tracking and to calculate wave phase speeds. This methodology has three significant advantages: i) it allows tracking of moisture in two dimensions, rather than simply the moisture at the latitude of the sweet spot, ii) it results in a stronger pouch signal if there is a meridional component to the translation, and iii) it allows for wave tracking when the moisture gradient is not as obvious, such as in the relatively moist region of the western North Pacific. Disadvantages of this methodology are evident when the pouch and/or the distribution of moisture within are not symmetric or the wave is relatively dry. This situation results in a weaker TPW signature since the potential for dry air on the outskirts of the wave pouch tends to be included in this average value. For the Nuri case, the advantages of the latitudinal averaging outweigh these disadvantages.

The phase speeds are calculated for two time periods, the first from 12Z 7 August–00Z 11 August and the second from 06Z 11 August–12Z 17 August. Once the zonal phase speeds are calculated, a streamline analysis in the co-moving frame is produced. In this analysis, the critical latitude is defined as the latitude at which zonal velocity equals the zonal phase speed, (i.e., $u = c$), the trough axis is defined as the locus of points for which the meridional velocity vanishes, (i.e., $v = 0$) and the relative vorticity is cyclonic (DMW09 and Wang et al. 2009).

b. Real-Time Marsupial Forecasts

Wang et al. 2009 demonstrate that the preferred location for tropical cyclogenesis can be predicted within 200 kilometers up to 72 hours in advance using operational numerical models. For GFS and NOGAPS marsupial forecasts produced

during TCS-08, an average phase speed was derived from Hovmoeller diagrams using three meteorological variables to minimize errors arising from individual tracking methods: i) a zonal phase speed is calculated using the zero contour line in the meridional wind field. For real-time forecasts with no filtering, the wave signal in the meridional wind field is noisier because of high frequency variations and/or short-lived mesoscale vortices within the pouch (Wang et al. 2009). ii) A phase speed based on local fluid rotation is calculated using either relative vorticity or OW. This has limitations in the cases of tracking weak waves where the rotational signature has yet to strengthen. iii) A phase speed based on the tracking of a zonal moisture gradient: TPW for GFS and RH for NOGAPS (Wang et al. 2009). The TPW signature is observed to be one of the stronger pouch tracking methodologies in the Atlantic (Wang et al. 2009); however, the signal is much weaker in the western North Pacific basin as much of this region is continuously moist and not vulnerable to outbreaks from the Saharan Air Layer.

Diagnostic output of pertinent field variables are presented as vertical cross-sections after averaging each variable horizontally within a $3^\circ \times 3^\circ$ box centered on and moving with the sweet spot (Montgomery et al. 2010a; Wang et al. 2010a,b). These diagnostics are considered as an approximate representation of the pouch evolution. Examples of variables used in vertical cross-sections include relative vorticity, OW, and detrained volume flux (Δ), which is calculated at each level according to:

$$\int_A \left(\frac{\partial u}{\partial x} + \frac{\partial v}{\partial y} \right) dA \quad (4.1)$$

where u denotes zonal velocity, v the meridional velocity and dA is the horizontal area element (Raymond et al. 1998).

C. RESULTS

1. Evolution of the Easterly Wave Precursor (12Z 7 August–00Z 10 August)

Although the ultimate origin of the pre-typhoon Nuri disturbance is beyond the scope of this work, the CIMMS morphed TPW analysis (Figure 14) suggests that it may have originated from a roll-up episode in the central Pacific Inter-tropical Convergence Zone (ITCZ) on 12Z 7 August. At this time the GFS FNL indicates a low-level¹⁷ southwest-northeast tilted easterly wave in the streamline analysis centered at 8N, 165E (not shown). The vorticity and moisture fields associated with the easterly wave are disorganized. Whether this roll-up is caused by an underlying hydrodynamic instability of the ITCZ (Ferreira and Schubert 1997; Wang and Magnusdottir 2006) or a nonlinear evolution of a nearly-neutral moist Rossby wave/vortex on the northern side of the ITCZ (DMW09) is unknown and beyond the scope of the current investigation. For the purposes of this study, the author accepts the existence of this finite-amplitude wave/vortex structure that can be tracked westward for ten days prior to the declaration of Tropical Storm Nuri.

Figure 15 depicts a GFS FNL Hovmoeller diagram of latitudinally-averaged TPW valid from 00Z 6 August–12Z 17 August. A wave signal (indicated by a region of higher TPW) is first evident in these data at 00Z 8 August. This signal is tracked coherently from this time until the TS stage is declared by the JTWC forecasters (12Z 17 August). Due to the extended period that this wave is tracked, the wave is not expected to maintain a constant phase speed throughout its lifecycle. Observed changes in propagation speed are attributed to synoptic-scale regime changes or variations in the vertical level of the maximum amplitude of the wave over time. Two distinct regimes are identified here and a zonal phase speed for each is calculated using the GFS FNL TPW Hovmoeller diagrams. The first time period lasts from 12Z 7 August–00Z 11 August and is

¹⁷ For the analyses presented in this chapter, low-level refers to levels below 850 hPa. The maximum amplitude of the easterly waves observed during TCS-08 was usually lower than what is typically observed in the Atlantic sector. This is consistent with Reed and Recker (1971) and Chang et al.’s (1970) findings, and is the primary reason why the author presents analyses at levels below 850 hPa rather than the original DMW09 methodology.

accompanied by a higher zonal phase speed (10.5 m s^{-1}). As the wave crosses the dateline, it enters a region of weaker synoptic-scale steering flow, that causes the phase speed of the wave to gradually decrease. The average wave phase speed over the later period (06Z 11 August–12Z 17 August) is 7.0 m s^{-1} . The evolution of the wave's phase speed, including the slowing down as the system moves westward, is consistent with the propagation speed of easterly waves observed by Serra et al. (2008) in the central/western North Pacific sectors.

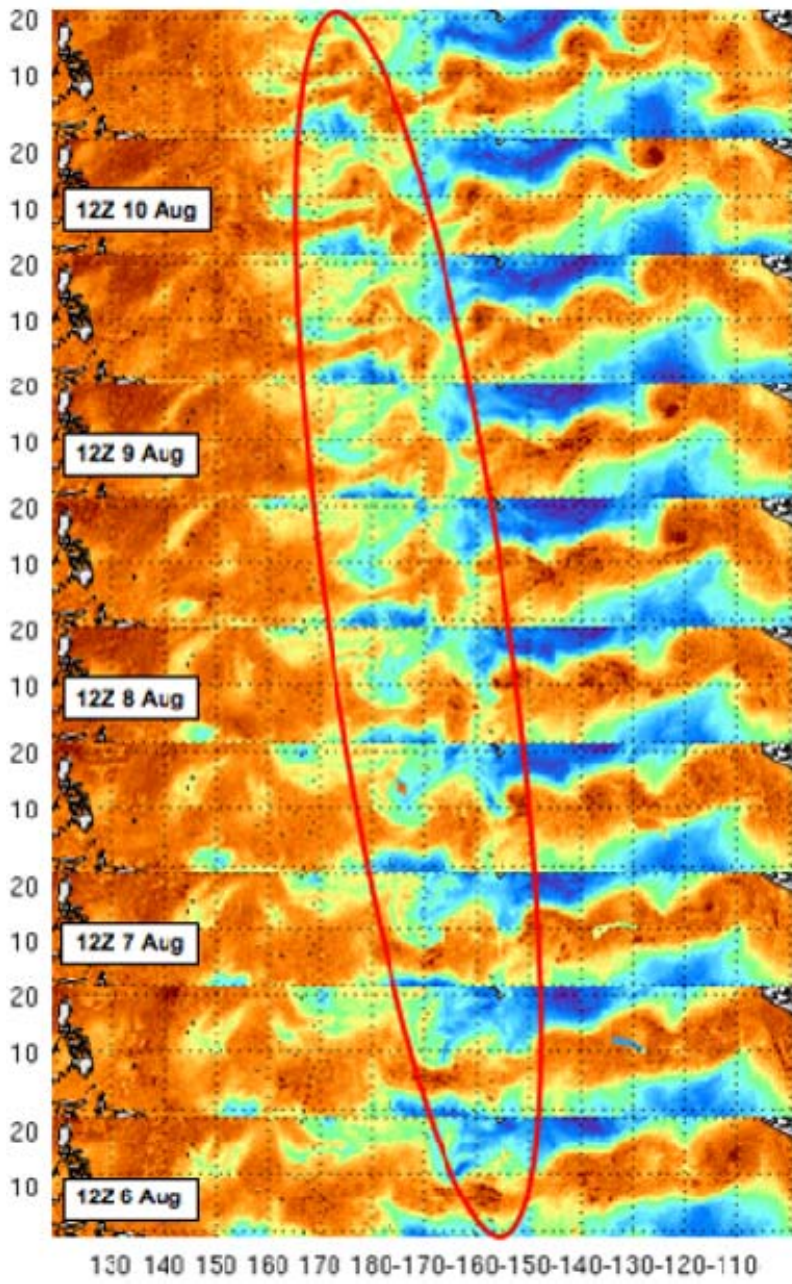


Figure 14. CIMMS Morphed TPW time series valid at 12-hour intervals beginning at 12Z 6 August. The red oval highlights the ITCZ roll-up event that is proposed to be the origin of the pre-Nuri disturbance.

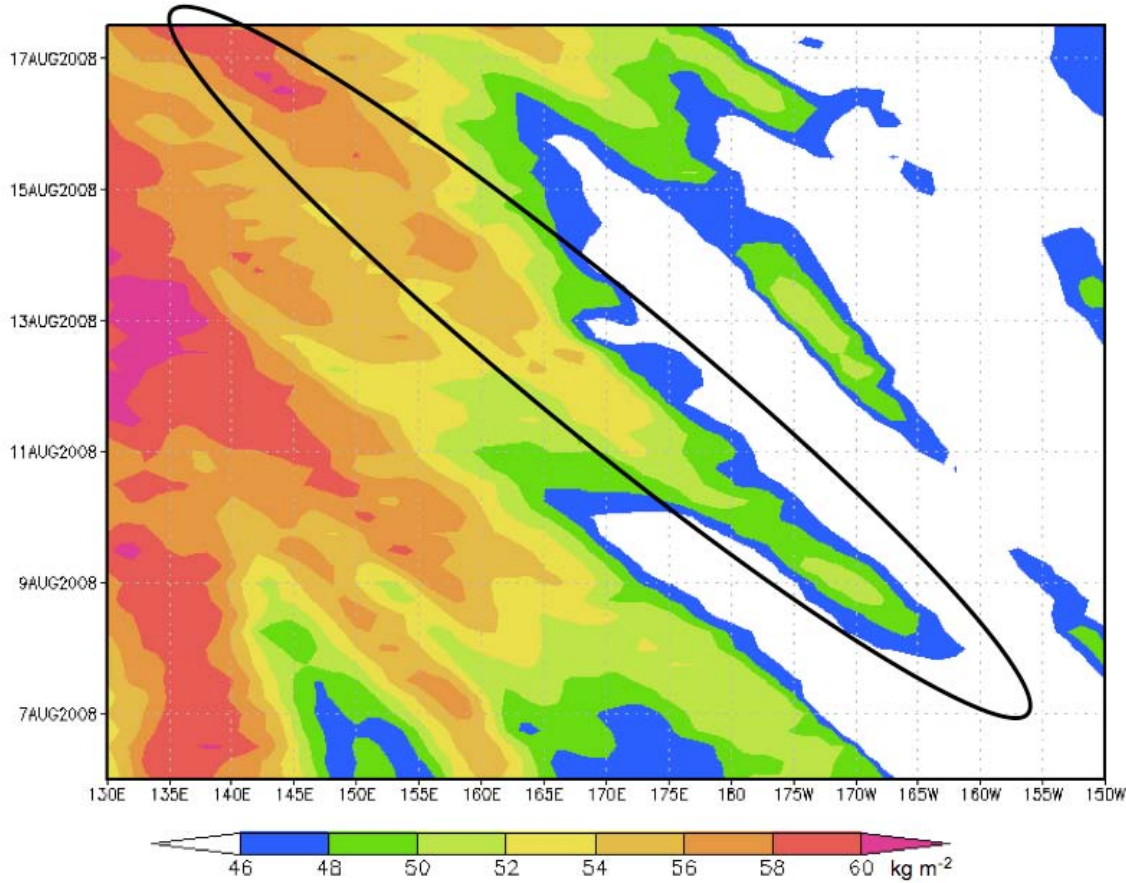


Figure 15. Latitudinally-averaged (9–17N) GFS FNL TPW Hovmoeller diagram valid 00Z 6 August–12Z 17 August (the time when the precursor Nuri disturbance is upgraded to a TS). The black oval highlights the higher moisture content observed in the pouch of the pre-Nuri disturbance versus its surrounding environment.

These phase speeds are used with the GFS FNL to construct an ‘official’ track of the sweet spot associated with the easterly wave that formed Typhoon Nuri. Figure 16 displays the location of the sweet spot (solid blue triangles) at the 925 hPa level at 12-hour intervals from 12Z 7 August–12Z 17 August, together with the JTWC Best Track position beginning at 00Z 16 August (red symbols). While the initial sweet spot of the wave trough is at approximately 10N, it propagates steadily westward and gradually northward, remaining between 14.5–17N from 14 August onward. The slight southward movement of the sweet spot on 16 August is believed to be due to the shift of the critical

latitude southward as a response to the strong convective activity observed by both satellite and aircraft radar data in the southern quadrant of the wave's pouch.

During the early evolution of this disturbance, a closed low-level cyclonic circulation is evident in the co-moving frame from 00Z 8 August–00Z 12 August. Values of OW within the pouch increase steadily (not shown) prior to the wave crossing the dateline (00Z 10 August). This is indicative of the disturbance showing favorable characteristics for tropical cyclogenesis (consistent with Wang et al 2009). Adverse environmental conditions during 10–14 August (discussed below) are argued to stall genesis during this time.

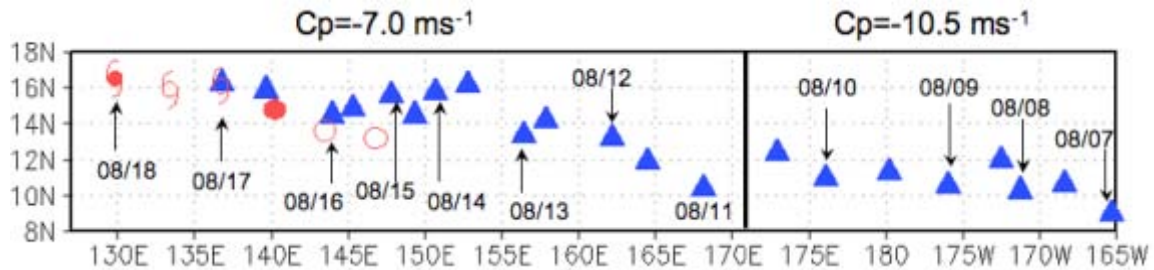


Figure 16. GFS FNL location of the sweet spot (blue triangles) valid at 12-hour intervals from 12Z 7 August–12Z 17 August. The thick black line delineates the time of the change in phase speeds used to calculate the sweet spot location. JTWC Best Track positions are indicated (red) at 12-hour intervals beginning at 00Z 16 August. An open circle designates an invest and a closed circle a TD. TS and typhoon symbols are shown when storm upgrades occurred.

2. Maintenance of the Pouch Through a Hostile Environment (12Z 10 August–00Z 15 August)

Gray (1968, 1975) introduced a set of necessary conditions for tropical cyclogenesis that remain generally accepted today. Here, they are summarized into the following four conditions: i) sea-surface temperatures $> 26^{\circ} \text{ C}$, ii) weak 850–200 hPa vertical wind shear, iii) sufficient cyclonic vorticity in the lower troposphere; and iv) moist convective instability and a moist mid-troposphere. This section focuses on the period from 12Z 10 August–00Z 15 August, a time when these favorable conditions

generally are not satisfied. It is suggested that this hostile synoptic environment has a profound influence on the evolution of the pre-Nuri disturbance.

As the pouch crosses the dateline, its translation takes on a northward component, which results in a displacement of the sweet spot from 10N to 15N over the next five days (consistent with the motion of western North Pacific easterly waves observed by Serra et al 2008). Concomitantly, the wave pouch enters a region with relatively dry low-mid-level air and strong vertical wind shear, conditions that are widely accepted to be hostile to tropical cyclone formation. Figure 17 displays a times series of the CIMMS Morphed TPW product valid at 12Z each day over a four-day period (9–12 August). The first panel (valid 9 August) shows the moist pouch¹⁸ of the pre-Nuri disturbance as an area of higher TPW centered at 10N, 175W. This relatively moist pouch is: i) surrounded on three sides by drier air (consistent with DMW09), with only the air in the south to southeast sector being moist, and ii) disconnected from the moist air in the western North Pacific. The pouch signal (identified as the area of relatively higher moisture) is more evident 24 hours later (10 August) when the pre-Nuri pouch (11N, 177E) takes on the shape of an elongated oval of higher moisture. Relatively drier air remains to the north through west and south quadrants upstream of the pouch.

On 11 August (Figure 17), the moist air associated with the pouch (12N, 172E) has propagated west and has begun to link with the moist air in the western North Pacific. There remains an area of relatively drier air separating this feature from the main pool of western North Pacific moisture. Furthermore, the pouch continues to exhibit higher TPW than its surrounding environment, and the TPW within the pouch increases over time. This supports DMW09’s second hypothesis (H2) that the marsupial pouch tends to protect the seedling embryo from the lateral intrusion of dry air. By 12 August (Figure 17), the moist pouch has almost entirely merged with the western North Pacific moisture pool. The moisture content within the pouch (12N, 162E) remains higher than the

¹⁸ The term pouch is defined in DMW09 (and Chapter II) as the flow bounded by the closed streamline that passes through the stagnation point closest to the sweet spot. In the analysis of the pre-Nuri disturbance, certain characteristics of the pouch, specifically the moisture gradient, are used to identify the horizontal extent and location of the pouch.

ambient environmental moisture. A small amount of relatively drier air remains west of the pouch, still separated from this moist airmass feature.

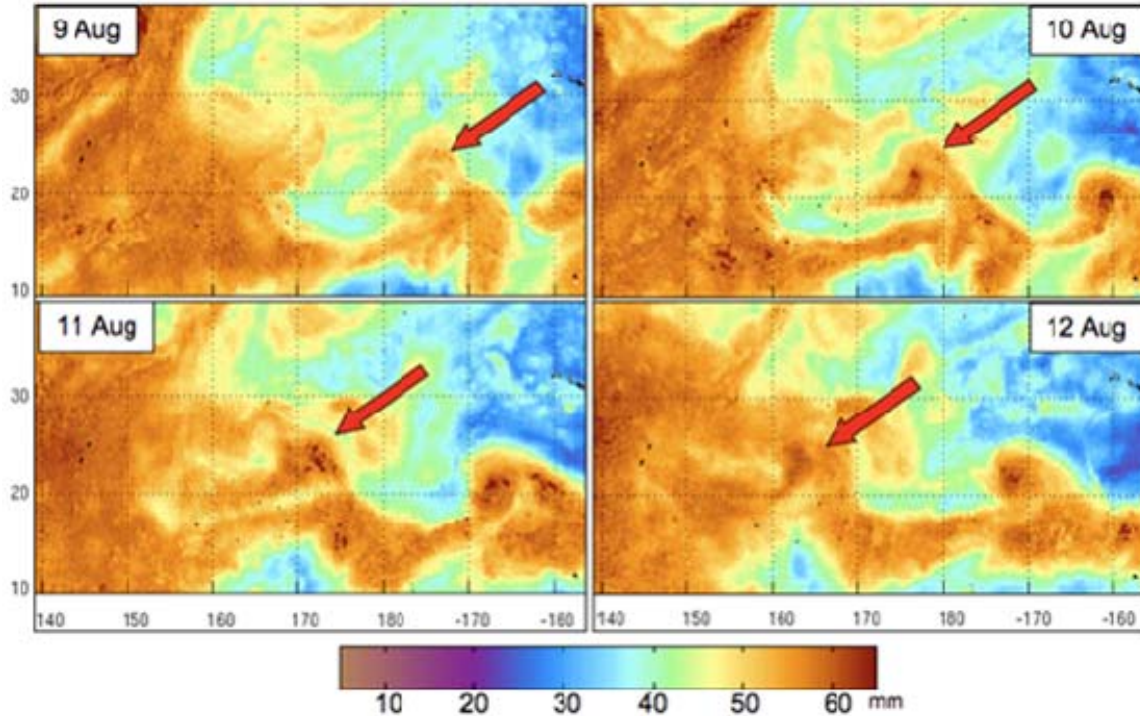


Figure 17. Four-day time series of CIMMS Morphed TPW valid at 12Z each day. Red arrows point to the location of the pouch, which is hypothesized by DMW09 to be an area of increased moisture in the low to mid-troposphere. The wave pouch protects the proto-vortex from lateral intrusions of dry air.

During the time period 9–13 August, the wave's presence in an area of low oceanic hurricane heat content (HHC)¹⁹ is an inhibiting factor to the development of deep convection and tropical cyclogenesis. Figure 18 shows the NRL Stennis HHC analysis for 12Z 15 August with the sweet spot track overlaid (solid blue triangles). As oceanic heat properties evolve slowly (time scale of weeks to months), this figure is representative of conditions over this time period. The motion of the wave pouch from

¹⁹ The NRL HHC plots use the definition presented in Leipper and Volgenau (1972), who define HHC as the integrated heat content down to the 26 °C isotherm relative to water of 26 °C: $HHC = \rho C_p \Delta T \Delta Z$ for $z > Z_{26}$. Here ρ is the density of ocean water near the mixed layer region, C_p is the specific heat of ocean water at constant pressure near the mixed layer region, ΔT is the average temperature difference above 26 °C for a given depth increment, and ΔZ is the incremental depth (taken at 0.5m).

10–13 August places it over an area of lower HHC, which tends to reduce the convective available potential energy (CAPE). This reduction in HHC results in a somewhat reduced potential temperature of the boundary layer air, which in turn tends to effectively stabilize the lower troposphere and thereby inhibit deep convection. This is known to be unfavorable for tropical cyclogenesis. After 12Z 14 August, the wave pouch moves into a region of higher HHC, which is favorable for tropical cyclogenesis.

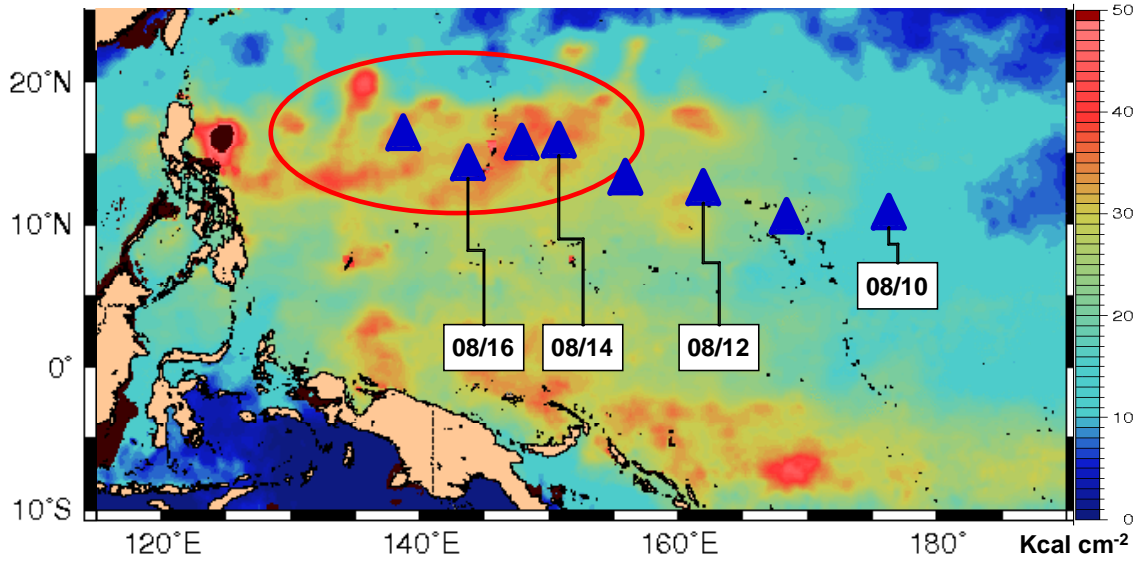


Figure 18. NRL Stennis oceanic HHC analysis valid 12Z 15 August overlaid with the track of the sweet spot from the GFS FNL analyses (solid blue triangles). The red oval indicates the area of higher HHC that the pouch passes over from the time convection is reinvigorated (12Z 15 August) until a TS is declared.

Another factor inhibiting tropical cyclogenesis during this time period is strong vertical wind shear. Figure 19 shows a six panel time series of deep layer (200–850 hPa) shear and 925 hPa streamlines in the co-moving frame from the GFS FNL valid at 12Z each day from 10–15 August (the solid blue triangle indicates the position of the sweet spot). On 10 August, a closed low-level cyclonic circulation has just crossed the dateline and is entering an unfavorable area of deep layer vertical shear greater than 21 m s^{-1} (40 kt). Over the next 24 hours, the areal extent of the strongest vertical wind shear ($>21 \text{ m s}^{-1}$) decreases and shifts to an area between 160–170E and 12–18N. This strong vertical shear is believed to have contributed to the weakening circulation observed on 11–12 August. By 12Z 12 August, the closed circulation in the co-moving frame is no longer

evident. Over the next two days (13–14 August), the area of strongest shear ($>21 \text{ m s}^{-1}$) is observed to retreat eastward and, as a result, the precursor disturbance encounters a less hostile environment. After 12Z 14 August, the pouch of the pre-typhoon Nuri disturbance enters and remains in a region of $2.5\text{--}5.1 \text{ m s}^{-1}$ (5–10 kt) of vertical shear until genesis.

The vertical depth of the wave pouch is examined during Typhoon Nuri’s genesis sequence to assess the potential effects this vertical wind shear may have had on pouch resiliency. For this exercise, the depth of the pouch (i.e., vertical extent) is defined as the upper-most level at which the area-averaged OW remains positive (the averaging domain is a $3^\circ\text{x}3^\circ$ box surrounding the translating sweet spot at the 925 hPa level). These data are plotted as vertical extent vs. time (Figure 20) and the three phases of the tropical cyclogenesis sequence described in this section are delimited by thick black lines. During the early evolution period (12Z 7 August–00Z 10 August) the pouch exhibits a trend of increasing vertical depth over time. After 12Z 10 August, when the wave propagates through the hostile environment, there is a decline in the average vertical extent of the pouch. When the wave emerges from these hostile conditions (00Z 15 August) there is a rapid increase in the vertical extent of the pouch through the troposphere. These data suggest that the hostile conditions encountered by the pre-Nuri wave are not favorable for building a coherent circulation throughout the depth of the troposphere. The increase in vertical depth of the wave pouch is thought to be a favorable condition for genesis and appears to have occurred in the Typhoon Nuri case.

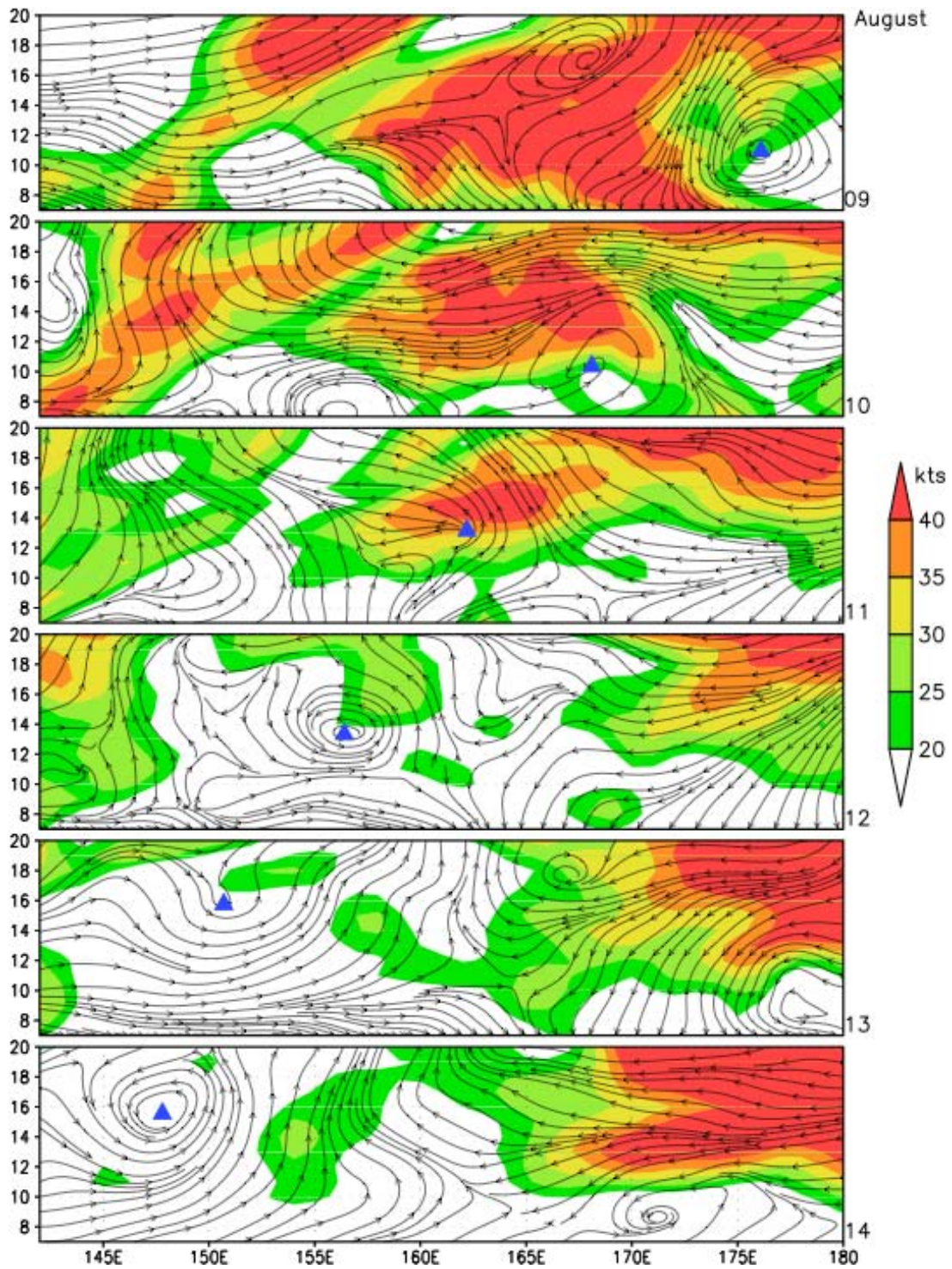


Figure 19. GFS FNL 850–200 hPa shear (kt, shaded), 925 hPa streamlines in the co-moving frame, and sweet spot location (solid blue triangles) valid at 12Z each day.

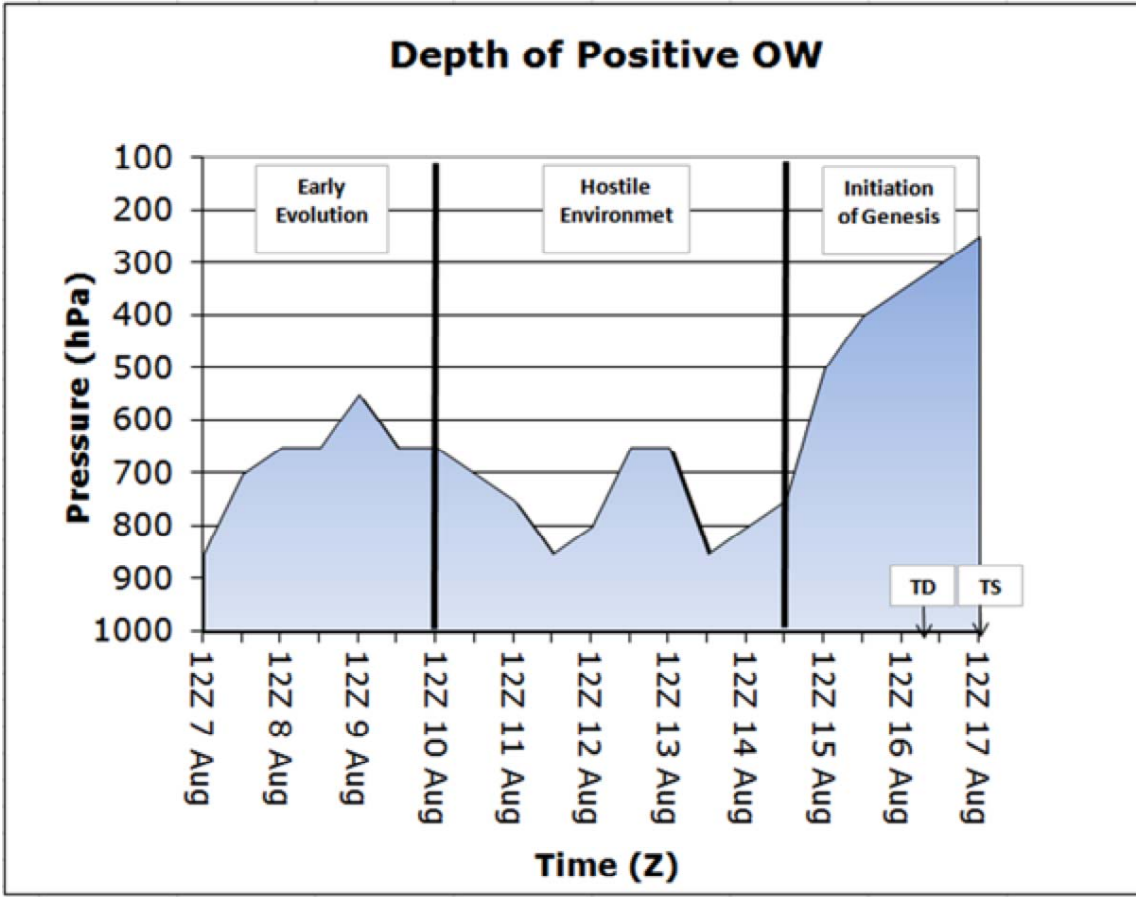


Figure 20. Time series of depth of areally-averaged positive OW (shaded) over time from the GFS FNL. The OW is areally-averaged within a $3^\circ \times 3^\circ$ box centered on and moving with the sweet spot at the 925 hPa level. The depth of positive OW is considered an estimate of the vertical depth of the pouch. The thick black lines delimit key time periods in pre-Typhoon Nuri's evolution as described in this study. TD and TS indicate JTWC upgrades of the storm.

3. Reinvigoration of Convection and Initiation of the Genesis Sequence (12Z 15 August–12Z 17 August)

Figure 21 depicts a times series of 925 hPa streamlines from the GFS FNL in the resting frame valid at 12-hour intervals from 12Z 15 August–12Z 17 August. Figure 22 shows the corresponding time series in the co-moving frame. Overlaid on these figures are MTSAT IR brightness temperature data. The images in the co-moving frame show the wave trough axis (black line) and critical latitude (purple line). The thick black line is

the approximate track of the sweet spot center.²⁰ On 12Z 15 August, strong convection begins to form on the eastern and southern portions of the wave trough (Figure 21, when viewed in the resting frame) or pouch (Figure 22, when viewed in the co-moving frame). This is concurrent with the feature moving an environment of low vertical wind shear (Figure 19) and higher HHC (Figure 18). A closed low-level cyclonic circulation is evident in the co-moving frame. Interestingly, this is not evident in the ground-based reference frame and is consistent with DMW09 who note that a closed circulation could be found in the co-moving frame up to 72 hours earlier than in the ground-based reference frame.

The second panels of Figure 21 and Figure 22 are valid during the first joint USAF C130/NRL P3 flights into the pre-Nuri disturbance (00Z 16 August, see Figure 12). The sweet spot location is at 14.9N, 145.3E. The strongest convection at this time is located to the south and east of the sweet spot, but remains largely within the pouch. This is consistent with DMW09, who argued that repeated convection within the pouch leads to continued moistening, favoring further deep convection, resulting in an important positive feedback process. The southern and eastern portions of the wave pouch are the favored regions for convection at this time, most likely because of their location in an area of higher HHC.

The C130/P3 research missions centered around 00Z 16 August sampled the horizontal extent of the pouch. Figure 23 depicts the dropwindsonde data from these flights overlaid with MTSAT IR data. The top panel represents 850 hPa wind barbs in the resting frame and the bottom panel shows the data in the co-moving frame. The red cross is the location of Guam. The blue triangle indicates the approximate location of the dropwindsonde-derived closed low-level cyclonic circulation in the co-moving frame. When viewed in the earth-relative frame the aircraft observations depict an open wave, confirming that the precursor disturbance to Typhoon Nuri is of the easterly wave type. In the co-moving frame, the dropwindsonde data (Figure 23) indicates a closed low-level

²⁰ It is noted that this is a linear approximation of the sweet spot track. The 12Z 16 August panel shows that the sweet spot is actually east of this line, likely due to a non-uniform instantaneous propagation speed of the wave.

cyclonic circulation at 146.7E, 14.3N. The author believes this to be the first in-situ observational evidence of the coherent cat's eye circulation that eventually becomes Typhoon Nuri.

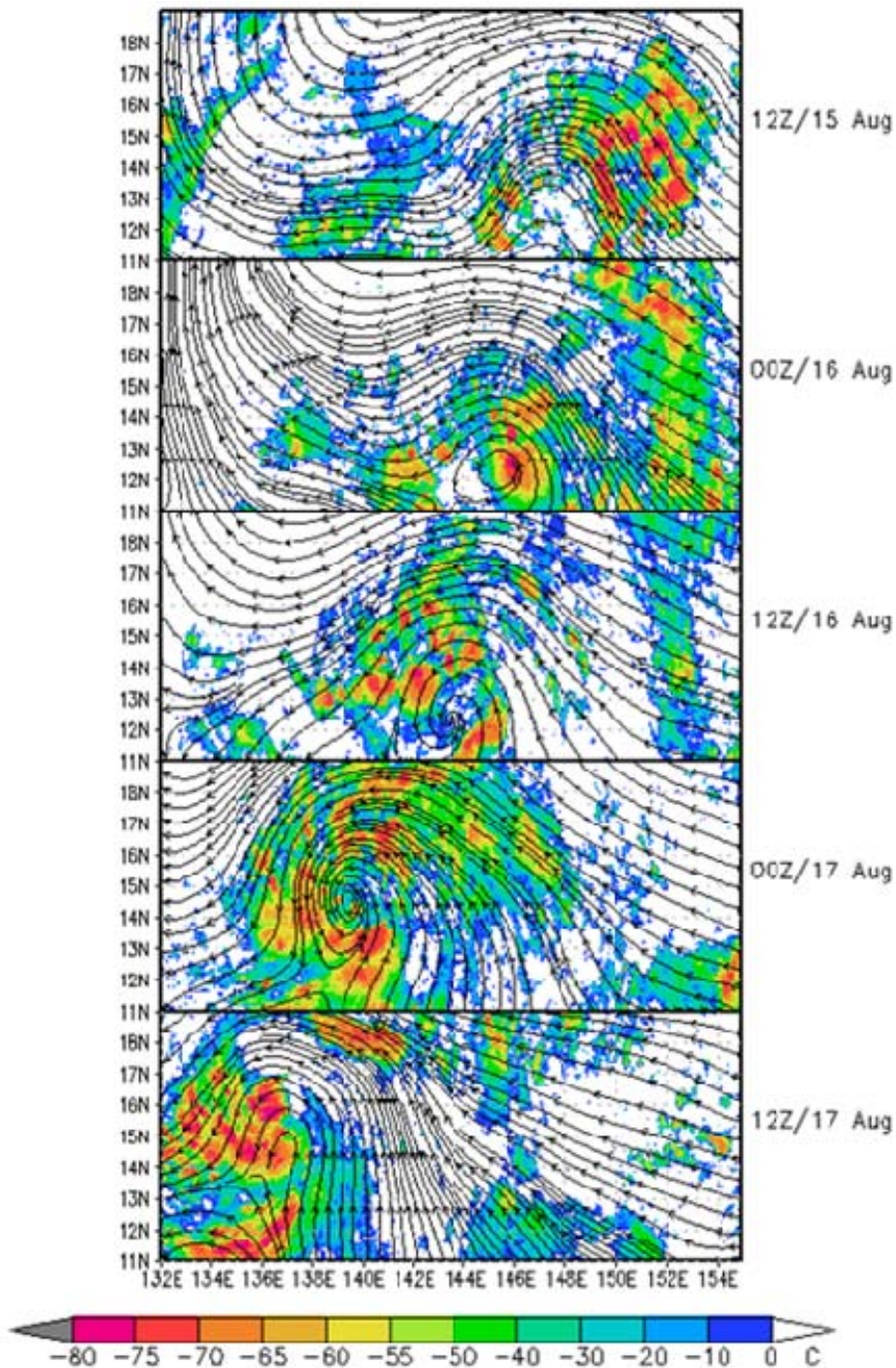


Figure 21. Time series of GFS FNL 925 hPa streamlines in the resting frame overlaid with MTSAT IR brightness temperature valid every 12 hours from 12Z 15 August to 12Z 17 August.

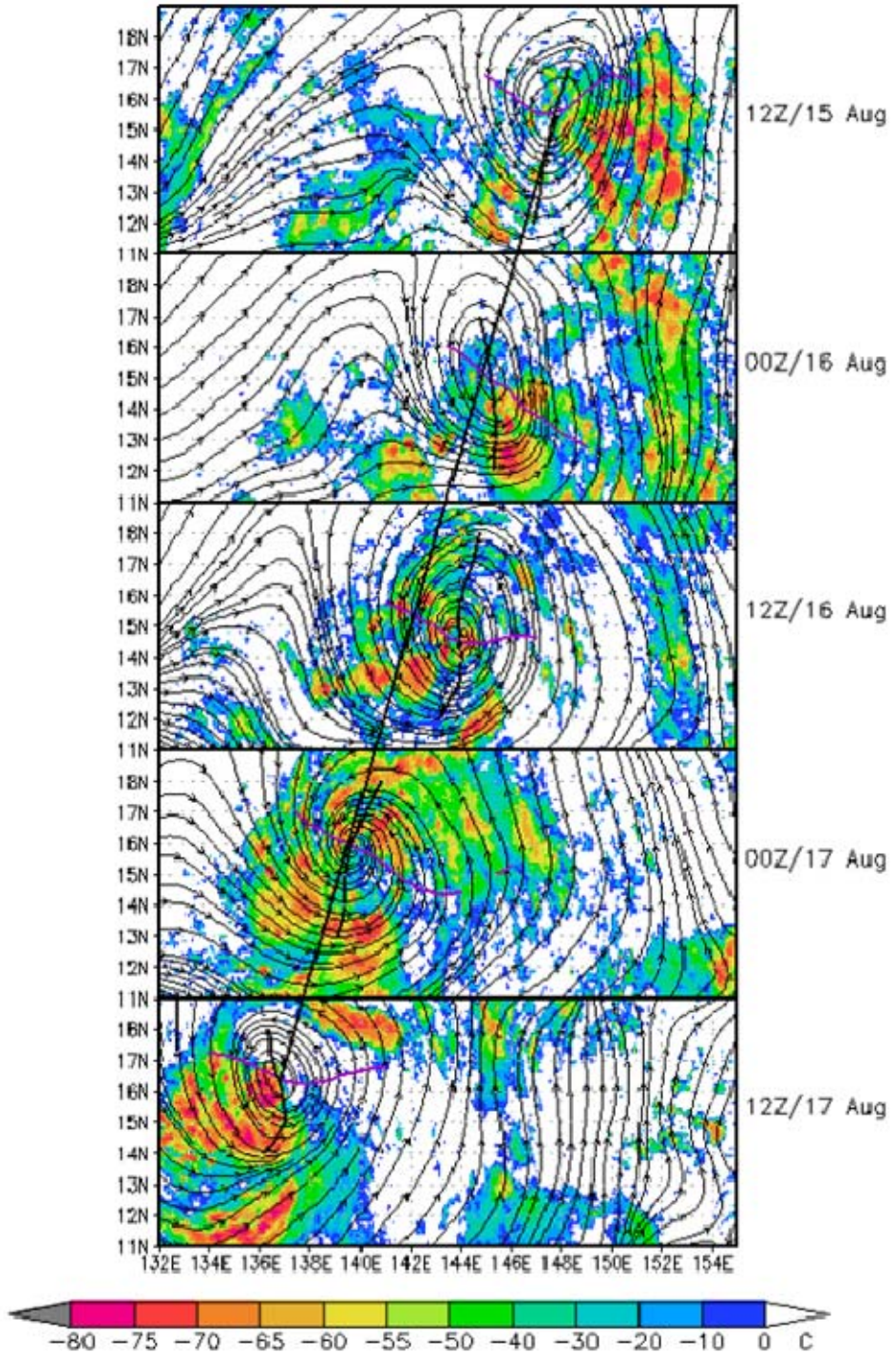


Figure 22. Time series of GFS FNL 925 hPa streamlines in the co-moving frame overlaid with MTSAT IR brightness temperature valid every 12 hours from 12Z 15 August to 12Z 17 August. The black line represents the wave trough axis and the purple line the critical latitude as seen by the wave plus sub-synoptic scale flow. The thick black line indicates the approximate propagation of the sweet spot.

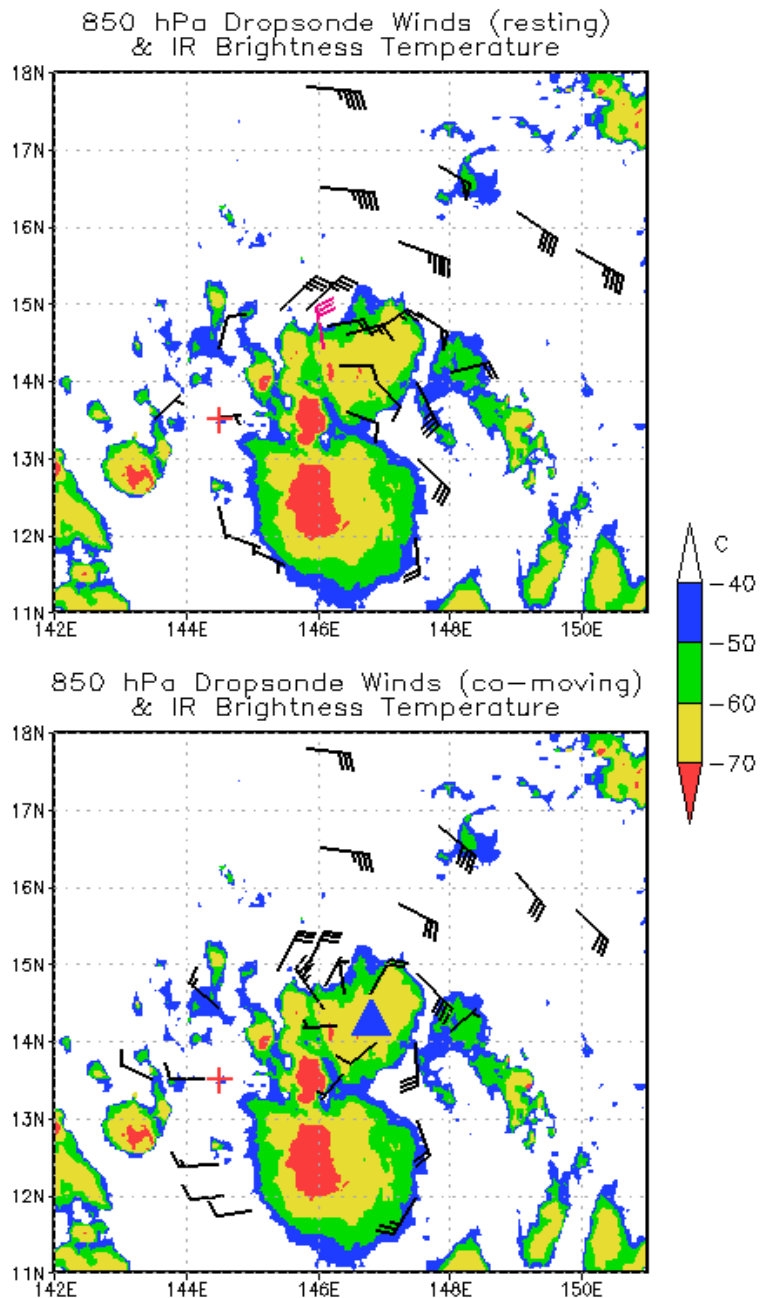


Figure 23. Combined USAF C130 and NRL P3 850 hPa dropwindsonde observations from the genesis flight centered on 00Z 16 August overlaid with MTSAT IR data. Wind barbs are in the resting (top) and co-moving (bottom) frames. Wind speeds are in knots with a full barb representing 10 kt. Magenta barbs indicate winds with a westerly component in the earth-relative frame. The red cross represents the location of Guam and the blue triangle represents the location of the low-level cyclonic circulation center in the co-moving frame. The C130 flight was centered along the wave trough axis and collected data throughout the pouch.

The GFS FNL/MTSAT analysis valid at 12Z 16 August (middle panels, Figure 21 and Figure 23) depicts a closed low-level cyclonic circulation in both reference frames. However, the center of this cyclonic circulation in the resting frame is located more than one-degree south of the circulation in the co-moving frame. It is noteworthy that the convective maximum is located west of the trough axis. The shifting of the precipitation maximum from east of the trough axis to the west as the wave moves westward is consistent with previous studies on western North Pacific easterly waves dating back to Reed and Recker (1971). Figure 24 is a zoomed-in view of this time period when the strong convection begins to occupy all quadrants of the pouch and is beginning to become centered on the sweet spot. Of particular interest is the initiation of convective bands to the south and northeast of the sweet spot (red arrows), which satellite loops show to spiral cyclonically inward towards the center of the circulation in the co-moving frame. At the time of the second joint USAF C130/NRL P3 sortie into the pre-Nuri disturbance (00Z 17 August), convection has filled all quadrants of the wave's pouch and the banding seen 12 hours earlier is even more evident (Figure 21 and Figure 22). These observations suggest that deep convection is beginning to wrap around the low-level cyclonic circulation center in the co-moving frame as the system is undergoing tropical cyclogenesis (JTWC upgraded this invest area²¹ to a TD prior to this time, Figure 12).

The second joint C130/NRL P3 flight identified a broad cyclonic circulation center at 850 hPa in the southwestern portion of the flight pattern at approximately 14N, 139.5E (Figure 25). This circulation center is observed to tilt with height and is weak and shallow (not shown). The area where this cyclonic circulation is observed is concurrent with the areas of strongest convection (Figure 21) and is consistent with the closed low-level cyclonic circulation in the GFS FNL resting-frame analysis (Figure 21). In the co-moving frame, however, the low-level cyclonic circulation is slightly farther east (140.5E) and north (15N) of the circulation center in the resting frame. In this co-moving frame, the circulation is well defined and more robust than the weakly observed circulation in the resting frame (Figure 25). This suggests that the flow pattern in the co-

²¹ The term 'invest' is used by operational tropical cyclone forecast centers to identify an area of interest for collection of specialized observations or running model guidance (NHC 2010). The designation of a system as an invest does not correspond to a likelihood of development (NHC 2010).

moving frame is more representative of the intrinsic atmospheric state (developing TD) than the less organized flow observed in the resting frame. This analysis illustrates the inherent benefit of viewing/tracking a developing tropical cyclone in the co-moving frame (as advocated in DMW09) for operational forecasters.

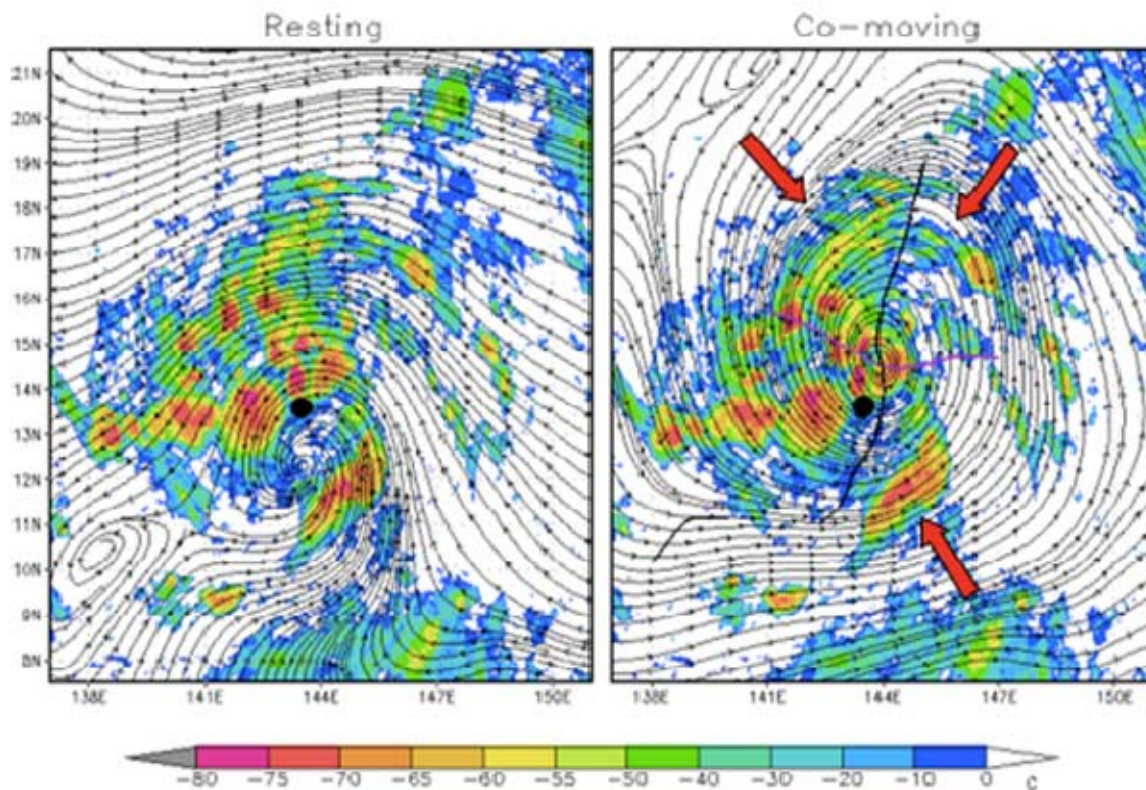


Figure 24. GFS FNL 925 hPa streamlines in the resting (left) and co-moving (right) frames overlaid with MTSAT IR brightness temperature valid 12Z 16 August. In the co-moving frame, the black line represents the wave trough axis and the purple line the critical latitude. The red arrows indicate the convective bands spiraling cyclonically inward towards the sweet spot in the co-moving frame. The black dot represents the JTWC Best Track position.

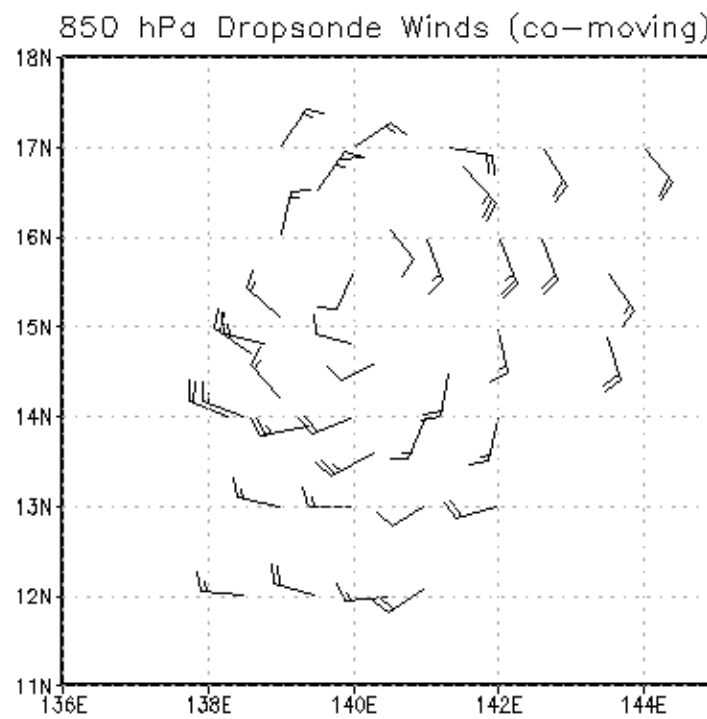
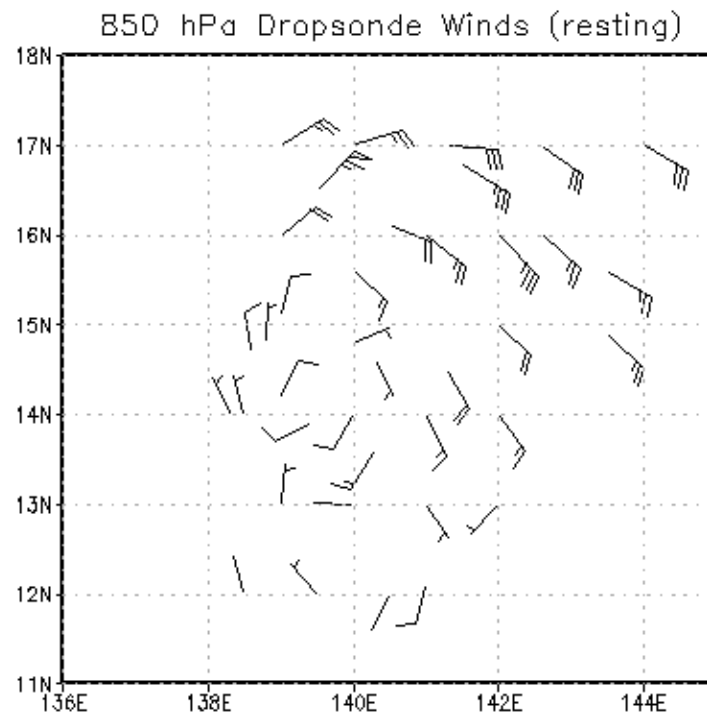


Figure 25. Combined USAF C130 and NRL P3 850 hPa dropwindsonde observations from the second genesis flight centered on 00Z 17 August in the resting (top) and co-moving frames (bottom). Wind speeds are in knots with a full barb representing 10 kt.

4. Consideration of Other Possible Factors in the Formation of Typhoon Nuri

a. The Possible Role of a Monsoon Trough

In the case of Typhoon Nuri, the presence of near equatorial westerlies near Palau (7N, 134E) is cited by other TCS-08 researchers as evidence of the presence of a monsoon trough leading to the genesis of Typhoon Nuri within this easterly wave (versus the non-development of previous easterly waves observed during TCS-08). The following analyses show that the westerly flow near Palau: i) is not indicative of the presence/formation of a monsoon trough in the Typhoon Nuri genesis area, and ii) has no discernible impact on the formation of Typhoon Nuri.

Analysis of vertical wind profiles derived from Skew-T data (shown in Appendix C) shows weak westerly flow (5–15 kt) in the lower troposphere at Koror, Palau from 00Z 14 August–00Z 16 August. During this time period, the sweet spot of the pre-typhoon Nuri disturbance is centered between 14.9–16.2N and moves from 152.8 to 145.3E. Therefore, the Guam sounding (13.8N, 144.5E) is more representative of the conditions influencing the formation of Typhoon Nuri. These data (shown in Appendix C) indicate deep easterly flow throughout the depth of the troposphere until 00Z 15 August. After this period, a classical easterly wave signature is evident in the Guam sounding (which is corroborated by aircraft data) as low-level winds shift from NE-E-SE during 12Z 15 August–00Z 17 August. At no point did the Guam sounding data indicate the presence of low-level westerly flow extending into this region.

These data are corroborated by the spatial evolution of the observed wind field in both satellite-derived cloud-drift winds and QuikSCAT observations. The author has argued that 12Z 15 August is a critical time in the tropical cyclogenesis sequence of Typhoon Nuri, as this coincided with the reintensification of convection within the marsupial pouch. The CIMSS low-level cloud drift winds prior to this time at 06Z 15 August (Figure 26, top) and QuikSCAT surface wind data (Figure 26, bottom) valid 15 August both show approximately uniform easterly flow from the dateline to points well west of 140E and north of 9N (the solid red line demarcates the transition between

easterly flow and westerly flow).²² The westerly winds near Palau do not extend farther than 138E during the formation sequence. This confirms that large-scale westerly winds are not present in the area of the pre-Nuri disturbance (indicated by the red circle in Figure 26); nor did they play any discernible role in the genesis of Typhoon Nuri. Examination of the CIMSS data for the period 00Z 14–18Z 16 August (when JTWC upgraded the disturbance to a TD) confirms that synoptic-scale westerly flow is not observed farther east than 138E (below 20N) and corroborates the lack of a monsoonal flow in the vicinity of the pre-Nuri disturbance. On 16 August both the QuikSCAT surface winds and GFS FNL data indicate the presence of isolated westerlies near the southeast portion of the wave in the resting frame. The author suggests this is evidence of the wave forming a closed cyclonic circulation at the lower levels, rather than a large-scale, organized monsoon flow.

In an attempt to quantify the relative role the monsoon trough may have played in Typhoon Nuri’s tropical cyclogenesis sequence, absolute angular momentum fluxes (AAMF) are calculated according to Holland (1983) and described in Cheung and Elsberry (2002). In a cylindrical coordinate system centered on and moving with the GFS FNL 925 hPa sweet spot position,²³ absolute angular momentum (AAM) is defined as:

$$AAM = v_T r + \frac{1}{2} f r^2 \quad (4.2)$$

where v_T is the tangential wind, r is the radius from the sweet spot, and f is the Coriolis parameter: $2\Omega \sin \phi$, where Ω is the angular speed of the earth and ϕ is the latitude. If the

²² The QuikSCAT data show a small area of isolated westerly winds located between 148E, 8–9N on 15 August. These westerlies are spatially separated from the large-scale westerlies that extend through the Philippine Sea and northward. These westerly winds at 148E, 8–9N are potentially signs of cross-equatorial flow extending into the developing low-level cyclonic circulation. They are not evidence of monsoonal flow impacting the genesis of Typhoon Nuri, as the flow is too limited in horizontal scale and not evident in the analysis prior to this time.

²³ Although there is some inherent dependence on the accuracy of the sweet spot position in the AAMF analysis, in case of Typhoon Nuri there are two dominant synoptic-scale features. These features are distinct in the analysis and small potential errors in the sweet spot position will likely have no impact to the interpretation presented here.

wind components are broken into symmetric and asymmetric components, the angular momentum fluxes can be calculated across a circle of a certain radius (Cheung and Elsberry 2002):

$$AAMF(r) = \overline{rv_R} v_T + \overline{rv'_R v'_T} + \frac{f_o r^2 \overline{v}_R}{2} + \frac{r^2 \overline{fv'_R}}{2} \quad (4.3)$$

where v_R is the radial wind, f_o is the Coriolis parameter at the center of the disturbance (in this case, the sweet spot), the overbars indicate azimuthal averages and the primes denote the asymmetric portion. The four terms on the right hand side of Equation 4.3 are called: the symmetric relative angular momentum (RAM) flux, the asymmetric RAM flux, the symmetric Coriolis torque, and the asymmetric Coriolis torque (Cheung and Elsberry 2002).

Challa and Pfeffer (1980, 1990) suggest that AAMF are important in tropical cyclone formation because the radial circulation enhances the cyclogenesis process by drawing warm, moist air into the center of the developing storm. Cheung and Elsberry (2002) use the NOGAPS model to compare AAMF in developing versus non-developing tropical cyclones in the western North Pacific basin. They show that a net input of AAMF ($AAMF < 0$) at 850 hPa and a net output at 200 hPa ($AAMF > 0$) are favorable conditions for tropical cyclogenesis in the NOGAPS model. They also suggest that the symmetric RAM and symmetric Coriolis torque are the leading contributors to spin-up. Cheung and Elsberry (2002) note that azimuthal variations in magnitude of AAMF are attributed to synoptic-scale features (i.e., the monsoon trough). Harr et al. (1996) analyze the development of Typhoon Robyn which formed during the Tropical Cyclone Motion 1993 (TCM-93) field campaign. They suggest that interaction of the pre-typhoon disturbance with the monsoon trough leads to an increase in low-level spin-up through RAM fluxes within 4° latitude radius of the storm. Prior to interaction with the monsoon trough, there is no spin-up through RAM fluxes (Harr et al. 1996).

For the case of the formation of Typhoon Nuri, AAMF are used here to quantify the relative contribution of different synoptic-scale features play in the low-level spin-up. Figure 27 is a six-panel time series of AAMF valid every 12 hours from the GFS FNL beginning at 00Z 15 August. The plot is radial distance from the sweet spot (abscissa, $\times 100$ km) versus pressure (ordinate). Warm colors represent $AAMF < 0$ (net influx of AAMF) and cool colors represent $AAMF > 0$ (net outflow of AAMF). At the first time period, 00Z 15 August, the monsoon trough is well over 10° longitude (> 1100 km) from the sweet spot position. In the AAMF analysis (Figure 27), the AAMF from the monsoon trough are represented as negative values in the low to mid troposphere beyond 1100 km. Closer to the sweet spot there are areas of negative AAMF throughout the wave pouch (within ~ 400 km). At 12Z 15 August, there is a deep layer of negative AAMF from 200–400 km and negative AAMF stretch from this point to the end of the domain. The AAMF signal from the monsoon trough is similar to 12 hours prior and remains approximately 10° longitude from the location of the sweet spot. At 00Z 16 August, the low to mid-level AAMF pattern is similar to the pattern from 12 hours previous except that the deep layer of negative AAMF within the wave pouch now only extends upward only through the low-levels. Recall that by this time, there is already a closed circulation in the co-moving frame. This analysis suggests that in the early stages of development, the negative AAMF within the wave pouch (within ~ 400 km of the sweet spot) are able to spin-up the proto storm independent of the remote influence of the monsoon trough. Over the next 36 hours, the negative AAMF entering the pouch deepen through the middle troposphere. These fluxes are likely a result of the convergent component of the wind into the center of the growing circulation. The upper levels display the favorable condition of positive AAMF that helps enhance storm outflow.

Summary: This foregoing analysis suggests that AAMF associated with Typhoon Nuri’s easterly wave precursor contribute to the spin-up of the low-level vortex and supports the hypothesis that the monsoon trough has no discernable influence of the development of Typhoon Nuri.

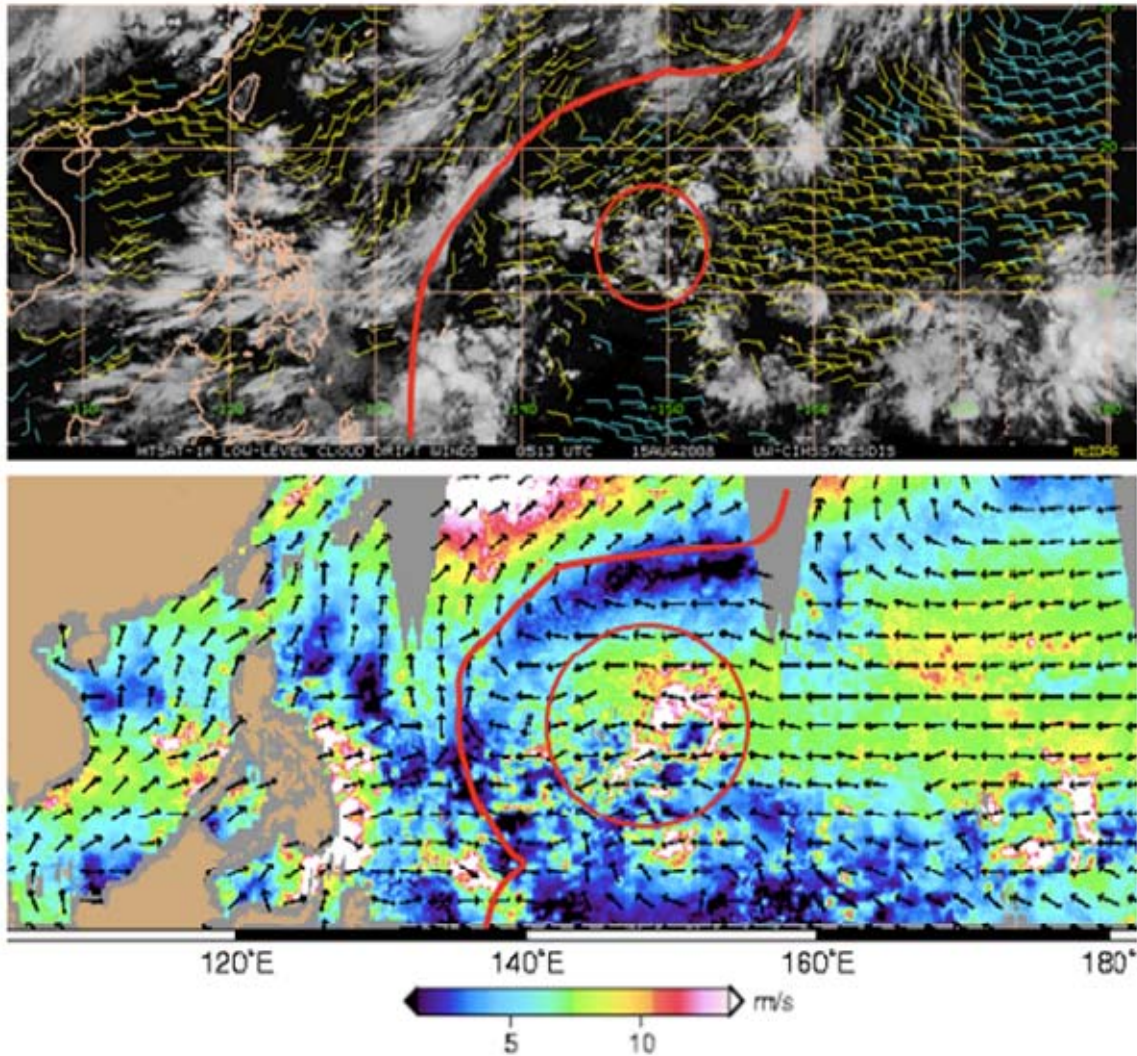


Figure 26. CIMMS low-level cloud drift winds (top) valid 06Z 15 August and QuikSCAT Level-3 retrieved wind vectors and wind speed (shaded) valid 15 August (bottom). The blue wind barbs in the CIMMS product are retrievals between the levels of 950–851 hPa and the yellow are retrievals between 850–700 hPa. The red circle highlights the easterly wave that is the precursor to Typhoon Nuri and the red line indicates the easternmost extent of large-scale organized westerly flow. Note that westerly winds are more than 10 degrees from the pre-Nuri disturbance in both analyses.

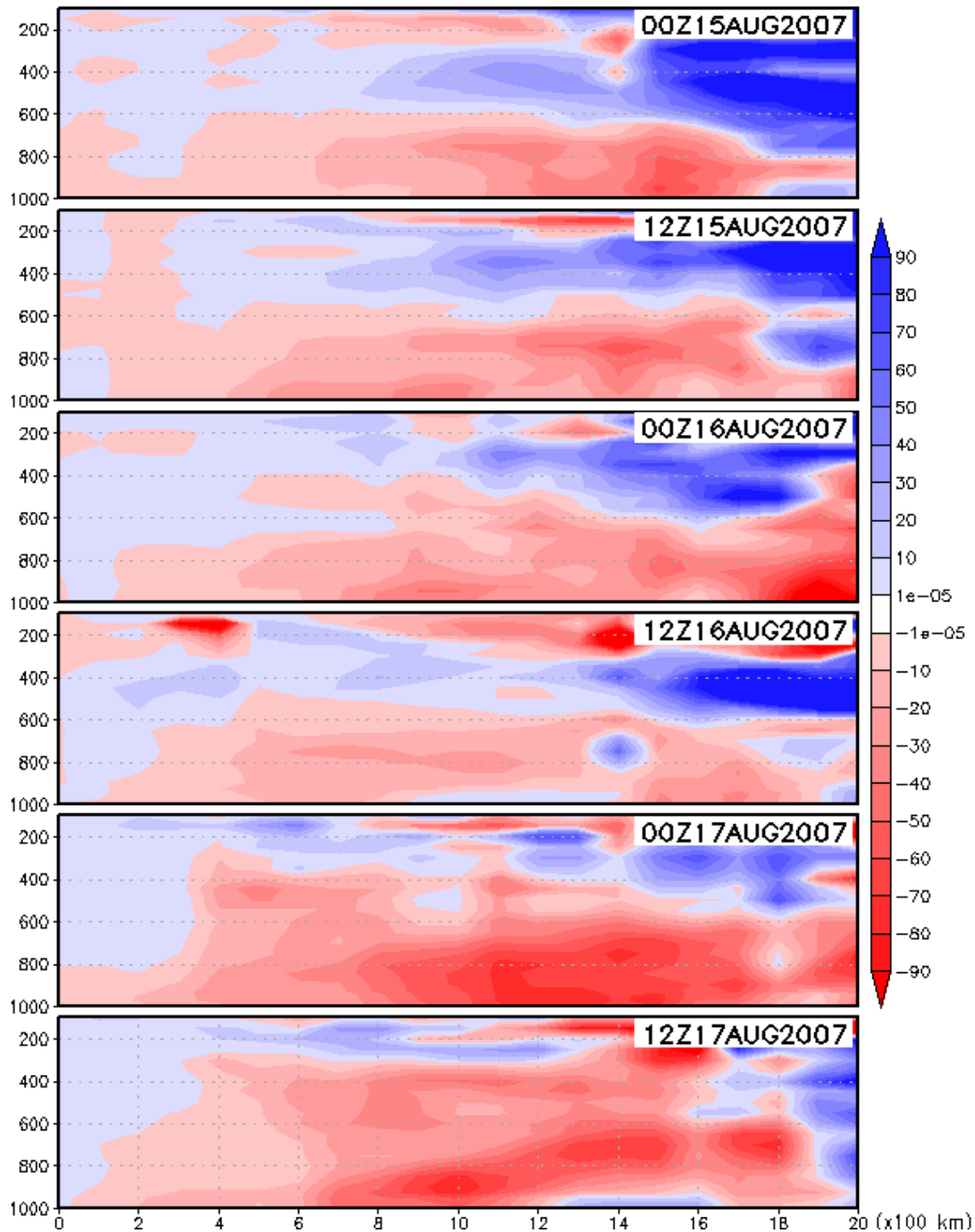


Figure 27. Six-panel time series of AAMF ($\times 10^7 \text{ m}^3 \text{ s}^{-2}$) from the GFS FNL. The AAMF are calculated at radial distances from the sweet spot. The abscissa is radial distance ($\times 100\text{km}$) from the sweet spot and the ordinate is pressure.

b. The Possible Role of a TUTT

It is next argued that the presence of TUTT cells have no impact on the genesis of Typhoon Nuri. Two upper-level cyclonic circulations are identified by the CIMMS upper level cloud drift winds (Appendix C) in the general region of pre-Nuri disturbance. The first is a weak, nearly stationary cyclonic circulation at 15N, 160E present from 01Z 14 August–21Z 14 August. After this time, this circulation center drifts slightly south to 11N and is present until 06Z 15 August. Subsequently, it is no longer distinguishable, as weak convection is initiated in the area. The second is a stronger upper-level cyclonic circulation that entered the western North Pacific (28N, 175E) on 12Z 15 August. This TUTT moved southwest, eventually reaching 24N 168E by 00Z 17 August. However, these upper-level cyclonic circulations observed in the CIMMS data are not believed responsible for the genesis of Typhoon Nuri. The first TUTT circulation is too weak and became indistinguishable as the genesis process began. The second TUTT, which represents a much better fit to Sadler's (1976, 1978) classical definition, is too far removed (approximately 19°) from the genesis region to have any significant dynamical or thermodynamical influence on the pre-Nuri disturbance. This contention is supported by the AAMF analysis that shows a net outflow of AAMF near the location of the TUTT (Figure 27) that is disconnected from the developing wave pouch.

5. Evaluation of Real-time Forecasts (00Z 11 August–12Z 17 August)

The construction of real-time forecasts incorporating the methodology outlined in Wang et al. 2009 was applied successfully during the TCS-08 field experiment to provide forecast guidance for operational flight planning. This methodology is based on the assumption that, while global forecast models currently do not have the spatial and temporal resolution needed to represent the mesoscale processes in tropical cyclogenesis, they can do an adequate job capturing the synoptic scale evolution (Montgomery et al. 2010b). In the context of the new tropical cyclogenesis model, this suggests it is possible to track the easterly wave's critical layer, and predict the preferred location for tropical cyclogenesis to occur (Wang et al. 2009), even in instances where tropical cyclogenesis is

not predicted by the model (Montgomery et al. 2010b). It is in this context that real-time marsupial forecasts can provide very useful information for the forecasting of tropical cyclogenesis.

Figure 28 depicts an example of the T+72 hour NOGAPS (initial time: 12Z 14 August) marsupial forecast valid at 12Z 17 August (when the pre-Nuri disturbance was upgraded to a TS by JTWC). The left panel displays 925 hPa streamlines in the co-moving frame along with OW, the critical latitude, and trough axis. The location of Guam is indicated by the red plus sign. The right hand side depicts vertical cross-sections of pouch diagnostics for OW, relative vorticity, and detrained volume flux. This forecast was used in the 15 August Daily Planning Meeting to make a go/no go decision for reconnaissance flights and was a significant factor in the decision to fly this disturbance.

At this forecast hour, all of the four global models used during TCS-08 (NOGAPS, GFS, the ECMWF’s International Forecast System [IFS], and United Kingdom Meteorological Office’s [UKMO] Unified Model [UM]) depict an easterly wave moving through the region. However, none develop the wave into a closed circulation in the earth-relative frame or a tropical cyclone at any validation time. The marsupial forecast product shown depicts a closed low-level cyclonic circulation (in the co-moving frame) along with a strong area of OW surrounding the sweet spot. This marsupial forecast predicted the favored region for genesis, should it occur, within 1.5° latitude of the JTWC Best Track position.²⁴

The model diagnostics (Figure 28) predict low-level convergence around the genesis time, leading to an enhancement of low to mid-level relative vorticity. The OW/relative vorticity plot shows an increase in both variables in the lower levels;

²⁴ The author has shown that operational numerical prediction models have the capability to predict genesis *location* in an operational environment using marsupial analysis methods. Although the success of these marsupial forecasts is dependent on the forecast skill of the global model, the diagnosis based on the new tropical cyclogenesis model provides additional insights to the standard model forecast. In the Nuri case, operational models did well in forecasting the favored latitude for genesis. However, the error in longitude was approximately 4° for the 72-hour NOGAPS forecast, primarily due to the model’s inaccurate representation of the propagation of the parent easterly wave (due to errors in representing the background easterly flow).

variations in the two are qualitatively similar in the vertical (especially in the lower troposphere). This suggests that almost all of the vorticity being produced is from the curvature rather than shear, a favorable feature for tropical cyclogenesis (DMW09).

The author believes that these pouch diagnostics have the potential to assist operational forecasters in easterly trade wind regimes because they offer the advantages of: i) a wave-centric viewpoint for diagnostic analyses, and ii) centering intense observations or satellite positioning around the preferred genesis location.

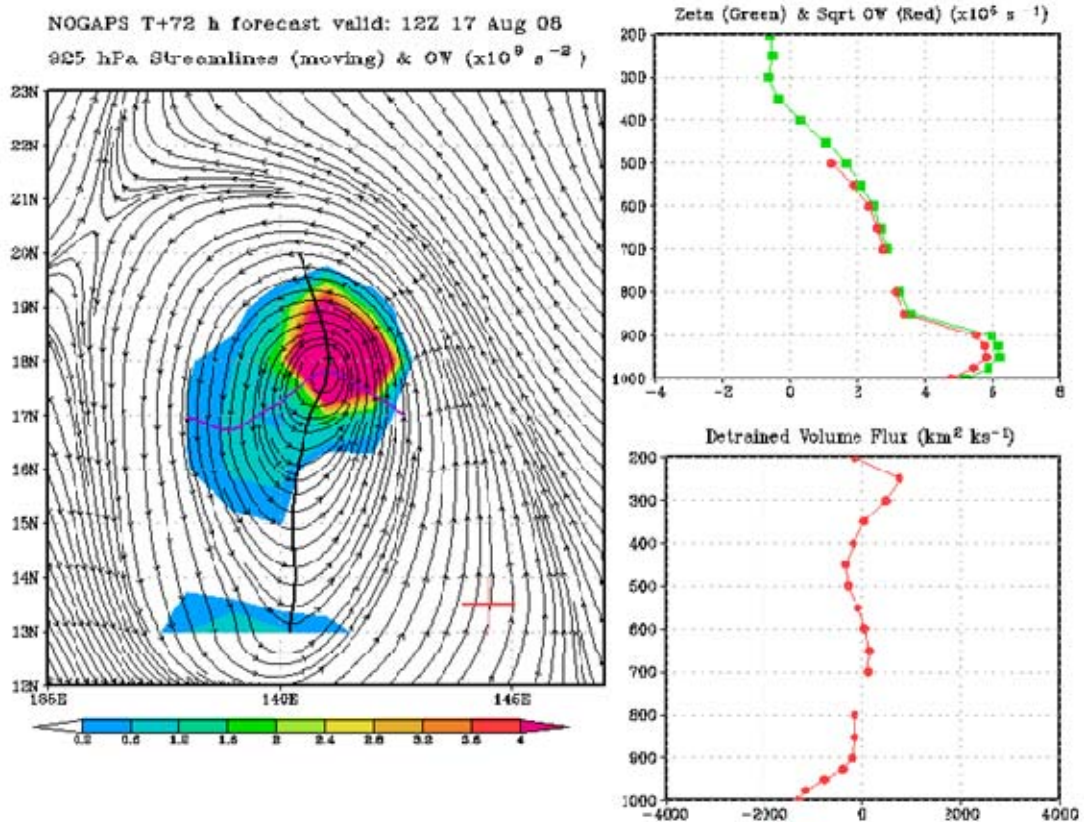


Figure 28. Real-time 72-hr NOGAPS forecast for the potential genesis of Typhoon Nuri. Model initialization time is 12Z 14 August and is valid at 12Z 17 August (time of TS declaration by JTWC). The left panel is 925 hPa streamlines in the co-moving frame with OW (shaded), the wave trough (black line), critical latitude (purple line), and location of Guam (red plus). The right panels are area-averaged diagnostics calculated within a $3^\circ \times 3^\circ$ box moving with the pouch so as to quantify the dynamic features within the pouch. The top depicts average relative vorticity (green trace) and the average square root of OW (red trace). The bottom is detrained volume flux. Unplotted data in the vertical profile are due to missing model data at that level.

D. INTERPRETIVE DISCUSSION

JTWC began tracking the pre-Nuri disturbance at 00Z 16 August with an initial center position of 146.8E, 13.2N (Figure 16), and it is classified as DB (depression beginning). At this time, the 925 hPa sweet spot in the GFS FNL²⁵ is located at 145.3E, 14.9N. Twenty-four hours later, JTWC upgrades the developing storm to a TD centered at 140.2E, 14.8N, while the sweet spot is located at 139.7E, 15.9N. Finally, at 12Z 17 August 2008, JTWC upgrades the TD to a TS located at 136.7E, 16.1N while the sweet spot is at 136.8E, 16.3N. Of particular interest to this study is the abrupt shift north in the JTWC Best Track between 00Z and 06Z 17 August. According to JTWC, the center of the developing TD shifts from 14.8N to 16N in the span of six hours, whereas it had shifted only 1.6 degrees north over the previous 36 hours. Furthermore, the position of the sweet spot varies by only 1.8 degrees in 36 hours and remains well north of the JTWC Best Track position until TS declaration. These facts motivate the following question: Is this evidence of a sudden northward propagation of this disturbance, or a potential tracking error in the best track data?

As discussed in Section C, on 00Z 16 August (Figure 22), the strongest convection associated with the pre-Nuri disturbance is located within the southern (and to a lesser extent the eastern) quadrant of the wave pouch. Figure 29 displays the GFS FNL from this time with 925 hPa streamlines in the co-moving frame, OW (shaded), the wave trough axis (thick black line), critical latitude (purple line), and JTWC Best Track position (black circle). These data are consistent with satellite observations in that the OW maximum (and by proxy, the strongest vorticity and low-level convergence) is located in the southern portion of the pouch. With limited conceptual models and guidance on locating the center of a developing typhoon, declaring its position in the

²⁵ While there are certainly limitations to the GFS FNL (data assimilation, resolution, etc.), the GFS analysis is employed extensively here due to the limited amount of observational data available in the western North Pacific basin. The GFS FNL is in broad agreement when verified against observations. Furthermore, operational ECMWF and NOGAPS analyses provide a broadly consistent evolutionary picture of the easterly wave and vorticity field from 7 August until genesis, which are also similar to the GFS FNL. These comparisons give the author confidence that that the GFS FNL is representative of the synoptic-scale conditions leading up to the genesis of Typhoon Nuri.

middle of the strongest convection and vorticity maximum is understandable.²⁶ However, deep tropical convection is generally chaotic and unpredictable (Nguyen et al. 2008). Furthermore, maxima in vorticity do not necessarily coincide with the emerging circulation center and small vorticity anomalies may be present throughout the pouch (Montgomery et al. 2010a; Wang et al. 2010a, b).

By 12Z 16 August, the GFS FNL (Figure 29) data show an increase in the aerial coverage of OW, as the higher OW values are now observed throughout most of the pouch. While the OW maximum remains in the southern quadrant, it has moved closer to the sweet spot. At this time, the IR data shows evidence of banded structures beginning to wrap around the sweet spot²⁷ (red arrows in Figure 24). When viewing this sequence in the resting frame (Figure 21), the cyclonic circulation is farther south (12.5N). Additionally, the banding features seen in the IR data appear more symmetrically organized around the circulation in the co-moving frame, rather than the southern circulation in the resting frame. Although this difference is subtle, it is important and provides evidence that the preferred region for genesis is the sweet spot at the northern portion of the wave, rather than the southern circulation. DMW09 suggest that the high frequency of storm formation occurred at or near the center of the translating gyre in almost all of the Atlantic cases they studied: “... *seems almost uncanny and suggests to our minds an invisible ‘guiding hand’ from synoptic and meso-a scales.*” The so-called guiding hand principle is summarized therein:

...whereas upscale aggregation of vorticity and its amplification by deep convection are essential to TC formation, they are not entirely responsible for the formation of a closed tropical depression in the first place. This formation is at least partly due to the dynamics of moist waves and involves a direct enstrophy cascade from larger synoptic-scale disturbances to mesoscale vorticity anomalies. This argument rests on the coherent relationship observed between the critical layers of tropical waves and tropical cyclogenesis events occurring in such regions.

²⁶ Although typhoon reconnaissance flights are typically not available in the western North Pacific, the JTWC Best Track data was influenced by the aircraft missions flown during TCS-08 because the potential low-level cyclonic circulations identified by the USAF C130 were incorporated into their best track determinations.

²⁷ While perhaps not transparent in the static images shown, movie loops of these satellite images suggest banded structures spiraling cyclonically inward toward the sweet spot.

Initial analysis of the observational data in the Typhoon Nuri case suggests that this guiding hand principle is indeed at work.

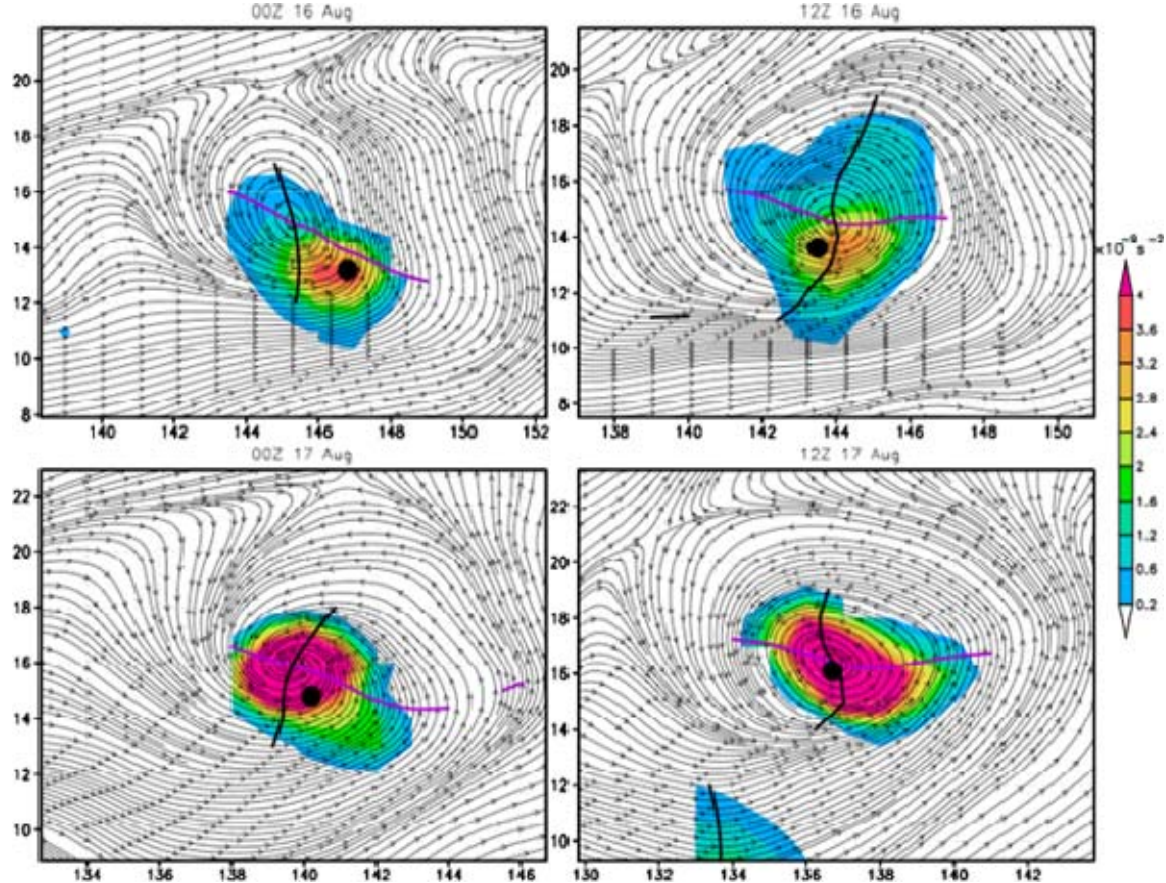


Figure 29. Thirty-six hour (00Z 16 August–12Z 17 August) GFS FNL time series encapsulating the genesis phase of Typhoon Nuri. Thin black line are 925 hPa streamlines in the co-moving frame, OW is shaded, the thick black line is the wave trough axis, and the purple line the critical latitude. The black dot indicates the JTWC Best Track position. The OW increases in intensity and centers on the sweet spot as genesis nears.

At 00Z 17 August, the convection is more evenly distributed throughout the pouch (Figure 22) and there is a significant area of banded convection to the northeast, wrapping around into the sweet spot. The GFS FNL OW maximum has increased in aerial extent and intensity, and has organized around the center of the sweet spot (Figure 29). At this point, the JTWC Best Track position has the center at 14.8N (Figure 24), which appears to be close to the location of the strongest convection. However, it

remains well south of the sweet spot and the OW maximum. By 12Z 17 August (the time JTWC upgraded the disturbance to a TS), both centers are almost identical (Figure 29). The OW has increased over the last 24 hours, consistent with the evolution seen in Wang et al. (2009).

The evolution of convection described above is consistent with high-resolution (inner-most grid of 3 km) idealized numerical simulations performed by Montgomery et al. (2010a), which examines the transition of an easterly wave critical layer to a tropical storm. Figure 30 portrays an 84-hour time interval from said study of surface precipitation (explicitly resolved on the 3 km grid with warm-rain microphysics), 850 hPa streamlines in the co-moving frame, the wave trough (black line), and critical latitude (purple line). For a complete description of the model set-up, initial conditions, and physics, see Montgomery et al. (2010a). The first three panels of this time series (120 h-144 h) depict light unorganized precipitation in all quadrants of the pouch with a maximum to the northeast (akin to the unorganized convection seen in the pre-Nuri disturbance prior to 12Z 16 August). By the 156 h time period, the precipitation structures are beginning to organize and banding features emerge. The 166 h time period shows organized bands wrapping around the sweet spot. The next three periods (180 h-204 h) show these banded structures spiraling into the sweet spot, an increase in the intensity of the precipitation, and heavy precipitation moving closer to the center and filling all quadrants of the wave's pouch. The evolution of the model-simulated precipitation is similar to that observed in Nuri in the sense that convection is sustained and enhanced near the center of the pouch.

On the basis of the evidence presented, these data strongly suggest that: i) the dynamical genesis sequence proposed by DMW09 can be useful for understanding the evolution of easterly waves in the western North Pacific basin. The juxtaposition of the closed cyclonic circulation in the co-moving frame and sweet spot in the GFS FNL is consistently farther north and shows a less abrupt shift than the center positions issued by JTWC. The evolution of banded features in the IR data and evolution of OW in GFS FNL strongly support the viewpoint that following this northern center is the simplest and superior way to track the pre-Nuri disturbance. ii) Deep convection alone should not be

relied upon to identify the center of a developing tropical cyclone because deep convection is inherently chaotic and has been shown elsewhere to be an unreliable indicator of genesis location (DMW09). While OW and/or vorticity at the 850 hPa level may be more robust, neither is as good as streamline (or streamfunction) analysis, which is superior for resolving the potential genesis location as shown by DMW09 and confirmed in this case. iii) Using the sweet spot model to track potential genesis locations should be a useful tool for identifying low-level cyclonic circulation centers operationally in the early genesis stages and may ultimately prove superior to methods being currently employed.

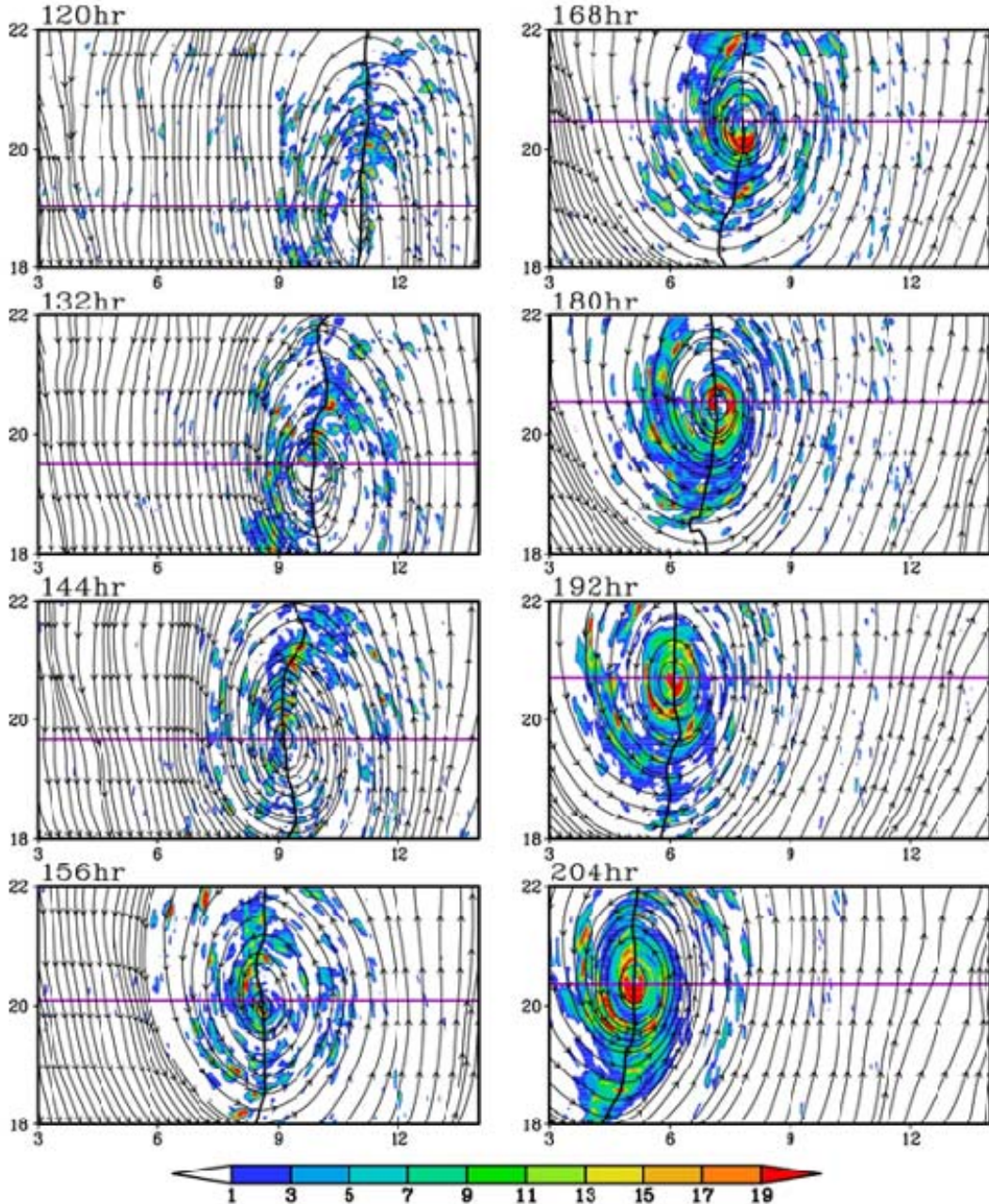


Figure 30. Summary of idealized numerical simulation of the spatial and temporal evolution of precipitation within the critical layer of a developing easterly wave (Montgomery et al. 2010a). The time series depicts surface rain rate (mm h^{-1}), 850 hPa streamlines in the co-moving frame, the wave trough (thick black line), and critical latitude (purple line) at 12-hour intervals beginning 120 hours into the model run. The abscissa is longitude and the ordinate is latitude. The simulated evolution of precipitation is consistent with the observed data in the pre-Nuri case.

E. CONCLUSIONS AND FUTURE WORK

This chapter presents a first analysis of the tropical cyclogenesis of Typhoon Nuri that occurred in the western North Pacific basin during the TCS-08 field campaign. The basic state flow within which Typhoon Nuri formed is an easterly trade-like flow and the progenitor disturbance is an easterly wave that propagates approximately zonally over a ten-day interval with an earth-based zonal phase speed varying between 10.5 m s^{-1} and 7.0 m s^{-1} . The observed phase speed, motion, and precipitation structure of the precursor disturbance are all consistent with the structure of typical easterly waves studied in the western North Pacific basin dating as far back as Reed and Recker (1971). Given the easterly wave character of this formation event, it was considered a viable candidate to test the new tropical cyclogenesis conceptual model proposed recently by DMW09. Evidence is presented here in support of H1-H3 of DMW09 for the Typhoon Nuri case.

The following factors provide observational support of H1 in the tropical cyclogenesis sequence of Typhoon Nuri: i) convection, despite beginning in the southern quadrant of the pouch, remains largely within the pouch and became organized around the sweet spot as genesis nears. Infrared satellite imagery shows the beginning of banded convection around this location on 12Z 16 August. ii) The dominant circulation that emerges as Typhoon Nuri is located within the highly vortical region of the wave's cat's eye near the intersection of the wave trough and the critical latitude (confirmed by GFS FNL and IR satellite data).

Similarly, in the case of H2: i), the GFS FNL identifies a set of closed streamlines in the co-moving frame of reference representing the wave's pouch. This pouch is evident approximately nine days prior to formation. The pouch significantly weakens as it traverses through a hostile environment, and then re-emerges as a coherent circulation two days prior to TS declaration. ii) The reinvigoration of convection at 12Z 15 August occurs largely within the pouch and the author suggests it is most likely triggered by an area of higher HHC and vorticity located in the southern quadrant of the pouch. Over the next 36 hours, the deep convection becomes more vigorous and the CIMMS TPW analysis suggests continual moistening of the column. iii) CIMMS TPW analysis shows

that the dry air surrounding the pouch moves approximately in the same background flow as the moist air within it. Despite surrounding it on three sides, little if any of this air appears to enter the pouch (consistent with the increase in TPW). iv) Whereas the strong environmental vertical wind shear may have temporarily decreased the vertical coherence of the pouch and temporarily stalled genesis, the critical layer evidently remains resilient enough to keep the low to mid-level proto-vortex intact until it is able to enter a more favorable environment. In this regard, the tropical cyclogenesis sequence of Typhoon Nuri seems to provide a useful illustration of the new tropical cyclogenesis model. In a conducive environment, the vertical extent of the pouch as captured in the analysis data is able to extend upward. The apparent upward growth of the pouch is hypothesized to be due to persistent deep convection within and the low to mid-level convergence of ambient cyclonic vorticity that would accompany a predominantly convective mass-flux profile (Montgomery et al. 2010b). When the local vertical shear increases significantly, the organization process seems to stall, yet, the low-level moisture remains protected within the pouch. Once the vertical shear weakens for an extended period of time, the pouch again extends upwards with time in conjunction with enhanced mid-level moisture (Montgomery et al. 2010b).

The tracking of the parent easterly wave disturbance for 10 days and the maintenance of its structure as it propagates through a hostile environment are consistent with H3 of DMW09. It is conceivable that the easterly wave is enhanced by the presence of diabatically amplified eddies within the pouch and that this hybrid wave-vortex system maintained its coherence and eventually strengthened through this symbiotic interaction.

Following the forecast and diagnostic techniques outlined by Wang et al (2009), real time marsupial forecasts were produced in support of TCS-08 operations that were able to predict the latitude of tropical cyclone development out to 72 hours within 1.5° . These forecasts provide useful insight that raw operational numerical model data could not. As an example, none of the four forecast models used in the experiment predicted a closed low-level cyclonic circulation in the earth-based frame of reference.

While a wealth of data is presented herein to suggest that this new conceptual model can be a useful forecaster/diagnostic tool in the western North Pacific basin during easterly trade wind regimes, much work remains to be done. At the synoptic and sub-synoptic (meso- α) scales, the data presented herein does support the tropical cyclogenesis sequence hypothesized by DMW09. The specific mesoscale pathway to the emergent tropical cyclone vortex has yet to be elucidated for this case. The first hypothesis of DMW09 (H1) states: “This multi-scale interaction provides a dynamical pathway to ‘bottom-up’ development of the proto-vortex from below.” The next step in the author’s analysis will be to examine aspects of the mesoscale development within the pouch of the pre-Nuri disturbance. Specifically, properties of the convection and kinematic flow observed within the pouch will be evaluated using the data from the ELDORA radar in order to assess the contribution of VHTs to the spin up of the meso- β scale tropical cyclone vortex. Aircraft flight level data, SFMR data, and additional remote sensing data including microwave imagery and ground-based Doppler radar will be used to augment the analysis presented here and further scrutinize the mesoscale evolution of Typhoon Nuri’s tropical cyclogenesis sequence.

V. TESTING THE HYPOTHEZIZED ROLE OF AN EQUATORIAL ROSSBY WAVE CRITICAL LAYER IN THE GENESIS OF SUPER TYPHOON MAN-YI—PART I: SYNOPTIC- SCALE OBSERVATIONS AND ANALYSES

A. INTRODUCTION

1. Paradigms of Tropical Cyclogenesis in the Western North Pacific Sector

Molinari (2004) describes two conceptual models for tropical cyclogenesis in the western North Pacific basin. Supporters of the first paradigm contend that the presence of a monsoon trough in the lower levels of the troposphere is *essential* for tropical cyclogenesis (e.g., Harr and Elsberry 1991, 1995) and conversely, that the role of westward propagating disturbances is minor (e.g., Ritchie and Holland 1999). They argue that the monsoon trough region meets the favorable environmental conditions for tropical cyclogenesis originally articulated by Gray (1968, 1975). Climatologically, the western North Pacific basin exhibits sea surface temperatures $>26^{\circ}\text{ C}$ over much of the year and is typically moist in the lower troposphere, conditions favorable for increased convection (Elsberry 2009). The monsoon trough assists in the moistening and destabilization of the mid-troposphere and provides an environment with minimal vertical wind shear (Gray 1998). Furthermore, cross-equatorial westerly flow converging with trade-wind easterlies in the western North Pacific provides a favorable environment for low-level cyclonic vorticity generation (Elsberry 2009). Several studies (e.g., Briegel and Frank 1997) have shown that the eastern end of the monsoon trough is the favored region for tropical cyclogenesis.

Supporters of the second paradigm (Molinari 2004) contend that the primary mechanism for tropical cyclogenesis in the western North Pacific basin is the intensification of westward propagating disturbances or easterly waves. While the presence of these westward propagating disturbances (manifesting as either equatorial modes or off-equatorial waves) is well established in the western North Pacific basin

(Chang et al. 1970; Reed and Recker 1971; Numaguti 1995; Wheeler and Kiladis 1999), their role in tropical cyclogenesis is less well understood. Frank and Roundy (2006) use composite analysis to examine the relationship between tropical waves and tropical cyclone formation in all basins. They conclude that: “The northwest Pacific shows strong annual cycles in mixed-Rossby gravity (MRG), Tropical Depression (TD) type and equatorial Rossby (ER) wave activity that coincides well with the cyclone season.” Dickinson and Molinari (2002) and Numaguti (1995) document examples of MRG waves transitioning to tropical cyclones. Takayabu and Nitta (1993) document the transition of a MRG wave to a TD-type wave that eventually formed a tropical cyclone.

Of interest to this work is the potential role an $n=1$ ER wave can play in tropical cyclogenesis in the western North Pacific. Analytical solutions of these linearized equatorial modes have existed for decades (e.g., Matsuno 1966) and observational studies have documented their presence in the real atmosphere (Gruber 1974, Zangvil 1975, Kiladis et al. 1994, Kiladis and Wheeler 1995, Wheeler et al. 2000, Yang et al. 2007, Kiladis et al. 2009). Bessafi and Wheeler (2006) examine the role ER waves play in tropical cyclogenesis in the north Indian Ocean. They show that a relatively large and significant number of tropical cyclogenesis events are modulated by ER waves and that tropical cyclogenesis occurs both east and west of the ER wave center. Molinari et al. (2007) examine tropical cyclogenesis events in the western North Pacific within an ER wave packet. They show that 8 of the 13 tropical cyclogenesis events that occurred during that time period they examined are associated with an ER wave packet. The favorable formation location is east of the ER center, in a region of strong convection with a relative vorticity maximum independent of the ER wave low (Molinari et al. 2007). These results are consistent with the findings of Frank and Roundy (2006) whose composite analysis shows that development occurs several hundred kilometers southeast of the ER wave center. Frank and Roundy (2006) also suggest that ER waves play a role in tropical cyclogenesis by altering the local environment. In their composites, the ER wave acts to increase upward vertical motion, increase low-level cyclonic vorticity, and alter the vertical shear pattern. Frank and Roundy (2006) suggest: “ER waves also appear to enhance genesis by increasing both the large-scale rotation and convection.”

2. Theoretical and Observed Characteristics of n=1 ER Waves

Matsuno's (1966) groundbreaking work uses an invicid, non-divergent barotropic model to examine wave motions in the near equatorial region. His numerical solutions indicate the presence of trapped quasi-geostrophic motions near the equator including westward propagating inertio-gravity waves and westward propagating Rossby waves. In the theoretical n=1 Rossby wave solution (Figure 31), symmetric cyclonic circulations on either side of the equator exist in geostrophic balance between the pressure and wind fields. The maximum zonal wind component is expected to be along the equator. In this solution of a series of westward propagating cyclonic and anticyclonic circulations, low-level convergence is favored $\frac{1}{4}$ wavelengths east of cyclonic circulation centers (Figure 31). This in-turn is the favored region for the maximum convection. Matsuno (1966) cautions that his work is a theoretical study, and that its application to the real atmosphere must be approached cautiously.

Observational studies have been focused on linking moist dynamical processes with the theoretical solutions to document the existence and characteristics of ER waves in nature. Observations of these waves indicate a zonal wave number six structure and a period of 6–30 days (Kiladis and Wheeler 1995). They possess a maximum amplitude in the lower troposphere and they travel westward at zonal phase speeds between 5–10 m s⁻¹ (Kiladis and Wheeler 1995). In cases where these waves are coupled with convection, the overall phase speed tends to slow (Wheeler and Kiladis 1999). The horizontal size of observed ER waves ranges from 4000–10000 km and the latitudinal extent can span up to 20° for each circulation. The maximum amplitude of an n=1 ER wave is typically observed in the central and western Pacific and they have been noted to slow as they cross into the western Pacific (Kiladis and Wheeler 1995). Other structural changes to the ER wave occur as they enter the western Pacific (rapid decay, anti-symmetry, etc.) and are likely due to an increase in convection and diabatic heating in the region (Kiladis and Wheeler 1995). The observational studies discussed by Kiladis and Wheeler (1995) and Wheeler and Kiladis (1999) demonstrate wave modes with similar characteristics to the theoretical studies of Matsuno (1966). However, Kiladis and Wheeler (1995) note: "...invicid, dry shallow water theory with a constant zonal basic flow is not adequate for

explaining the details of the observed tropospheric equatorial Rossby waves.” Effects of friction, moist dynamics, or a zonally varying basic state flow could bring the theory more in line with observations.

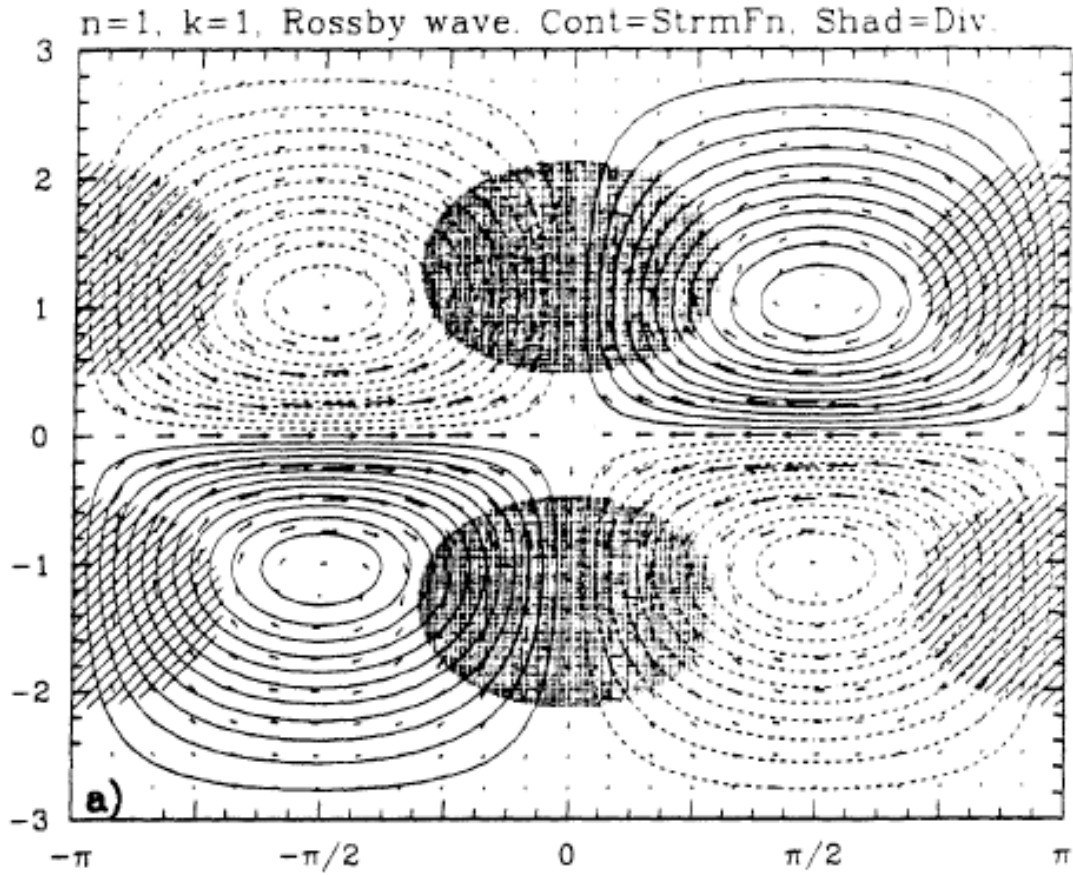


Figure 31. Idealized solution of Matsuno’s (1966) $n=1$ ER wave, negative contours are dashed. Shading represents areas of convergence and hatching is divergence.
From Kiladis and Wheeler (1995).

3. Synoptic-scale Background Relevant to the Formation of Typhoon Man-yi (2007)

Typhoon Man-yi (2007) was first identified by the JTWC as an area of disturbed weather near the equator on 4 July 2007. Initially, the convection was disorganized and the environment was only marginally favorable for development. The initial propagation of the disturbance was westward and by 7 July, the disturbance had entered a region of

low vertical wind shear and higher ocean heat content, conditions more favorable for formation. The JTWC upgraded the system to a TD on 7 July (Figure 32). The cyclone continued to intensify and was upgraded it to a tropical storm on 9 July (Figure 32). The developing storm passed south of Guam and continued to intensify and organize. It was upgraded to a typhoon on 10 July 2007. As the developing typhoon began to push into the Philippine Sea and turn northward toward Japan, it encountered warmer waters and rapid intensification. By 12 July, it had reached its maximum sustained winds of 64 m s^{-1} (125 kt). Typhoon Man-yi maintained its intensity and began to recurve over the next day and it passed over Okinawa on 14 July. The typhoon continued its movement to the northeast, and it began to weaken as it passed over southeastern Japan (15 July). Typhoon Man-yi began its extratropical transition that day (Figure 32).

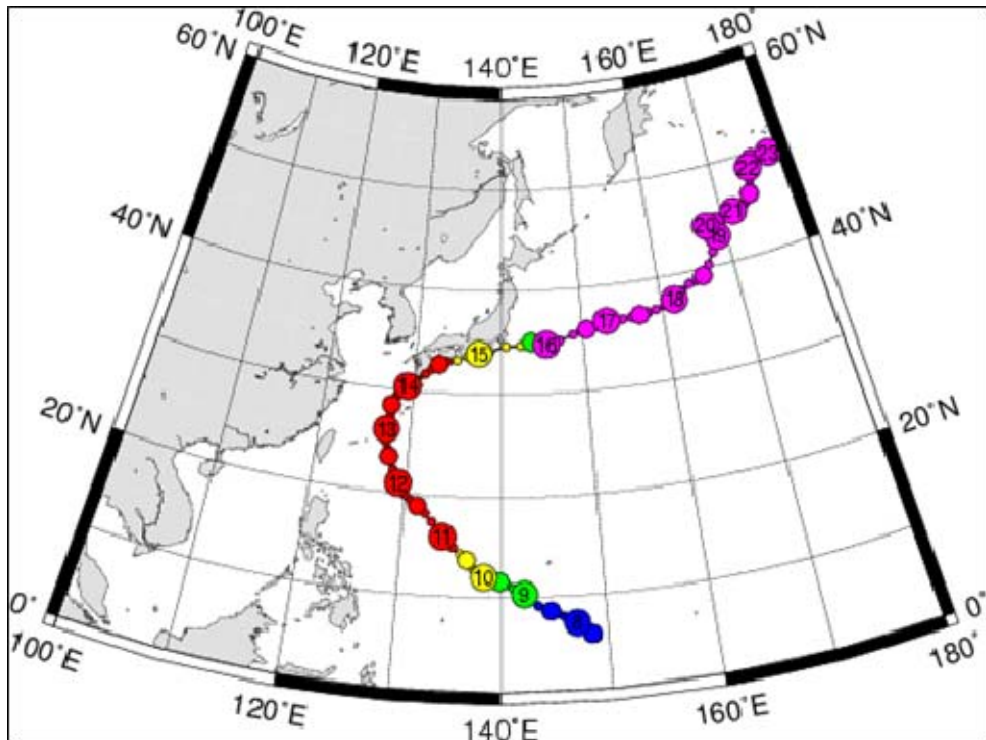


Figure 32. Track of Typhoon Man-yi from 8–23 July (Digital Typhoon 2010). The colored circles indicate storm intensity, with blue a TD, green a TS, red a typhoon, and purple denoting the transition to an extratropical system.

Typhoon Man-yi was originally examined during the TCS-08 dry run because it was considered an ideal case to meet all of the objectives laid out for the TCS-08 field campaign (Elsberry and Harr 2008). From a tropical cyclogenesis perspective, the origin and propagation of the original disturbance suggests that it may be a good case to test the viability of the new cyclogenesis model for a different wave type in the western North Pacific basin. This chapter uses observations and analyses: i) to define the synoptic-scale environment in which the genesis of Typhoon Man-yi occurred, and ii) to test the applicability of the new cyclogenesis model in the western North Pacific basin by analyzing the validity of H1-H3 in the tropical cyclogenesis sequence of Typhoon Man-yi at the synoptic and meso- α scales.

As discussed in Chapter I, DMW09 have developed a new model to describe the transition sequence from synoptic-scale easterly wave to a TD. Although DMW09 focus on the Atlantic and eastern Pacific sectors, it is hypothesized here that the *origin and type* of the easterly wave precursor may be of minimal importance to the DMW09 tropical cyclogenesis sequence. Rather, the essential dynamical ingredients are: i) the establishment of a favored region for the aggregation of diabatic vortices and their vortical remnants, and ii) the ability of the parent wave to provide a protective pouch for the proto-vortex. If one tentatively accepts these hypotheses, the newly proposed cyclogenesis model would be applicable in other tropical cyclone basins and for different wave types. The genesis sequence of Typhoon Man-yi is presented here as a test case for these hypotheses.

The outline of this chapter is as follows: Section B describes the data and methodology employed in this study. Section C examines the tropical cyclogenesis sequence of Typhoon Man-yi as presented in the GFS FNL. Section D uses observations to show evidence of the key synoptic and meso- α scale features present in the pre-Man-yi environment. Section E offers a discussion and concluding remarks.

B. DATA AND METHODOLOGY

1. Observational and Analyses Data

Several sources of data are used to characterize the synoptic-scale environment prior to the formation of Typhoon Man-yi. 1) Six-hourly GFS FNL, projected onto a one degree grid, 2) ECMWF analyses projected onto a 1.125° grid, 3) MTSAT hourly IR satellite data at 4-km resolution, 4) QuikSCAT Level-3 surface wind observations projected on a $0.25^{\circ} \times 0.25^{\circ}$ grid, and 5) 3-hourly TRMM 3B42 surface precipitation data, also projected onto a $0.25^{\circ} \times 0.25^{\circ}$ grid.

Before going further with this study, it should be recalled that there are always inherent limitations to these data. First, the GFS FNL and ECMWF analyses may or may not represent the “true” state of the tropical atmosphere. Additionally, there sometime is a lack of continuity in features tracked in the analyses, likely due to the assimilation of new data into the analysis systems. Second, the QuikSCAT data only provides observations at the surface and therefore the vertical structure of key features in the evolution of the pre-Man-yi disturbance cannot be observed with these data. Furthermore, the spatial and temporal resolution of these observations means that only two QuikSCAT passes traverse the area of interest each day. These passes may not intersect the developing circulation. Third, the TRMM 3B42 data is based on an algorithm that combines TRMM TMI data with geostationary IR data, therefore these data are likely not as accurate as radar or rain gauge data. Despite these limitations, these data are believed to be comprehensive enough to describe a plausible scenario for the tropical cyclogenesis sequence of Typhoon Man-yi on the synoptic and meso- α scales in the data sparse region of the western North Pacific region.

2. Wave Tracking

DMW09 argue that the tropical cyclogenesis sequence is optimally viewed in a frame of reference moving with the parent wave. In this so-called co-moving frame, the time evolution of the parent wave is slow and the corresponding streamlines are an

approximation of parcel trajectories. To derive the phase speed (C_p) of the parent wave, wave tracking was performed using GFS FNL latitudinally-averaged TPW (Wang et al. 2009; Montgomery et al. 2010b) meridional velocity (DMW09), and relative vorticity (Montgomery et al. 2010b). In this chapter the wave trough is identified using latitudinally averaged (2–10N) meridional velocity and the zonal phase speed of the parent wave, -4.5 m s^{-1} , is derived from this quantity. The latitudinal averaging allows for tracking of the synoptic-scale wave versus the short-lived meso- α scale cyclonic circulations found within the parent wave's pouch.

C. GFS FNL SYNOPTIC AND MESO- α SCALE EVOLUTION

1. GFS FNL Solution

Figure 33 is a time series of GFS FNL relative vorticity and streamlines at 850 hPa in the resting frame valid every six hours from 18Z 3 July–06Z 7 July. At 00Z 3 July there are large-scale cyclonic circulations straddling the equator in the Northern and Southern Hemispheres between 152–165E. At 18Z 3 July, a similar pattern exists as large-scale cyclonic circulation is apparent in the lower-levels north of the equator from 145–167E and an accompanying low-level cyclonic circulation is located in the Southern Hemisphere between 148–162E. Although not exactly symmetric about the equator, the size, location, and movement of these circulations suggest a structure similar to that of an $n=1$ ER wave. Within the Northern Hemispheric cyclonic circulation, there exist two meso-alpha scale cyclonic circulations centered near 4.5N, 160.7E and 4.8N, 165.5E respectively. On 3 July, a second pair of cyclonic gyres is present in the western North Pacific, centered near 6N, 132E in the Northern Hemisphere and 6S, 143E in the Southern Hemisphere. These circulations begin to enhance an area of weak cross-equatorial westerly flow in the Northern Hemisphere between 125–140E from 0–4N.

By 00Z 4 July, a monsoon trough begins to develop in the GFS FNL between 137–145E and 0–6N as flow near the ER wave interacts with the flow from around the Southern Hemispheric gyre centered at 5S, 141E. This monsoon trough is enhanced as the ER wave propagates west and contracts in horizontal scale. By 18Z 4 July, the GFS

FNL depicts a symmetric ER wave signature centered on 156E. The monsoon trough exists to the west of this feature from 140–153E. The meso- α scale cyclonic vorticity maxima located within the Northern Hemisphere ER low have weakened over the previous 24 hours. Low-level cyclonic vorticity is being enhanced by strong convergence within the monsoon trough at 4N, 142E and 1.5N, 149E.

Over the next 12 hours (00z–12Z 5 July), the large-scale cyclonic flow associated with the ER wave in the Northern Hemisphere interacts with the eastern end of the monsoon trough. By 12Z 5 July, the interaction of these two features modifies the Northern Hemisphere ER circulation and an equatorial depression (4N, 149E)²⁸ becomes the dominant synoptic-scale feature. The magnitude of the relative vorticity maximum (3N, 150E) originally associated with the ER wave has increased. A second vorticity maximum is located in the southwest corner of the equatorial depression (2N, 144E). This maximum is originally associated with a vorticity maximum in the monsoon trough.

Over the next 12 hours (12Z 5 July–00Z 6 July), two meso- α scale cyclonic vorticity maxima emerge at 4N, 146E and 3N, 152E, respectively. Additional regions of cyclonic relative vorticity are located in the southwest (0, 146E) and northeast (7N, 156E) quadrants of the equatorial depression. At 18Z 6 July, the synoptic-scale equatorial depression has a center near 4N, 149E and multiple meso- α scale cyclonic vorticity maxima are embedded within it. These meso- α scale cyclonic vorticity maxima are centered near 3N, 146E; 0, 147E; 5N, 153E; and 9N, 154E, respectively. Over the next 24 hours, the westward propagation of the equatorial depression slows and the areas of cyclonic vorticity rotate within the equatorial depression until a dominant low-level cyclonic vorticity maximum emerges near 5N, 152E on 12Z 7 July.

In an attempt to quantify the dynamical processes involved in the tropical cyclogenesis sequence of Typhoon Man-yi, an AAMF analysis is conducted similar to that in Chapter III. Figure 34 is a Hovmoeller diagram of AAMF calculated from the GFS FNL 850 hPa sweet spot location. The abscissa is time and the ordinate is radial

²⁸ An equatorial depression is defined herein a synoptic-scale cyclonic circulation that forms near the equator. It is a general term that is not tied to the region in which the depression forms, nor the precursor mechanism that leads to its formation.

distance from the sweet spot (x100 km). Two vertical levels are plotted: 850 hPa (top) and 1000 hPa (bottom).²⁹ The radial extent of the pouch ranges from 5°–6° latitude during this time period, but a larger radial domain is plotted in an attempt to assess the role of the monsoon trough in the formation sequence.

For the 850 hPa level, the author finds the following: at 00Z 3 July, there are negative AAMF across the entire radial extent of the domain (Figure 34, top), including within the wave pouch (~ 650 km radius from the sweet spot). The fluxes are strongest at the outer radii of the pouch, likely a result of the radial component of the wind flowing around and into the ER wave center. After 12Z 3 July, the AAMF remain negative from approximately 300 km outward. Between 18Z 5 July and 18Z 7 July, there are two areas of negative AAMF closer to the sweet spot. The first minimum (beginning at 18Z 5 July) is likely tied to the development of the equatorial depression as the ER wave interacts with the eastern end of the monsoon trough (Figure 33). This spin-up is dominated by the contribution of the symmetric RAM fluxes. Figure 35 is a six-panel vertical cross-section of the symmetric RAM valid every six hours from 00Z 5 July. The symmetric RAM flux analysis supports the idea that the influence of the large-scale flow led to the increase in magnitude of the negative symmetric RAM fluxes near the sweet spot beginning at 18Z 5 July. The second minimum near the sweet spot (Figure 34, top) occurs after the equatorial depression is already established. This minimum is largely driven by the changes in the asymmetric RAM fluxes. Figure 36 is akin to Figure 35, but depicts the asymmetric RAM fluxes beginning at 06Z 6 July. Prior to 12Z 6 July, the asymmetric RAM fluxes in the lower levels closest to the sweet spot are generally positive. While there is an increase in magnitude of the negative asymmetric RAM at 12Z 6 July, this feature is not persistent. Beginning at 00Z 7 July, there is an increase in magnitude of negative asymmetric RAM fluxes in the lower levels near the sweet spot. This feature is likely driven by the multiple meso- α scale cyclonic circulations located

²⁹ The distinction between the monsoon trough and the westward propagating disturbance is not as distinct in the Typhoon Man-yi genesis sequence as in the Typhoon Nuri genesis sequence. For this reason, AAMF analysis at the level of maximum amplitude of the ER wave (850 hPa) is used to assess the potential contributions of the ER wave and analysis at the lower level (1000 hPa) is presented as an estimate of the contribution of the monsoon trough. Although there is likely influence of these features throughout the vertical, this seems to be a reasonable assumption for a first order approximation.

within the wave pouch at this time. These data suggest the potential role meso- α scale vortices could play in the spin-up of a tropical cyclone.

At the 1000 hPa level, there are positive AAMF within the wave pouch during the first time period. The AAMF become negative within the pouch after 00Z 4 July. An interesting feature in this analysis occurs between 12Z 5 July–06Z 6 July. During this time, the AAMF near the sweet spot is positive, suggesting a spin-down of the developing vortex. Further investigation reveals that this time period is coincident with the interaction of ER wave with the eastern end of the monsoon trough. Some insight into this process can be gained by examining the symmetric RAM fluxes (Figure 35). At 00Z 5 July, negative symmetric RAM fluxes are evident near the surface throughout the domain. This is likely the reflection of the radial inflow of the monsoon trough into the sweet spot as the EW wave begins to approach the eastern end of the monsoon trough. As the equatorial depression begins to form at 18Z 5 July, the symmetric RAM fluxes indicate a deep layer of spin-up in the lower troposphere. After this period, the spin-up in the lower levels is taking place above the surface. This potentially suggests that the ER wave is also contributing to the development of the equatorial depression. After this time, the AAMF pattern within the wave pouch becomes predominantly negative (Figure 34, bottom) and the pattern is qualitatively similar to that observed at the 850 hPa level until the end of the time period.

The important points from this AAMF analysis are: i) at 850 hPa, the strongest negative AAMF generally remain on the outer edges of the wave pouch (300–650 km) and are likely associated with the inward radial flow around the ER wave; ii) at the 850 hPa level, the magnitude of fluxes within the pouch do not appear to substantially intensify until near the end of the time period; iii) analysis at the near surface levels indicate the potential spin-up from contributions of the monsoon trough beginning at 00Z 4 July; iv) the increase in spin-up by the negative AAMF throughout the lower troposphere centered around 00Z 6 August are dominated by increases in the symmetric RAM (this is likely attributed to the formation of the equatorial depression); and v) the spin-up near the sweet spot centered around 06Z 7 July evident in the 850 hPa

Hovmoeller diagram (Figure 34, top) can be mostly attributed to asymmetric RAM fluxes, suggesting that there is a contribution to spin-up near the sweet spot from the meso-vortices within the wave pouch.

The foregoing diagnoses support the idea that the development of the large-scale equatorial depression in the GFS FNL results from the interaction between a monsoon trough and a convectively modified $n=1$ ER wave. The twin cyclonic circulation first observed on 3 July possesses many of the observed characteristics of an $n=1$ ER wave discussed in Section A2 as: i) the twin cyclones straddle the equator. Although not symmetric initially, observations of ER waves have shown that this strict symmetry is not always observed in the atmosphere (Molinari et al. 2007), ii) its maximum amplitude is in the lower troposphere (850 hPa) and the strength of the circulations decrease both above and below. iii) Its initial horizontal scale is approximately 3000 km, which is generally consistent with the theorized and observed size of ER waves; iv) It propagates westward a phase speed of -4.5 m s^{-1} and slows as it progresses through the western North Pacific.

The origin of the multiple low-level cyclonic vorticity maxima and the contributions of each maximum to the genesis of Typhoon Man-yi are examined next. Specifically, the author will address the following questions: Can the ER wave's pouch and related equatorial depression provide a protective pouch for a proto-vortex and is this area favorable for the aggregation of cyclonic vorticity?

GFS FNL 850 hPa Streamlines & Relative Vorticity

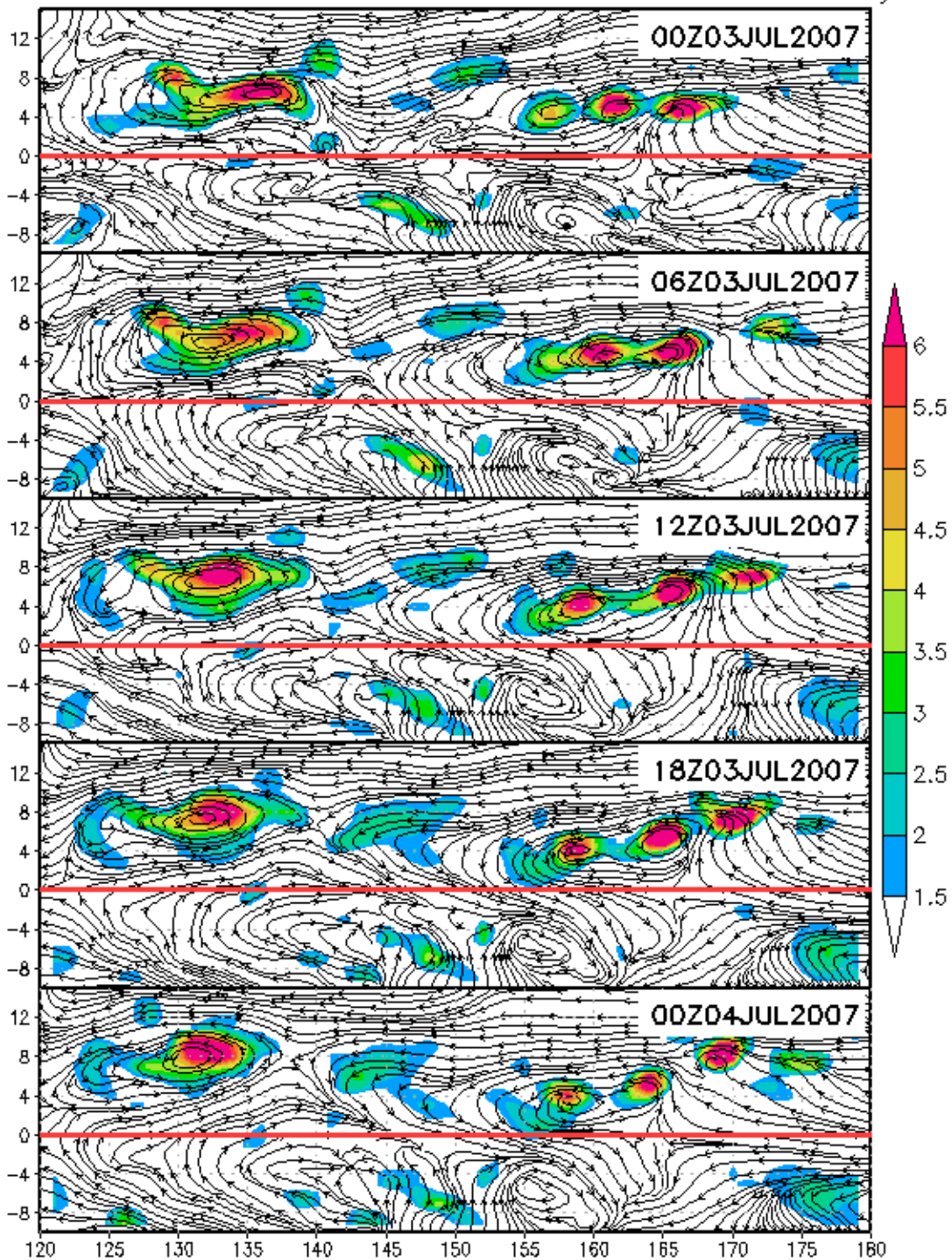


Figure 33. GFS FNL streamlines (resting) and relative vorticity (shaded $\times 10^{-5} \text{ s}^{-1}$) at the 850 hPa level, valid every six hours from 00Z 3 July–18Z 7 July. The red line denotes the equator.

GFS FNL 850 hPa Streamlines & Relative Vorticity

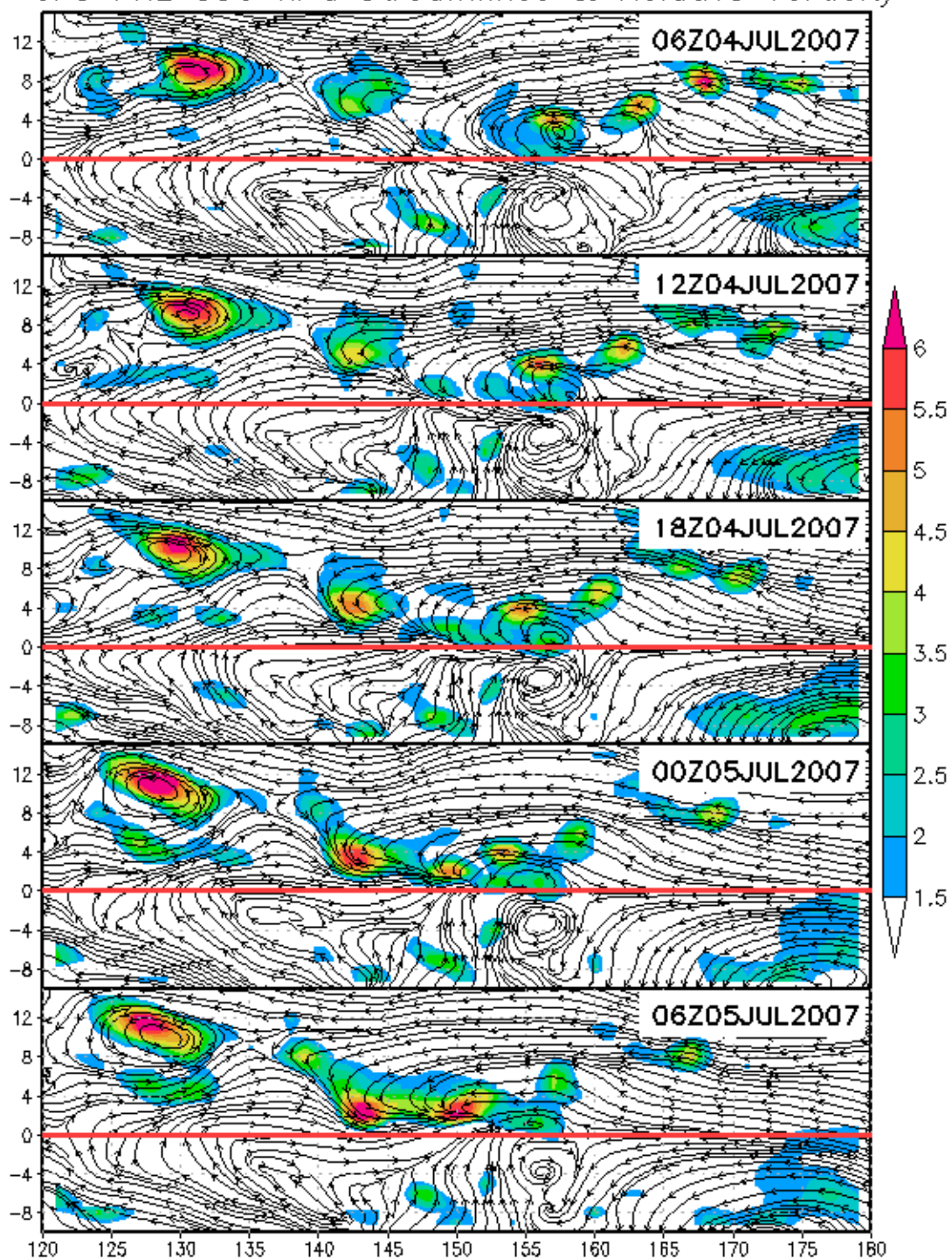


Figure 33. (Cont.)

GFS FNL 850 hPa Streamlines & Relative Vorticity

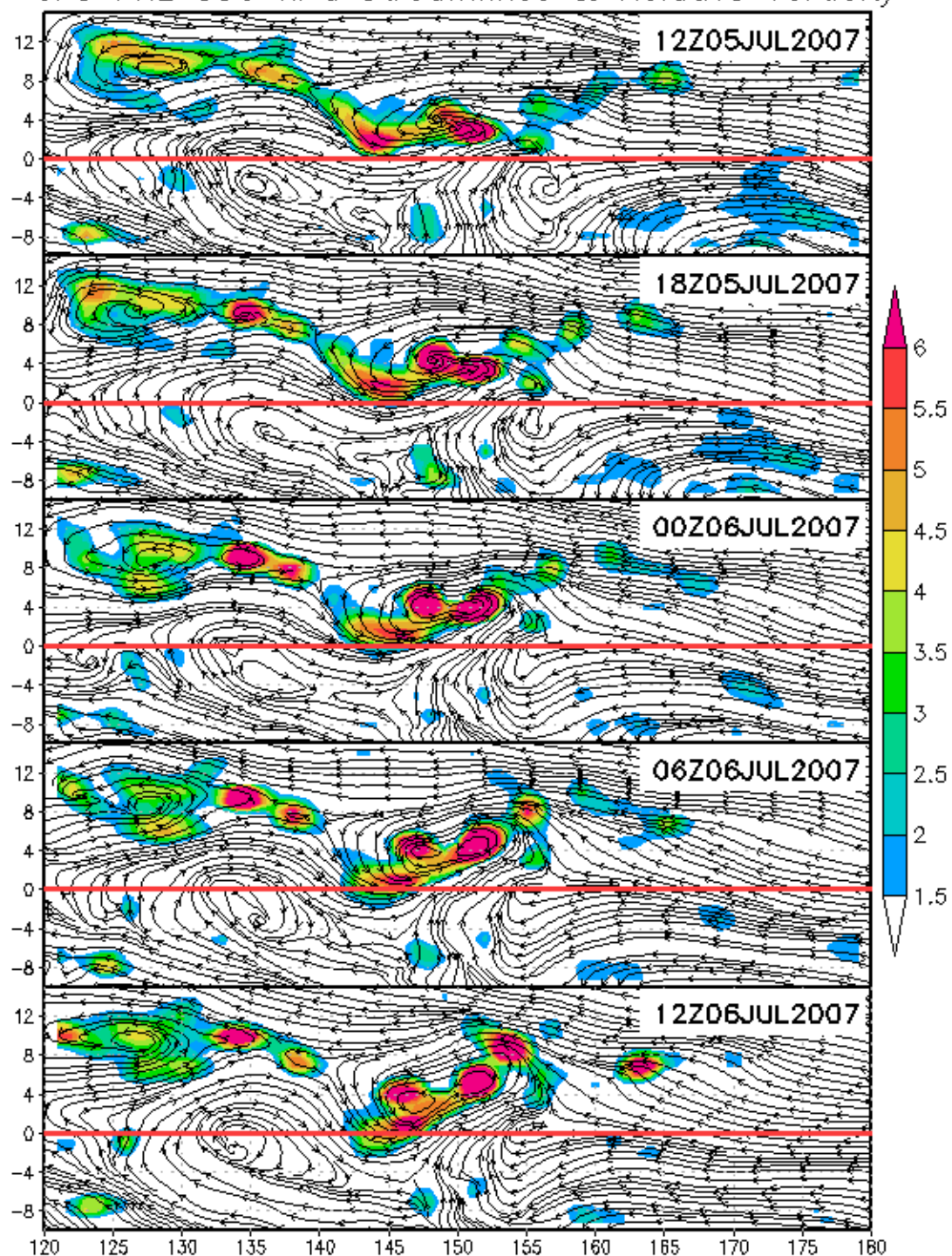


Figure 33. (Cont.)

GFS FNL 850 hPa Streamlines & Relative Vorticity

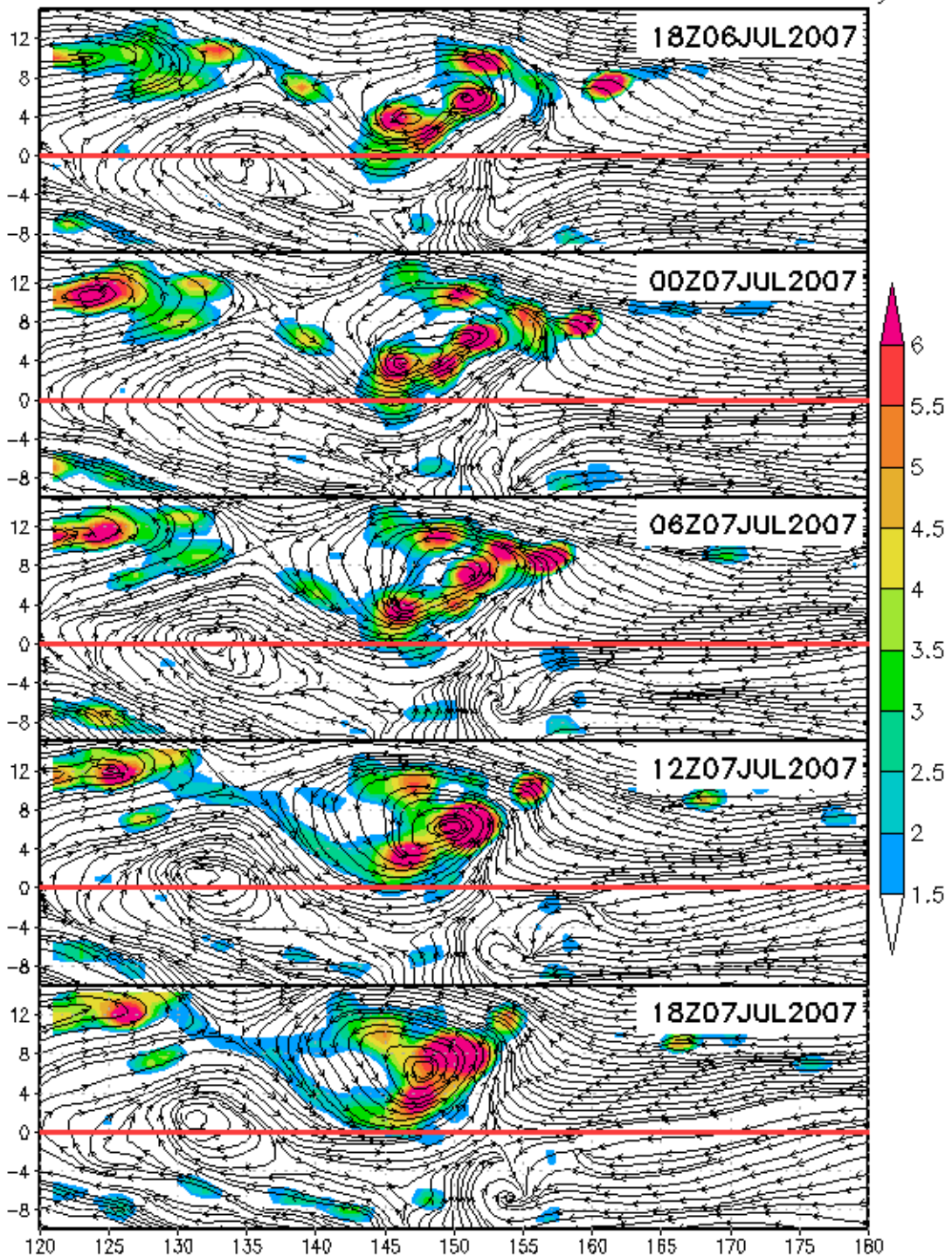


Figure 33. (Cont.)

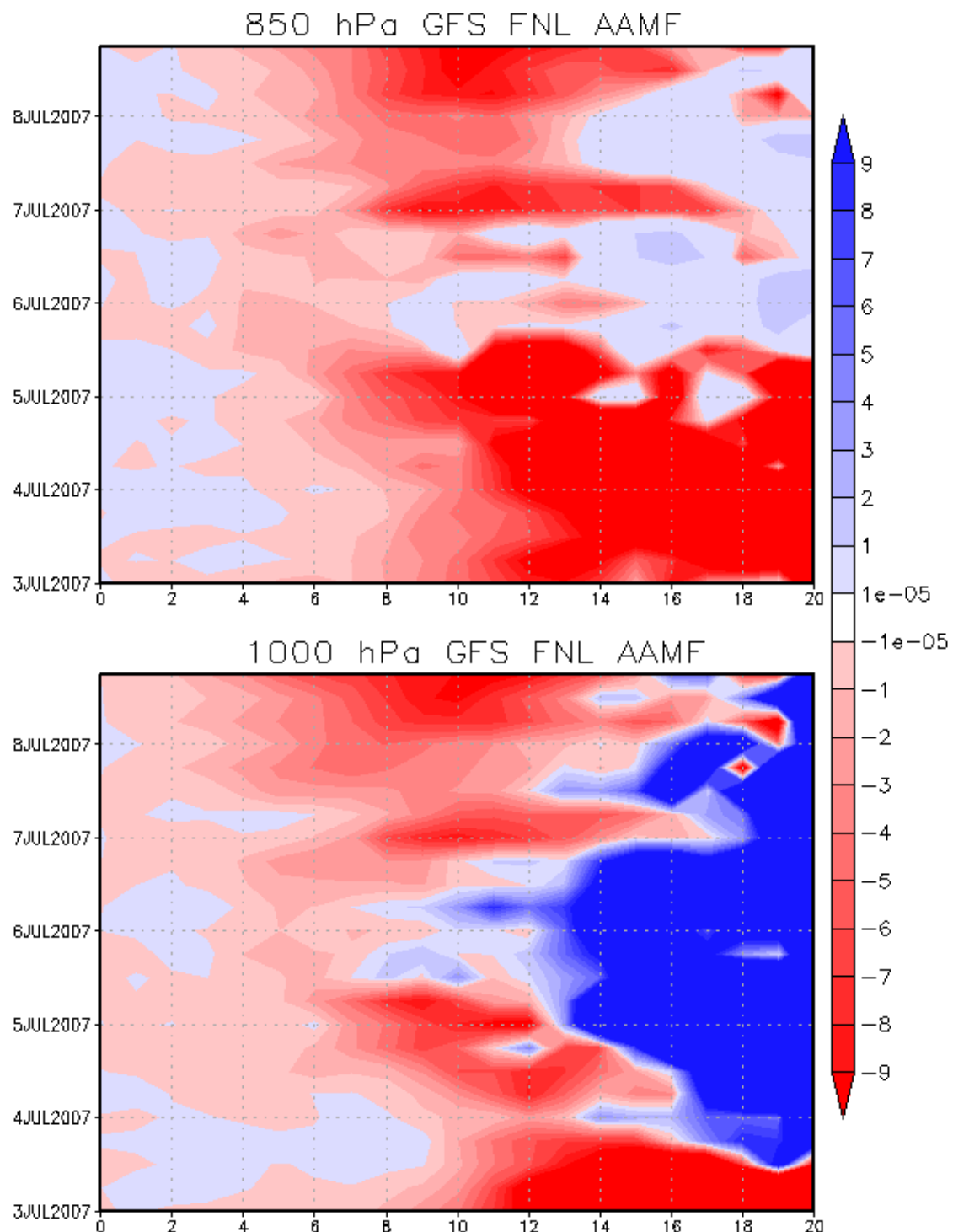


Figure 34. Two-panel Hovmoeller diagram of AAMF ($\times 10^7 \text{ m}^3 \text{ s}^{-2}$) from the GFS FNL for the tropical cyclogenesis sequence of Typhoon Man-yi. The abscissa is radial distance ($\times 100\text{km}$) from the sweet spot and the ordinate is time.

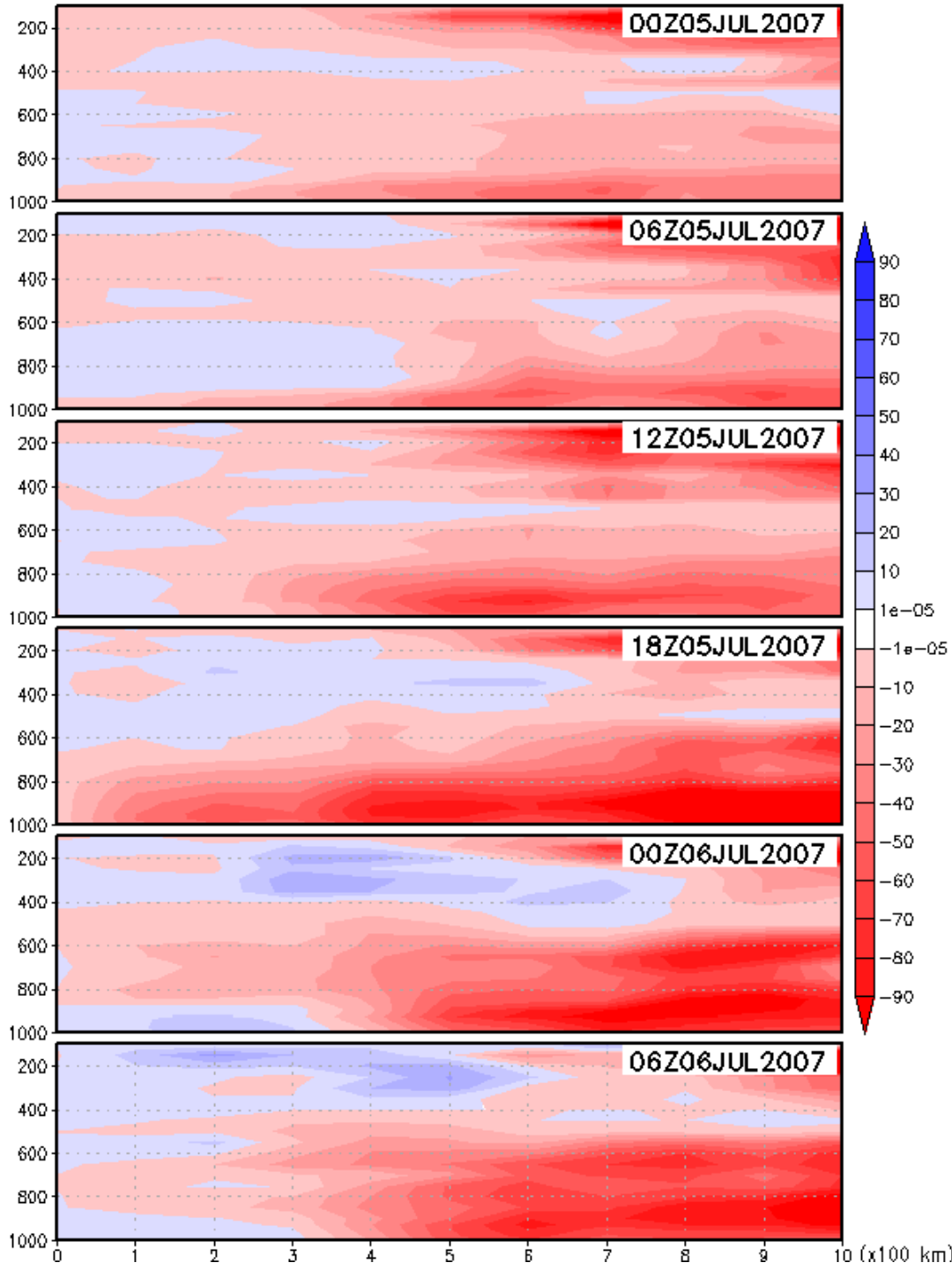


Figure 35. Six-panel time series of symmetric RAM fluxes ($\times 10^6 \text{ m}^3 \text{ s}^{-2}$) in the vertical from the GFS FNL. The fluxes are calculated at radial distances from the sweet spot. The abscissa is radial distance ($\times 100\text{km}$) from the sweet spot and the ordinate is pressure. Warm colors are negative symmetric RAM fluxes and cool colors are positive symmetric RAM fluxes.

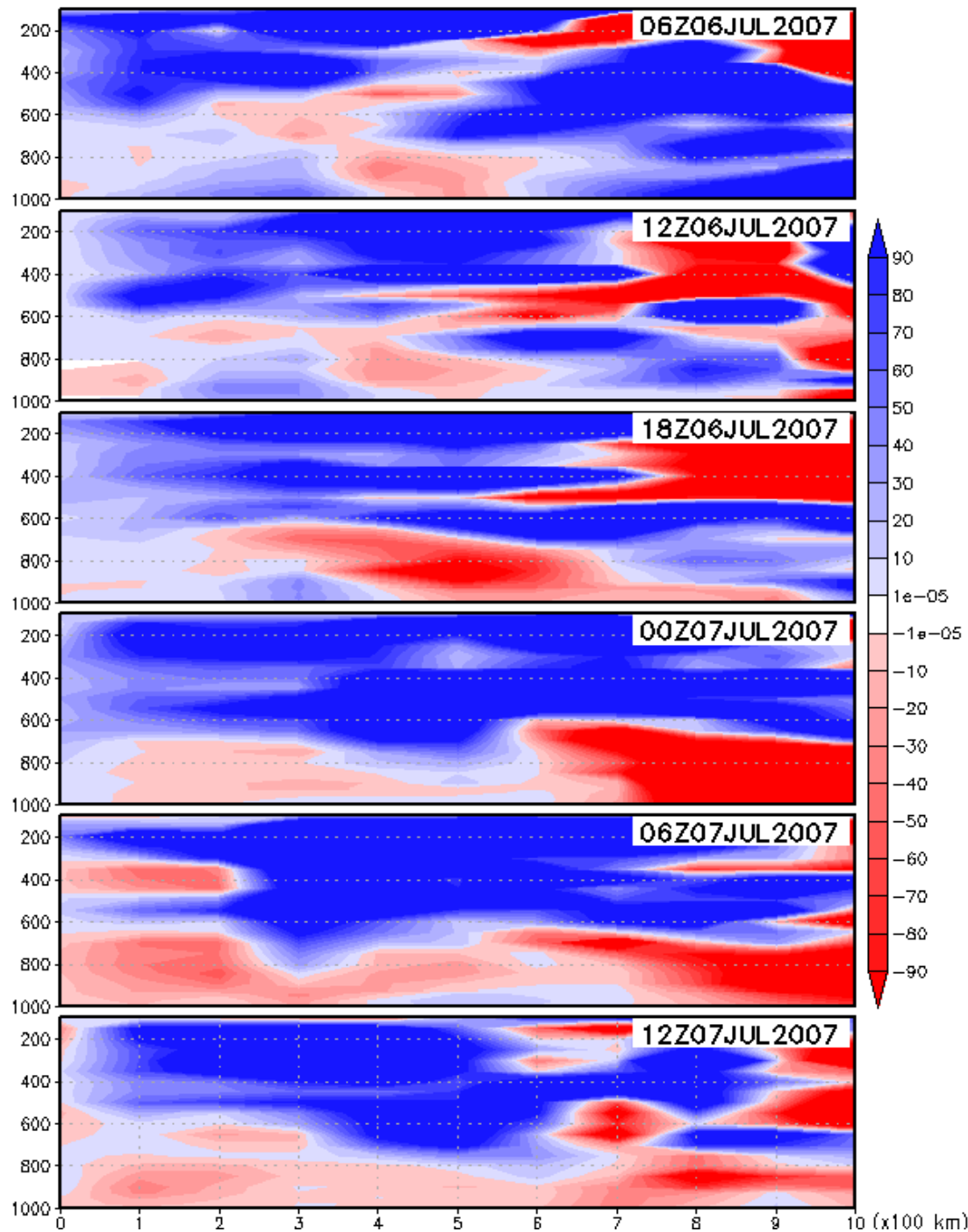


Figure 36. Six-panel time series of symmetric RAM fluxes ($\times 10^6 \text{ m}^3 \text{ s}^{-2}$) in the vertical from the GFS FNL. The fluxes are calculated at radial distances from the sweet spot. The abscissa is radial distance ($\times 100\text{km}$) from the sweet spot and the ordinate is pressure. Warm colors are negative symmetric RAM fluxes and cool colors are positive symmetric RAM fluxes.

2. The Origin of Typhoon Man-yi's Proto-vortex

At 00Z 3 July, the GFS FNL depicts three low-level cyclonic vorticity maxima at 5N centered at 157E, 161E, and 166E (Figure 37). The maxima at 161E and 166E are circulations at the meso- α scale embedded within the larger-scale ER wave (Figure 33). To examine the role of the ER wave's critical layer and the origin of Typhoon Man-yi's proto-vortex, it is necessary to view the system in a frame of reference moving with the parent wave. Subtracting a zonal phase speed of -4.5 m s^{-1} (derived from 850 hPa latitudinally-averaged meridional wind, Figure 38), GFS FNL 850 hPa streamline analyses in the co-moving frame are produced (Figure 39). The shading is relative vorticity and the purple cross is the location of the sweet spot. At 06Z 3 July, the ER wave pouch has a radius of approximately six degrees (Figure 39) and its sweet spot is located near 5.3N, 165E. Embedded within the synoptic-scale wave pouch are two meso- α scale vortices centered at 5.2N, 161.1E and 5.6N, 165.7E. These features are tracked coherently in the relative vorticity time series (Figure 37) until genesis and they move in-sync with the parent wave (suggesting DMW09 H3). The western-most vorticity maximum will be shown to be the proto-vortex that eventually forms Typhoon Man-yi in the GFS FNL.

At 00Z 5 July, in addition to the two westward propagating relative vorticity maxima, the GFS FNL vorticity time series (Figure 37) indicates a linear band of cyclonic relative vorticity stretching from the western edge of the domain to 151E. This feature is associated with the northwest-southeast oriented monsoon trough west of the ER wave. Within the monsoon trough, a stronger area of cyclonic relative vorticity is present at 3.3N, 149.5E. Interaction between the ER wave and the eastern end of the monsoon trough in this region likely led to vorticity enhancement through increased low-level convergence (Figure 40). In the co-moving frame (Figure 39), the sweet spot of the ER wave pouch is centered at 3.3N, 156.3E. At 06Z 5 July and the wave pouch remains large, approximately eight degrees longitude diameter. Both of the ER wave's original meso- α scale relative vorticity maxima remain in the wave pouch, although the closed streamlines originally associated with the eastern-most maximum are no longer evident.

This maximum has weakened considerably, likely because it originated in a convective burst that has decreased in intensity by this time (discussed in Section D). In the southwestern portion of the wave pouch, cyclonic vorticity originating in the monsoon trough appears to be entering the wave pouch and merging with the western-most cyclonic vorticity maximum. At 18Z 5 July, there is continued influx of low-level cyclonic vorticity from the monsoon trough that enhances the cyclonic vorticity in the wave pouch.

At 06Z 6 July, the synoptic-scale wave pouch is defined by the streamline passing through the stagnation point (7.9N, 142.2E) located in the northwestern quadrant of the domain (Figure 39). There are two meso- α scale relative vorticity maxima embedded within the wave pouch (Figure 39). The relative vorticity maximum that originated in the monsoon trough ahead of the ER wave is located at 4.8N, 147.8E and the relative vorticity maximum from the ER wave is located at 4.5N, 151.4E. This maximum has intensified through vortex merger with the secondary vorticity maximum originating in the ER wave pouch and the cyclonic vorticity from the monsoon trough. The sweet spot is located at 4.9N, 147.8E. A weak, convectively active easterly wave, which can be tracked in the vorticity Hovmoeller (Figure 37), is located in the northeast quadrant of the pouch (7.9N, 156.8E). On the southwestern periphery (1.8N, 145.8E) is another cyclonic vorticity maximum, which has migrated into the wave pouch from the monsoon trough.

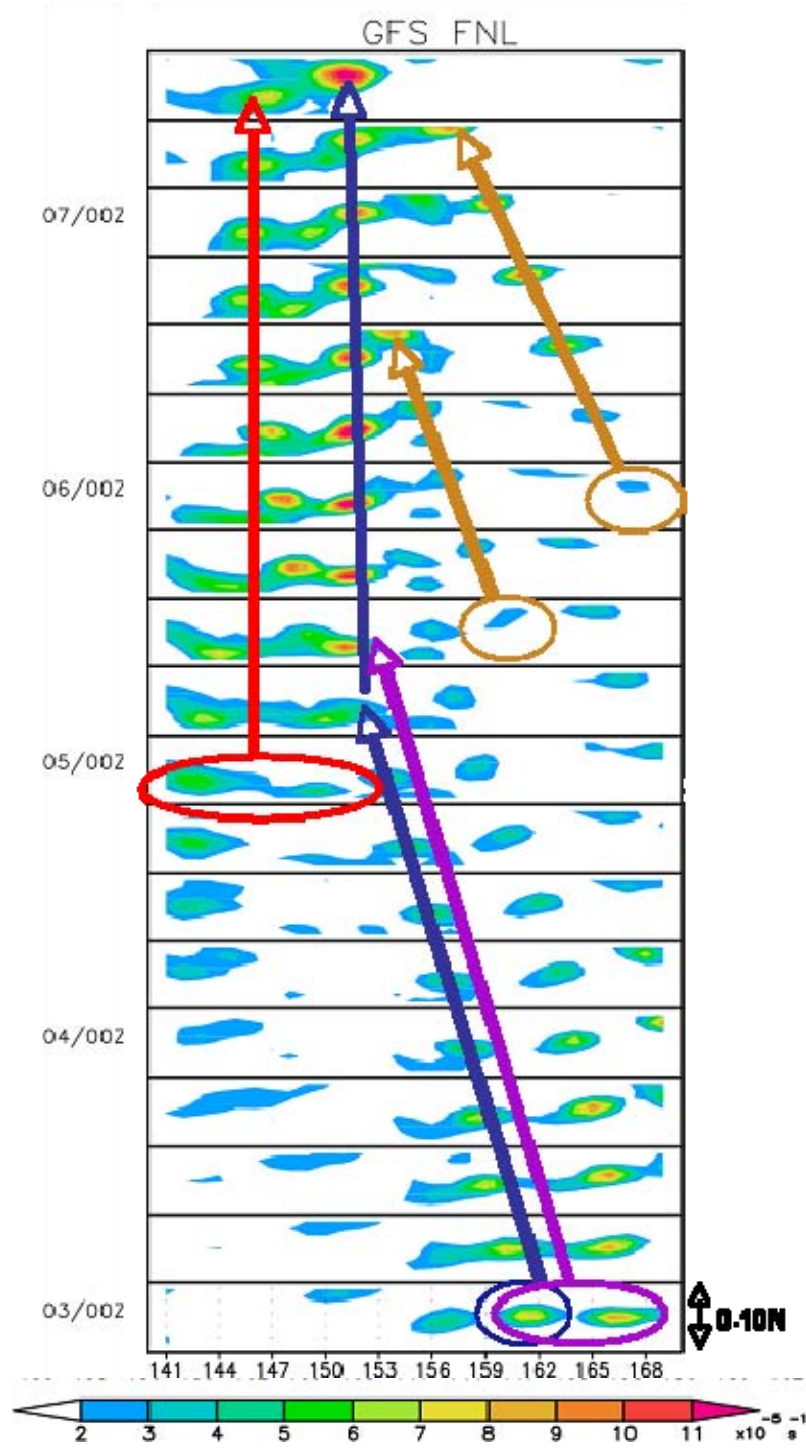


Figure 37. Time series of GFS FNL 850 hPa relative vorticity ($\times 10^{-5} \text{ s}^{-1}$) valid 00Z 3 July–12Z 7 July. Latitudinal range is 0–10N. The circles/arrows highlight key features in Typhoon Man-yi's tropical cyclogenesis sequence. Purple represents the ER wave, blue is Typhoon Man-yi's proto-vortex, red is the monsoon trough, and orange are easterly waves.

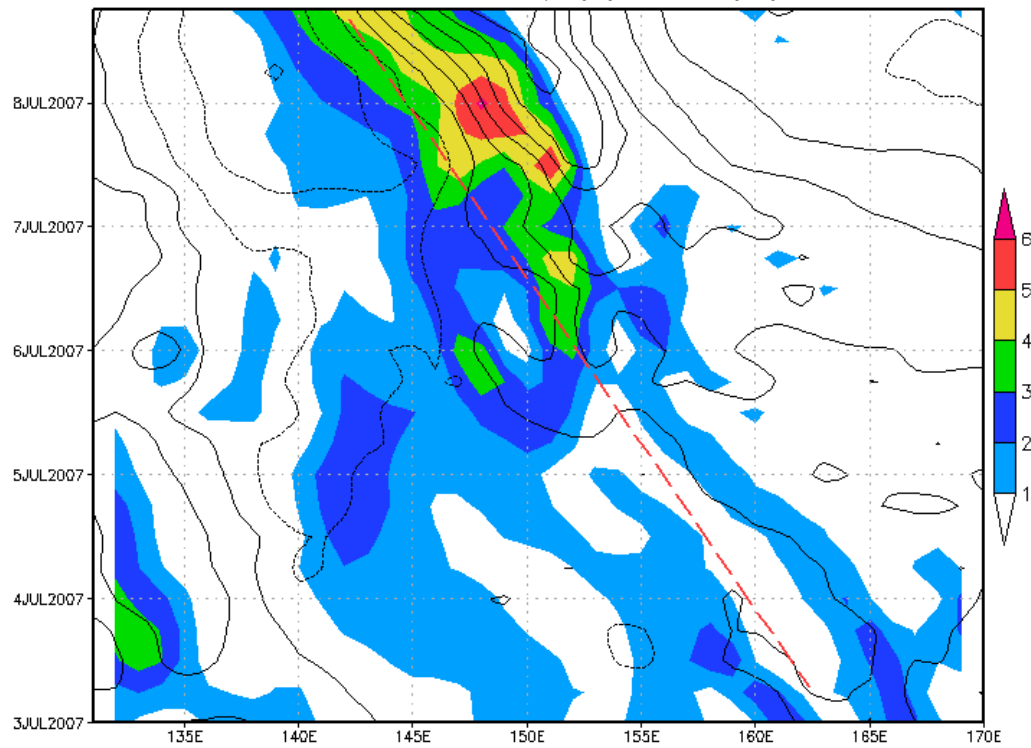


Figure 38. Hovmoeller diagram of GFS FNL latitudinal-averaged (2–10N) meridional wind and relative vorticity ($\times 10^{-5} \text{ s}^{-1}$). The dashed red line is used to derive the phase speed of the ER wave.

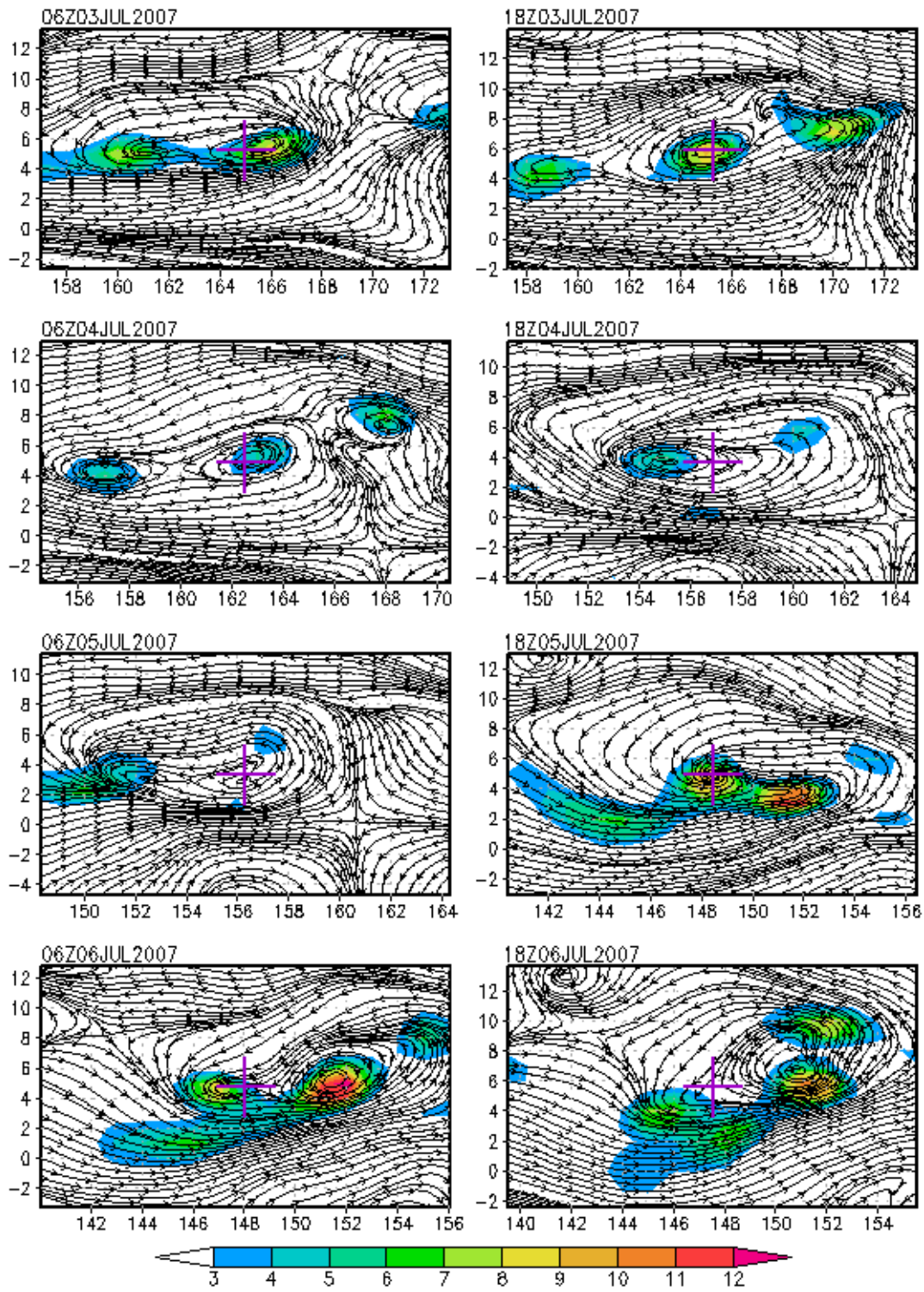


Figure 39. 850 hPa GFS FNL streamlines in the co-moving frame and relative vorticity ($\times 10^{-5} \text{ s}^{-1}$, shaded) valid at 12 hour intervals from 06Z 3 July–18Z 6 July. The purple cross indicates the location of the sweet spot.

At 18Z 6 July (Figure 39), the two cyclonic relative vorticity anomalies that originated in the monsoon trough west of the ER wave, are located in the southwest quadrant of the wave pouch (4N, 146E; 2.1N, 148E). The sweet spot is centered on 5.6N, 147.5E and is west of the relative vorticity maximum that originated in the ER wave (6.5N, 151E). The relative vorticity maximum in the northeast corner of the wave pouch (9N, 151E) originates in the easterly wave discussed above. The cyclonic vorticity is being enhanced by active convection associated with the wave.

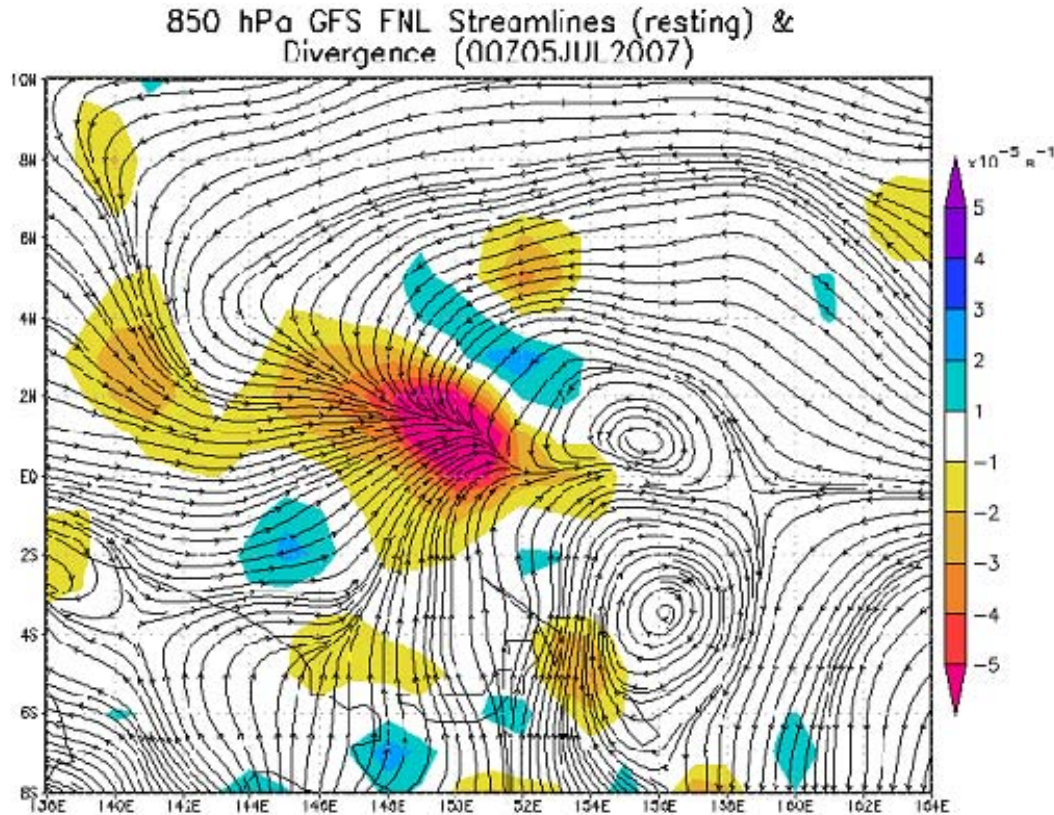


Figure 40. GFS FNL 1000 hPa streamlines in the earth-relative frame and divergence ($\times 10^{-5} \text{ s}^{-1}$, shaded). Note the strong area of low-level convergence ahead of the ER wave's twin cyclones.

Figure 41 is a 850 hPa streamline analysis in the co-moving frame valid at six-hour intervals between 00Z 8 July–18Z 8 July. At 00Z 8 July, the multiple relative vorticity maxima discussed above begin to merge in the GFS FNL. By 06Z 8 July, the large area of cyclonic relative vorticity within the wave pouch has consolidated around

the sweet spot and the relative vorticity maximum has intensified immediately east of the sweet spot location. Over the next 12 hours, the relative vorticity continues to organize and intensify around the sweet spot (suggesting DMW09 H1). These data show that: i) the ER wave and/or equatorial depression can provide a protective wave pouch for a proto-vortex, and ii) that this region is favorable for low-level cyclonic vorticity aggregation on the synoptic and meso- α scales.

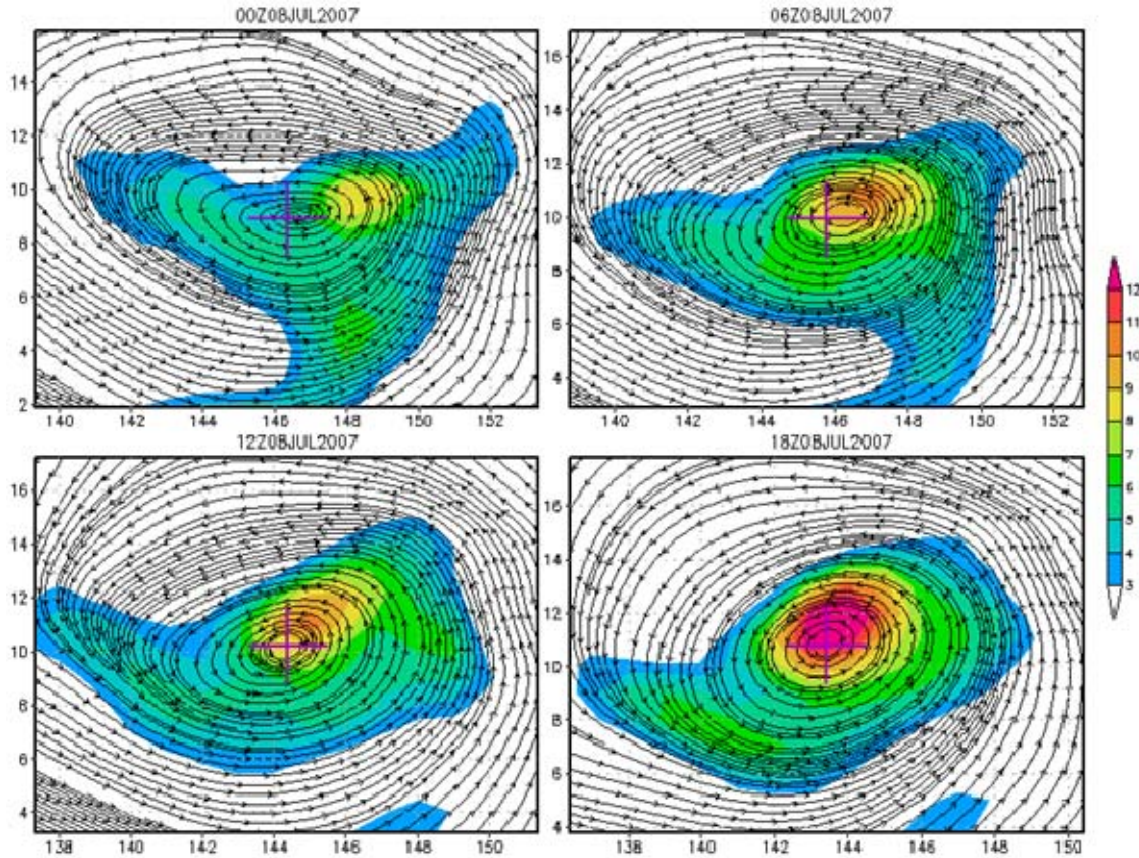


Figure 41. 850 hPa GFS FNL streamlines in the co-moving frame and relative vorticity ($\times 10^{-5} \text{ s}^{-1}$, shaded) valid at 6-hour intervals from 00Z 8 July–18Z 8 July. The purple cross indicates the location of the sweet spot.

D. OBSERVATIONS OF SYNOPTIC-SCALE FEATURES

1. QuikSCAT Observations

QuikSCAT Level-3 surface wind observations from 3–8 July are used to examine the observed surface wind field prior to the genesis of Typhoon Man-yi and assess the accuracy of the GFS FNL.³⁰ Two QuikSCAT passes are in the vicinity of the developing storm each day. The descending pass occurs at approximately 06Z and the ascending pass occurs at approximately 18Z. These observations are used to document the existence and location of: i) multiple areas of cyclonic circulations on 3 July (likely, the ER wave surface signal), ii) the northwest-southeast oriented monsoon trough on 4–5 July, and iii) the equatorial depression on 6–8 July. The limitations to the QuikSCAT observations discussed in Section B1 make it difficult to observe the ER wave, which typically have their maximum amplitude between 850–700 hPa (Kiladis and Wheeler 1995).

Analysis of the 06Z 3 July QuikSCAT pass reveals the surface representation of a mesoscale cyclonic circulation center at 3N, 153.8E that is embedded within the synoptic-scale GFS FNL ER wave (Figure 31). The 1000 hPa GFS FNL data, which is used to compare to the QuikSCAT observations, resolves this feature slightly east of its observed location (Figure 42). The second closed meso- α scale cyclonic circulation center (5.5N, 166E) in the GFS FNL is not observed in the QuikSCAT data. In the Southern Hemisphere, there is cyclonic flow observed by the QuikSCAT observations, but the closed cyclonic circulation center in the GFS FNL is east of the QuikSCAT pass.

On 18Z 3 July, the GFS FNL represents an ER wave in the lower troposphere and maintains this coherent synoptic-scale cyclonic circulation down to the surface (Figure 33). Within this synoptic-scale circulation are embedded meso- α scale cyclonic circulations that are also evident at the surface (Figure 43). The QuikSCAT observed wind field is characterized by large-scale cyclonic flow between 3–9N from the western

³⁰ As the GFS FNL incorporates QuikSCAT observations into their data assimilation scheme, there is some bias in this analysis. However, it is explored here as a means of assessing the validity of the analysis.

edge of the scan to 175E. The eastern-most meso- α scale cyclonic circulation (7N, 169E) in the GFS FNL is approximately a closed cyclonic circulation in the QuikSCAT observations. This QuikSCAT observed flow pattern is likely the surface representation of the Northern Hemisphere ER wave low. An area of disagreement between the QuikSCAT observations and the GFS FNL occurs between 0–5N, 172.5–180E. In this region, QuikSCAT observes easterly flow, while the GFS FNL flow remains predominantly southwesterly. This discrepancy is a result of the GFS FNL resolving a cyclonic gyre larger than observed by the QuikSCAT.

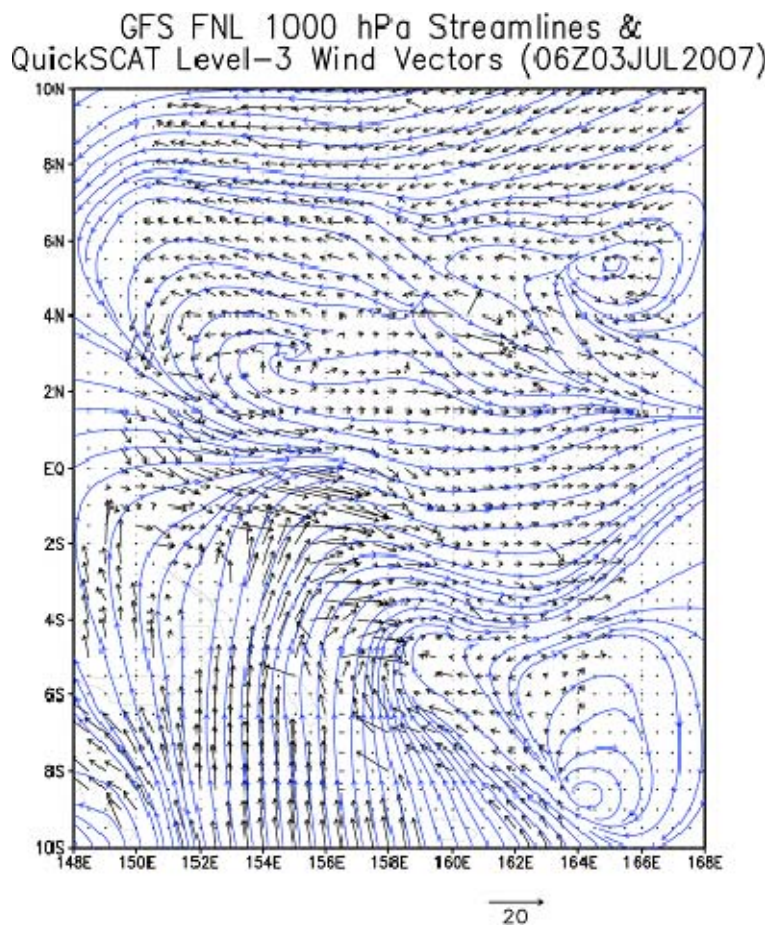


Figure 42. QuikSCAT surface wind vectors ($m s^{-1}$) and GFS FNL 1000 hPa streamlines (blue) valid 06Z 3 July.

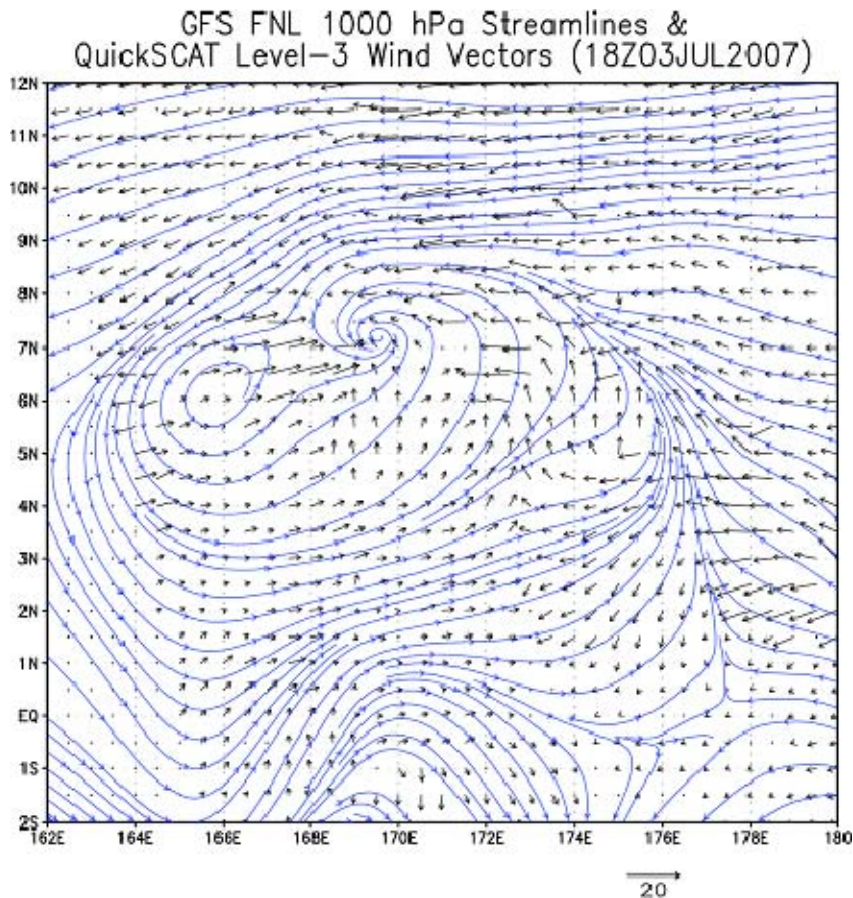


Figure 43. As in Figure 42, except valid 18Z 3 July.

During the 4 July ascending QuikSCAT pass (18Z), neither the GFS FNL nor the QuikSCAT observations represent a surface-based closed cyclonic circulation within the satellite overpass region. The dominant feature is the northwest-southeast oriented monsoon trough. Figure 44 is a plot of the QuikSCAT wind vectors (at 0.5° resolution) overlaid with the location of the monsoon trough in the QuikSCAT observations (black) and the GFS FNL (blue). The GFS FNL extends the monsoon trough farther east and is more zonally oriented than the QuikSCAT observations. The region between 150–155E depicts the QuikSCAT monsoon trough farther north than the GFS FNL.

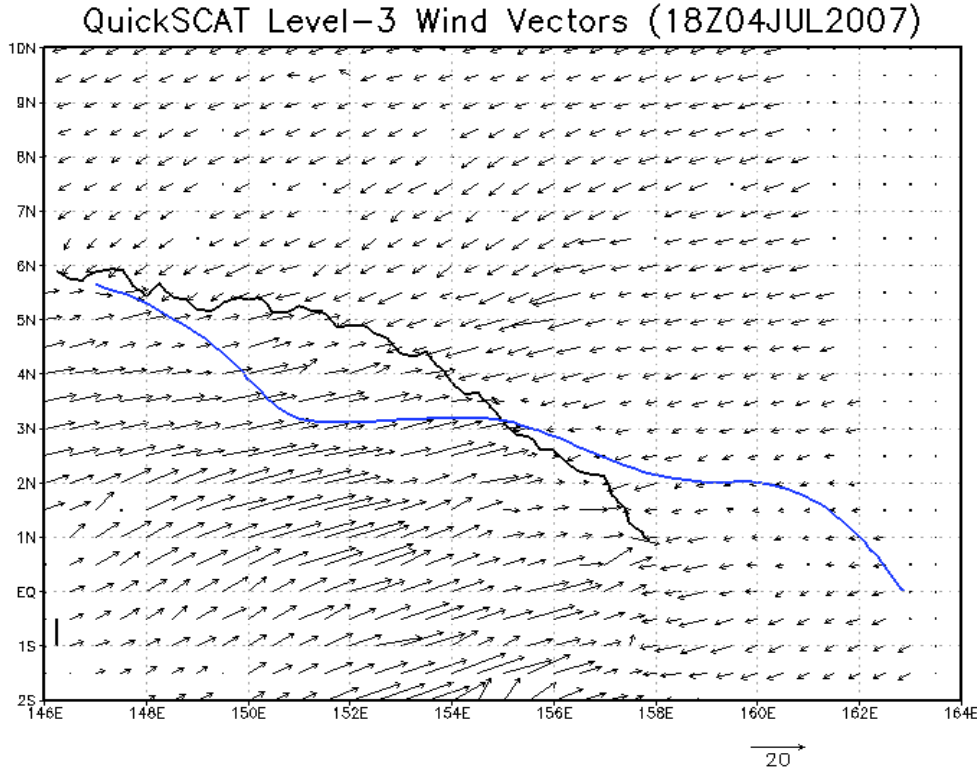


Figure 44. QuikSCAT Level-3 surface wind vectors (m s^{-1}) plotted every 0.5° overlaid with the position of the monsoon trough in QuikSCAT observations (black) and GFS FNL (blue). The position of the monsoon trough is defined as the location where $u=0$ and there is cyclonic relative vorticity in the Northern Hemisphere.

At 06Z 6 July, the synoptic-scale equatorial depression is depicted in the QuikSCAT observations north of the equator as a non-symmetric closed cyclonic circulation (Figure 45). On the western edge of the equatorial depression, there is a convergent region stretching from 7N, 148.5E to 2N, 150E. At the southern edge of this convergent region, there is evidence of a mesoscale cyclonic circulation center at 2.9N, 150.6E. The GFS FNL (Figure 45) reasonably depicts the large-scale cyclonic flow in the region, including the location and size of the equatorial depression. The location of the mesoscale cyclonic circulation center varies in the two representations, with the GFS FNL placing the dominant mesoscale 1000 hPa cyclonic circulation at 4.6N, 151.6E, approximately 2° north of the QuikSCAT observed center. The GFS FNL has an erroneous mesoscale circulation located at 5.7N, 147.8E (Figure 45). This area lay along the QuikSCAT observed convergent line.

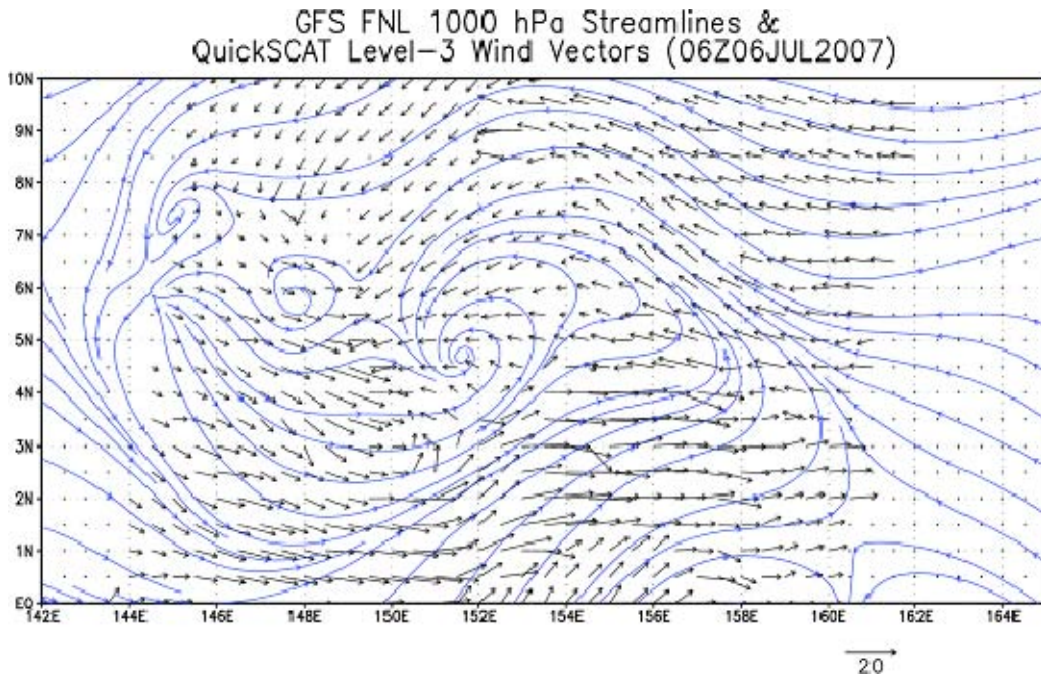


Figure 45. As in Figure 42, except valid 06Z 6 July.

Figure 46 is a four-panel streamline analysis of the QuikSCAT observations and 1000 hPa GFS FNL valid at 18Z 7 July (left) and 06Z 8 July (right). On 18Z 7 July, the GFS FNL performs well in identifying the equatorial depression when compared to the QuikSCAT data. Eighteen hours later, the QuikSCAT passes directly over the center of the equatorial depression, and the GFS FNL once again accurately represents the position of this feature (Figure 46).

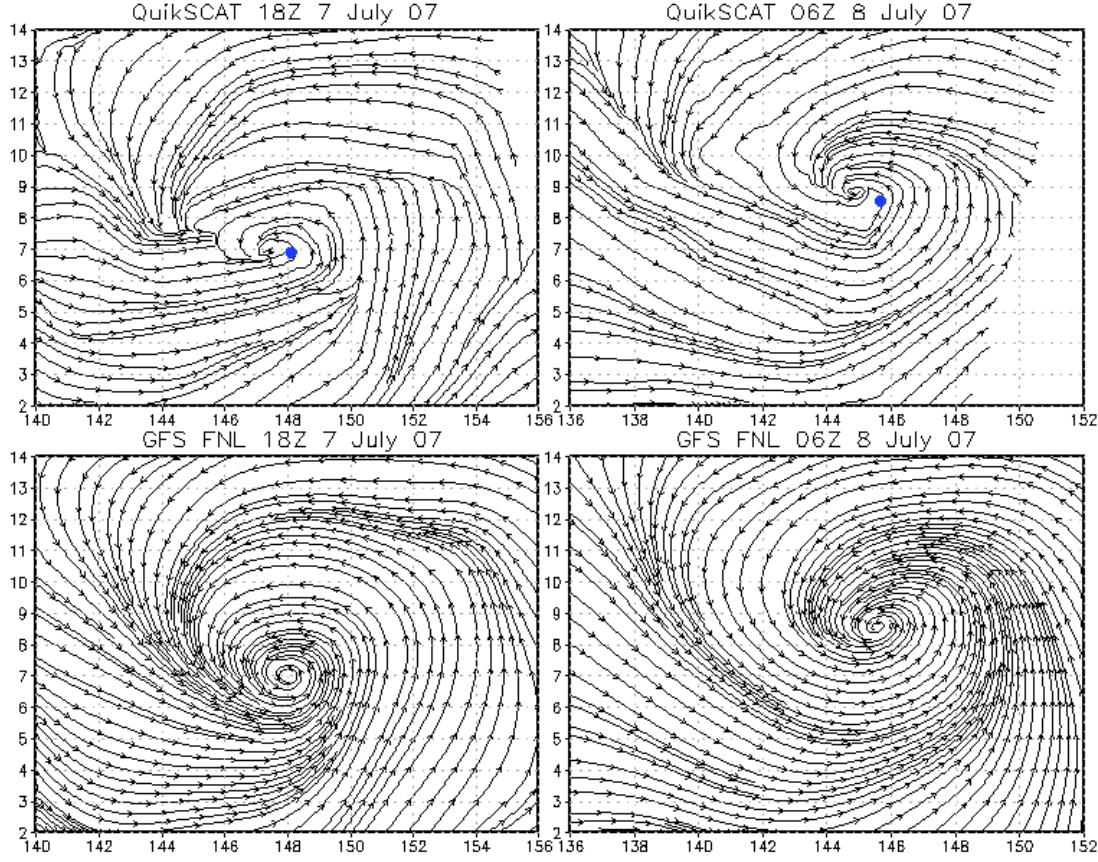


Figure 46. QuikSCAT (top) and GFS FNL (bottom) low-level streamline analysis valid 18Z 7 July (left) and 06Z 8 July (right). The blue dots represent the position of the GFS FNL low-level cyclonic circulation center.

2. MTSAT IR and TRMM Observations

MTSAT IR data and TRMM 3B42 surface rain rate data are used to examine the evolution of precipitation in the early stages of Typhoon Man-yi's tropical cyclogenesis sequence. The temporal evolution of convection in the western North Pacific basin is examined using a Hovmoeller diagram of latitudinally-averaged (0–10N) IR brightness temperature (Figure 47) valid from 00Z 1 July through 00Z 8 July. The white horizontal lines indicate missing data. At 00Z 2 July, there is evidence of active convection associated with the GFS FNL derived ER wave between 165–175E. This convection is sustained through 12Z 3 July. After this point, the convection associated with the westward propagating ER wave becomes nearly non-existent. While GFS FNL and

observations indicate that the geographic area the ER wave is moving through during this period remains moist, the overall stability in the region increases. Both the GFS FNL and observed Skew-T data (not shown) indicate regions of lower CAPE and higher surface convective inhibition (CIN) from 00Z 4 July–12Z 5 July over the western half of the GFS FNL ER wave position. While this could potentially explain the suppression of convection associated with the ER wave at this time, it must be examined more closely.

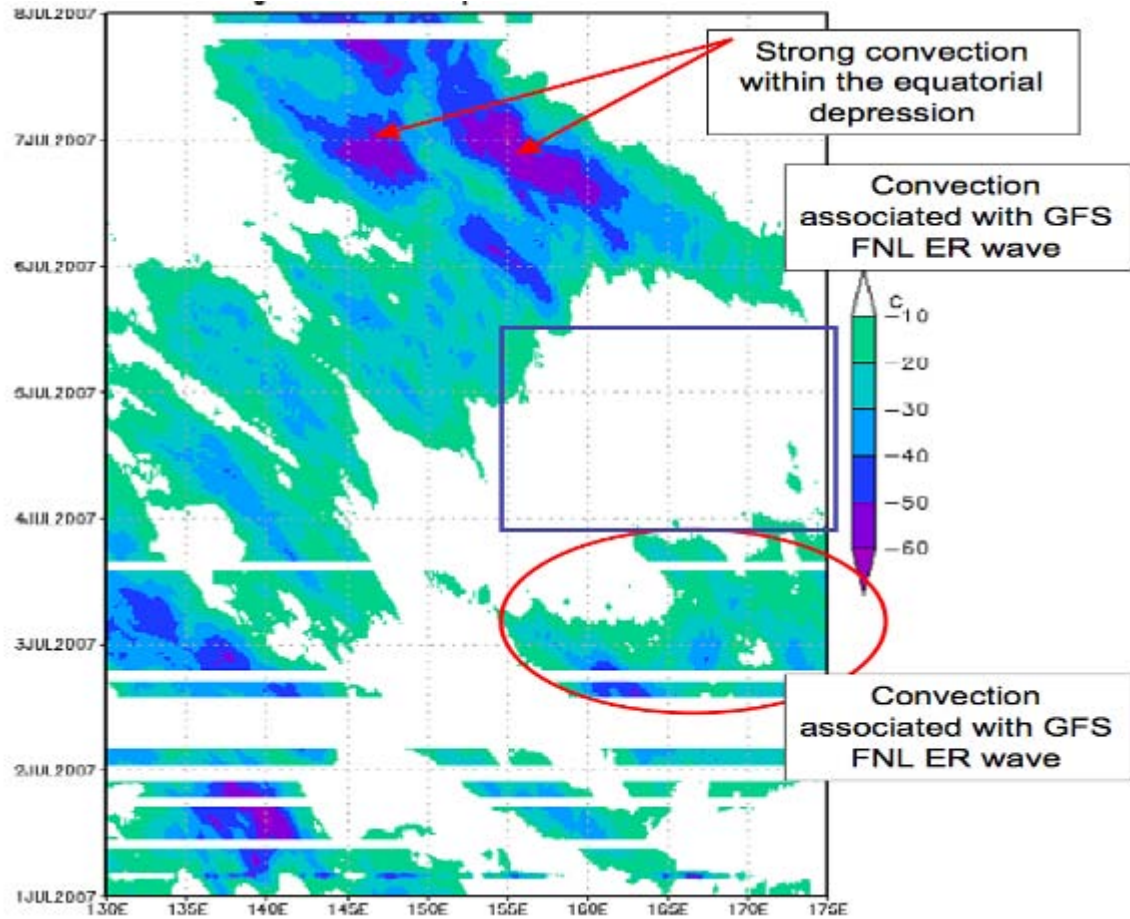


Figure 47. Hovmoeller diagram of MTSAT latitudinally-averaged (0–10N) IR brightness temperature ($^{\circ}\text{C}$). The horizontal white lines indicate missing data. Key features are highlighted. The blue box highlights the suppressed convection as the ER wave propagated westward.

At 18Z 4 July, there are two areas of stronger convection observed in the IR Hovmoeller diagram (Figure 47). The western-most area, centered at 143E, is concurrent with an area of convergence resolved in the GFS FNL (Figure 48). This convection maintains its intensity for approximately 24 hours before dissipating. The area of convection centered at 150E (Figure 47) represents the leading edge of the westward propagating ER wave in the GFS FNL (Figure 48). In the GFS FNL this area of convection is semi-stationary and forced by the ER wave/monsoon trough interaction through 00Z 6 July. It is noted that the two areas of convection discussed above are more intense than they appear in the Hovmoeller (as verified in Figure 48) due to their limited latitudinal extent.

By 18Z 5 July, the GFS FNL depicts the presence of an equatorial depression. TRMM 3B42 observations show active convection in the southern and eastern quadrants of this circulation (Figure 48). The strong convection on the eastern edge of the equatorial depression is a result of convergence between the southwesterly flow encircling the equatorial depression and the easterly trade-wind flow (Figure 48). There is an area of weaker convection at 170E associated with an easterly wave in the GFS FNL.

Between 18Z 6 July–00Z 7 July, the IR Hovmoeller (Figure 47) shows two strong areas of convection centered near 147E and 156E surrounding an IR brightness temperature minimum. At this point, the convection is beginning to fill all quadrants of the equatorial depression (Figure 48). The eastern-most convective maximum is driven by low-level convergence (as discussed above) and interaction with a convectively active easterly wave that is nearing the eastern edge of the equatorial depression (Figure 48). By 06Z 7 July, the TRMM 3B42 data indicates convection in all quadrants of the equatorial depression as resolved by the GFS FNL (Figure 49). However, the large size (approximately 12° in diameter) of the equatorial depression and disorganized nature of the convection within suggests that further organization at the sub-synoptic scales is necessary to complete the transition to a tropical cyclone vortex.

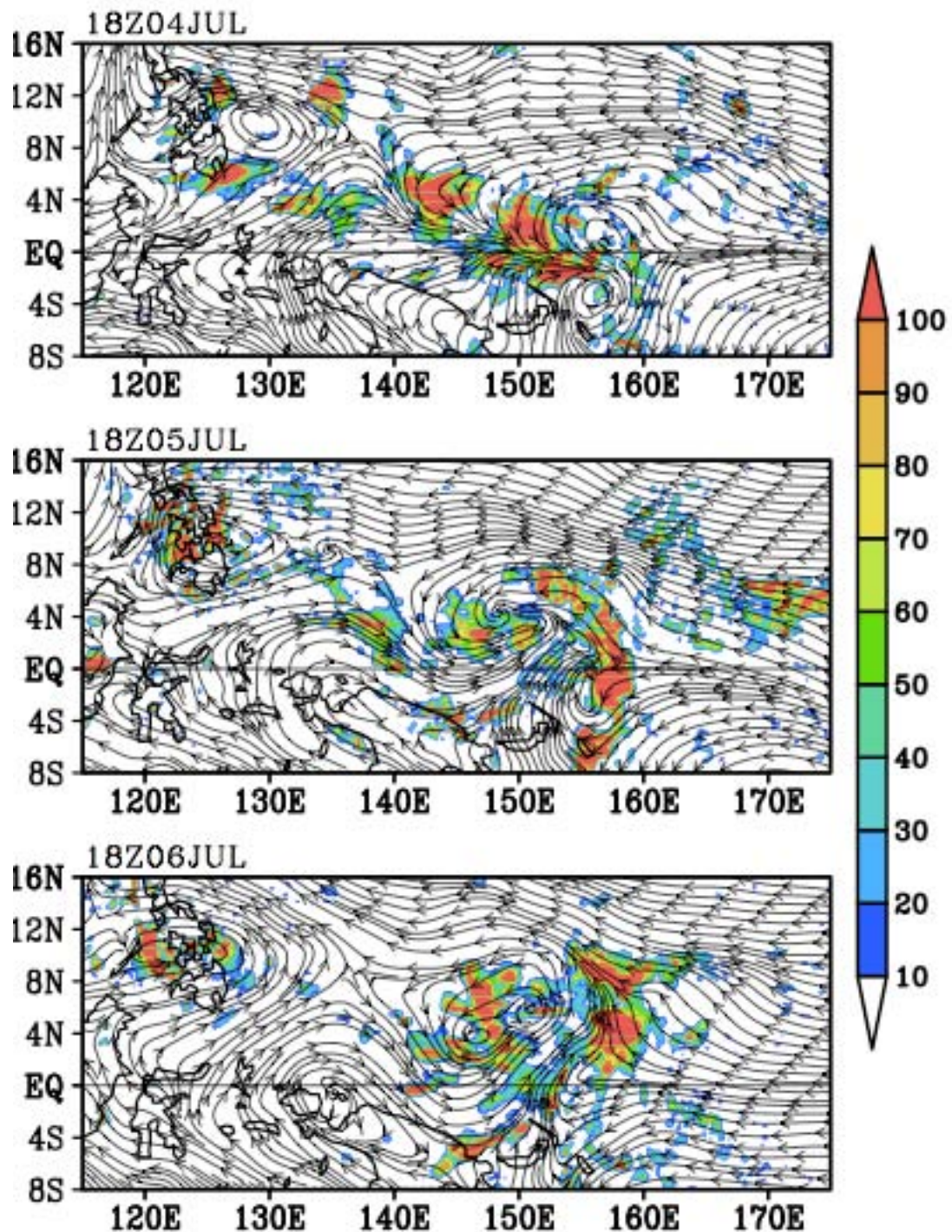


Figure 48. TRMM 3B42 24-hour accumulated surface rain (mm) with 850 hPa streamlines in the resting frame from the GFS FNL valid 18Z 4 July–18Z 6 July.
Figure courtesy of Dr. Zhuo Wang.

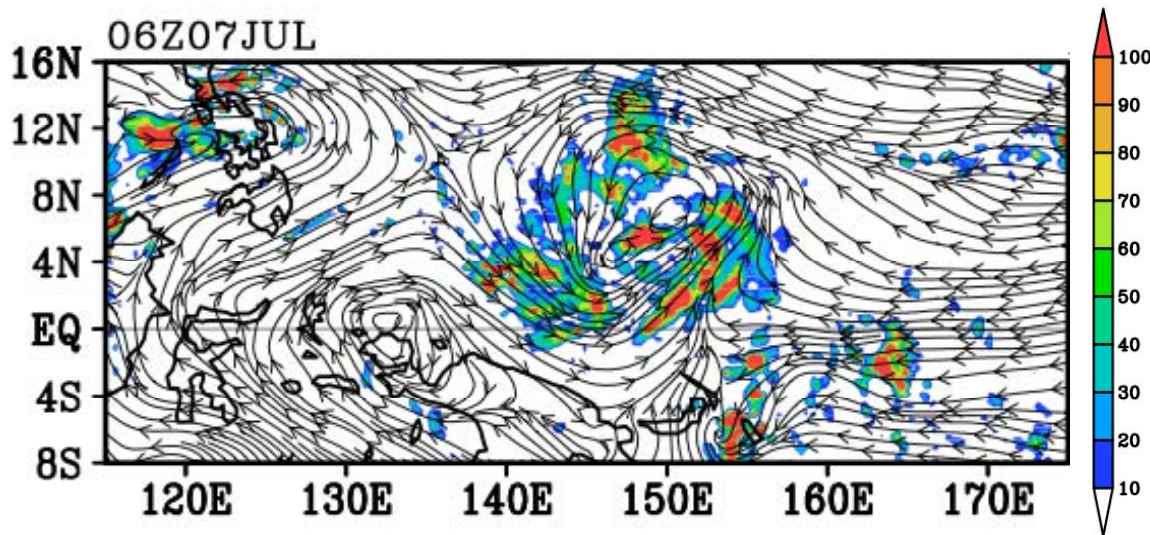


Figure 49. TRMM 3B42 24-hour accumulated surface rain (mm) with 850 hPa streamlines in the resting frame from the GFS FNL valid 06Z 7 July. Figure courtesy of Dr. Zhuo Wang.

E. DISCUSSION

1. Prevailing Paradigms of Tropical Cyclogenesis in the Western North Pacific Sector

Observations show that the GFS FNL provides a fairly accurate representation of the synoptic-scale features (location/size of ER wave, equatorial depression, orientation of monsoon trough) in the pre-Man-yi environment. However, the exact position of observed features, especially on the meso- α scale is sometimes erroneous when compared to QuikSCAT, TRMM, and MTSAT IR observations. It has been shown that the GFS FNL is consistent with the QuikSCAT observed wind field and the satellite-derived precipitation patterns from 3–6 July. Therefore, the GFS FNL is considered to offer a plausible synoptic-scale analysis to examine the tropical cyclogenesis sequence of Typhoon Man-yi. It is noted that while the QuikSCAT surface wind retrievals are not optimum to view a potential ER wave, the observations depict the surface reflection of the Southern (3, 4, 6 July) and Northern (3, 4 July) Hemisphere cyclonic gyres on

multiple days. The GFS FNL resolves an equatorial depression in the lower troposphere by 6 July, which verifies well with QuikSCAT observations.

The author would be remiss at this point not to mention the characteristics of ECMWF analysis. Both the GFS FNL and ECMWF analysis depict the existence of an ER wave on 3 July and resolve a synoptic-scale equatorial depression prior to tropical cyclogenesis. The evolution of these features between 3–6 July are, however, slightly different. The most distinct difference is that by 18Z 4 July, the ER is no longer represented by closed 850 hPa streamlines north of the equator in the ECMWF analysis. However, the region between 140–165E remains characterized by cyclonic flow and the cyclonic gyre in the Southern Hemisphere remains evident. By 12Z 5 July, an equatorial depression centered at 5N, 150E has emerged. This equatorial depression appears to have formed by a roll-up of the eastern edge of the monsoon trough as it interacts with the remnant cyclonic curvature from the ER wave. In the ECMWF analysis, the aggregation of positive relative vorticity at the eastern end of the monsoon trough appears to provide the vorticity seedling that eventually became Typhoon Man-yi.

In terms of the conceptual models put forth by Molinari (2004) and described in Section A, it can be argued that neither the ER wave nor the monsoon trough is the single driver for the development of the equatorial depression and eventual transition into a tropical cyclone. However, it can be argued that the ER wave, as represented by the GFS FNL, has contributed to the genesis of Typhoon Man-yi in the following ways:

- The interaction between the Northern Hemispheric ER wave low and monsoon trough directly leads to the formation of the equatorial depression.
- The vorticity seedling that eventually forms Typhoon Man-yi's low-level vorticity center is embedded within the parent ER wave.
- The convergence generated on the western edge of the ER wave packet/at the edge of the monsoon trough is favorable for initiation of deep convection and generation of additional source of cyclonic relative vorticity anomalies on 4–5 July.

Similarly, the monsoon trough appears to play a role in the development of a tropical cyclone as the persistent, large-scale cyclonic flow on its eastern edge leads to enhanced convergence. This results in generation of additional cyclonic relative vorticity at the lower-levels.

While difficult to assess the relative contribution of each feature, the author's AAMF analysis suggests that both features play a role in the low-level spin up that eventually forms the equatorial depression. Additionally, observational studies (Ferreira and Schubert 1997) and numerical simulations (Wang and Frank 1999) show that although a monsoon trough-like disturbance may break down to form a TD, interaction with a westward propagating disturbance enhances the process. Numerical simulations (Wang and Frank 1999) show that it takes 10–14 days for an unperturbed ITCZ-like disturbance to break down in the western North Pacific. In this case, just over three days elapse from the time the monsoon trough is established in the GFS FNL (00Z 4 July) until a TD is declared by JTWC (12Z 7 July). It is unlikely that a monsoon trough could have transitioned to a TD in this short amount of time *without* interaction with a westward propagating disturbance.

Figure 50 is a schematic of the hypothesized tropical cyclogenesis sequence of Typhoon Man-yi on the synoptic and meso- α scales in the lower-levels of the troposphere. In the initial state (Figure 50, panel a), the twin cyclones of the ER wave are depicted propagating westward. Multiple mesoscale cyclonic vorticity anomalies are embedded within the ER (depicted by the red hatching) and move in-sync with the parent ER wave. Over time, the ER wave begins to interact with the eastern end of the vorticity-rich monsoon trough (Figure 50, panel b). This interaction leads to the development of a large-scale equatorial depression (Figure 50, panel c). The equatorial depression has multiple mesoscale cyclonic vorticity anomalies embedded within that have originated from: i) the ER wave; ii) the monsoon trough; and iii) westward propagating easterly waves that have bombarded the equatorial depression and exchanged vorticity into the synoptic-scale depression (this idea has been presented in Montgomery and Enagonio [1998], but as far as the author knows, this is the first time this process has been observed in the western North Pacific basin and applied to an ER wave formation case). After this

point, mesoscale organization is required to complete the transition of the equatorial depression into a tropical cyclone strength vortex (discussed in Chapter VI).

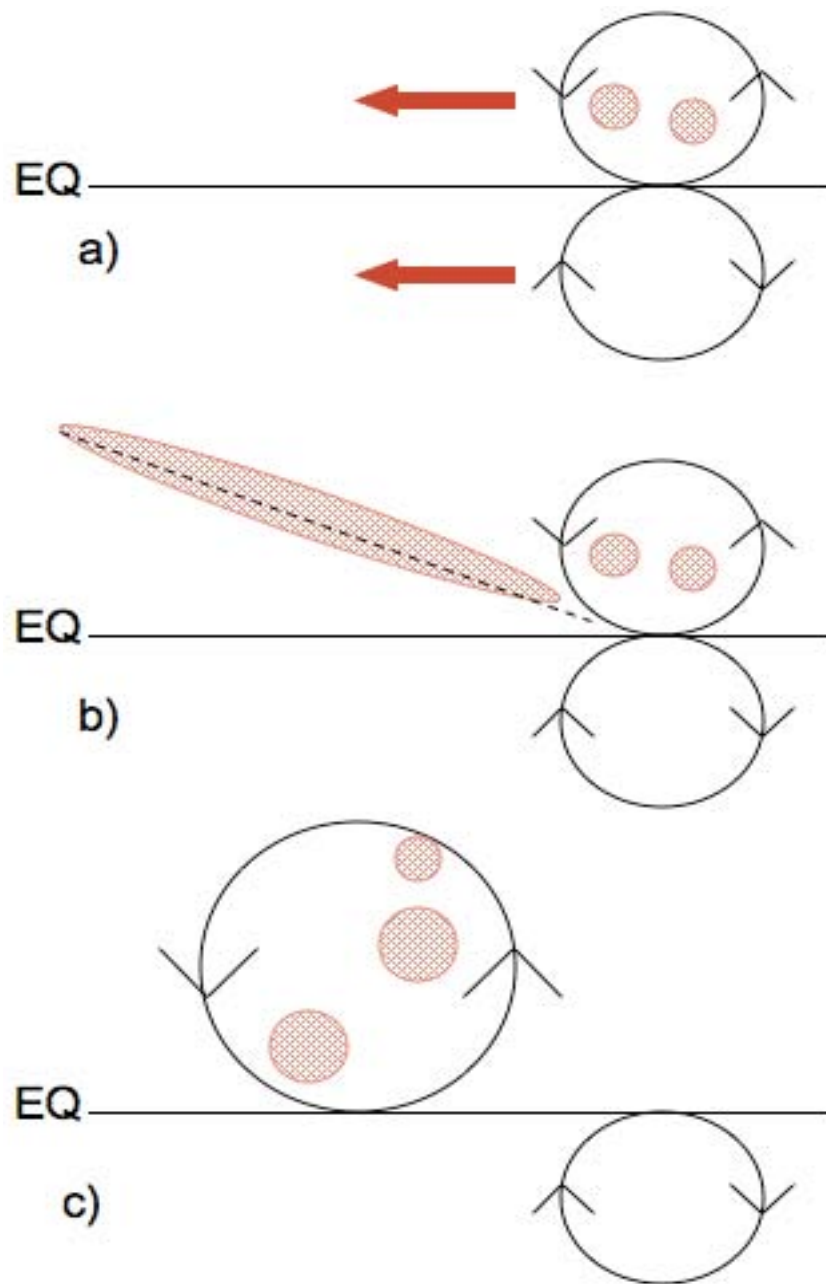


Figure 50. Schematic of the hypothesized tropical cyclogenesis sequence of Typhoon Man-yi on the synoptic and meso- α scales in the lower-levels of the troposphere. The red hatching are areas of cyclonic relative vorticity, the dashed line depicts the monsoon trough, the solid line indicates the location of the equator, and the circles with arrows indicate closed low-level circulations.

2. Marsupial Analysis

An analysis from the new tropical cyclogenesis model is performed using the GFS FNL data by tracking the ER wave as it transitioned into an equatorial depression and eventually a tropical cyclone. In the GFS FNL, the proto-vortex that becomes Typhoon Man-yi originates within the ER wave and is tracked coherently from 3 July until genesis. This suggests that the ER wave pouch is able to protect the proto-vortex (DMW09 H2). Furthermore, the hybrid wave-vortex system propagates together and amplifies (DMW09 H3). The presence of short-lived mesoscale vortices within the wave pouch observed here has been documented in numerical simulations (Montgomery et al. 2010a; Wang et al. 2010a). In Typhoon Man-yi’s tropical cyclogenesis sequence, the ER wave pouch has two meso- α scale cyclonic vorticity anomalies embedded within on 3 July. Over time additional meso- α scale cyclonic vorticity anomalies enter the pouch from both westward propagating disturbances and from the monsoon trough west of the wave pouch. Although coarse in resolution, the GFS FNL merges and axisymmetrizes these individual vorticity anomalies to form Typhoon Man-yi’s vorticity monolith. Although multiple mesoscale vorticity maxima intensify and weaken over time, the vorticity organization and amplification eventually occurs at the sweet spot of the parent wave (DMW09 H1). This sequence is emblematic of DMW09’s “guiding hand” principle, which states that upscale organization from the meso- γ to meso- α scale within the Kelvin cat’s eye is most efficient at the intersection of the wave trough and critical latitude (the sweet spot).

VI. TESTING THE HYPOTHEZIZED ROLE OF AN EQUATORIAL ROSSBY WAVE CRITICAL LAYER IN THE GENESIS OF TYPHOON MAN-YI PART II: MESOSCALE OBSERVATIONS AND NUMERICAL SIMULATIONS

A. INTRODUCTION

1. Background

Competing theories exist to describe the transformation of a synoptic-scale disturbance to a mesoscale tropical cyclone vortex. The first school of thought places emphasis on the role of mesoscale convective vortices (MCV) located in the stratiform rain region of a tropical MCS. This point of view is traditionally referred to as the “top-down” model of tropical cyclogenesis. This model has been advocated in Bister and Emanuel (1997) and Ritchie and Holland (1997). These theories emphasize the role of a mid-level positive vorticity maximum that must burrow downward to generate the low-level cyclonic relative vorticity anomaly required for tropical cyclogenesis. The downward advection of vorticity has been hypothesized to occur via increasing Rossby penetration depth, advective process, or some other mechanism (Houze et al. 2009). As the initial mid-level cyclonic circulation reaches the lower levels it becomes the initial low-level vortex that leads to tropical cyclone formation.³¹ The essence of this traditional “top-down” development pathway is that the mid-level MCV precedes surface spin-up and is essential for tropical cyclogenesis.

The second school of thought places the emphasis on vorticity aggregation in the lower-levels to build the tropical cyclone vortex from the “bottom-up”. This theory focuses on the updrafts of deep convective cells in the vorticity rich environment of a preexisting depression (Houze et al. 2009). In Montgomery and Enagonio’s (1998)

³¹ Detractors of this theory point out that when the mid-level cyclonic vorticity is transported down to the surface, the corresponding vortex tubes will compress, resulting in near surface divergence. This low-level divergence leads to the generation of anticyclonic relative vorticity near the surface. This process counteracts the effects of the downward transport of cyclonic vorticity required to build the tropical cyclone strength vortex in the lower-levels.

numerical simulations, intense deep convective elements rotate and generate vertical vorticity near the surface. These so-called VHTs (Montgomery et al. 2006; Hendricks et al. 2004) generate small-scale positive PV anomalies in the lower troposphere. Since these VHTs exhibit maximum diabatic heating in the mid troposphere (a convective-type heating profile) PV generation through diabatic processes is favored in the lower-troposphere (Montgomery et al. 2006). The near-surface PV anomalies generated from both VHTs and diabatic processes undergo what has been called diabatic vortex merger and axisymmetrization. These processes enhance the near-surface positive PV even after the individual VHTs have dissipated (Montgomery et al. 2006). In this theory, the role of the mid-level circulation from a MCV in the stratiform precipitation region can be complimentary. However, it is not a necessary condition for tropical cyclogenesis. The presence of VHTs during the tropical cyclogenesis sequence have been documented in observational data (Reasor et al. 2005; Houze et al. 2009; Raymond et al. 2010) and this so-called “bottom-up” sequence has been examined in high-resolution numerical models at near cloud resolving scales (Hendricks et al. 2004; Montgomery et al. 2006).

The previous chapter uses observations and analyses to describe the transition of an ER wave critical layer to a tropical cyclone at the synoptic and meso- α scales. However, a critical component to the tropical cyclogenesis sequence proposed by DMW09 has not yet been addressed. That is, that the Kelvin cat’s eye region provides a favorable dynamical environment for “bottom-up” type development, because: i) convection is favored in the Kelvin cat’s eye circulation. This in-turn favors a convective-type heating profile with a heating maximum in the lower-mid troposphere. Additionally, ii) vorticity aggregation is favored at the lower levels within the Kelvin cat’s eye region because the cut-off vortices travel with the parent wave allowing them to amplify together (DMW09 H3). The author will employ numerical simulations here to thoroughly examine these two concepts in the mesoscale transition of Typhoon Man-yi’s critical layer.

2. Numerical Simulations

While DMW09's initial study focuses on the synoptic and meso- α scales, Montgomery et al. (2010a) use high-resolution (3 km horizontal grid spacing) idealized WRF numerical simulations to present a multi-scale analysis of the transition of an easterly wave critical layer into a tropical storm. Their simulations support DMW09's hypotheses (H1-H3) including that: i) "bottom-up" development is the principle pathway for tropical cyclogenesis with the Kelvin cat's eye of an easterly wave critical layer, and ii) despite different WRF configurations (i.e., simulations with different model physics, cumulus parameterizations etc.) DMW09's proposed tropical cyclogenesis sequence appears to be robust. While some numerical simulations may have taken longer to form a tropical storm strength vortex, or formations occur in slightly different geographical locations, all simulations show that the sweet spot is the favored location for vorticity aggregation and tropical cyclogenesis. Wang et al. (2010a) use high-resolution (3 km horizontal grid spacing) WRF simulations to evaluate the role of an African Easterly Wave's (AEW) critical layer in the genesis of Hurricane Felix (2007). They suggest that Hurricane Felix forms from an interaction between a westward propagating AEW and the Atlantic ITCZ. Their WRF simulations indicate that tropical cyclogenesis on the mesoscale follows the "bottom-up" pathway to tropical cyclogenesis. They note also that upscale merger and organization of vorticity is guided by the wave's critical layer at the 700 hPa level and favored near the sweet spot (an example of the guiding hand principle in DMW09).

In this chapter, three high-resolution WRF numerical simulations (3 km horizontal resolution on the inner-most grid) of the genesis sequence of Typhoon Man-yi are used to show that: i) despite employing different model physics and cumulus parameterizations, all simulations essentially follow the new tropical cyclogenesis model for this western North Pacific case, and ii) the "bottom-up" pathway to tropical cyclogenesis is the preferred route in development in all of the numerical simulations.

This chapter proceeds as follows. Section B describes the numerical simulations used in this study. Section C presents an analysis of the three high-resolution WRF numerical simulations. Section D provides a summary of the work presented along with possible broader implications.

B. DESCRIPTION OF NUMERICAL SIMULATIONS

1. Model Configuration

Three high resolution numerical experiments are carried out here using the Advanced Research WRF for the purpose of testing the applicability of the “bottom-up” model of development within a precursor wave critical layer. In particular, the author wishes to assess the validity of H1-H3 (DMW09) for this western North Pacific tropical cyclogenesis case. The 3.0 version of WRF is a fully compressible non-hydrostatic model. Each simulation consists of four nested grids (the approximate location of the inner three grids are depicted in Figure 51) with horizontal grid spacing of 81, 27, 9, and 3 km and 28 vertical levels in a terrain following, pressure vertical coordinate system. The simulations use six-hour GFS FNL at one degree horizontal grid spacing for initialization and boundary conditions. Parameterizations are used for the planetary boundary layer (Yonsei University scheme), longwave radiation (the rapid radiative transfer model [RRTM]), and shortwave radiation (the Dudhia scheme). The WRF simulations are initiated on 18Z 6 July and run in forecast mode for 48 hours. Convection is resolved explicitly on the inner two domains (9 and 3 km) and cumulus parameterizations are used on the outer two domains (81, 27 km, Table 1). The first simulation uses the Kain-Fritsch (KF1) cumulus parameterization (Kain and Fritsch 1990; Kain 1993) and six species ice microphysics (Hong et al. 2004). The second simulation uses Betts-Miller-Janjic (BMJ1) (Betts and Miller 1986; Janjic 1994) cumulus parameterization scheme with six classes of ice microphysics. The third simulation uses the Betts-Miller-Janjic (BMJ) cumulus parameterization with warm rain microphysics.

2. Model Initial Conditions

The GFS FNL is chosen over the ECMWF analysis for the initial conditions for the following reasons:

- The GFS FNL positions the equatorial depression more accurately than the ECMWF analyses from 6–8 July when compared against QuikSCAT observations.
- Despite taking slightly different pathways, both the ECMWF analyses and GFS FNL depict a similar atmospheric state on 6 July. At this time an equatorial depression is the dominant feature in both analyses. Therefore, the dynamical processes that occurred prior to this time are of lesser importance to the simulations, which begin at 18Z 6 July.
- The observed TRMM precipitation patterns are consistent with the GFS FNL synoptic-scale features.

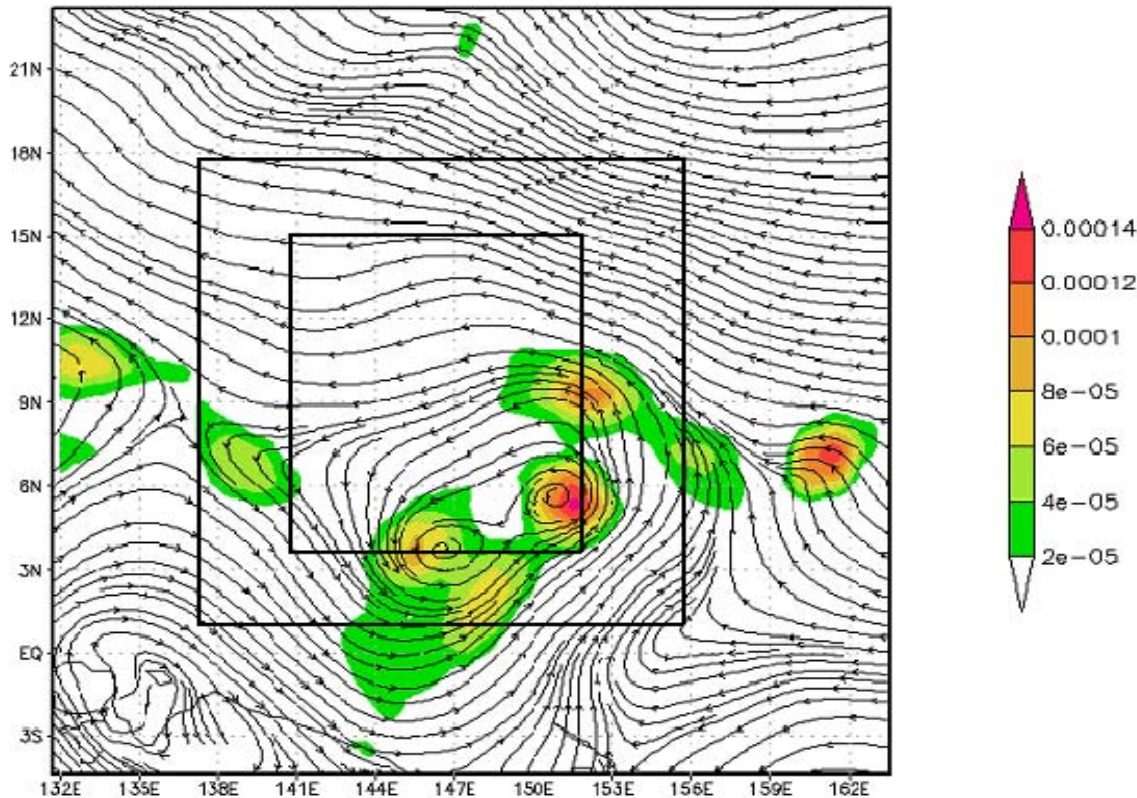


Figure 51. Initial conditions for the WRF numerical simulations. The black lines are streamlines in the resting frame and the shading is relative vorticity (s^{-1}). The boxes indicate the approximate location/size of inner three domains (d02–d04) of the numerical simulations.

Table 1. Summary of WRF numerical simulations.

Simulation Name	Physics	Precipitation Representation	Phase Speed (ms^{-1})
KF1	Six class ice microphysics	81, 27 km: Kain-Fritsch 9, 3 km: Explicit	-3.3
BMJ1	Six class ice microphysics	81, 27 km: Betts-Miller-Janjic 9, 3 km: Explicit	-3.8
BMJ	Warm rain scheme	81, 27 km: Betts-Miller-Janjic 9, 3 km: Explicit	-3.2

C. ANALYSIS OF THE NUMERICAL SIMULATIONS

1. Wave Tracking

Wave tracking is accomplished using the one-dimensional zonal wave tracking algorithm (DMW09; Wang et al. 2009). Latitudinally-averaged (0–12N) SF and meridional wind \bar{v} are used to track the wave (Montgomery et al. 2010b). The large meridional extent is necessary because: i) of the large diameter of the equatorial depression, and ii) it allows for separation of the large-scale wave (equatorial depression) feature from the mesoscale cyclonic circulations observed within. In these simulations, the sweet spot is defined as the position where the mean wave trough ($\bar{v} = 0$) intersects the critical latitude ($u = c_p$).

A Hovmoeller diagram for the 81 km domain (d01) of the KF1 simulation (Figure 52) indicates a strong moisture gradient between the moist wave pouch and the relatively dry surrounding environment. These findings are consistent with the increased moisture within the pouch (DMW09 H2) and demonstrate the potential for the use of the moisture gradient as a pouch tracking mechanism (Wang et al 2009, Montgomery et al. 2010b) in the western North Pacific sector. The latitudinally-averaged meridional wind field also depicts the presence of a westward propagating disturbance in this simulation. Phase speeds (Table 1) derived from the latitudinally-averaged meridional wind (not shown for the BMJ simulations) are then used to create streamline analyses in the co-moving frame.

Despite differences in model physics and cumulus parameterizations, the three simulations indicated similar phase speeds for the pre-Man-yi disturbance.

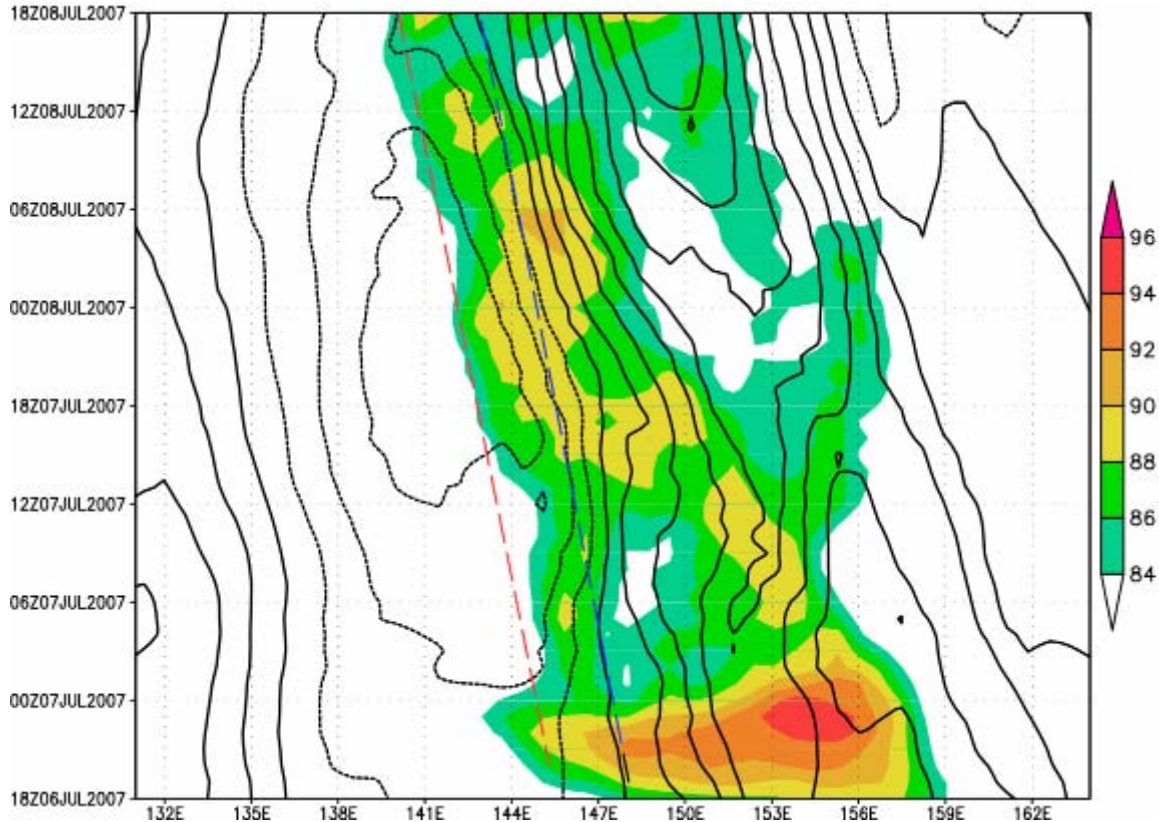


Figure 52. Hovmoeller diagram of latitudinally-averaged (0–12N) SF (%, shaded) and meridional wind (m s^{-1} , contours) for the outer domain (d01) of the KF1 WRF simulation. The red dashed line is used to derive the phase speed based on the moisture gradient and the blue dashed line is used to derive the phase speed based on the location of wave trough ($\bar{v} = 0$).

2. The Marsupial Sequence on the Synoptic and Meso- α Scales

Figure 53 shows a time series of the 850 hPa streamline and relative vorticity (shaded) fields for d01 of the KF01 simulations. The co-moving frame is in the left column and the resting frame is in the right. At 06Z 7 July, there are multiple meso- α scale cyclonic vorticity anomalies located within the wave pouch (co-moving) or equatorial depression (resting). In the KF1 simulation, the center of the equatorial

depression in the resting frame at 06Z 7 July is well south (4.5N) of the center of the wave pouch in the co-moving frame (7.8N). Over the next 12 hours, the KF1 simulation weakens the northern-most vorticity maximum and increases the areal extent and intensity of the cyclonic relative vorticity maxima in the southern quadrant (~4N) of the wave pouch. By 06Z 8 July, the cyclonic relative vorticity maximum is co-located with the sweet spot. By 8 July, there is little difference between the position of the closed circulation in the co-moving and resting frames. While the sweet spot in the KF1 simulation initially shifts northward towards the northern vortex, as time evolved, vorticity aggregation is favored near the sweet spot.

The evolution of moisture (represented by SF) within the wave pouch of the KF1 simulation is examined in Figure 54. At the initial time period, there is a relatively moist pouch surrounded by drier air to the north. Over the next 24 hours, the pouch remains more moist than the surrounding environment. At 18Z 7 July, the moisture maximum in the KF1 simulation is in the southern quadrant of the wave pouch (co-located with the most intense cyclonic vorticity anomaly). At 18Z 8 July, the area of maximum moisture in the KF1 simulation remains in the southern quadrant of the pouch. This evolution on the synoptic-scale in the KF1 simulation generally supports the tropical cyclogenesis sequence proposed in DMW09 as vorticity aggregates around the sweet spot and the pouch is more moist than the surrounding environment.

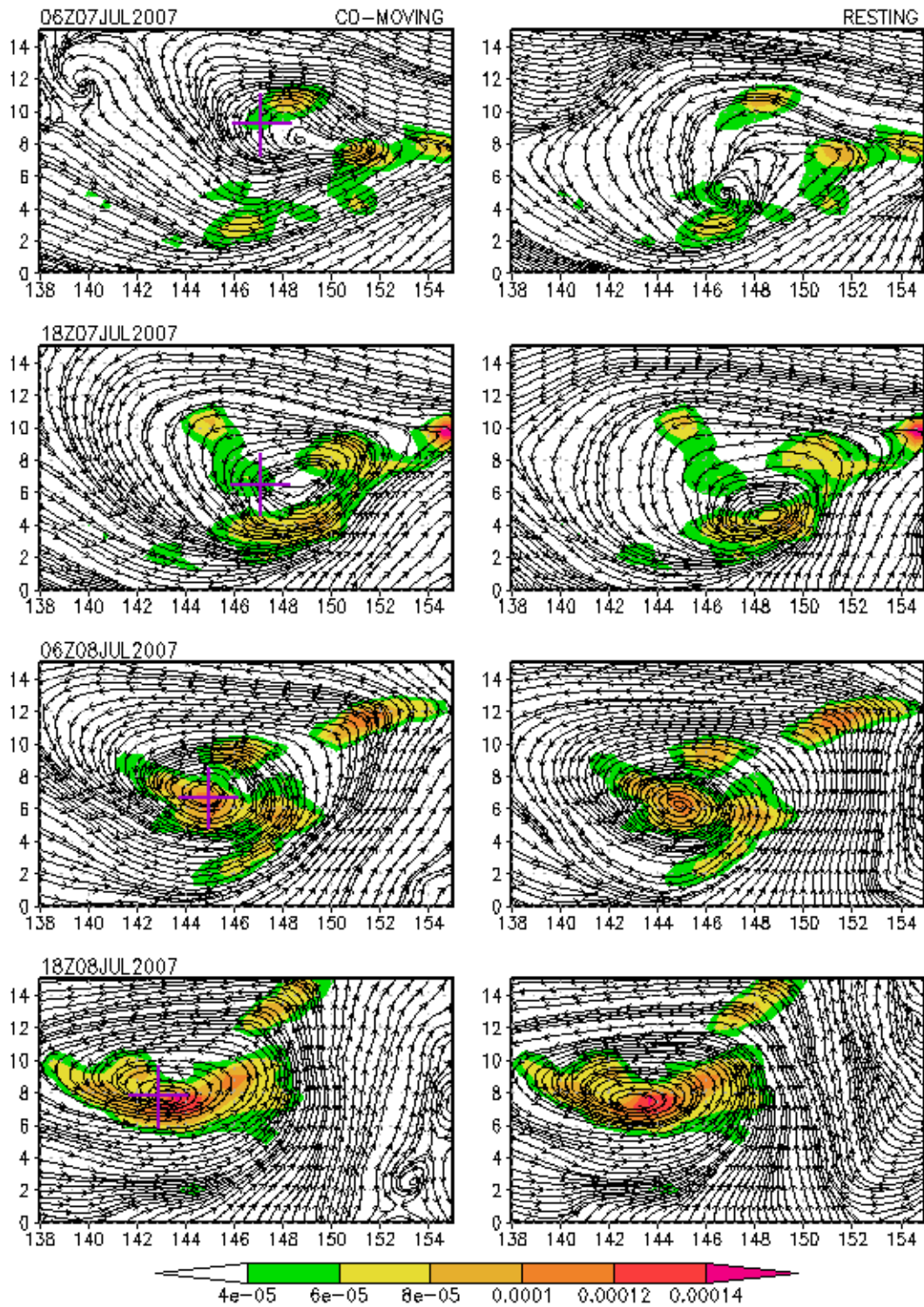


Figure 53. Eight panel plot of 850 hPa streamlines in the co-moving (left) and resting frames (right) from the KF1 d01 simulation valid every 12 hours from 06Z 7 July. The shading indicates relative vorticity (s^{-1}) and the purple plus sign in the co-moving frame indicates the location of the sweet spot.

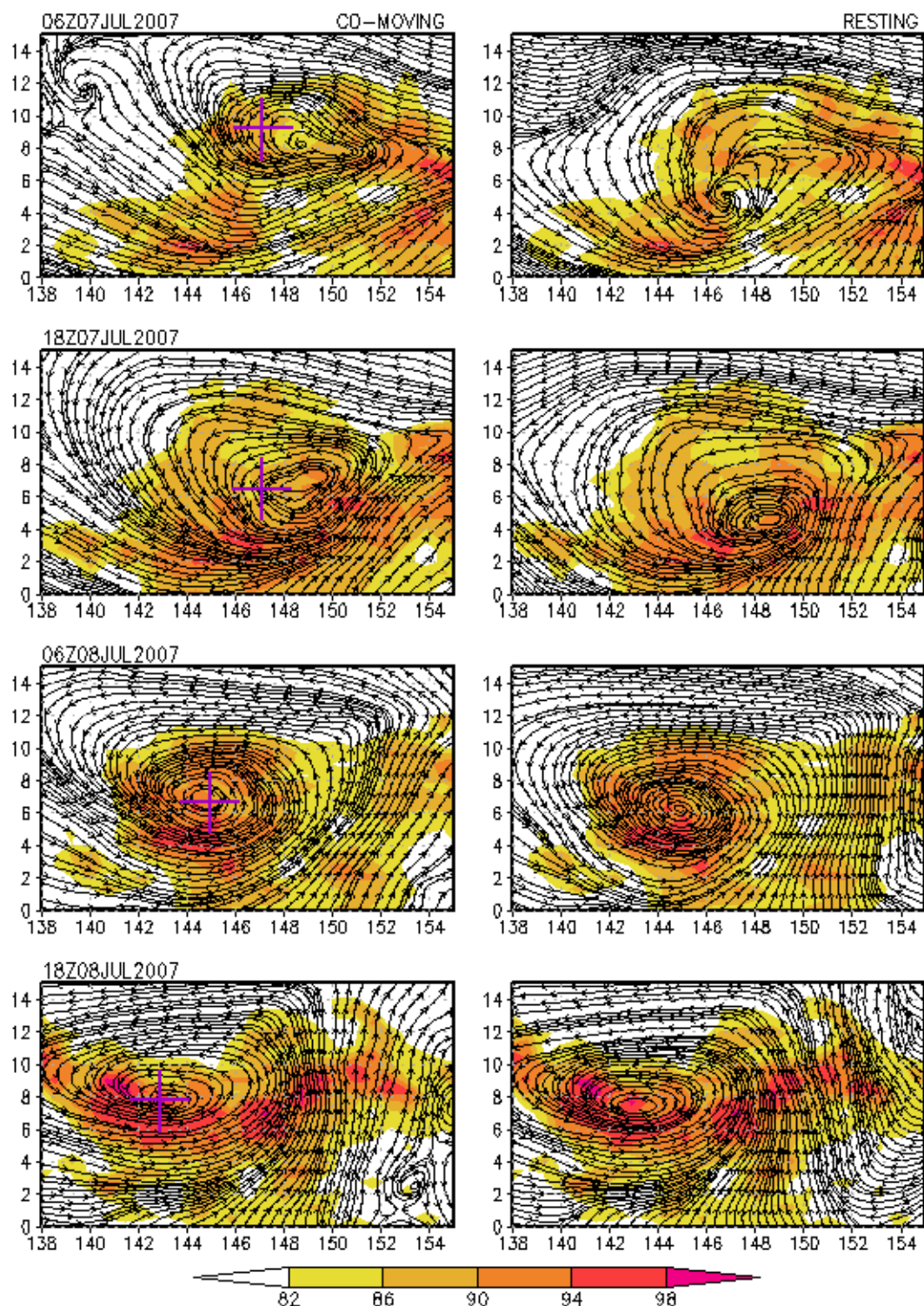


Figure 54. As in Figure 53, except for SF (%), shaded).

3. The Tropical Cyclogenesis Model on the Meso- β /Meso- γ Scales

a. Evaluation of “Bottom-up” vs. “Top-down”

Time-height cross sections of relative vorticity, divergence, and relative humidity averaged within a $3^\circ \times 3^\circ$ box centered on the sweet spot and moving with the pouch are created for the KF1 9 km domain (d03) data (Figure 55). These diagnostics are used to assess the processes within the Kelvin cat’s eye circulation, located within the wave’s critical layer. The initial distribution of relative vorticity within the cat’s eye is represented as a layer of weak positive vorticity spanning from 1000 to 500 hPa (Figure 55). The vorticity maximum initially weakens as the model initial conditions evolve. The area-averaged vorticity then reintensifies immediately prior to 06Z 7 July. After this point, the vorticity intensification occurs in the lower troposphere and there is no evidence of a mid-level MCV preceding low-level spin-up in this simulation. While there is evidence of mid-level convergence (Figure 55) at several points for the KF1 time series (12Z 7 Jul, 03Z and 18Z 8 July) these are not accompanied by a strong mid-level MCV (Figure 55). The generation of cyclonic relative vorticity near the surface is likely due to increased surface convergence prior to 06Z 7 July (Figure 55). In the KF1 simulation, spin-up is tempered (12Z–18Z 7 July) after this initial enhancement of cyclonic vorticity within the lower levels. At 00Z 8 July, intense cyclonic relative vorticity, coincident with strong low-level convergence (Figure 55), is being amplified in the KF1 scheme (Figure 55). After 06Z 8 July, the cyclonic vorticity monolith that eventually forms Typhoon Man-yi continues to intensify in the lower troposphere.

The KF1 simulation shows maximum moisture in the lowest levels of the troposphere throughout the entire simulation period (Figure 55). After 00Z 8 July, there are moisture maxima at the surface and 600 hPa (Figure 55), with a relative minimum in-between. After 15Z, 8 July, the moisture throughout the column (up to 400 hPa) increases. The presence of a relatively dry mid-troposphere within the pouch is an interesting feature of this simulation. However, it should be noted that: i) while these anomalies exhibit relative minima in moisture, the RH values are generally $>80\%$ up to 500 hPa throughout the time period, ii) this does not suggest “top-down” development

nor confirm the importance of a moistening mid-levels as the catalyst for cyclogenesis (e.g., Nolan 2007). In the KF1 simulation, there is spin-up occurring in the lower-levels prior to and during this relatively dry period. The lack of a prominent mid-level MCV and the initial spin-up of near surface cyclonic relative vorticity seen in the data from the d03 simulation suggest that the “bottom-up” pathway is favored within the pre-Man-yi wave pouch.

In the next section, the author will first examine data from the 3 km domain of the KF1 simulation to evaluate the evolution of precipitation and to assess the presence of VHTs, to determine whether diabatic vortex merger and axisymmetrization occur in the vicinity of the sweet spot, and finally to quantify their contributions of these aspects to building the cyclonic vorticity monolith within Typhoon Man-yi’s critical layer.

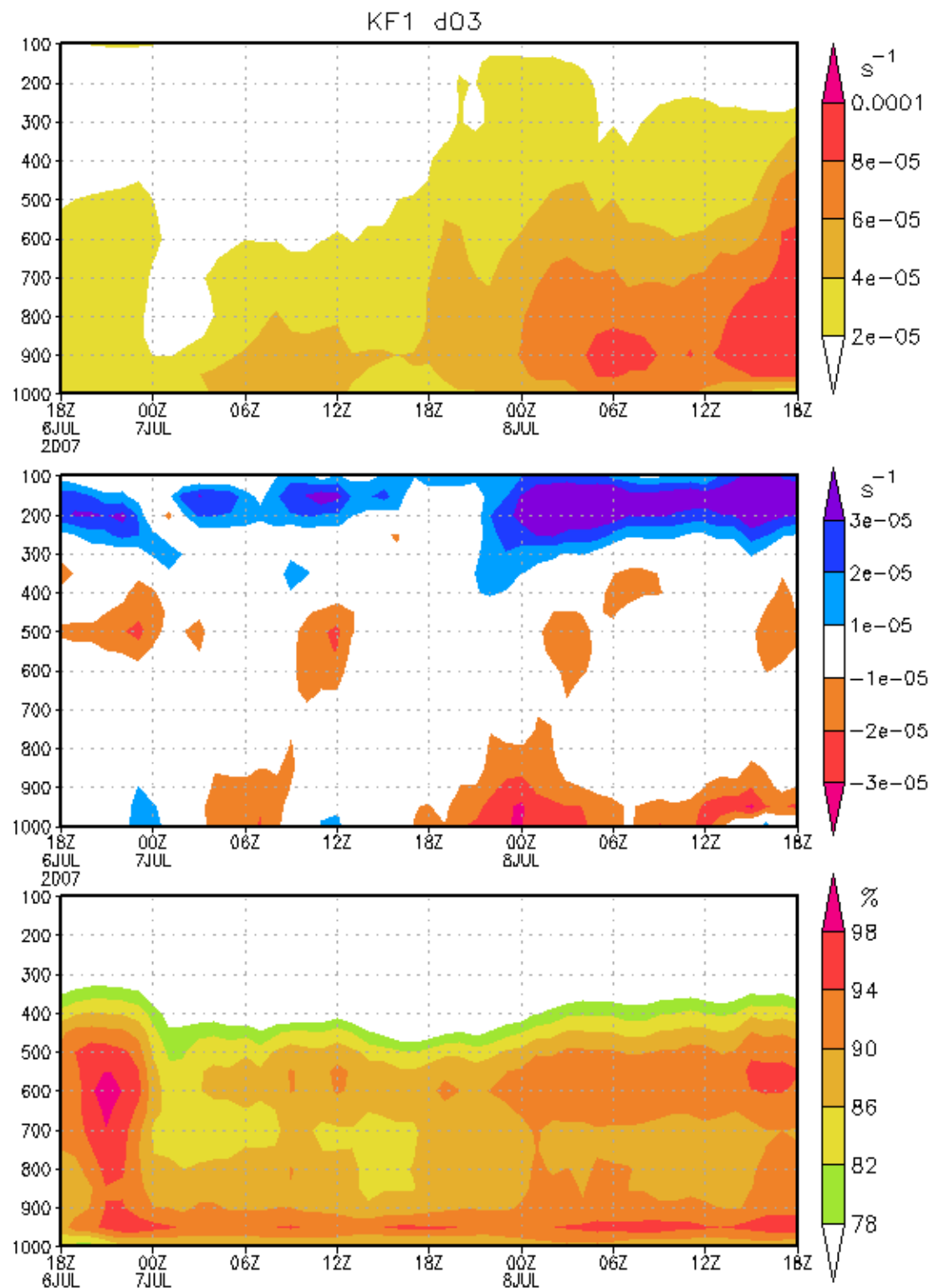


Figure 55. Time-height cross-section relative vorticity (s^{-1} , top), divergence (s^{-1} , middle), and relative humidity (%), bottom) averaged in a $3^\circ \times 3^\circ$ box centered on the sweet spot and moving with the parent wave.

b. The Evolution of Precipitation and VHTs

The evolution of precipitation from the KF1 innermost domain (d04) simulation is evaluated in this section. At the earliest time periods of the simulation (6–7 July), precipitation is present at all radii within the pouch (not shown). After 00Z 8 July, heavy precipitation begins to organize around the sweet spot. Figure 56 is a six-panel plot of 3-hour accumulated precipitation from the KF1 d04 simulation. At 03Z 8 July, there are bands of strong precipitation in the western and southern quadrants of the pouch at approximately 2° radius from the sweet spot. The areal extent of the precipitation decreases over the next six-hours and the precipitation moves closer to the sweet spot. By 15Z 8 July, heavy precipitation elements (> 24 mm) are present northwest and southeast of the sweet spot within the 1° radius. The heavy precipitation near the sweet spot continues through the final time period.

To assess the relative role of stratiform and convective precipitation within the wave pouch, a dynamically based precipitation type classification scheme (Montgomery et al. 2010a) is applied to the KF1 d04 simulation. This scheme is based on the work of Tao et al. (1993) and Braun et al. (2009), but is modified to include stricter thresholds to minimize the false classification of convection (Montgomery et al. 2010a). This methodology uses three different definitions to identify convective type precipitation: i) grid points with rain rates twice as large as their nearest four neighbors as identified as convective. In this case, the neighboring grid points are also identified as convective. ii) Grid points with a rain rate $> 25 \text{ mm h}^{-1}$ are identified as convective. iii) Grid points with upward vertical motion $> 5 \text{ m s}^{-1}$ or cloud liquid water below the melting level larger than 0.5 g kg^{-1} are identified as convective. This allows for identification of convective processes when rain is not reaching the surface. All other grid points with surface rain rate $> 0.1 \text{ mm h}^{-1}$ are identified as stratiform. Although this methodology is likely to overestimate the coverage of convective type precipitation, this study is interested in the qualitative evolution of the precipitation. For this purpose, the above methodology is adequate.

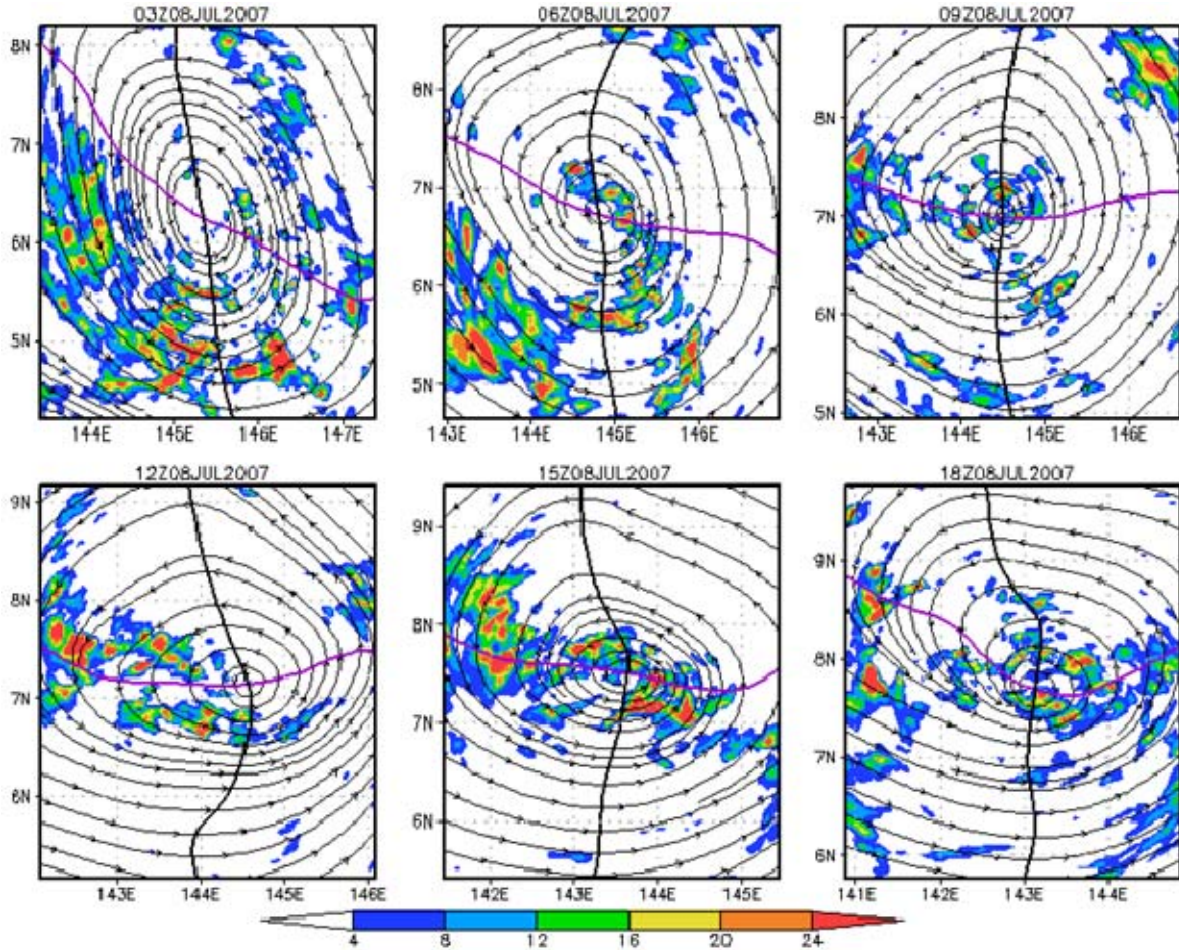


Figure 56. Three-hour accumulated precipitation (mm) from the KF1 d04 simulation overlaid with 850 hPa streamlines in the co-moving frame. The thick black line is the wave trough and the purple line is the critical latitude. The panels are valid at three-hour intervals beginning at 00Z 8 July.

Rain type distribution from the KF1 d04 simulation is presented in Figure 57 and Figure 58. Figure 57 is laid out as in Figure 56; the green shading represents stratiform type precipitation and red shading is convective. From 03Z–06Z 8 July, there is convective type rain surrounding the sweet spot and the maximum coverage of the stratiform rain type is located mainly in the west through southeast quadrants in the outer radii of the pouch (Figure 57). At 06Z 8 July, there is stratiform type coverage immediately over the sweet spot. Over the next six hours, convection is favored near the sweet spot and a majority of the stratiform coverage is at the outer radii of the pouch (Figure 57). By 15Z 8 July, convective coverage has surrounded the sweet spot and the

stratiform coverage is a maximum at the outer radii. This stratiform coverage maximum is concentrated to the west of the sweet spot. At 18Z 8 July, much of the convective coverage from three hours earlier has decreased and stratiform coverage dominates the lower half of the wave pouch.

Figure 58 is a Hovmoeller diagram of percent coverage of each precipitation type plotted by radius from the sweet spot. This presentation uses a five point running mean in order to eliminate short-term fluctuations in these data. There is a large area of stratiform precipitation coverage from 15Z–21Z 7 July located 2.5° – 5.0° from the sweet spot (Figure 58). There are weak convective maxima surrounding this stratiform maximum. At approximately 18Z 7 July, there are maxima in convective coverage within 0.5° and 1.0° – 2.0° of the sweet spot. A large area of stratiform coverage is located between 1.0° – 4.0° from the sweet spot from 00Z–12Z 8 July. Two large areas of convective coverage centered around 04Z and 13Z 8 July emerge within 0.5° radius of the sweet spot. These convective coverage maxima are followed by stratiform maxima within these inner radii. The Hovmoeller diagram indicates that the overall trend of the convective coverage is to grow in areal extent and move closer to the sweet spot towards the end of the model run. The stratiform precipitation maxima are generally at farther radii from the sweet spot throughout the simulation. The stratiform coverage maxima that occur close to the sweet spot towards the end of the simulation appear to follow convective maxima and are likely due to the demise of strong convection and the subsequent production of larger stratiform rain regions.

Figure 59 is used to evaluate the potential for VHTs within Typhoon Man-yi's wave pouch. It is a time series of 850 hPa relative vorticity (shaded) and upward vertical motion (contours, left) and surface equivalent potential temperature (θ_e , right) from the KF1 d04 simulation. All plots are overlaid with streamlines in the co-moving frame and the location of the wave trough (thick black line) and critical latitude (purple line).

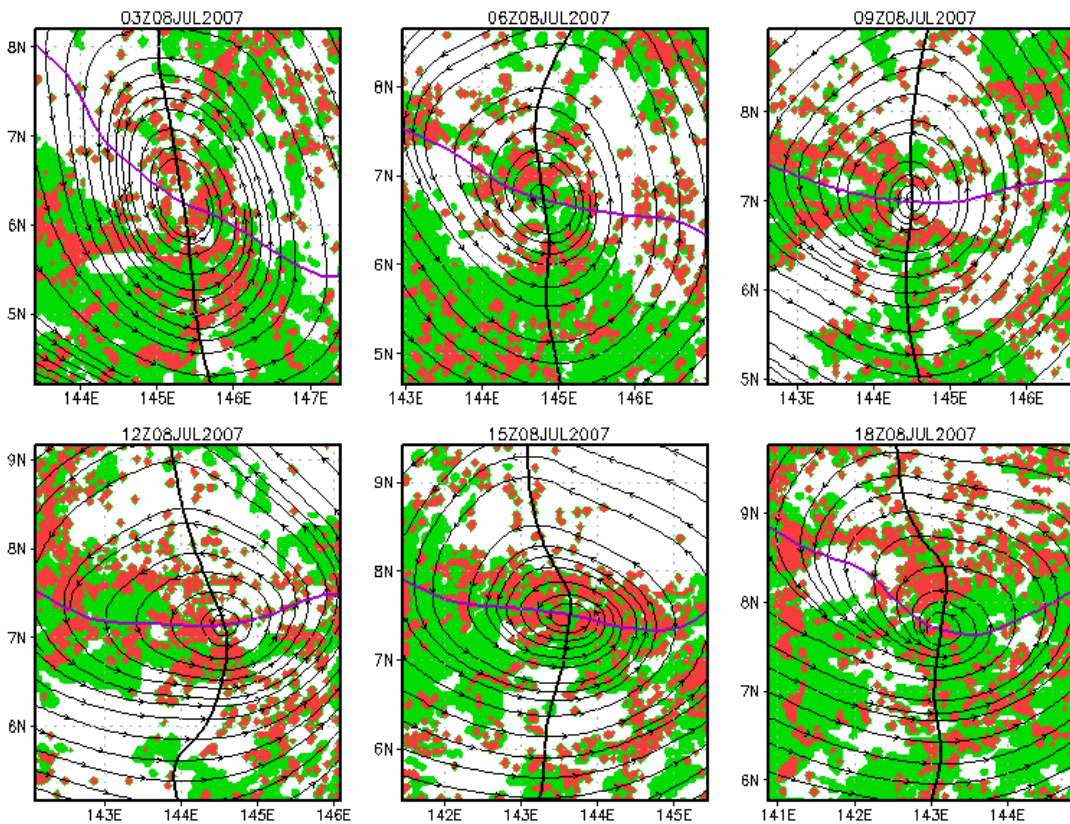


Figure 57. Precipitation type time series from the KF1 d04 simulation laid out as in Figure 56. Green shading represents stratiform pixels and red convective.

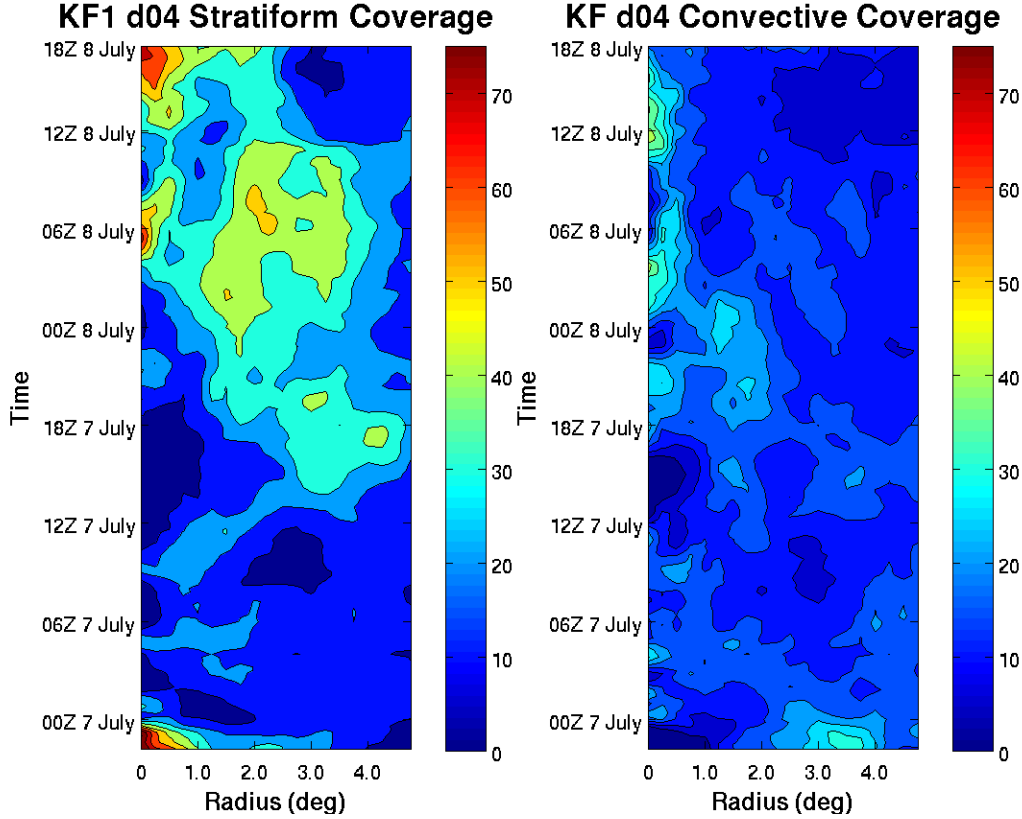


Figure 58. Percent coverage of stratiform (left) and convective (right) rain types plotted by radial distance from the sweet spot. The data are from the KF d04 simulation and are plotted with a five point running mean.

Figure 59 will be used as an example to show that multiple areas within Typhoon Man-yi's wave pouch contain VHTs (indicated by high values of near surface cyclonic vorticity coupled with upward vertical motion and high near surface θ_e) and that diabatic vortex merger and axisymmetrization are active near the sweet spot. Area A (Figure 59) is located to the east-northeast of the sweet spot and contains an intense low-level relative vorticity maximum (0.004 s^{-1}) accompanied by an updraft. A weaker cyclonic vortex (0.002 s^{-1}) is observed to its southwest. The second and third time snapshots (Figure 59) show that these two low-level vortices merge, resulting in a stronger low-level cyclonic vorticity signature (0.005 s^{-1}). Between 14:24Z–14:48Z 8 July additional diabatic vortex mergers occur in the same area, and although the low-level vorticity maximum does not intensify, the upward vertical motion increases to (5.5 m s^{-1}).

This succession of repeated diabatic mergers and axisymmetrization leads to an intense symmetric vortex in the lower troposphere in area A. Although events shown here occur east of the sweet spot, they occur within the Kelvin cat's eye circulation. These diabatic mergers continuously pre-conditioned the environment and the cumulative effects of these processes create an increasingly moist, vorticity-rich environment in the lower troposphere. This juxtaposition of factors creates favorable conditions for the continued building of a cyclonic vorticity monolith from the lower-levels.

Area B (Figure 59) identifies VHTs south and west of the sweet spot that fuse together over the first two time periods. By the third time period, a diabatic vortex has emerged at the center of the sweet spot. After vortex merger, the VHT reaches its maximum intensity in terms of both low-level vorticity (0.045 s^{-1}) and upward vertical motion (9.0 m s^{-1}). Over time, this vortex begins to weaken (0.003 s^{-1} vorticity maximum) and does not appear to become the vorticity monolith for the developing tropical cyclone. However, the sweet spot remains a favored region for the aggregation of diabatic vorticities and their vortical remnants as seen in area C (Figure 59). Figure 60 is akin to Figure 59 but for the last four time periods in the KF1 simulation. During this time there are multiple low-level relative vorticity maxima near the sweet spot. However, most do not have strong updrafts. The evolution of the VHTs and low-level cyclonic vorticity anomalies in the KF01 d04 simulation is consistent with the simulations conducted by Montgomery et al. (2006). In the Montgomery et al. (2006) simulations, mature VHTs consume much of the ambient CAPE from the environment. Once the VHTs have lost their convective signature, they leave behind remnant cyclonic vorticity anomalies in the lower troposphere. The KF1 d04 simulation shows that these cyclonic vorticity anomalies do eventually aggregate near the sweet spot and a relatively large, concentrated area of cyclonic relative vorticity develops by 17:48Z 8 July. Whether or not this eventually becomes Typhoon Man-yi's vorticity monolith is not examined further. However, the processes occurring in the KF1 simulation are consistent with "bottom-up" development.

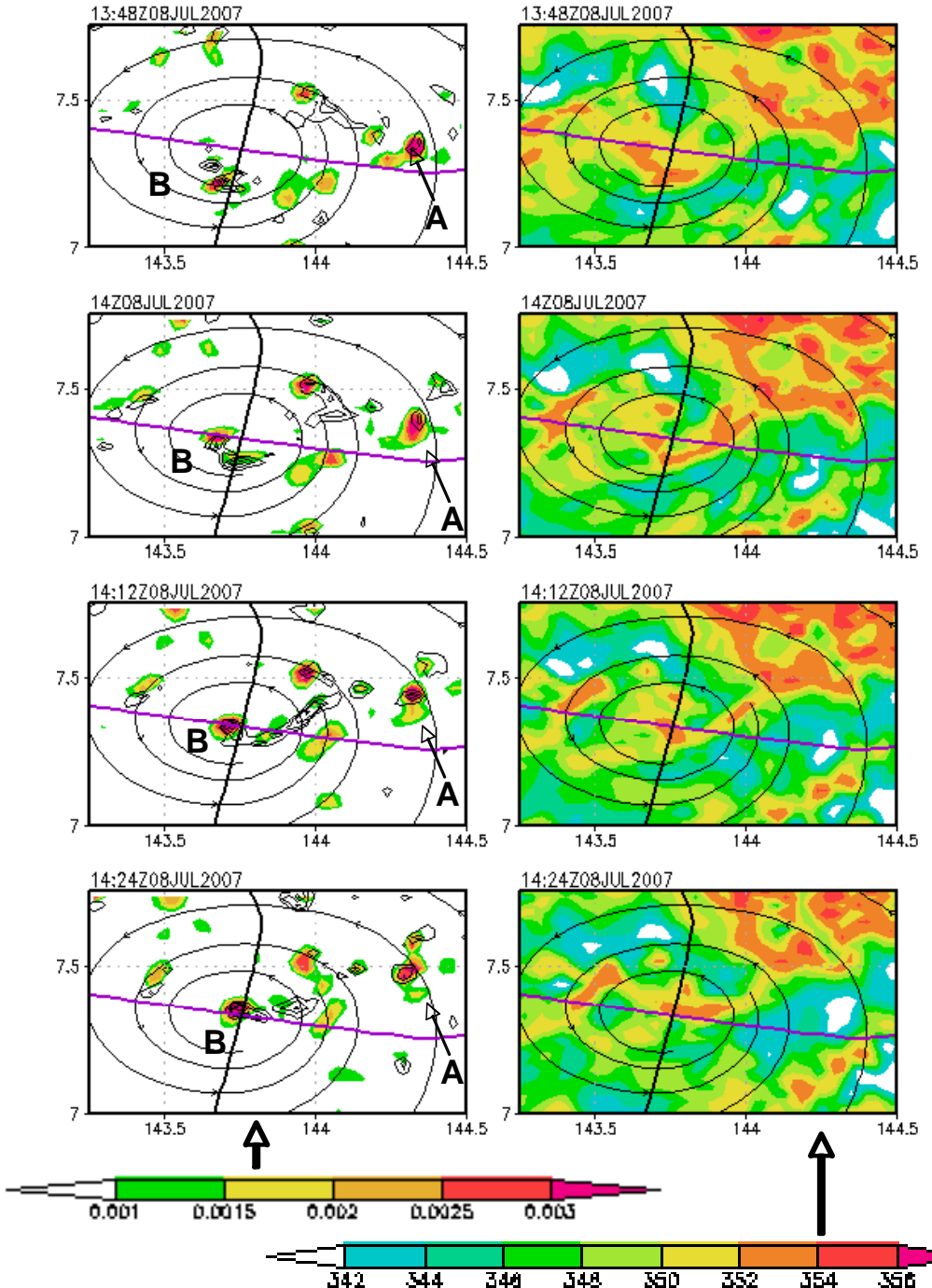


Figure 59. Time series of KF1 d04 850 hPa relative vorticity (s^{-1} , shaded) and upward vertical motion ($m s^{-1}$, black contours) are shown in the left column. Surface θ_e ($^{\circ}\text{K}$) is in the right column. Both columns are overlaid with streamlines in the co-moving frame. The thick black line is the wave trough and the purple line is the critical latitude. The time series is valid at 12 minute intervals from 13:48Z–15:12Z 8 July. Areas of interest are labeled A–C.

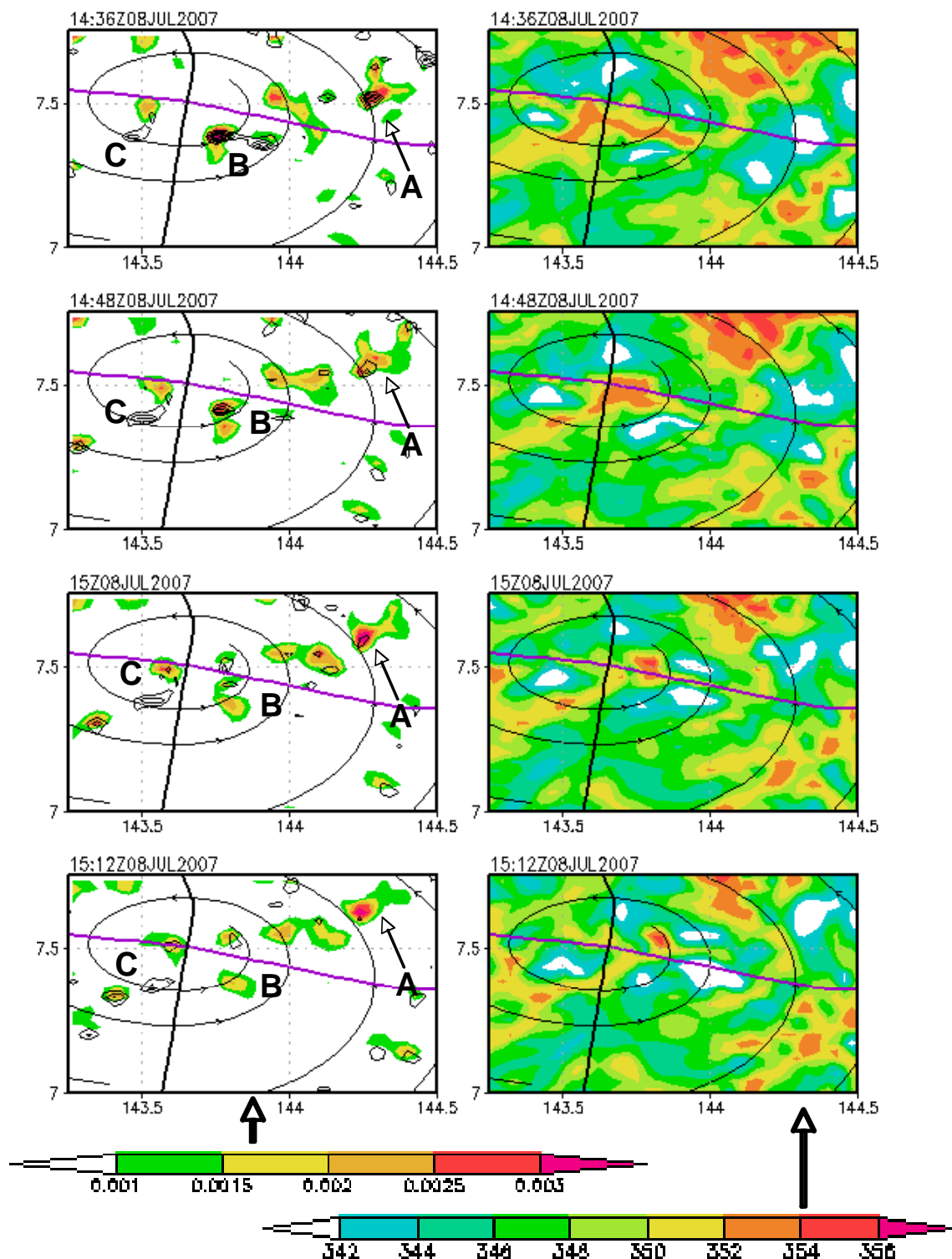


Figure 59. (Continued).

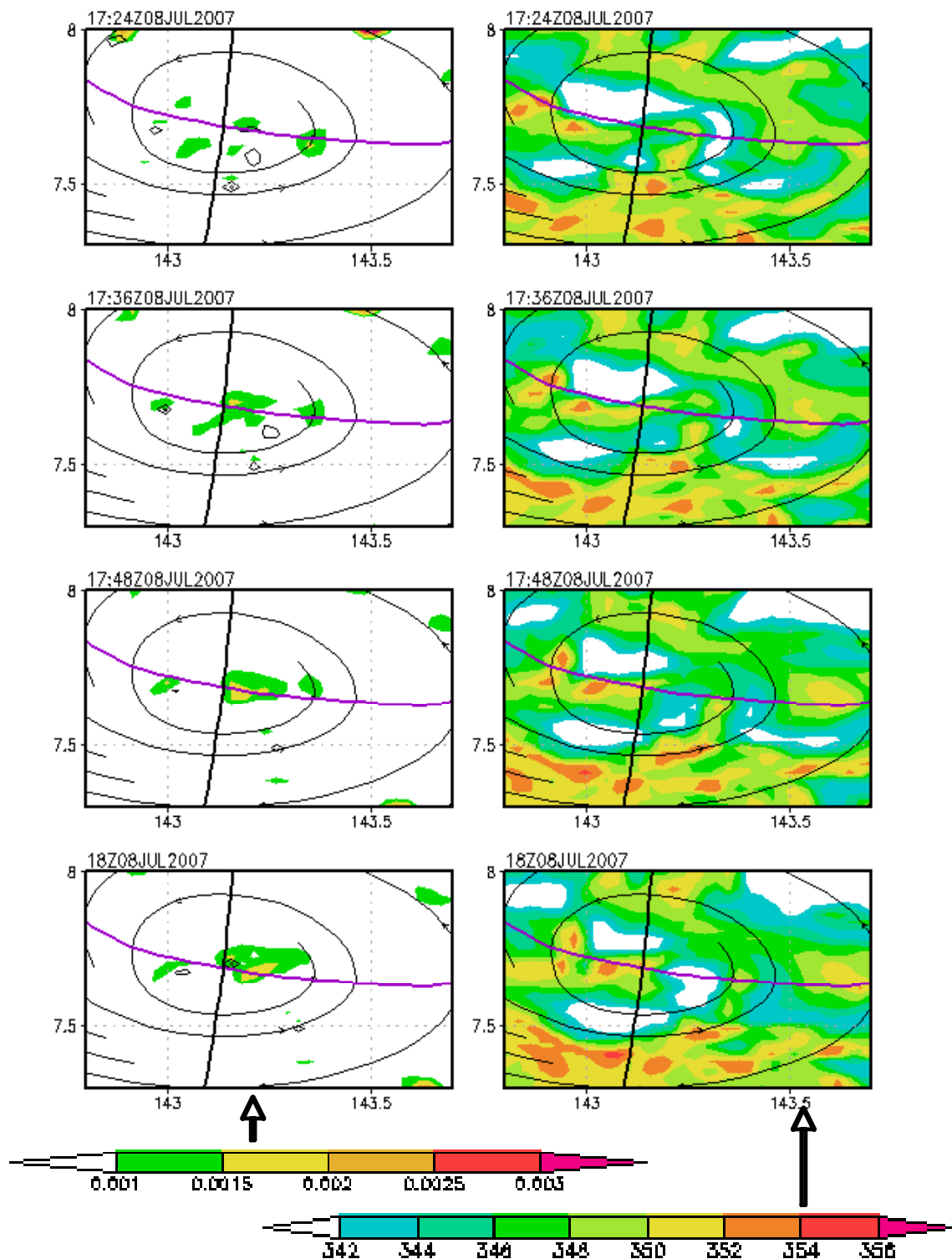


Figure 60. As in Figure 59 except valid 17:24Z–18:00Z 8 July.

4. Differences in Cyclone Evolution Between the Three Numerical Simulations

To evaluate the differences in the evolution of the meteorological features amongst the three simulations, a three panel time series of key meteorological variables is presented in Figure 61. It is clear that the BMJ simulation develops the strongest vortex and that the BMJ1 simulation develops a vortex of similar strength to the KF1. The top panel (minimum sea-level pressure) shows that the KF1 and BMJ1 simulations intensify the developing vortex at a similar rate over time. While the BMJ simulation initially intensifies the vortex at a similar rate as the other two simulations, the BMJ simulation deepens the storm more rapidly after 00Z 7 July. The maximum wind speed evolution is similar to the trends observed in the minimum sea-level pressure data. After 12Z 7 July, the BMJ simulation steadily increases the maximum 850 hPa wind speed until the end of the model run (28 m s^{-1}). These finding are consistent with the faster spin-up in the BMJ simulation discussed above. It is interesting to note that although a closed low-level cyclonic circulation is evident in the GFS FNL on 5 July, its intensification into a mesoscale tropical cyclone vortex is a slow process in the numerical simulations.

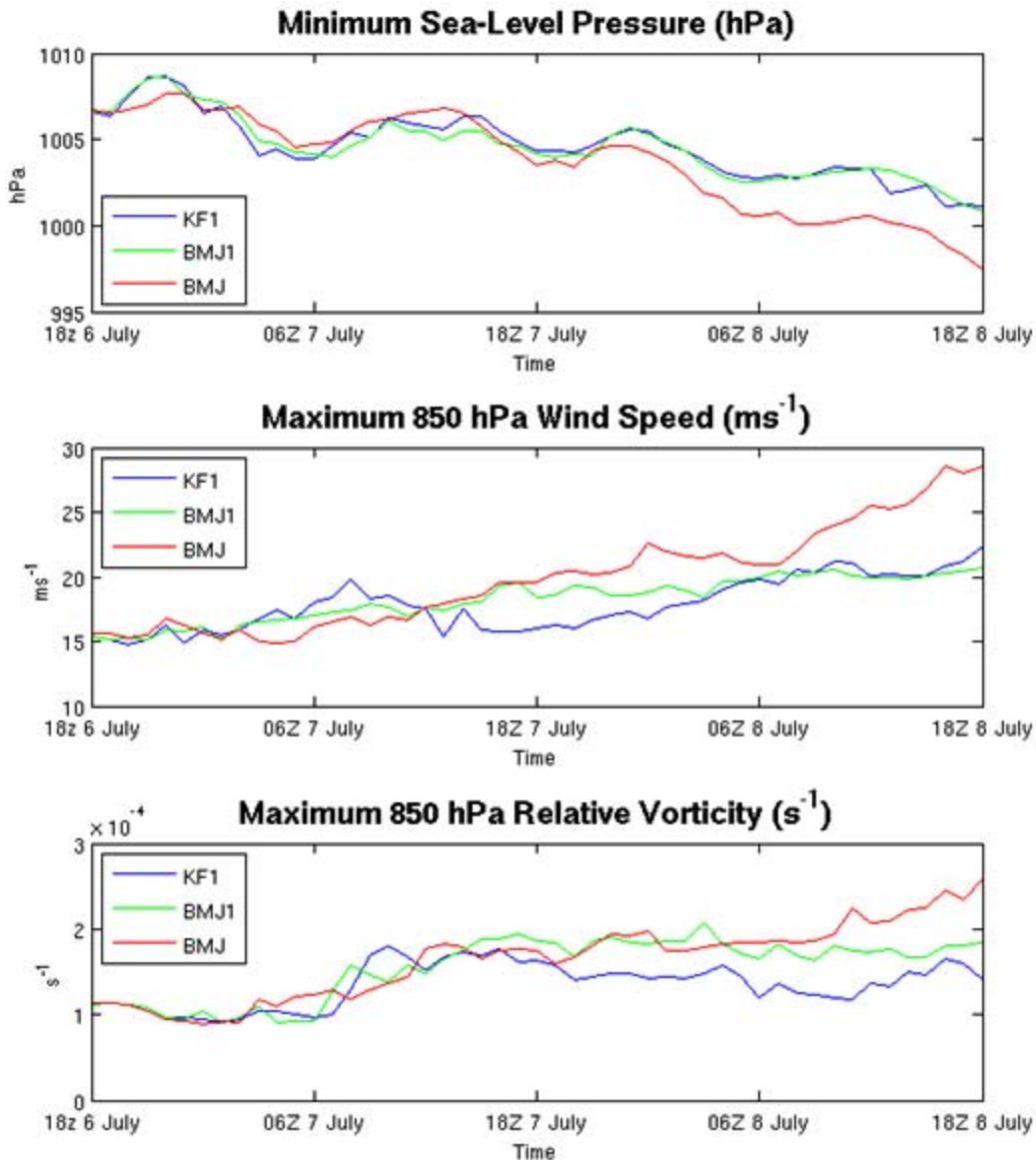


Figure 61. Time evolution of key meteorological variables for d01 of each simulation.

Examining these simulations more carefully, it is seen that despite variations in the position of the sweet spot and intensity of relative vorticity maxima among the three simulations, they each follow the tropical cyclogenesis sequence proposed by DMW09 on the synoptic and mesoscales. The best example of this is the BMJ simulation (Figure 62). While the geographical distribution of cyclonic vorticity maxima in this simulation is similar to the KF1 simulation (Figure 53), the intensity of the northern-most vorticity maximum (10.5N, 148.5E) in the BMJ simulation is stronger than in the other two

simulations at 06Z 7 July (Figure 62). Over time (18Z 7 July) the BMJ simulation intensifies both the northern positive vorticity anomaly (10N, 146E) and the positive vorticity anomaly to the east of the sweet spot (9N, 151E). This results in the BMJ having a sweet spot position farther north than the KF1 simulation. Despite the different geographical location of the sweet spot, over time the vorticity organizes around this location (Figure 62, bottom). This region proves to be the favored location for upscale organization of vorticity (H1) in all simulations, suggesting that the guiding hand principle (DMW09) is at work in each simulation.

Additionally, data from the BMJ and BMJ1 simulations indicate the presence of VHTs and shows that the vortex merger and axisymmetrization processes are favored near the sweet spot (not shown). This suggests that the “bottom-up” method is favored in all simulations. To further illustrate this point, the potential for “bottom-up” development is examined using the BMJ simulation. Using the BMJ d03 data, a series of vertical cross-sections through the cyclonic vorticity maxima in Figure 62 is examined. These plots are at three hour intervals beginning on 15Z 7 July and the latitude is fixed on, and moving with, the center of the growing vortex (located near the sweet spot) in Figure 62. At 15Z 7 July, the vorticity monolith is confined to the lower troposphere and is limited in vertical extent. During the second time period (18Z 7 July), the initial surface based positive relative vorticity maximum is accompanied by a relative vorticity maximum at 750 hPa north of the building vorticity monolith. By 21Z 7 July, the low-level vorticity monolith is intensifying and building through the mid-troposphere. The intensification of the vorticity monolith is not linear with time. However, a strong vorticity monolith has built throughout the mid troposphere by 03Z 8 July. Since the initial vortex began near the surface and there is no evidence of a mid-level circulation burrowing down to the surface, this supports the hypothesized “bottom-up” interpretation of tropical cyclogenesis. The BMJ simulation is consistent with the diabatic vortex merger and axisymmetrization processes that are associated with the “bottom-up” route.

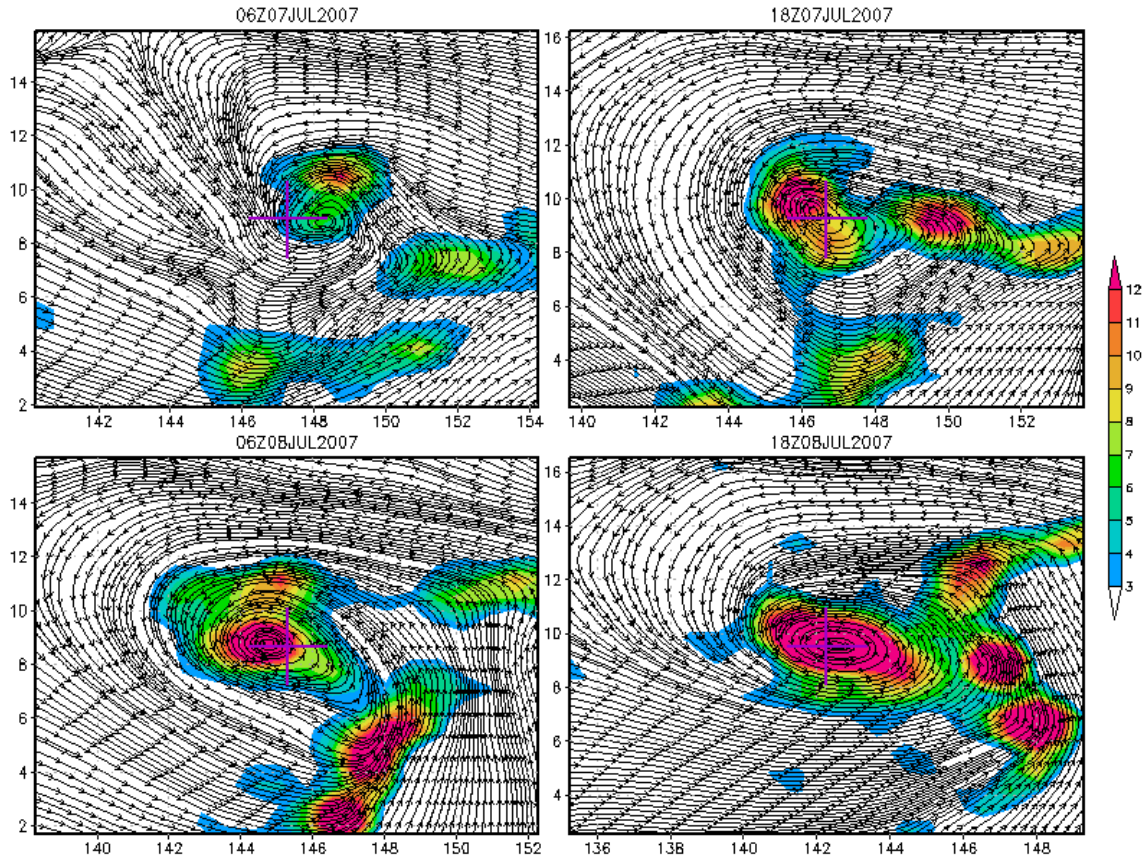


Figure 62. 850 hPa streamlines (co-moving) and relative vorticity ($\times 10^5 \text{ s}^{-1}$, shaded) from the BMJ d01 simulation valid at 12-hour intervals beginning at 06Z 7 July. The purple plus sign indicates the location of the sweet spot.

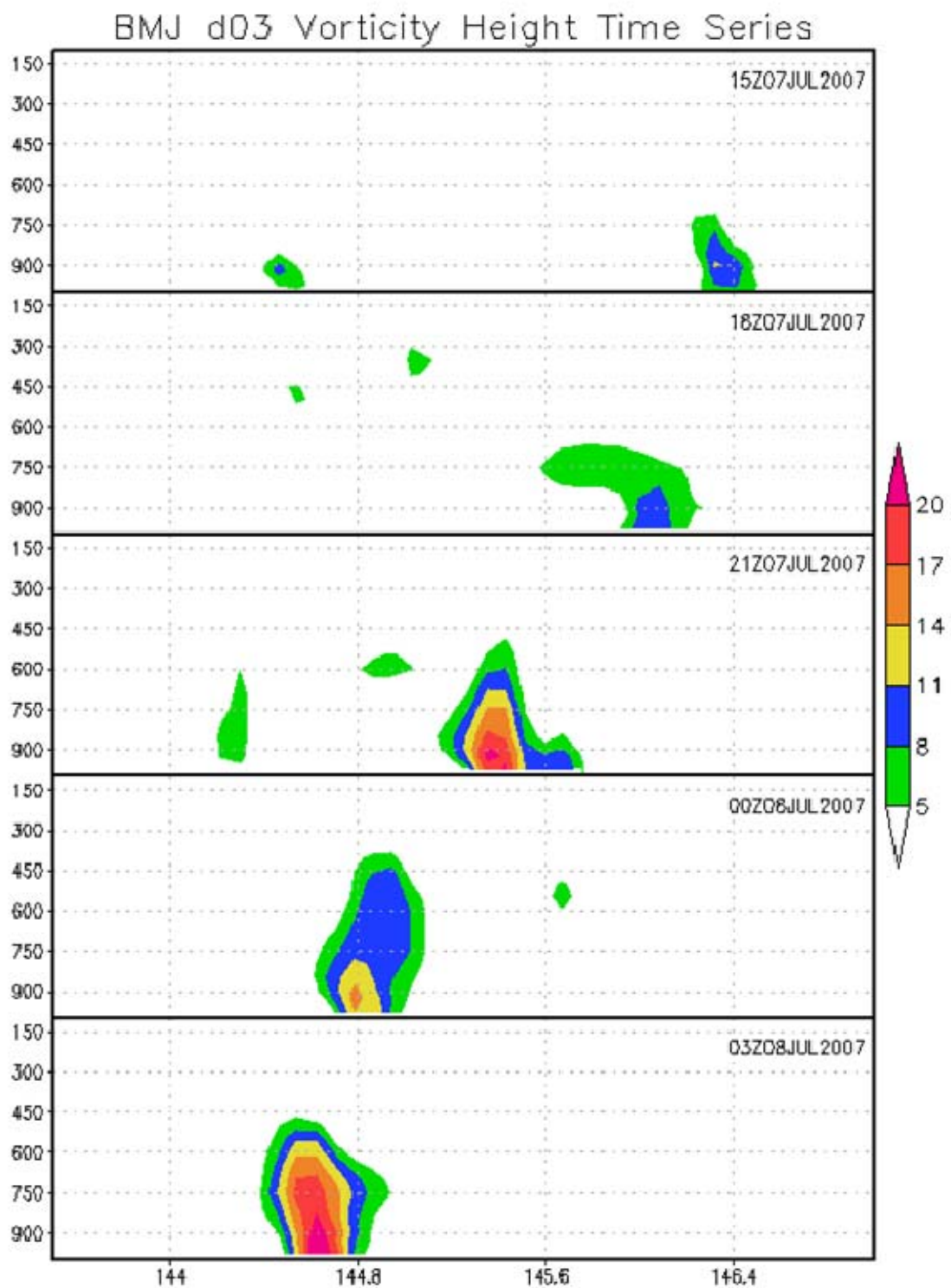


Figure 63. Cross-sections of relative vorticity ($\times 10^{-4} \text{ s}^{-1}$) from the BMJ d03 simulation centered on the latitude of the building vorticity monolith. Plots are every three hours beginning at 15Z 7 July.

D. SUMMARY

Chapter V uses observations and analyses to document the existence of an ER wave and suggest its role in the tropical cyclogenesis sequence of Typhoon Man-yi. The GFS FNL indicates that direct interaction between the Northern Hemisphere ER low and a monsoon trough to its west leads to the formation of an equatorial depression near 4N, 149E at 12Z 5 July. Chapter V uses also the GFS FNL to examine the applicability of the new tropical cyclogenesis model (DMW09) to this tropical cyclogenesis case on the synoptic and meso- α scales. This chapter uses high-resolution WRF simulations to examine mesoscale aspects of the transition of an equatorial depression to a tropical cyclone. These simulations support the hypothesis that the “bottom-up” pathway to tropical cyclogenesis is favored within the critical layer of a developing equatorial depression in the Typhoon Man-yi case.

A small ensemble of high-resolution WRF simulations is used to examine the mesoscale evolution of the Typhoon Man-yi’s critical layer into a tropical cyclone vortex. The simulations use GFS FNL for the initial conditions, have 28 vertical levels, and horizontal domains of 81, 27, 9, and 3 km. The simulations begin at 18Z 6 July and are integrated forward 48 hours. Sensitivity tests are conducted by using different convective parameterization schemes on the outer domains (Kain-Fritsch vs. Betts-Janic-Miller) and differing microphysics (ice vs. warm rain). There are distinct differences between the three simulations at the synoptic and meso- α scales, that are likely attributed to the differing microphysics schemes, as: i) the BMJ warm rain simulation develops a more intense vortex at a faster rate than the two simulations with ice microphysics,³² ii) the BMJ simulation favors the intensification of a meso- α scale vorticity maximum in the northern quadrant of the wave pouch. In the KF1 simulation, the vorticity amplification occurs in the southern quadrant of the wave pouch. Finally, iii) the latitudinal difference of the sweet spot between the three simulations is 2° by 18Z 8 July, with the BMJ scheme farthest north and the KF1 scheme farthest south. Despite differences in sweet spot

³² In the BMJ simulation, northern vorticity maximum continues to intensify throughout the duration of the simulation (as opposed to the KF1, BMJ1, and GFS FNL). This multi-scale interaction likely contributed to the more northerly location of the critical latitude and thus the sweet spot.

position and intensity of the meso- α scale cyclonic vorticity anomalies within the ER wave’s pouch, the pathway to tropical cyclogenesis within the critical layer of easterly waves proposed by DMW09 generally held true in each simulations as vorticity organization eventually occurs around the sweet spot. This is despite differences in model physics and cumulus parameterizations among the three simulations.

Analysis of the data from the near-cloud resolving inner-most domains of the three model simulations indicate the occurrence of processes that support “bottom-up” type development as: i) VHTs are abundant near the sweet spot, and ii) diabatic vortex merger and axisymmetrization of the VHTs and their vortical remnants are prominent within the Kelvin cat’s eye circulation. In addition to these findings, none of the simulations indicates the presence of a prominent mid-level MCV within the wave pouch prior to low-level spin-up. It could be argued that mesoscale organization into a tropical cyclone has not occurred by the end of the KF1 and BMJ1 simulations even though the large-scale equatorial depression was already declared a TD by JTWC. However, the KF1 and BMJ1 simulations show concentrated cyclonic relative vorticity near the sweet spot by the end of the simulations (18Z 8 July). Given a longer model integration time, it stands to reason that the processes described in Section C would have likely led to the development of a stronger vorticity monolith (i.e., tropical storm) on the sub-synoptic scales.

THIS PAGE INTENTIONALLY LEFT BLANK

VII. CONCLUSIONS AND FUTURE WORK

A. CONCLUSIONS

The work presented herein uses in-situ and remote sensing observations, analyses data, operational global models, and high-resolution numerical simulations to present a multi-scale analysis of tropical cyclogenesis within the critical layer of easterly waves. Several interrelated studies are undertaken to advance the understanding of the recently proposed tropical cyclogenesis sequence (DMW09).

The first study is an initial evaluation of the temporal and spatial evolution of precipitation and latent heat distribution within the pouch of the 55 developing tropical cyclones. Composite pouches are created using 355 TRMM TMI and 227 TRMM PR passes. Although the spatial patterns of the TRMM TMI rain rate distribution and the TRMM PR data may be subject to errors due to the small and non-uniform sampling, the author believes this to be a valid first look at the evolution of precipitation and latent heating within the pouch of developing easterly waves. Results from the TRMM TMI data indicate that convective precipitation is favored near the center of the Kelvin cat's eye circulation and that the intensity and areal extent of this convection increases with time and organizes around the sweet spot as genesis nears. While both CRR and STRR increase from T3 to T1, CRR becomes increasingly dominant and is the major contributor to the total SRR. Initial results also reveal asymmetries in the SRR and CRR maxima at the T1 time period in the west-southwest and northeast quadrants of the pouch. Tests of the sensitivity of these organized precipitation structures to errors in pouch location arising from zonal phase speed estimation errors confirm the robustness of these organized structures migrating toward the sweet spot as genesis nears.

Initial results from the TRMM PR data indicate that the temporal and spatial evolution of CRR within the composite pouches is qualitatively similar to the TRMM TMI results. The TRMM PR data indicate a CRR maximum at 0.75° radius from the sweet spot six hours prior to genesis. However, from T-06–T-00 the STRR intensity is

greater than CRR intensity within 1.5° of the sweet spot. The TRMM PR also allows an evaluation of the areal coverage of precipitation within the composite pouch. These data show that the areal coverage of precipitation within is dominated by stratiform and anvil type precipitation at all time periods and radii. Maxima in areal coverage of convective type precipitation occur within the innermost 1.5° of the composite pouches between T–30 and T–06. Latent heating profiles are constructed for each time period using the TRMM PR 2B31 data. These profiles indicate a convective type heating profile with heating throughout the entire depth of the troposphere. A low-level heating maximum occurs from 3.5–4.5 km during all time periods. The TRMM observations are consistent with and verify many of the concepts presented in DMW09 including the preference for convection to organize around the sweet spot as genesis nears. These initial findings suggest “bottom-up” development as: i) the convective heating profile is favorable for column moistening and thus “bottom-up” development, and ii) low-level PV generation is favored because of the lower tropospheric heating maximum.

The second and third studies show that the dynamical pathway for tropical cyclogenesis within the critical layer of easterly waves first proposed by DMW09 is applicable in the western North Pacific basin and for different types of precursor wave disturbances.

The first case, Typhoon Nuri (2008) formed from an easterly wave precursor during the TCS-08 field campaign. Prior to tropical cyclogenesis, real-time marsupial forecasts were produced that accurately predicted the potential genesis location of the storm and were used for the planning of aircraft research missions. During the first joint USAF C130/NRL P3 flight (16 August) in-situ aircraft observations confirmed the presence of an easterly wave, which made this case an ideal candidate to test the new tropical cyclogenesis model. Post analysis of observations and analyses suggest strong consistency with H1-H3 from DMW09 at the synoptic and meso- α scales during Typhoon Nuri’s tropical cyclogenesis sequence. Specifically, i) deep convection, despite beginning in the southern quadrant of the pouch, remains largely within the pouch and becomes organized around the sweet spot as genesis nears (H1), ii) The dominant low-level circulation that emerges as Typhoon Nuri is located within the highly vortical

region of the wave's cat's eye circulation near the intersection of the wave trough and the critical latitude (H1), iii) CIMMS TPW analyses show that the dry air surrounding the pouch moves in approximately the same background flow as the moist air within. Despite surrounding it on three sides, little if any of this air appears to enter the pouch (H2). iv) Whereas strong environmental vertical wind shear $>21 \text{ m s}^{-1}$ ($>40 \text{ kt}$) may have temporarily decreased the resilience of the pouch and temporarily stalled genesis, the critical layer evidently remains resilient enough to keep the proto-vortex intact until it is able to enter a more favorable environment (H2). v) The tracking of the parent easterly wave disturbance for 10 days and the maintenance of its structure as it propagates through a hostile environment are consistent with H3.

The second case uses observations and analyses to test the hypothesize role an $n=1$ ER wave plays in the genesis sequence of Typhoon Man-yi (2007) on the synoptic and meso- α scales. Observational evidence is presented that identifies the surface reflection of the ER wave at times from 3–6 July and it is argued that the ER wave plays a key role in tropical cyclogenesis. In the GFS FNL the ER wave interaction with a monsoon trough directly leads to the formation of an equatorial depression. It is argued that without the presence of the ER wave, the equatorial depression and tropical cyclone would not have formed on the time scales observed.

Using the GFS FNL, an interpretive analysis is performed on the synoptic and meso- α scales. These analyses indicate that the proto-vortex that became Typhoon Man-yi originated within the ER wave and can be tracked coherently from 3 July until TS declaration occurs. Although multiple meso- α scale vorticity maxima intensify and weaken over time within the wave pouch, the vorticity organization and amplification eventually occurs at the intersection of the wave trough and critical latitude (H1). Additionally, the ER wave/equatorial depression provides a wave pouch for the proto-vortex to amplify in until it strengthens into a self-sustaining entity (H2). Finally, the hybrid wave-vortex system propagates together and amplifies for 5+ days, suggesting H3.

In addition to these data, three high-resolution WRF numerical simulations are carried out to explore the hypothesized transformation of an $n=1$ ER wave critical layer to a mesoscale tropical cyclone. At the synoptic and meso- α scales, these simulations show that despite differences in geographic location of formation and intensity of the vortex among the three simulations, the dynamical pathway to tropical cyclogenesis within the critical layer of easterly waves proposed by DMW09 generally holds true. This is despite differences in model physics and cumulus parameterizations. Having established the plausibility of the new tropical cyclogenesis sequence in these simulations, these data are then used to study the mesoscale aspects of the transition of the wave pouch to a mesoscale vortex.

On the meso- β and meso- γ scales, analysis of the data from the near-cloud resolving simulations indicate processes that support the “bottom-up” pathway to tropical cyclogenesis in all simulations. Specifically: i) VHTs are favored near the intersection of the wave trough and critical latitude, and ii) vortex merger and axisymmetrization of VHTs and their highly vortical remnants are favored within the Kelvin cat’s eye circulation. In addition to these findings, none of the three simulations indicates the presence of a pronounced mid-level MCV within the Kelvin cat’s eye circulation prior to low-level spin-up. These numerical simulations support the idea that the “bottom-up” pathway to tropical cyclogenesis is favored within the critical layer of a developing easterly wave in the Typhoon Man-yi genesis sequence.

B. FUTURE WORK

While the author believes that this work has made substantial strides in advancing the notion of the new tropical cyclogenesis model to cases in the western North Pacific basin, there remains much work to be done. First, continued examination of the mesoscale transition of Typhoon Nuri is underway. This analysis will use additional remote sensing platforms including the Guam Doppler radar, TRMM and other microwave satellites, and the NRL P3 ELDORA radar to identify the structure and evolution of precipitation and the three-dimensional wind field within the critical layer of the pre-Nuri disturbance. Second, a more in-depth analysis of the pouch exchange/pouch

merger concepts seen in the tropical cyclogenesis sequence of Typhoon Man-yi needs to be accomplished. Based on my recent survey with other group members, this pathway to tropical cyclogenesis appears prominent in the western North Pacific basin. Specific examples include recent formations such as Typhoon Fengshen (2008) and Typhoon Rammasun (2008) where initial analysis appears to suggest a similar genesis sequence. Third, more cases, including those observed during TCS-08, need to be examined in order to more thoroughly test the relevancy of the new tropical cyclone model in the western North Pacific basin.

Additionally, the concept of pouch resiliency to vertical wind shear needs to be more thoroughly examined. Although the author presented some evidence that supports the resiliency of the pouch to vertical wind shear in the case of Typhoon Nuri, a more in-depth analysis needs to be performed. This will provide an understanding of the evolution of the wave pouch in regions of strong vertical wind shear. Finally, the evolution of precipitation and latent heating within the pouch needs to be more thoroughly understood. More genesis cases need to be added to the data set used in Chapter III and Appendix B. Additional cases will help overcome the noted undersampling of the composite pouches and in order to draw definitive conclusions on the latent heating profiles and distribution of convection and stratiform precipitation within the pouch of developing tropical waves in the Atlantic, east Pacific, and western North Pacific sectors.

THIS PAGE INTENTIONALLY LEFT BLANK

APPENDIX A: GLOSSARY

Bottom-up model: A sequence of events that describes the transition of a synoptic-scale depression into a mesoscale tropical cyclone vortex that places emphasis on the lower-levels to build the tropical cyclone vortex up through the troposphere (DMW09). This model focuses on the role of active deep convective cells embedded in a preexisting depression (Houze et al. 2009). In this vorticity rich environment, the strong updrafts of these convective cells develop vertical vorticity anomalies (Houze et al. 2009). These so-called VHTs are viewed as the building blocks of the tropical cyclone strength vortex (Houze 2009).

Critical latitude: In linear wave theory, if one considers a wave propagating in a background sheared flow, the critical line (or latitude) is the locus of points where the phase speed of the wave is equal to the background flow.

Critical layer: The region surrounding a nonlinear wave's critical latitude (DMW09).

Co-moving frame: A frame of reference translating horizontally at the velocity of the parent wave or proto-vortex (DMW09). Unless the phase speed of the wave is zero, the flow pattern in the co-moving and resting (or earth relative frame) will be different.

Dividing streamline: In steady 2D flow, the streamline that runs through a nearby saddle point (DMW09).

Equatorial depression: A synoptic-scale cyclonic circulation that forms near the equator. It is a generalized term that is not tied to the region the depression forms in, or the precursor mechanism that leads to its formation.

Kelvin cat's eye: In geophysical fluid dynamics, an area of closed circulation in which particles are trapped and recirculate, rather than being removed from the flow by the environmental shear (DMW09). It is located within the parent wave's critical layer.

Marsupial paradigm/sequence: A term introduced in DMW09 to describe the transition of a hybrid Rossby wave/vortex into a tropical cyclone. The sequence describes the transition of the synoptic-scale wave into a tropical cyclone as it undergoes the processes described in DMW09's three hypotheses (H1-H3, summarized in Chapter I).

Okubo-Weiss: A measure of the shape-preserving component of the flow as opposed to shear and stretching, which destroy the shape of the flow (DMW09). It is considered a more robust indicator of genesis potential than vorticity because it removes the contribution of shearing deformation that destroys potential genesis regions (DMW09).

Proto-vortex: The initial mesoscale vortical structure within a hybrid diabatic Rossby wave-vortex (DMW09). It is hypothesized (DMW09) that the proto-vortex is protected by the wave pouch and, given the right conditions, has the potential to grow into a tropical cyclone strength vortex.

Sweet spot: The intersection of the wave trough and the critical latitude (DMW09). This area has been shown to be the favored area for upscale aggregation of vorticity and the favored location for tropical cyclogenesis (DMW09).

Top-down model: In the traditional interpretation, this model relies on one or more MCVs located in the stratiform rain region of a synoptic-scale depression act to reinforce the depression (Houze et al. 2009). The mid-level vortex must then burrow down to the surface via increased Rossby penetration depth, advective process, or some other mechanism to initiate the low-level cyclonic circulation required for tropical cyclogenesis (Houze et al. 2009).

Vortical Hot Tower: Deep moist convective clouds that rotate and/or contain updrafts that rotate in a helical nature (DMW09).

Wave pouch: The flow bounded by the closed streamline that passes through the stagnation point closest to the sweet spot (DMW09).

APPENDIX B: ADDITIONAL FINDINGS FROM THE TRMM DATA DISTRIBUTION AND INITIAL RESULTS FROM THE TRMM PR PRECIPITATION OBSERVATIONS

This appendix accompanies Chapter III and will present additional information on the TRMM TMI data distribution and evolution of precipitation. Additionally, initial results from the TRMM PR analysis are presented herein.

A. THE DISTRIBUTION OF TRMM 2A12 DATA

Figure 64 is a contour plot of the total number of TRMM TMI retrievals in each bin for the composite pouches used in this study. If these data are evenly distributed throughout the composite pouches, there would be concentric contours of increasing pixel count as radius increases (due to the increase in size of bins). The biases discussed in Chapter III are apparent in this figure. These biases, especially in the latter two time periods are minor and the data are fairly equally distributed within each composite pouch. This, along with the fact that there are on the order of 300,000 samples in each composite leads the author to believe that this sample is adequate to provide a first look at the TRMM TMI precipitation distribution within the pouch of developing easterly waves. It is noted that the design of the experiment leads to the under-sampling on the eastern edge of the pouch that cannot be overcome regardless of sample size. Due to the westward movement of the parent wave, the eastern portion of the pouch will always move off land last. Therefore, even if there is an even geographic distribution of samples, the omission of rain rate data over land would still result in a low bias to the east. While this has the largest impact on T3, it is still evident in the other two time periods due to formation events close to Africa or Central America. If the total number of TRMM passes is large enough, this bias could be eliminated by removing all data from any passes where any part of the pouch was over land or using TRMM PR data as these retrievals are valid over land.

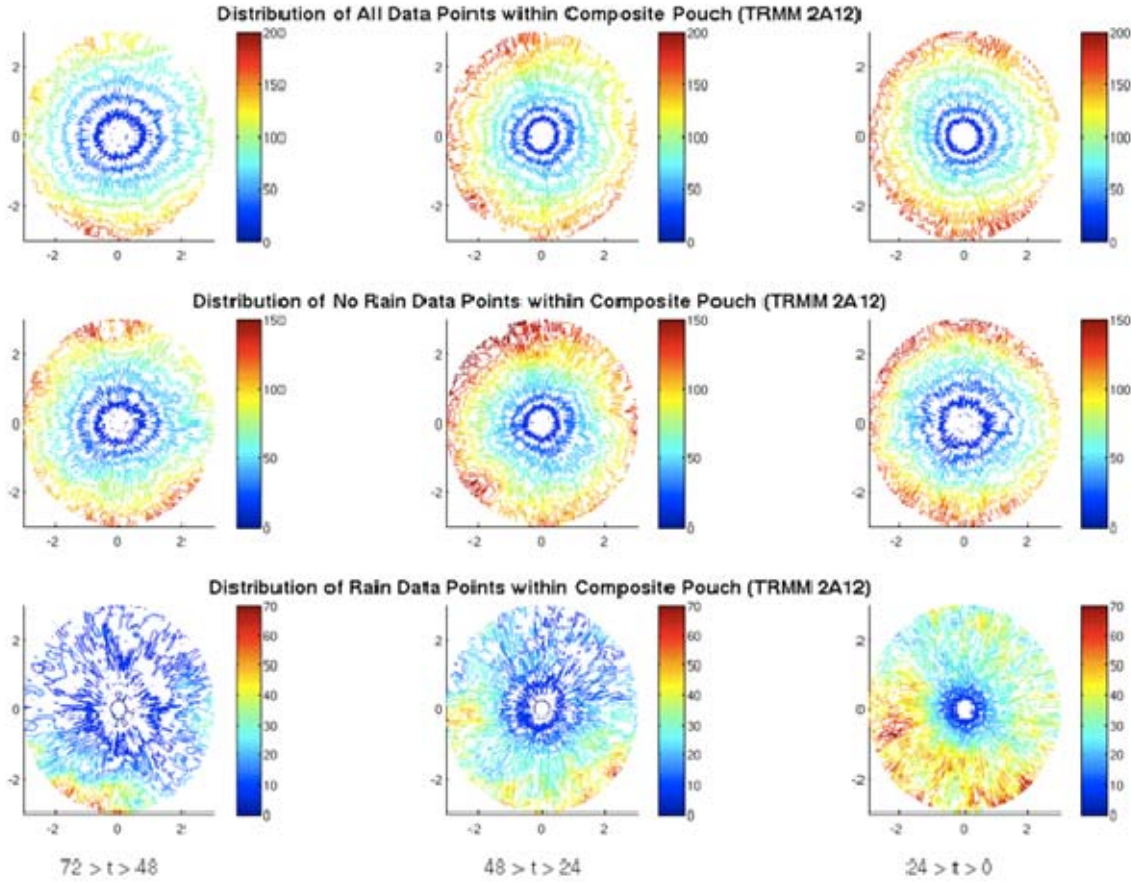


Figure 64. Contour plot of number of TRMM TMI retrievals in each bin for the composite pouches by time (columns) and type (rows).

Figure 65 is a 9-panel plot of TRMM 2A12 pixel distribution normalized by annulus area. These data are contoured as a deviation from the mean number of area normalized pixels. Warm colors represent sampling greater than the mean and cool colors are areas that are under-sampled when compared to the mean. These data provide a closer look at the biases mentioned above and insight into the areal coverage of precipitation and its evolution over time. The under-sampling on the eastern side of the composite pouches at each time period is evident in these plots (top row). Note also that over-sampling does not necessarily equate to increases in precipitation sampling (or higher rain rates). For example, both the T3 and T2 bins exhibit overall sampling maxima to the northwest, yet these areas did not coincide with rainfall maxima (Figure 10). Note that the SRR maximum to the northeast of the sweet spot in the T1 time period

is in an under-sampled area. This area is also at or below the mean in number of precipitation samples. These data serve as a proxy for the areal coverage of precipitation and its evolution with time. The most interesting aspect of this analysis occurs at the T1 time period. During this period, the no rain sampling maximum is at the outermost radii for all azimuths (Figure 65). This maximum is surrounded by a no rain sampling minimum near the sweet spot. The areal coverage of the precipitation sampling at this time exhibits the opposite pattern, with minima at the outermost radii surrounding a maximum near the sweet spot. These data suggest that the areal coverage of precipitation is increasing near the sweet spot as genesis nears.

Figure 66 displays area normalized sampling data as in Figure 65, but the contours depict the number of standard deviations each binned sample is from the mean. While the same pattern of sampling is evident in this figure, there are key points that can be drawn from this analysis. First, note that in the total pixel sampling, almost all of the bins are within two standard deviations of the mean at all time periods. The main exceptions are the over-sampling in the south-southwest quadrant of the pouch at T3 and the under-sampling in the northeast quadrant of the pouch in the T2 time period. The over-sampling in the T3 time period is reflected in the number of rain pixel sampling. Second, at the T1 time, all bins are within two standard deviations of the mean except for a small area 1.5° south of the sweet spot position. Although these data are not perfect, this analysis provides additional confidence in the robustness of the results presented in Chapter III and this appendix.

Figure 67 (top) is a plot of TRMM TMI retrieval counts by radius and time and Figure 67 (bottom) is the same data normalized by annulus area. In Figure 67 (top) the cyan line represents the area of each annulus. If the pouch is well-sampled, the slope of the TRMM TMI sample count lines would be equivalent to the slope of the annulus line. Upon visual inspection, T3 does not meet this criterion, while the results for T1 and T2 are not as obvious. Figure 67 (bottom) confirms that the T3 time period is not well-sampled, while the results at T2 and T1 exhibit sampling deficiencies at the outermost radii. Two-way analysis of variance (ANOVA) is performed on each of the three time composites to test if these data are evenly distributed within each bin in both the radial

and azimuthal dimensions. ANOVA is a higher dimensional application of the two sample T-test that tests whether or not the means of multiple samples are equal. Results of this test in the radial dimension indicate that the author is unable to reject the null hypothesis that the sample means are equal at the $\alpha=0.05$ significance level out to a 2.5° radius for both T2 and T1 (and out to a 0.75° radius for T3). For the azimuthal direction, the null hypothesis that the sample means are equal at the $\alpha=0.05$ significance level for all time periods is rejected. This suggests that the annuli are well-sampled in the radial dimension at T1 and T2 (out to 2.5°). Because the null hypothesis is rejected, in the azimuthal direction, it is not clear whether the geographic distribution of the precipitation shown in Chapter III is robust.

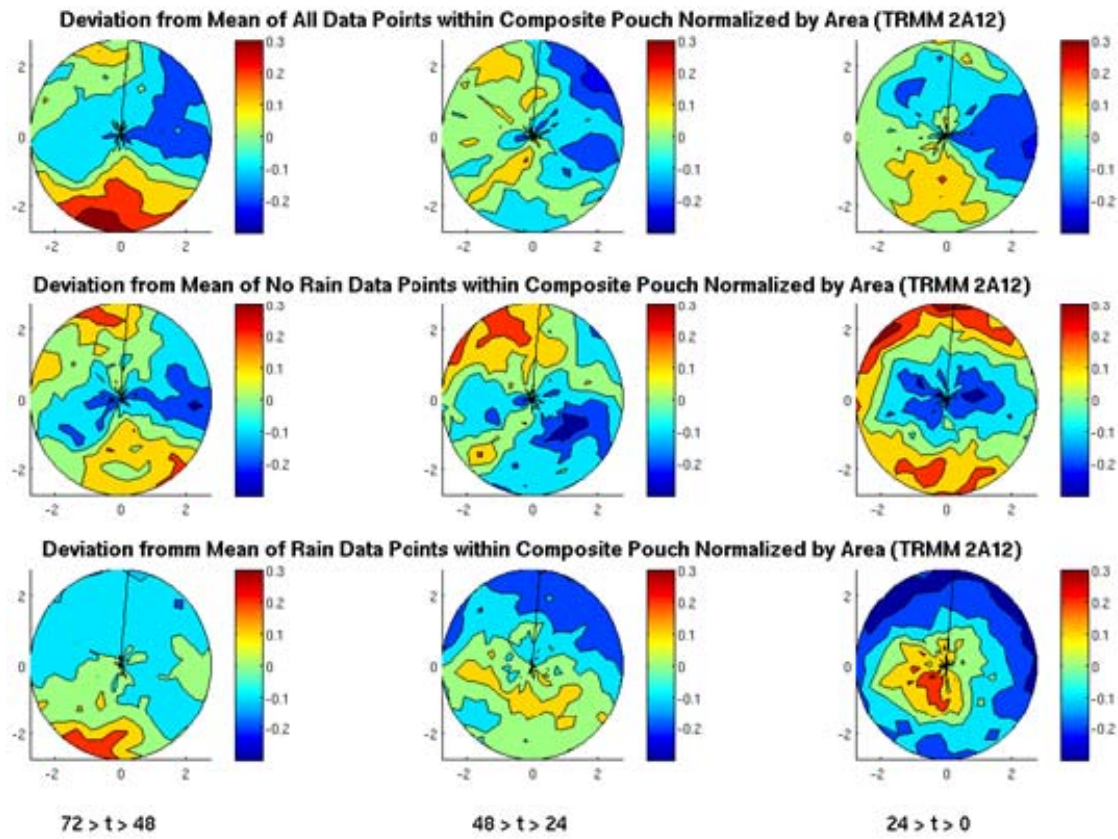


Figure 65. Deviation from the mean number of area normalized pixel counts for the TRMM 2A12 data. Layout as in Figure 64.

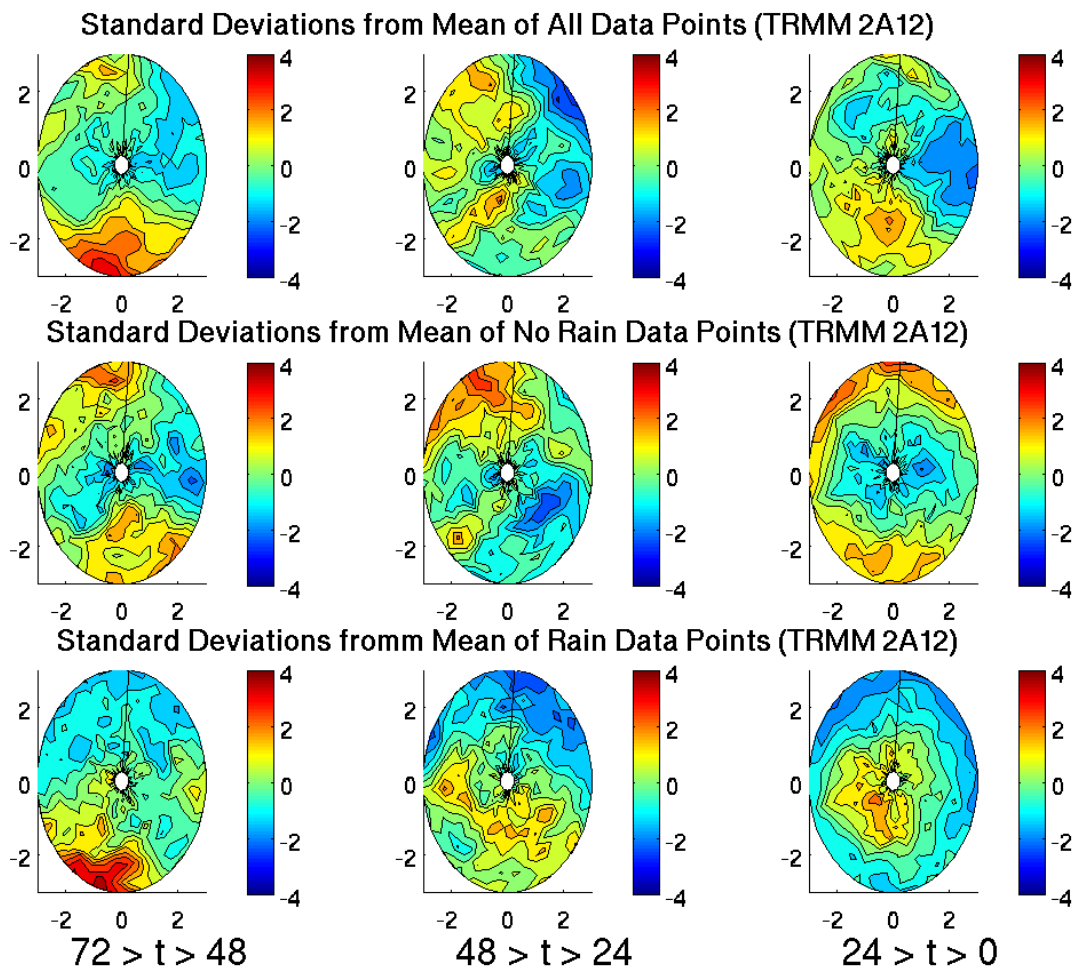


Figure 66. Number of standard deviations from the mean for the area normalized pixel count TRMM 2A12 data. Layout as in Figure 64.

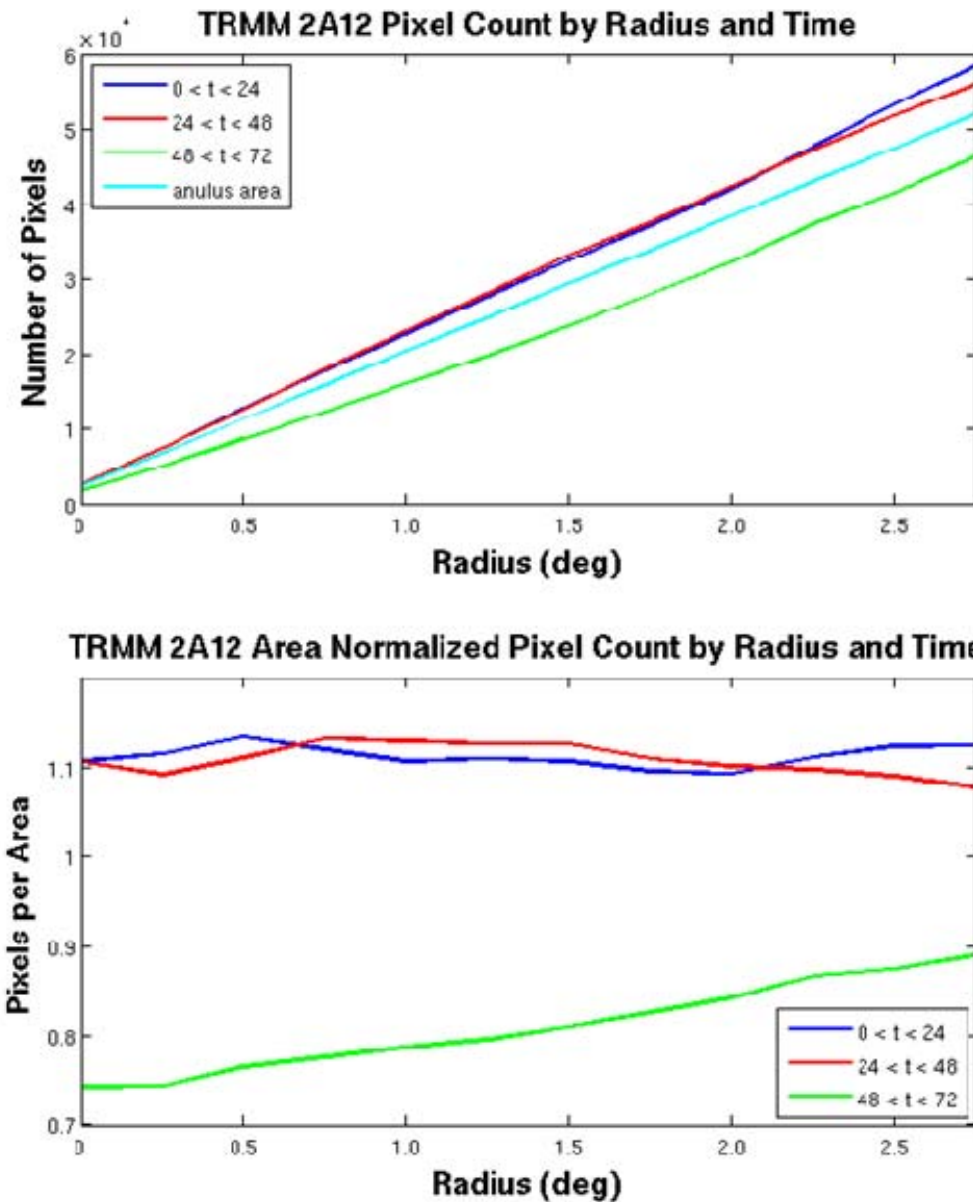


Figure 67. Radial distribution of TRMM 2A12 retrievals in each annulus by time: total pixel counts (top); and pixel counts normalized by annulus area ($\# \text{ km}^{-2}$, bottom).

To test the robustness of the organized precipitation structures, composite pouches are created for each 24-hour time period (e.g., 72–48, 71–47, 70–46, 24–0) prior to genesis. By viewing the data in this manner (not shown), the evolution of the organized precipitation structures are able to be seen. This allows the author to determine whether or not the precipitation maxima systematically move closer to the sweet spot or if these data are skewed by precipitation maxima in a small number of TRMM passes.

The early time periods (24-hour data beginning at T-72–T-60) show generally disorganized precipitation within the composite pouch. The SRR maximum in the southeastern quadrant of the T2 composite pouch begins to emerge at T-60 and is evident until T-37, suggesting that this may be a coherent structure. At T-34, higher SRR (especially convective) begin to appear near the center. The two maxima (observed in Figure 10) are beginning to form at this time near the locations seen in T1. These maxima grow in areal extent, intensity, and move closer to the sweet spot over the next 33 hours. While these tests provide some confidence in the robustness of the organized precipitation features, there are still concerns. Specifically, the precipitation evolution appears discontinuous as genesis nears. That is the maximum in the southern portion of the pouch grows and dissipate prior to the precipitation forming near the center. This suggests that a larger sample size is needed to confirm the significance of these maxima.

B. ADDITIONAL ANALYSIS OF TRMM PRECIPITATION AND LATENT HEATING PROFILES

Houze (1982, 1989, 1997) uses observational data to construct an idealized model of the evolution of precipitation within a typical tropical cloud cluster and its associated vertical latent heating profile. He concludes that the overall vertical latent heating profile is determined by the contributions of the stratiform and convective portions. Figure 68a is a schematic of this widely accepted (e.g., Mapes and Houze 1995; Johnson 1984) heating profile. In this representation, a stratiform component with heating in the mid-upper troposphere and cooling in the lower troposphere is combined with a convective profile. The convective profile exhibits heating throughout the depth of the troposphere and has a maximum in mid-low troposphere. The superposition of these heating profiles results in a “top-heavy” heating profile (Figure 68a), as the mid-upper level stratiform heating maximum interacts favorably with the positive convective heating profile and the low-level evaporative cooling counteracts the low-level convective heating.

DMW09 hypothesize that the precipitation and latent heating distribution within the Kelvin cat’s eye region of a developing easterly wave is inherently different from the typical tropical cloud cluster discussed above. DMW09 propose:

Bottom-up development is inextricably linked to column moistening, which **favors convective over stratiform heating as the leading contribution** to the vertical heating profile.

For low-level mass convergence and vorticity amplification, a convective type of heating profile in the lower troposphere critical layer - without significant stratiform heating/cooling, or **with less stratiform component than typical elsewhere** - favors bottom-up development...

Studies have proposed that there are two ways in which the vertical latent heating profile within the Kelvin cat's eye region could take on a convective-type profile:

- An increase in the **areal coverage** of the convective type precipitation at the expense of stratiform precipitation (Montgomery et al. 2010a; Wang et al. 2010a).
- An increase in the **intensity** of the convective type precipitation that is not met by the stratiform precipitation (Chapter III).

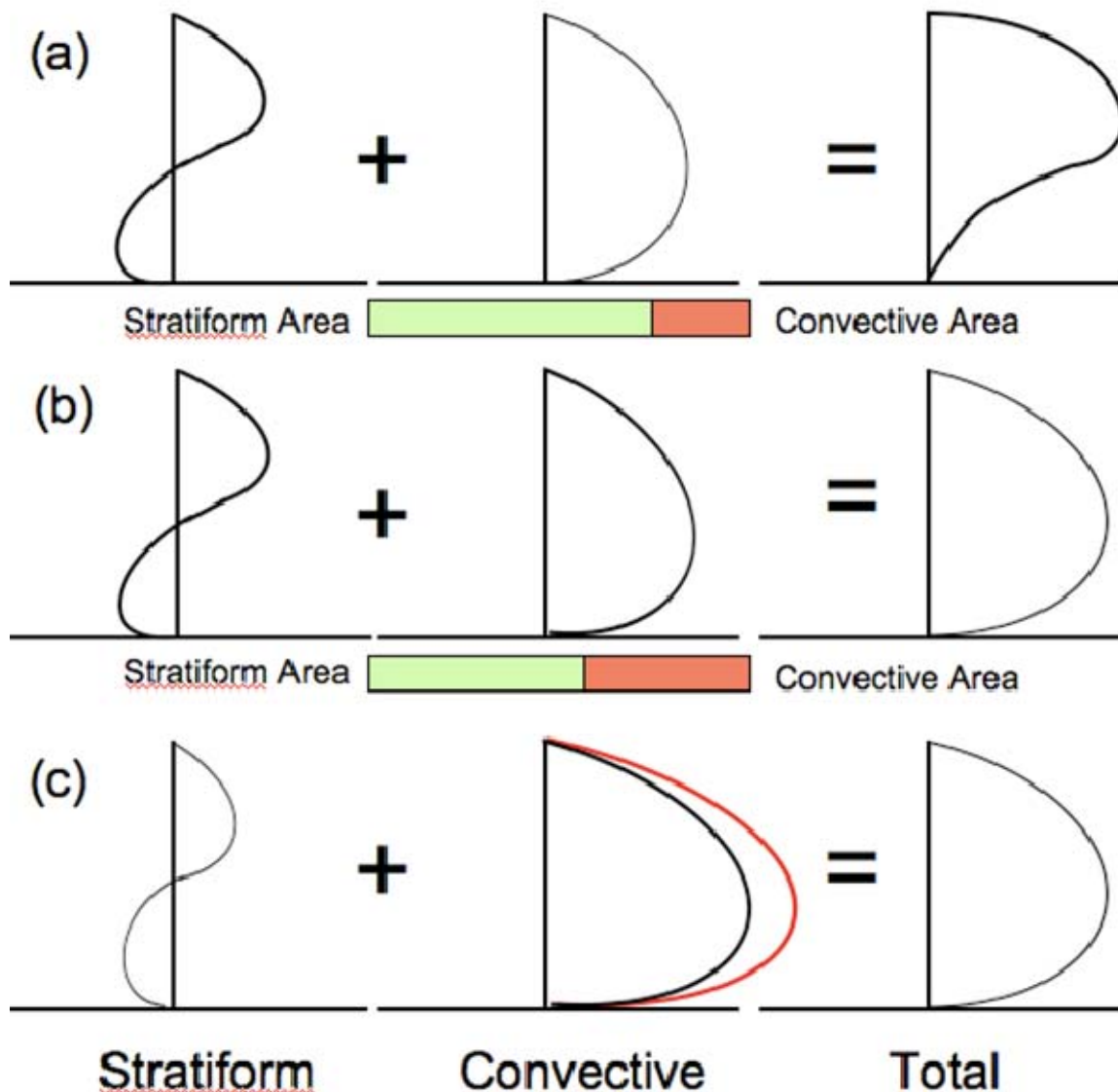


Figure 68. Schematic illustrating idealized latent heating profiles for different precipitation distributions. (a) Observed by Houze (1982, 1989, 1997); (b) hypothesized by Montgomery et al. (2010a) and Wang et al. (2010b); and (c) hypothesized in Section III. The red line indicates the addition latent heating expected during vigorous convective events (i.e., Olson et al. 1999).

1. Analysis of Areal Coverage of Precipitation

Schumaker and Houze (2003) use three years of TRMM PR data to show that the climatological average of areal coverage of stratiform precipitation is 73% across the global tropics (20N–20S). However, high-resolution numerical simulations

(Montgomery et al. 2010a; Wang et al. 2010b) show that the areal coverage of convective type precipitation *within the cat's eye of a developing easterly wave* could be larger than 50%. In the above simulations, the areal coverage of the convective type precipitation increases at the expense of the stratiform precipitation coverage. Therefore, in these simulations, the areal coverage of each precipitation type is inherently different than a “typical tropical cloud cluster” and the latent heating profile is expected to be different. It is expected that the convectively generated mid-low tropospheric heating maximum will begin to dominate the stratiform heating profile. This results in the convective signal dominating the overall latent heating profile (Figure 68b).

As a proxy for areal coverage, the TRMM TMI 2A12 rain rate observations (Schumaker and Houze 2003) are used to examine the contribution of each type of rain rate to the total rain. Schumacher and Houze (2003) use TRMM PR data to show that the mean percent contribution of stratiform precipitation to total precipitation globally from 20N–20S is 40%. This percentage generally holds true across the Atlantic and east Pacific oceanic regions examined in DMW09’s original study. Additionally, they show that the percent contribution of precipitation is proportional to the areal coverage. Figure 69 displays the TRMM 2A12 percent contribution of convective and stratiform precipitation to total precipitation by time and radius for the 55 storms evaluated by DMW09. These data indicate that the percent contribution of stratiform precipitation to total precipitation within the pouch typically varies between 35–45%, values similar to those observed by Schumaker and Houze (2003). There is a general trend of higher stratiform percentages as genesis nears. Of particular interest are the values within the 0.5° radius at T3 and T1. At these times, the percent of stratiform precipitation increases to values above the climatological mean. Whether these increases are artifacts of the small sample size at the innermost radii needs to be examined further.

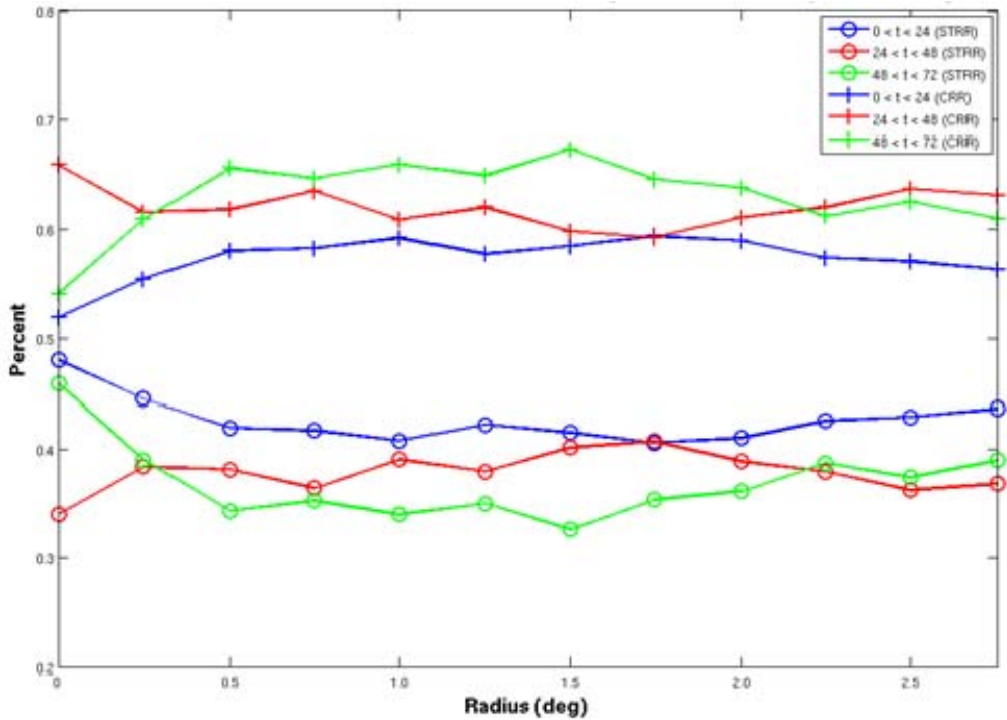


Figure 69. Percent contribution of each rain type, stratiform (o) and convective (+), to total rain rate by radius and time.

To compliment the TRMM TMI analysis, initial results from 227 TRMM PR passes that intersect the composite pouches are examined. The TRMM PR is a space-borne active microwave radar possessing a horizontal resolution of 5 km at nadir and a swath width of 247 km. The TRMM PR 2A25 data uses the hydrometer profile to classify precipitation into four types: stratiform, convective, anvil, and shallow convective (Schumaker and Houze 2006; TRMM 2009). This process is summarized herein from the description provided by Schumaker and Houze (2006): characteristics of the reflectivity profile including the echo top height, maximum reflectivity, and the presence of a bright band are used to distinguish among the rain types. The convective identification algorithm in the TRMM 2A25 date classifies young, active convective cores possessing strong vertical motions as convective cells. The algorithm identifies vertically oriented cores reaching up to 17 km. Stratiform precipitation is identified by precipitation reaching the surface accompanied by the presence of a bright band and/or

by areas possessing very little horizontal variability in echo density. The anvil precipitation category (or ‘other’ as listed in the TRMM documentation) is comprised of rain echoes that do not reach the surface. They may be attached to stratiform or convective echoes. Finally, the shallow convective echoes consist of echoes that are a few kilometers wide and high and are typically found over ocean in low rain regions (Schumaker and Houze 2003). They are defined by echoes having a top height at least 1 km below the 0° C level. Additional details on the TRMM PR can be found in Kummerow et al. (1998).

The small number of TRMM passes coupled with a narrower swath width (~215 km pre-boost and ~247 km post-boost) than the TRMM TMI results in an under-sampling of the composite pouches (Figure 70). Although the absolute number of samples is not far removed from the TRMM TMI data, the radial distribution is vastly different. At no time period does the slope of the pouch composites equal the slope of the annulus area (Figure 70, top). The area-normalized distribution plots bear out these large fluctuations in normalized pixel counts per radius (Figure 70, bottom). Figure 71 shows boxplot diagrams for the area-normalized number of pixels within each radius for the TRMM 2B31 data. The large differences between the mean in the three time periods indicate that the samples do not have equal means and cannot be assumed to have come from the same distribution. Therefore comparisons between composite pouch times are likely not robust. The T3 bin is most evenly sampled at all radii and has the smallest standard deviation (0.0209). The T2 time period had the largest standard deviation (0.0490). While there are noted sampling issues in the TRMM PR data, these results are presented as a ‘first look’ at the evolution of TRMM PR precipitation and vertical latent heating within the pouch of a developing easterly wave.

A four-panel plot of percent contribution of each precipitation type to total precipitation coverage (Figure 72) within the composite pouches is created from the TRMM PR 2A25 data. Convective type precipitation is responsible for less than 30% of the areal coverage at all time periods and all radii. Between T-30–T-06, the percent of convective coverage increases within the innermost two degrees of the composite pouch. The convective coverage maximum occurs at T-12 and is within 0.75° of the sweet spot.

The six hours closest to genesis exhibit a decrease in convective coverage. The dominant contributors to the areal coverage at all times are the stratiform and anvil type precipitation, which account for up to 80% of the coverage. Coverage of stratiform and anvil precipitation generally have an inverse relationship, as maxima in one type typically coincides with minima in the other. The areas of strongest stratiform precipitation typically coincide with or immediately follow the maxima in convective coverage. There is a maximum in stratiform precipitation coverage in the innermost 1.5° radius from T-06 until genesis. The maximum in anvil type precipitation coverage occurs at the earliest time periods at all radii. As genesis nears the areal coverage of the anvil type, precipitation decreases. Shallow convection is a minor contributor to total precipitation coverage at all time periods. There are two shallow convective maxima at T-24 and T-03 within 1.0° of the sweet spot. While the precipitation patterns generally look as hypothesized, the increase in stratiform precipitation coverage at the expense of convective coverage in the innermost radii as genesis neared is contrary to the hypotheses presented by DMW09. Whether this is due to the small TRMM PR sample size or different precipitation classification algorithms between the TRMM TMI and TRMM PR needs to be more comprehensively examined.

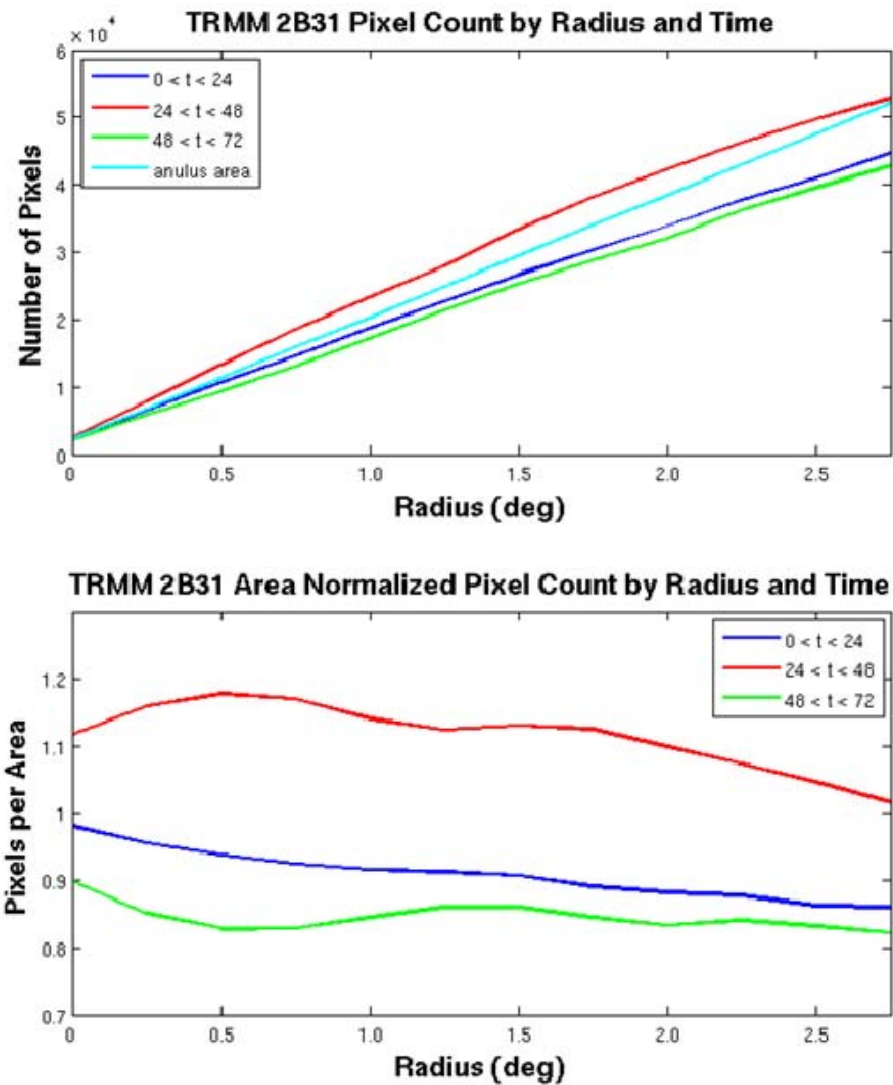


Figure 70. As in Figure 67, except for the TRMM PR data.

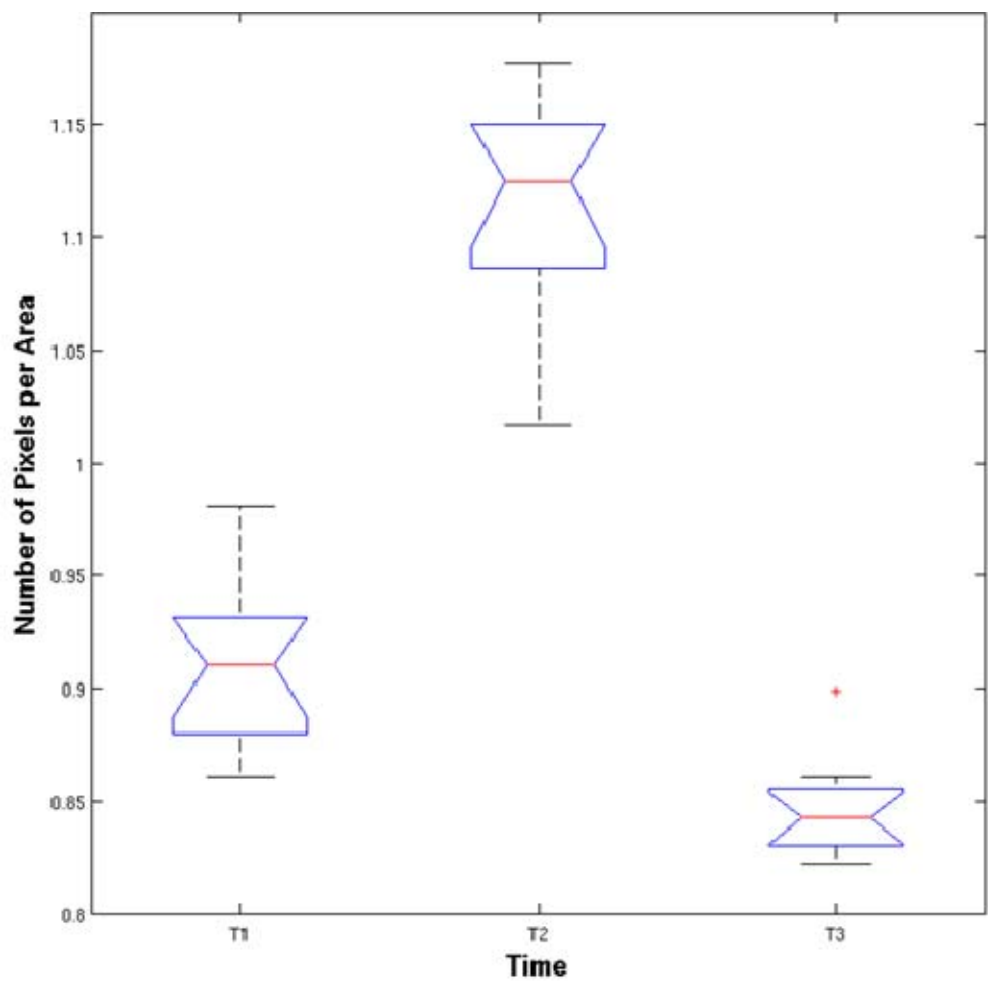


Figure 71. Boxplots for the area normalized pixels distribution ($\# \text{ km}^{-2}$) within each annulus for the TRMM 2B31 data.

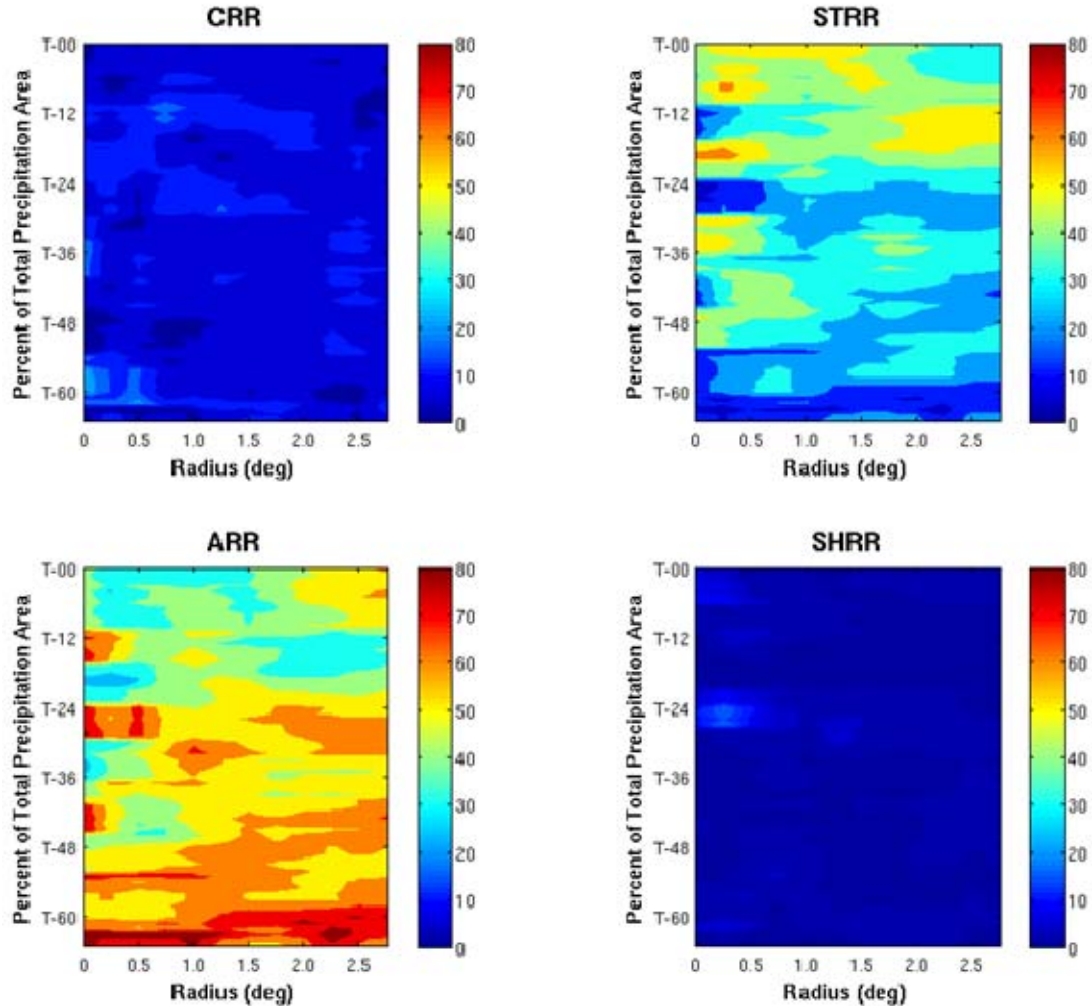


Figure 72. Percent contribution to total rain coverage by each rain type (CRR, STRR, anvil rain [ARR], and shallow rain [SHRR]), within the composite pouches derived from the TRMM PR 2A25 data. These data are plotted as a six-hour running mean to reduce high frequency fluctuations arising from the limited sample size.

2. Additional Analysis of TRMM Rain Rate Data

The second hypothesized way to generate a convectively dominated latent heating profile is for the convective rain rate to increase at a rate not matched by the increase in stratiform rain rate (as discussed in Chapter III). In this scenario, it is assumed that the magnitude of the heating in the vertical is proportional to rain rate (e.g., Yanai et al. 1973) therefore, the strength of the lower-tropospheric convective heating maximum is

much stronger than the top-heavy stratiform precipitation maximum (Figure 68c). Furthermore, the additional source of latent heat release as described by Olson et al. (1999) in Chapter III enhances the magnitude of this maximum (Figure 68c). The result of combination of these profiles would result in a convective-type heating profile (Figure 68c).

Figure 73 is a Hovmoeller diagram of TRMM TMI observed rain rate plotted by precipitation type and radius. These data are normalized by annulus area and are plotted as a six-hour running total. The CRR is the dominant contributor to total rain rate at all time periods and radii. As genesis nears, coherent maxima begin to emerge in both precipitation types within the innermost radii. A weak convective maximum at T-24 is initially observed between 1.0° - 1.5° . A more continuous CRR maximum emerges just prior to T-12 and migrates toward the sweet spot over the next 12 hours. The highest CRR is located within 1.25° radius and immediately precedes genesis. This CRR maximum is accompanied by a weaker STRR maximum. These observations show that convective processes begin dominating stratiform processes within the Kelvin cat's eye circulation within the 15 hours prior to genesis in the TRMM TMI observations.

Figure 74 is akin to Figure 73, but for TRMM PR data (the contribution to total rain rate for anvil and shallow type precipitation are not presented as they are at least an order of magnitude lower than the convective and stratiform contributions). The temporal and spatial evolution of CRR in the TRMM PR observations is qualitatively similar to the TRMM TMI observations, as convection is occurring at all radii and all time periods. As genesis nears, there is an observed CRR maximum covering the innermost 1.5° radii. The strongest CRR are observed between 1.0° - 0.5° of the sweet spot at this time. The intensity of this maximum is weaker than that observed in the TRMM TMI data and the heaviest CRR are confined to a smaller radial extent. From T-72-T-12 the TRMM PR observations show that STRR coverage is larger in radial extent and has a greater intensity than the TRMM TMI STRR coverage. As genesis nears, the areal coverage of the stratiform precipitation increases in the TRMM PR observations (consistent with Montgomery et al. 2010a). The TRMM PR observations indicate that the STRR is greater than the CRR as genesis nears. The differences between the TRMM

PR and TRMM TMI results could be attributed to the small sample size of the PR data, or uncertainties in rain type retrieval in the TRMM TMI data (discussed in Appendix D).

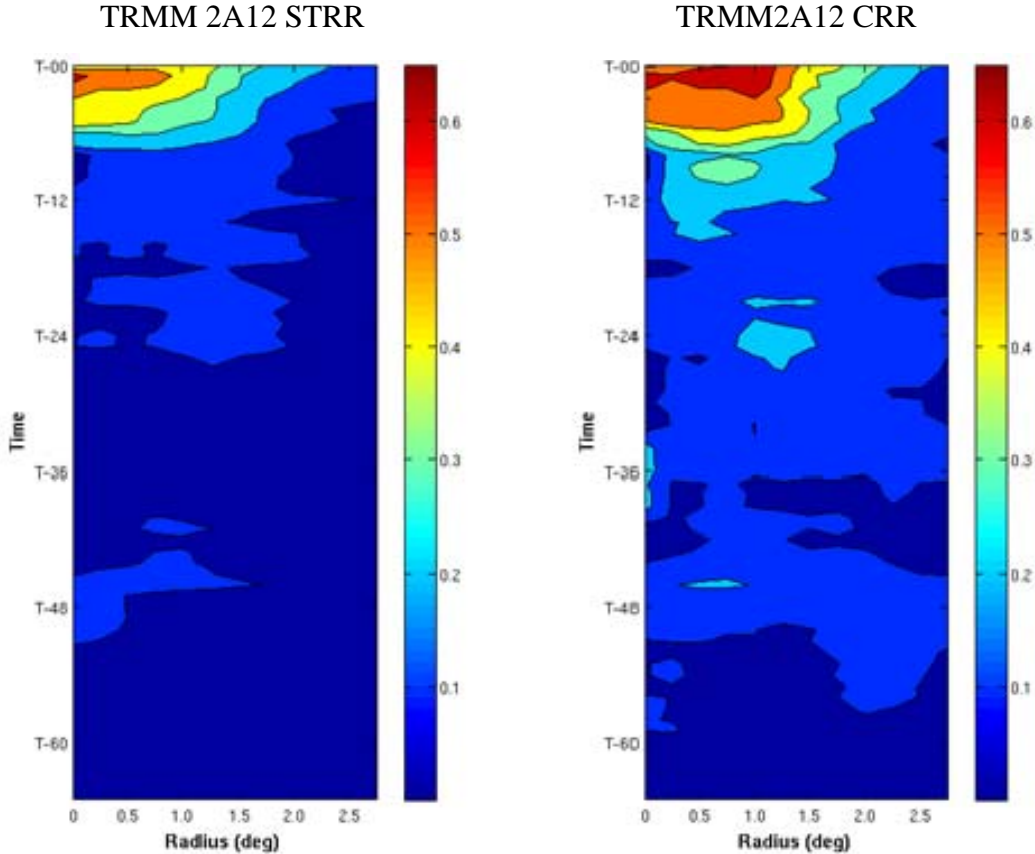


Figure 73. Hovmoeller diagrams of area-normalized rain rates (mm km^{-2}) from the TRMM TMI 2A12 data. These data are plotted by precipitation type with STRR on the left and CRR on the right. The abscissa is time and the ordinate is radial distance from the sweet spot. These data are plotted as six-hour running totals to eliminate high frequency variations.

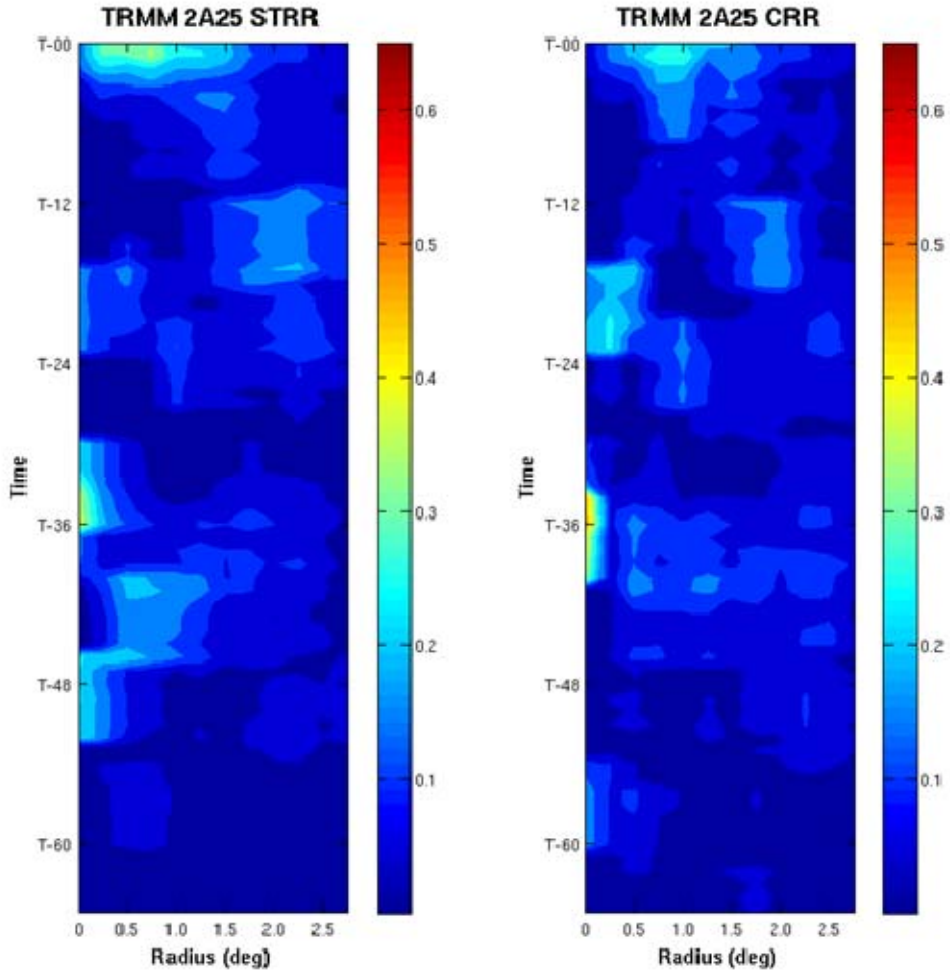


Figure 74. As in Figure 73 except for the TRMM PR data.

3. Preliminary Analysis of TRMM PR Vertical Latent Heating Profiles

Finally, TRMM 2B31 PR latent heating profiles are examined for the composite pouches. The TRMM 2B31 data provides the vertical structure of rainfall and hydrometer distribution based on TRMM PR and TRMM TMI retrievals (TRMM 2009). The latent heating rate is calculated for 13 layers by comparing the vertical fluxes of the different hydrometer species to latitude and longitude dependent archived temperature/pressure/humidity soundings (TRMM 2009). The key input parameters to the latent heating algorithm are the vertical distribution of hydrometers, the surface rain (including type), and the mass exchange among cloud layers (Zuluaga et al. 2010). The main limitations of this methodology include imperfections in the lookup-tables (Tao et

al. 2006), the reliance on rain type partitioning (Tao et al. 2001), and that the latent heating profile is only calculated in areas with surface rainfall (Tao et al. 2001).

Studies have been conducted to assess the overall validity of these observations, but verification is difficult because latent heating is not an observed parameter. As a result, the conclusions garnered from these studies are mixed. Tao et al. (2000, 2001) conclude that TRMM latent heating retrievals are generally in good agreement with the diagnostically determined values. However, they note that the vertical latent heating profiles computed by the TRMM PR generally display a heating maximum lower in the troposphere and are weaker than the diagnostically determined profiles. Zuluaga et al. (2010) use TRMM PR derived vertical latent heating profiles to study the spatial and temporal evolution of latent heating in the South Asian Monsoon region. They conclude that the TRMM PR handles the mean tropical rainfall distribution quite well and that the latent heating algorithms are generally capable of representing the vertically integrated latent heating. However, the ability of the TRMM PR algorithm to accurately represent the vertical profile of latent heating is not captured as accurately (Zulauga et al. 2010). Park et al. (2010) compare TRMM PR latent heating retrievals to ELDORA derived latent heating profiles in tropical cyclones at various stages of their development. They show that the TRMM PR heating profile is generally reliable, however, the TRMM PR fails to correctly identify the intensity of low-level cooling in almost all cases.

Initial analysis from the TRMM PR indicates the presence of a lower-mid troposphere heating maximum (Figure 75–Figure 77). The top panels show latent heating per pixel within each annulus plotted by height and radius. The bottom panels show latent heating profiles within the 1° and 3° radii of the sweet spot. The dotted lines

represent potential errors in the data.³³ These composite profiles show positive heating throughout the depth of the troposphere at all times and for all radii (Figure 75–Figure 77). The heating maxima in the T2 and T3 time periods (Figure 76 and Figure 75, top) are centered at approximately 3.5 km. The vertical extent of the maximum during the T1 time period is greater, stretching from 3.5–4.5 km (Figure 77, top). All time periods exhibit a heating maximum within 0.75° radius of the sweet spot. Figure 75–Figure 77, (bottom) show that the magnitude of the maximum heating does not change appreciably between T3 and T1 as the magnitude and shape of the 1° and 3° profiles at each time period are similar. This suggests that the heating is fairly uniformly distributed throughout the all radii within the composite pouches. The T1 time period exhibits a negative temperature gradient ($\frac{d\theta}{dz} < 0$) in the lowest two layers of the atmosphere and an increase in the vertical depth of the heating maxima when compared to the other two time periods. This could be due to the increased influence of the stratiform component of the heating, which would be consistent with the evolution of precipitation in the TRMM PR. A secondary possibility is that the stronger near surface heating observed during T2 and T3 (Figure 76 and Figure 75, top) is not as pronounced at the T1 time period (Figure 77). These initial results show heating maxima in the mid-low troposphere coupled with positive heating throughout the depth of the troposphere and present evidence of a convective-type heating profile at all radii and time periods. For reasons discussed above, these observations are favorable to “bottom-up” type development. However, the narrow swath width of the PR leads to a large under-sampling of the composite pouches. Work is currently underway to add more cases to this data set so as to achieve statistically

³³ Problems arise when trying to define the error bounds for TRMM latent heating retrievals for a two reasons. First, latent heating is a derived parameter that it is not directly observed. For this reason, the "truth" with which to compare TRMM retrievals is unknown. Second, most of the studies that attempt to verify these retrievals are qualitative in nature. That is, conclusions are typically along the lines of: "...the TRMM latent heating retrievals are in good agreement with the observed profile (e.g., Johnson, 1984, Houze 1989)." The error bounds used in this dissertation come from TRMM latent heating verification presented in Shige et al. (2007) who show that the Spectral Latent Heating (SLH) algorithm compares well to the Convective Stratiform Heating (CSH) algorithm. By comparing TRMM retrievals with calculated profiles from observed data, they suggest that if latent heating profiles are averaged over 30 km, the error is reduced to 1° K h⁻¹. Due to the lack of robust verification data/studies, this value is used to estimate error bounds.

robust results from the TRMM PR latent heating profiles and also to assess the initial results of the spatial and temporal distribution of precipitation presented herein.

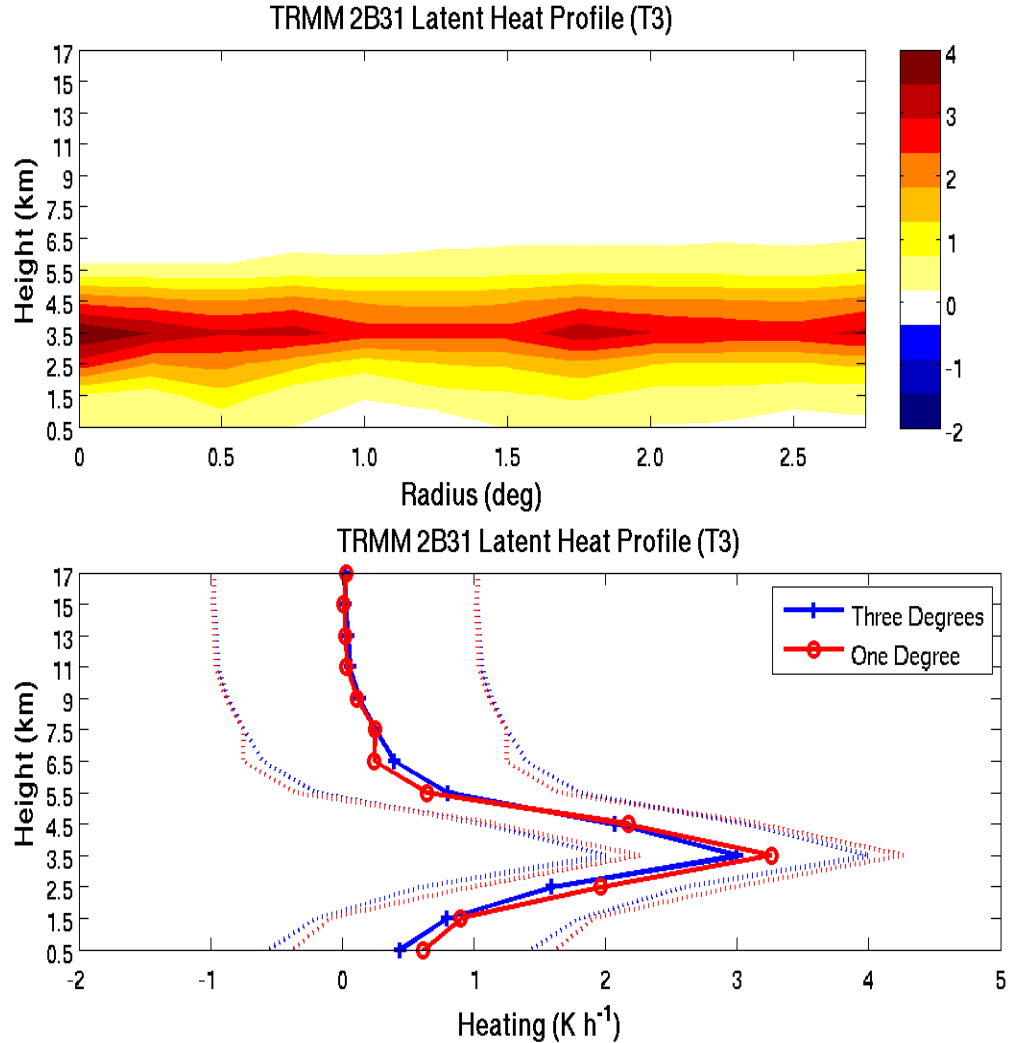


Figure 75. TRMM 2B31 retrieved latent heating profiles for the T3 composite pouch. These data are average heating per pixel ($^{\circ}\text{K h}^{-1}$), which retrieved a latent heating value. The top panel is a radial height cross-section of latent heating per pixel within each annulus and the bottom is latent heating per pixel within the 1° and 3° radii. The dotted lines represent the error bounds of the retrievals.

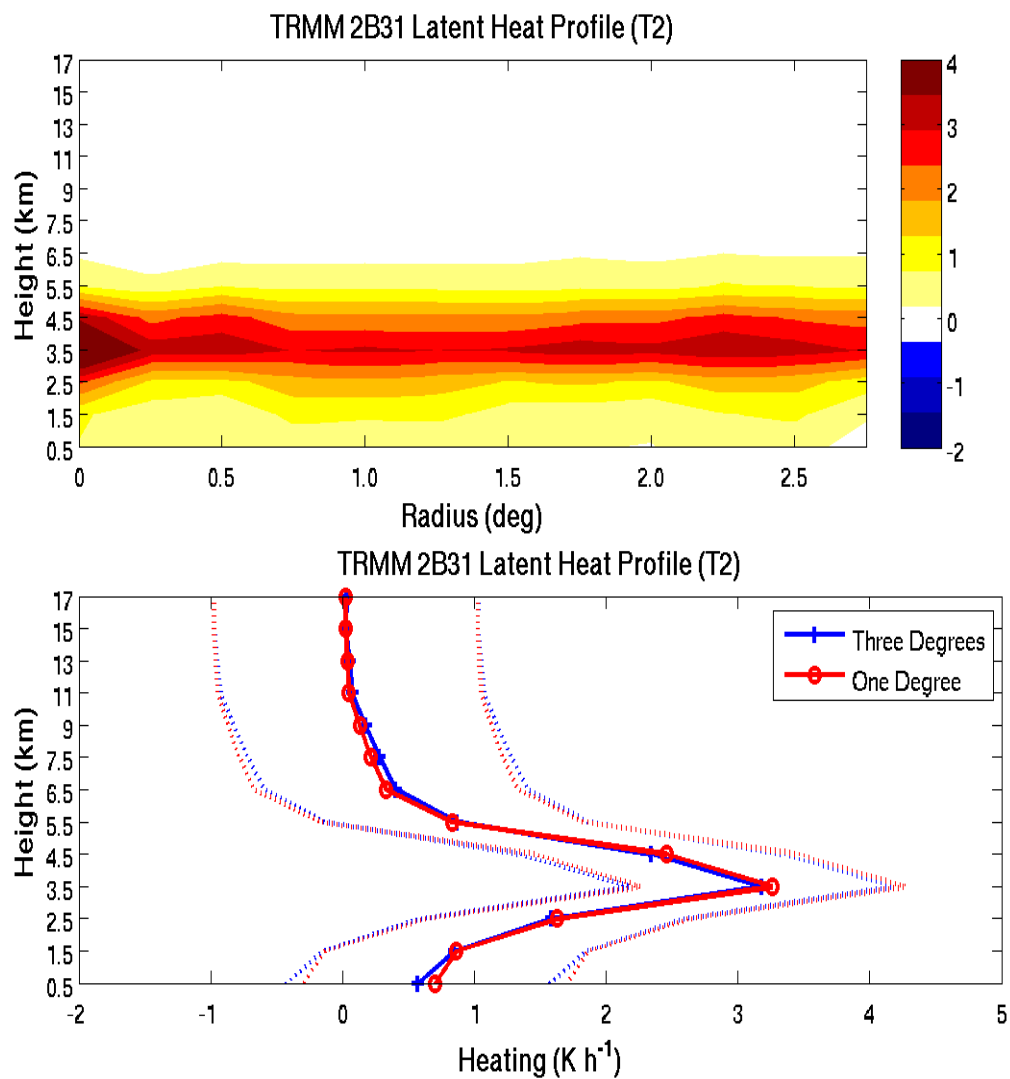


Figure 76. As in Figure 75, except for T2.

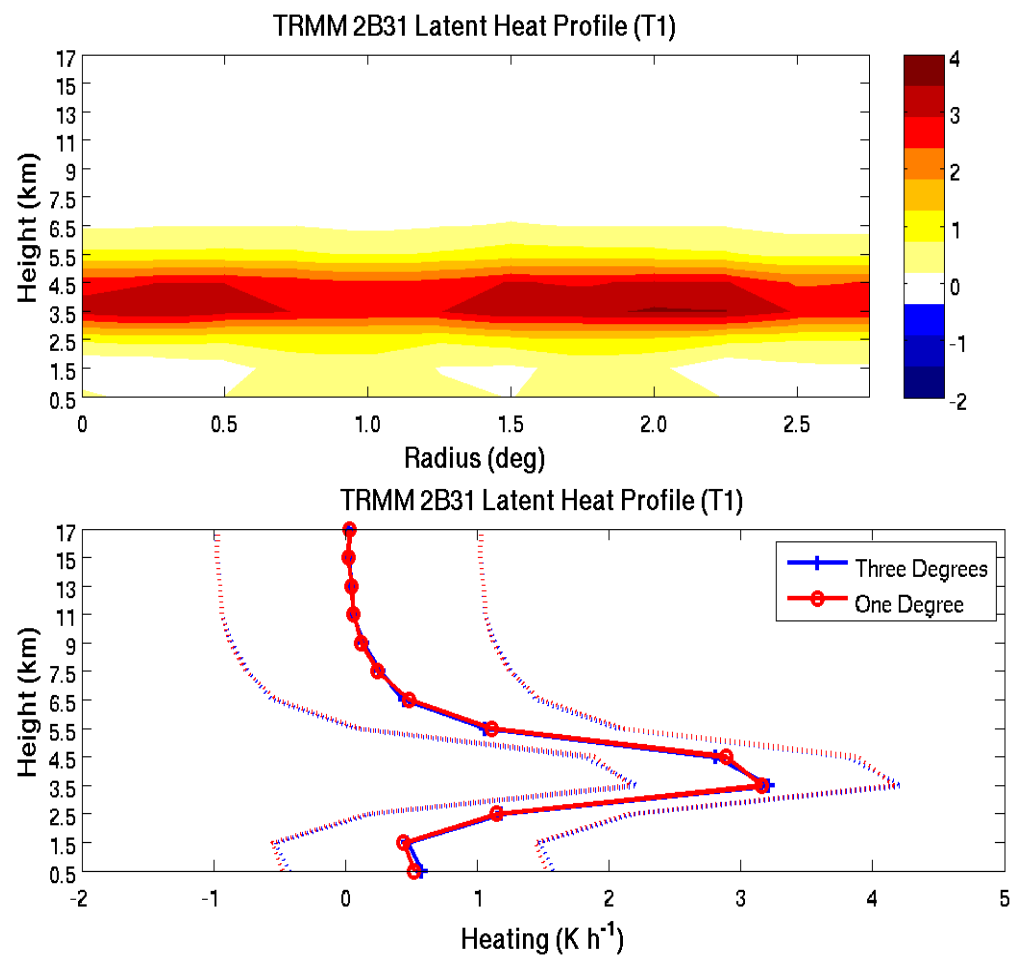


Figure 77. As in Figure 75, except for T1.

APPENDIX C: ADDITIONAL CONSIDERATION ON THE TROPICAL CYCOGENESIS OF TYPHOON NURI

This appendix provides additional analysis and supporting data to describe the tropical cyclogenesis sequence of Typhoon Nuri (2008) at the synoptic and meso- α scales presented in Chapter IV.

A. SUPPLEMENTARY COMMENTS ON THE ORIGIN AND EVOLUTION OF THE PRECURSOR WAVE

To study the evolution of the pre-Nuri disturbance, a time series of GFS FNL 850 hPa relative vorticity and OW (Figure 78) is used. At the initial time period (00Z 9 August), Typhoon Nuri's proto-vortex is located at 172E as indicated by areas of higher positive relative vorticity and OW. There is active convection associated with this disturbance prior to this time (8 August, Figure 79). However, by 9–10 August, the convective activity becomes nearly non-existent. As noted in Chapter IV (and evident in Figure 78), there is enhancement of the low-level relative vorticity and OW (9–10 August) prior to the pouch entering the hostile environment. Despite this increased low-level spin-up, the cessation of convection eliminates any chance of formation at this time. As the pouch transgresses through the hostile environment (12Z 10 August–00Z 15 August), the intensity of the cyclonic vorticity maximum steadily deceases through 14 August. The OW is at a minimum between 18Z 13 August–12Z 15 August. Concomitantly, between 11–12 August, convective activity associated with the westward propagating disturbance continues to be nearly non-existent (Figure 80). While there are occasional convective blow-ups over the next two days (13–14 August), the convection is disorganized and intermittent. After 14 August, when the pouch emerges from the hostile environment, the convective activity and the magnitude of its associated cyclonic vorticity maximum increases (discussed in Chapter IV). The reinvigoration of deep convection that occurs at 12Z 15 August is accompanied by an increase in low-level cyclonic vorticity and a reintensification of OW (Figure 78).

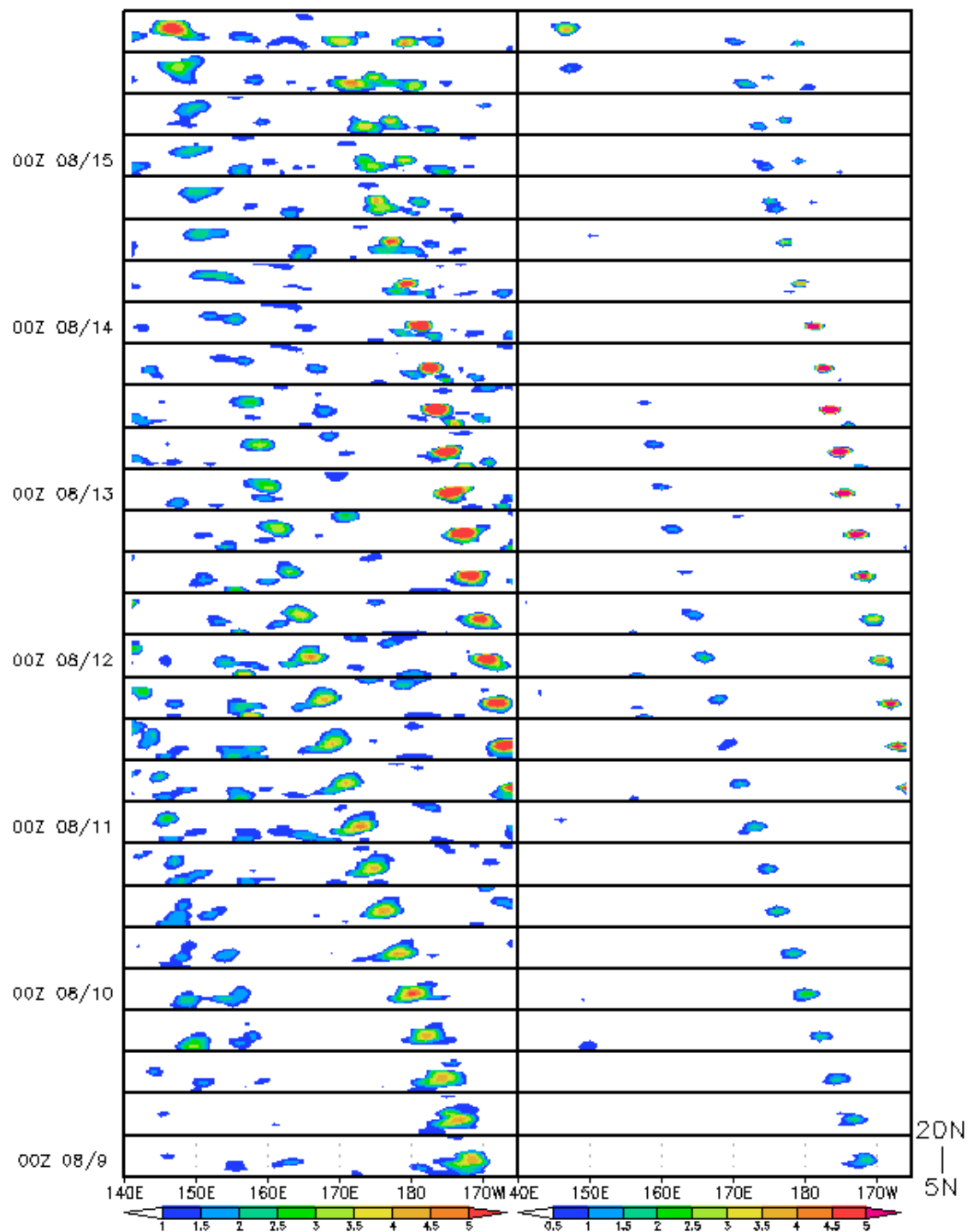


Figure 78. Time series of 850 hPa GFS FNL relative vorticity ($\times 10^{-5} \text{ s}^{-1}$, left) and OW ($\times 10^{-9} \text{ s}^{-2}$, right) beginning at 00Z 9 August. The location of Typhoon Nuri's initial vorticity seedling at this time is 172W. The vorticity/OW maxima entering the domain from the east at 06Z 11 August is Tropical Storm Kika. The abscissa longitude and the ordinate latitude ranging from 5–20N.

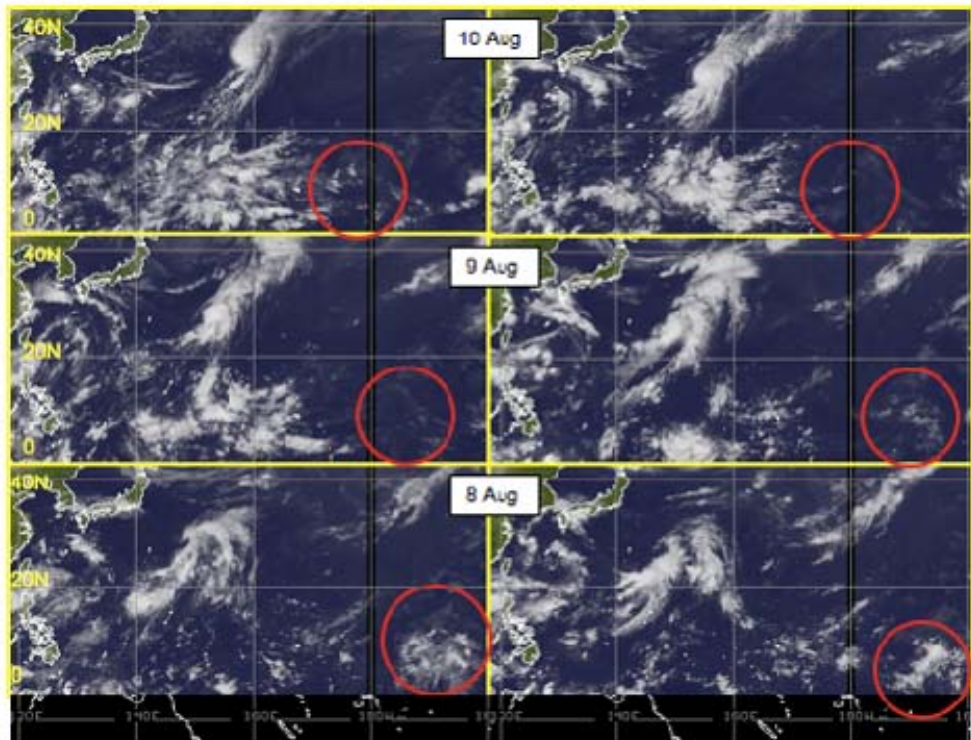


Figure 79. Time series of NRL stitched IR imagery. Images are valid at 00Z and 12Z from 8–10 August. The red oval highlights the cloud features associated with the pre-Nuri wave pouch.

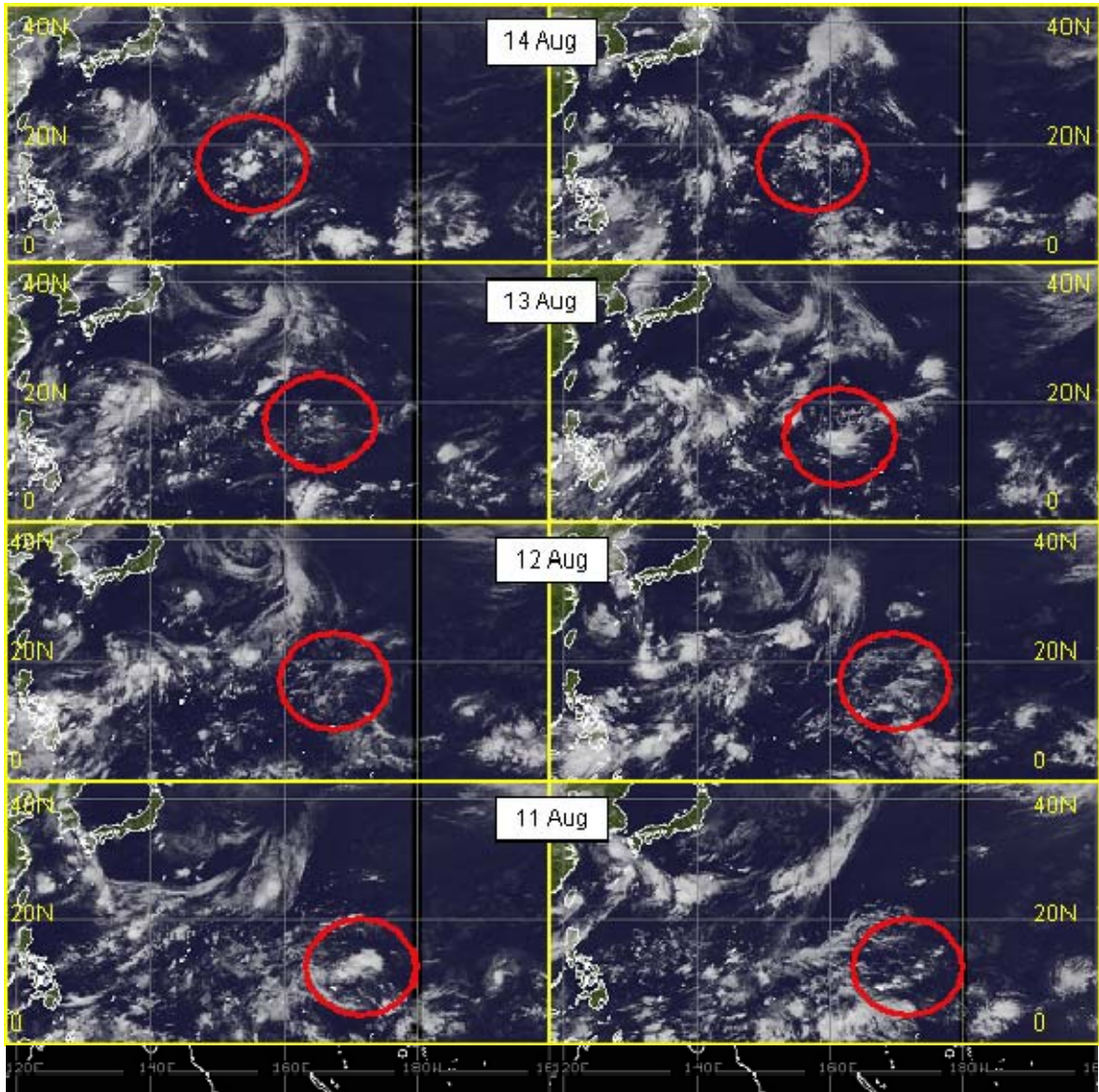


Figure 80. Time series of IR imagery valid at 00Z (right) and 12Z (left) for the time period between 11–14 August. The red oval highlights the cloud features associated with the pre-Nuri wave pouch.

The northward component of propagation of the wave pouch observed in the GFS FNL after it crosses the dateline and the associated reduction in phase speed is discussed at length in Chapter IV. Figure 81 shows the track of Typhoon Nuri’s sweet spot as derived from the GFS FNL (as in Figure 16) overlaid with the magnitude (contours) and direction (vectors) of the steering flow. For this analysis, the steering flow is defined as the average flow between 1000–500 hPa for the period from 12Z 8 August–12Z 17 August. At 12Z 9 August, the wave pouch enters a region of maximum wind speed that

leads to the higher average propagation speed observed prior to 12Z 11 August. After this point, the wave begins to emerge from this maximum and move into an area of weaker background flow, thus the reduction in average phase speed. On 1 August, the dominant easterly flow acquires a northerly component at points west of 165E. This is consistent with the northwesterly propagation of the track and previous studies on easterly wave propagation in the western North Pacific basin (Serra et al. 2008).

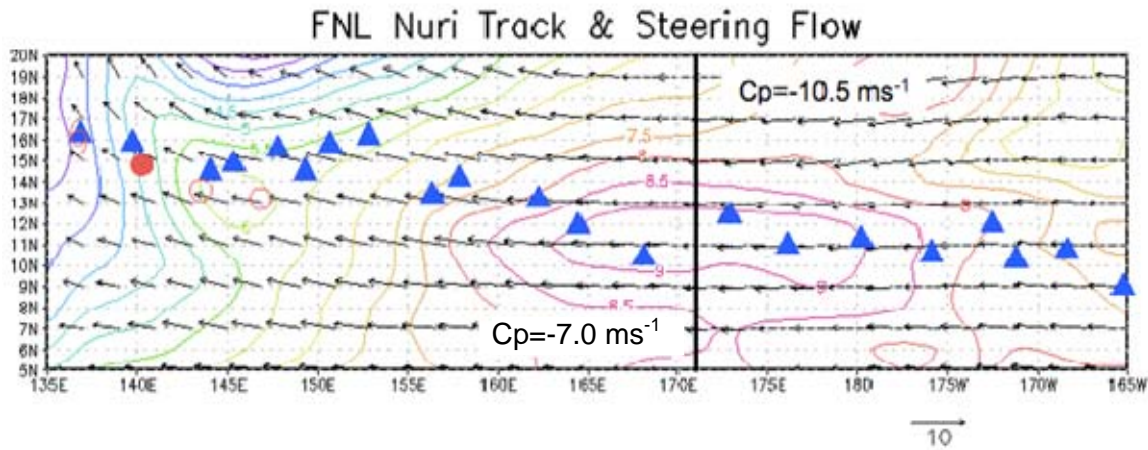


Figure 81. GFS FNL 1000–500 hPa steering flow. The magnitude (m s^{-1}) of the average flow from 12Z 7 August–12Z 17 August (contours) and direction (vectors) are plotted. The thick black line represents the point at which the average phase speed of the wave decreased. The symbols are positions of the sweet spot as in Figure 16.

B. DISCUSSION OF OTHER POSSIBLE FACTORS IN TYPHOON NURI'S GENESIS

Figure 82 and Figure 83 are Skew-T diagrams from Koror, Palau and Guam respectively. While the presence of westerly winds is evident in the lowest levels in the Palau sounding, the series of soundings for Guam clearly show the passage of an easterly wave (as discussed in Chapter IV). Figure 84 is a four panel plot of GFS FNL 1000 hPa streamlines (resting) and westerly winds (shaded) valid from 06Z 15 August–00Z 16

August.³⁴ The locations of Guam (blue circle) and Palau (blue square) illustrate the reasoning behind using the Guam sounding versus the Palau sounding when discussing the genesis sequence of Typhoon Nuri. At the first time period, a small area of westerly winds is located at the base of the pre-Nuri easterly wave (7N, 147E), consistent with the observed QuikSCAT wind field. The large-scale westerly winds are well west ($>10^\circ$) of this location (red shading). Six hours later there is no evidence in the GFS FNL of the westerly winds at the base of the open wave and the eastern-most extent of the monsoon trough remains stationary. The next two time periods show westerly winds at the base of the wave completely isolated from the monsoon trough region. This is argued to be evidence of the formation of a closed circulation in the resting frame rather than the influence of a monsoon trough contributed to Typhoon Nuri's development.

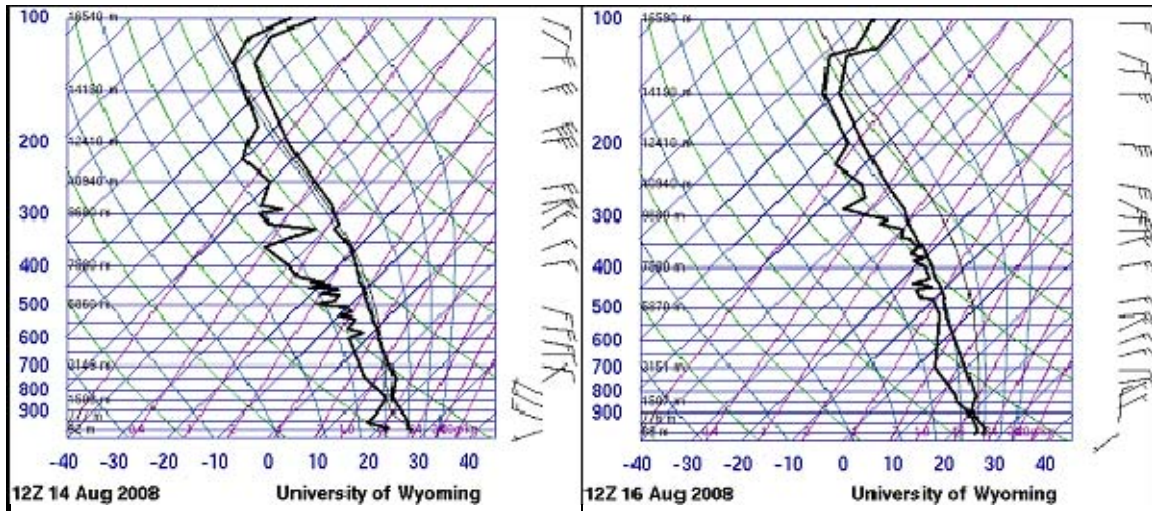


Figure 82. Skew-T plots from Koror, Palau showing the low-level westerly flow (left) and the cessation of this flow (right).

³⁴ Although not as good as observations, the GFS FNL low-low-level wind field verifies well with QuikSCAT observations, and is used to provide spatial and temporal information about the wind field evolution that QuikSCAT observations cannot.

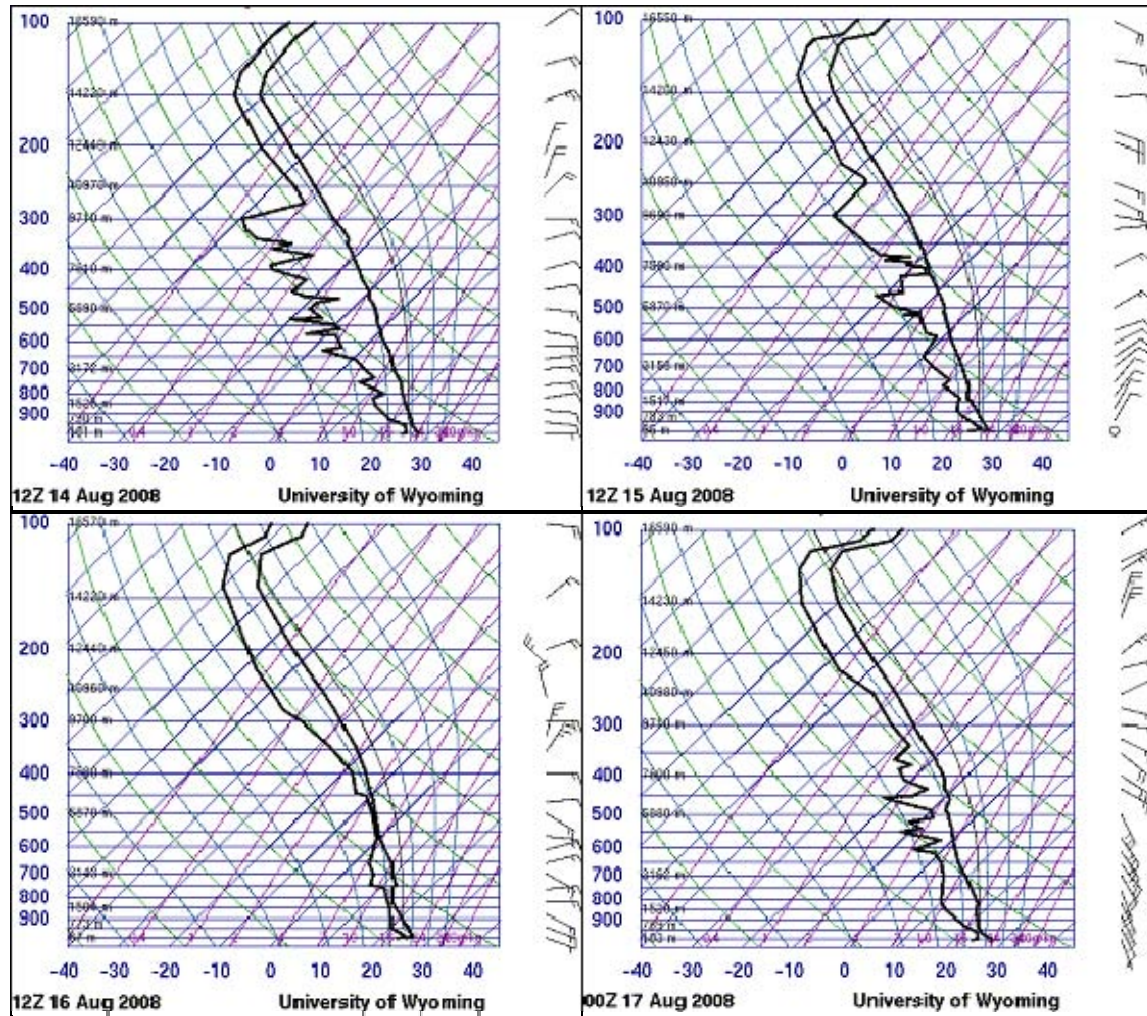


Figure 83. Skew-T diagrams from Guam. The time evolution of the low-mid level wind field in these plots shows the pre-Nuri easterly wave passing over the island.

Figure 85 is a three-panel plot of the CIMMS upper-level cloud drift winds. Potential TUTTs are enclosed in red circles and the red arrow indicates the location of the pre-Nuri disturbance. These figures (along with the data/discussion presented in Chapter IV) illustrate that the presence of a TUTT is unlikely to have played a significant role in the formation of Typhoon Nuri.

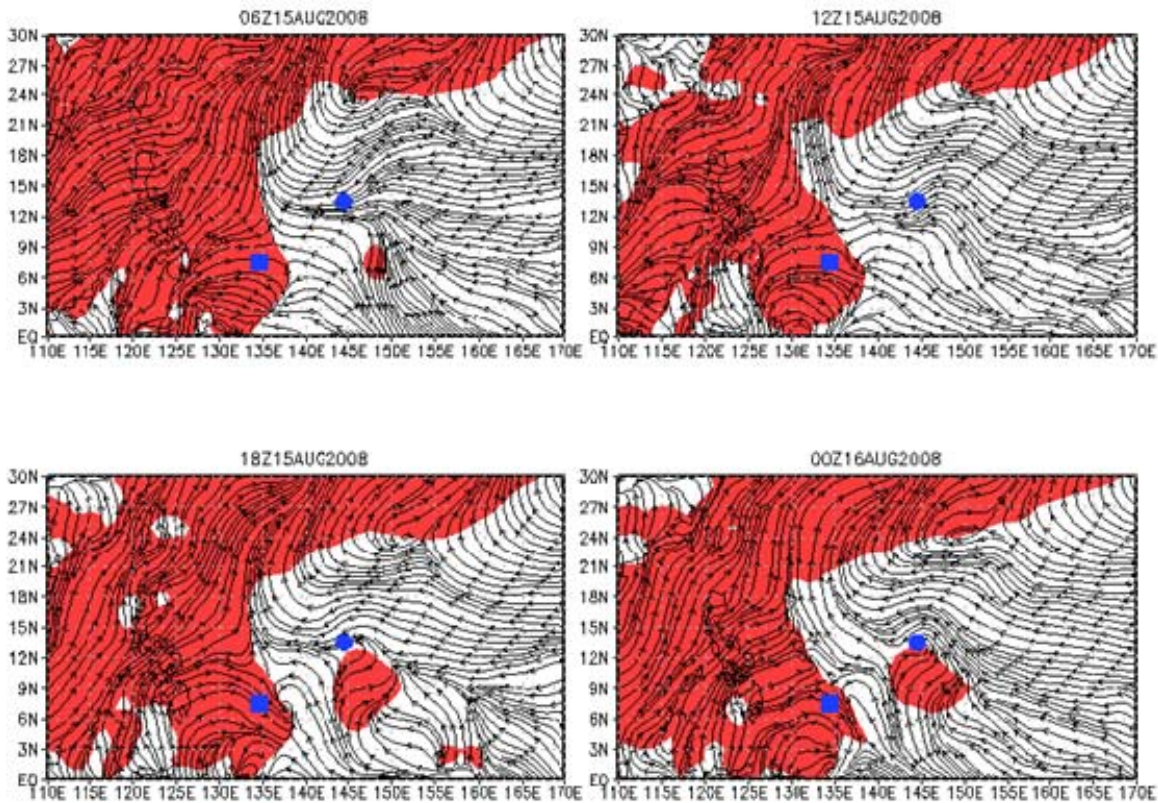


Figure 84. GFS FNL 1000 hPa wind field valid at six-hour intervals beginning 06Z 15 August. The black lines are streamlines in the resting frame and the red shading indicates areas with a westerly wind component. The blue circle is Guam and the blue square is Palau.

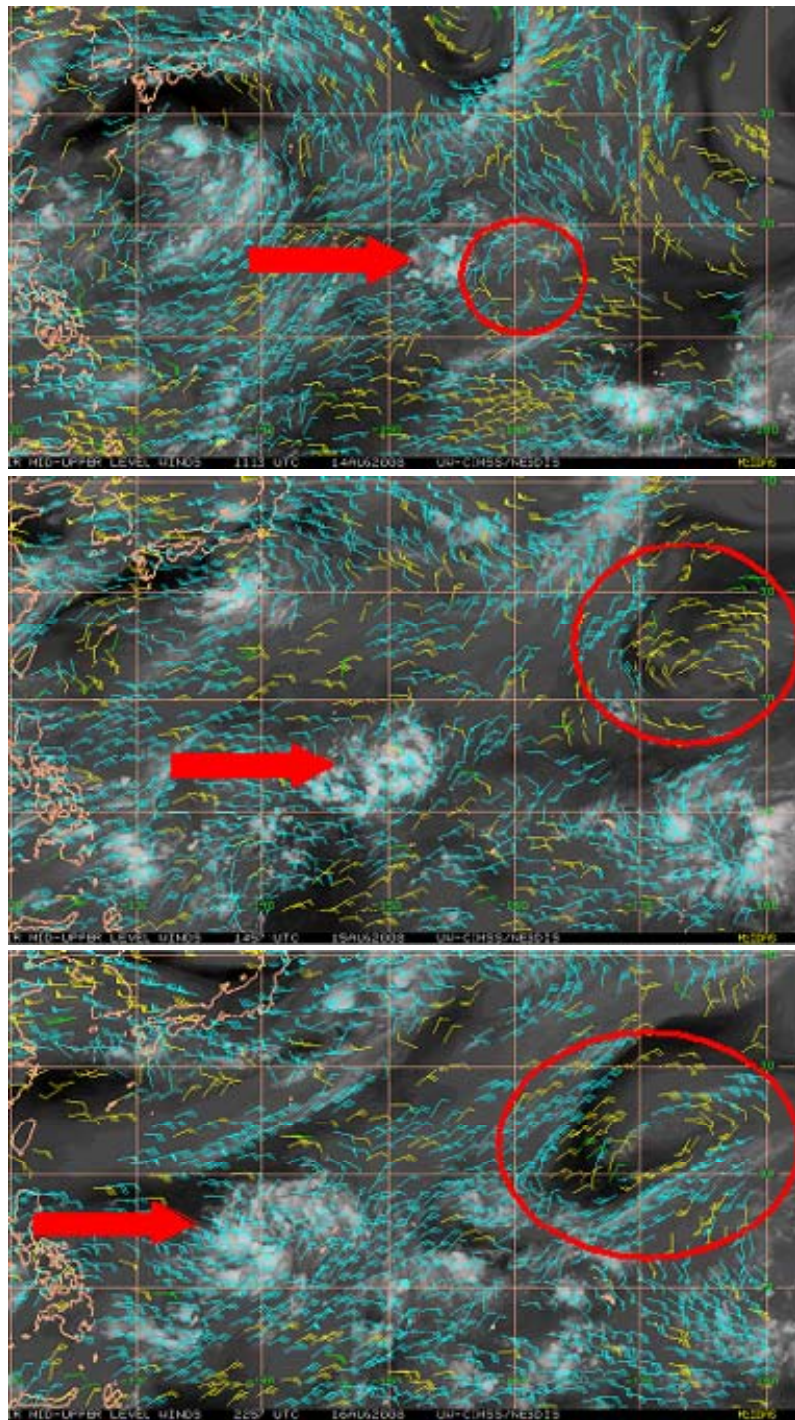


Figure 85. CIMMS upper-level cloud drift wind plots valid: 12Z 14 August (top), 15Z 15 August, and 00Z 16 August. The red circles highlight potential TUTT activity. The red arrows point to the pre-Nuri disturbance. The cyan barbs are winds at 100–250 hPa level, the yellow barbs are winds at 251–350 hPa level, and the green barbs are winds at 351–500 hPa level.

THIS PAGE INTENTIONALLY LEFT BLANK

APPENDIX D: TRMM PR OBSERVATIONS OF TYPHOON MAN-YI

Analysis of several TRMM PR passes through Typhoon Man-yi’s wave pouch are presented. The author acknowledges that the combination of the small swath width of the TRMM PR and the limited number of passes prevent these results from being statistically robust. They are presented as a potential path forward for using TRMM data to analyze tropical cyclogenesis within the framework of the new cyclogenesis model.

A. BACKGROUND

Both numerical simulations (Montgomery et al. 2010a; Wang et al. 2010b) and observational diagnoses (DMW09; Chapter III) show that convection is favored in, but not limited to the Kelvin cat’s eye region of an easterly wave critical layer as genesis nears. These studies show that convection is favored over stratiform precipitation in terms of overall contribution to rain rate as tropical cyclogenesis approaches. These results suggest the presence of a convective-type heating profile, with a heating maximum in the low-mid troposphere, as opposed to the more commonly observed “top-heavy” heating profile documented in typical tropical MCS (Houze 1982, 1989, 1997; Johnson 1984; Mapes and Houze 1995). In addition, a convective-type heating profile favors column moistening, which is amenable to “bottom-up” development (DMW09). Furthermore, a heating maximum in the low-mid troposphere favors diabatic PV generation in the lower troposphere. Initial analysis of TRMM PR latent heating profiles shows that a convective-type heating profile is observed within the critical layer of a composite easterly waves (Appendix B). However, these results lack statistical robustness as the composite pouches used in this analysis are under-sampled. This chapter examines TRMM PR precipitation retrievals and observed latent heating profiles within the Kelvin cat’s eye circulation of the pre-Man-yi disturbance. The limitations of the TRMM sampling (discussed in Section B1) prevent the results of this analysis from being statistically robust. However, they are presented to demonstrate the type of

analysis that can be accomplished using the TRMM PR. Additionally, this analysis shows that aspects of DMW09 H1-H3 are observed during Typhoon Man-yi's tropical cyclogenesis sequence.

B. TRMM PR PRECIPITATION DISTRIBUTION AND LATENT HEATING PROFILES

This section examines the precipitation distribution and latent heating profiles from the TRMM PR orbits that intersect Typhoon Man-yi's critical layer. The goal of this study is to provide a preliminary evaluation of the precipitation and vertical latent heating profiles *within the wave pouch*. Therefore, retrievals outside of the pouch, even in a strong MCS are not considered. The center of the pouch is determined by the location of the GFS FNL sweet spot (defined in Chapter V). A five-degree radius circle centered on the sweet spot location is used to approximate the spatial extent of Typhoon Man-yi's wave pouch. Despite the limited number of passes and sampling limitations discussed in Section B, these data are presented to examine the areal coverage of different precipitation types and assess the potential for a convective-type latent heating profile within the critical layer of the pre-Man-yi disturbance.

The TRMM PR sampling distribution for each of the four passes used in this study is plotted with respect to radius from the sweet spot (Figure 86). This plot is created by assuming that each TRMM retrieval is circular with a 2.5 km radius. A percent coverage for each annulus is created by dividing the number of TRMM PR retrievals within each annulus by the maximum possible number of retrievals. This estimation does not take into account unsampled area in the swath between retrievals, resolution differences of the retrievals off nadir, or changes in annulus area based on latitude. The swath width of the TRMM PR is 247 km (approximately 2.5°). Therefore, annuli inside of 1.25° have the potential for 100% of their area to be sampled. At larger radii, the maximum percent area coverage of each annulus decreases to 50% at 2.5° , and approximately 41% at 3° etc.

For all passes except the 6 July pass, the innermost radii are generally not well sampled (Figure 86). This is due to both the small size of the innermost annuli and the

low probability of a TRMM orbit passing directly over this location. The sampling coverage on 7 and 8 July is typically between 30–50% for radii between 0.25° – 3.0° , before tailing off at larger radii. The 4 July pass has the lowest percent area coverage and the 6 July pass exhibits the most robust sampling. On 6 July, The innermost radii are sampled at 100% out to 0.5° before areal coverage decreases with radius. Because of this, the 6 July pass is considered the most representative of conditions within the wave pouch. The other passes exhibit limited geographic sampling and thus are unlikely to represent the predominant conditions within the wave pouch.

At approximately 2024Z 4 July, the TRMM satellite passes over the convective burst initiated at the leading edge of the ER wave. Figure 87 shows a two-panel plot with the TRMM PR 2A25 rain type data (top) and the MTSAT IR imagery with a BD enhancement (bottom) overlaid with the approximate location of the TRMM pass (yellow line), the sweet spot (plus sign), and the approximate 5° radius circle representing the wave pouch (red circle). While the convection is not at its most vigorous level, there remain small convective elements embedded within a larger stratiform precipitation area (Figure 87). The TRMM PR samples the large MCS and areas of scattered convection to its east. TRMM latent heating profiles within the pouch are derived from this pass (Figure 88). These observations are plotted as vertical profiles of average heating per pixel within the 3° and 5° radii centered on the sweet spot (solid lines). The dotted lines represent potential error in these data. The 3° and 5° heating profiles exhibit positive heating throughout the depth of the troposphere with a lower tropospheric heating maximum at 3.5 km (i.e., a convective-type heating profile). In this instance, there are no TRMM PR latent heat retrievals within 1.0° of the sweet spot.

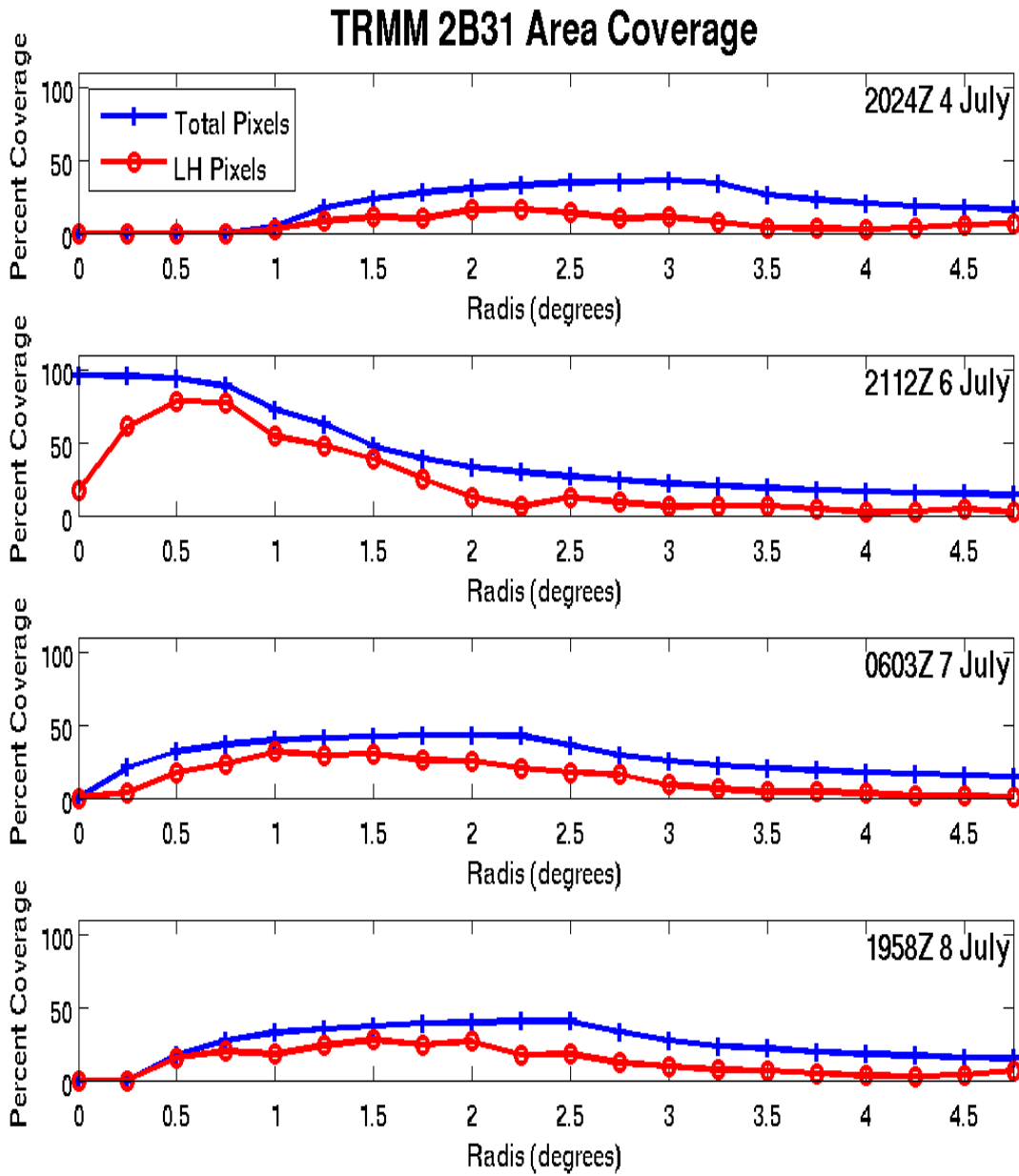


Figure 86. Percent coverage of the TRMM PR within each 0.25° radius annulus for the four cases used in this study. The blue line represents the total number of retrievals and the red line is the number of latent heating retrievals.

At 21Z 6 July, the TRMM PR passes directly over the GFS FNL derived sweet spot (Figure 89). During this time, the TRMM PR samples two large convective bursts (Figure 89) within the inner radii of the wave pouch. The convective burst centered at approximately 8N, 149E appears to contain more mature convection than the burst

centered on 7N, 147E. Figure 90 is a two-panel plot of composite heating profiles (the top panel is a radial height plot of average heating per pixel and the bottom panel is as in Figure 90 with the addition of a 1° heating profile. The composite latent heating profiles are convective in nature and the most intense heating ($>7 \text{ } ^\circ\text{K h}^{-1}$) is centered between 3.5–4.5 km altitude and occurs within 1° radius of the sweet spot (Figure 90). There is low-level cooling in the lowest layers between 1.5° – 3.75° , suggesting the presence of stratiform precipitation in the outer radii of the wave pouch. The heating profiles (Figure 90, bottom) show the most intense latent heating ($>6 \text{ } ^\circ\text{K h}^{-1}$) within the 1° radius. All three radial profiles show an area of $\frac{d\dot{\theta}}{dz} < 0$ below 2.5 km. Within the 1° radius, this is likely due to the observed surface heating (Figure 90, top), while in the 3° and 5° profiles, the area of $\frac{d\dot{\theta}}{dz} < 0$ is likely a combination of the surface heating within 1° and the low-level stratiform cooling in the outer radii. This time period (Figure 90) exhibits the largest difference between the 3° and 5° profiles as the intensity of the heating maximum in the 5° radius circle is approximately 0.5 K h^{-1} less than the 3° circle, likely due to the additional stratiform cooling beyond 3° .

At 06Z 7 July, the TRMM PR passes through the eastern quadrant the pouch (Figure 91). The MCS centered near 11N, 148E has vigorous convection immediately northeast of the sweet spot surrounded by stratiform precipitation at the outer radii of the pouch. The latent heating profile (Figure 92) is consistent with this precipitation pattern. The strongest heating is centered between 3.5–4.5 km in the vertical within all three radii. The 1.0° radius profile is convective, while the 3.0° and 5.0° profiles are almost identical and show areas of $\frac{d\dot{\theta}}{dz} < 0$ below 2 km, perhaps indicative of the weak layer of stratiform precipitation. The overall heating profiles remain positive throughout the depth of the troposphere for each radius.

At 20Z 8 July (Figure 92) the TRMM pass covers the northwest quadrant of the pouch. At this time, JTWC had declared the storm a TD and upgraded it to a TS 18 hours later. The satellite imagery shows active convective complexes with a mix of stratiform

and convective cells throughout the pouch (Figure 92). The latent heating profiles remain overall convective (Figure 93) for the TRMM sampled area within the wave pouch. Heating per pixel within 1° radius of the sweet spot approaches 6 K hr^{-1} . The positive heating through the troposphere coupled with the heating maximum in the lower troposphere are characteristics of a convective-type heating profile.

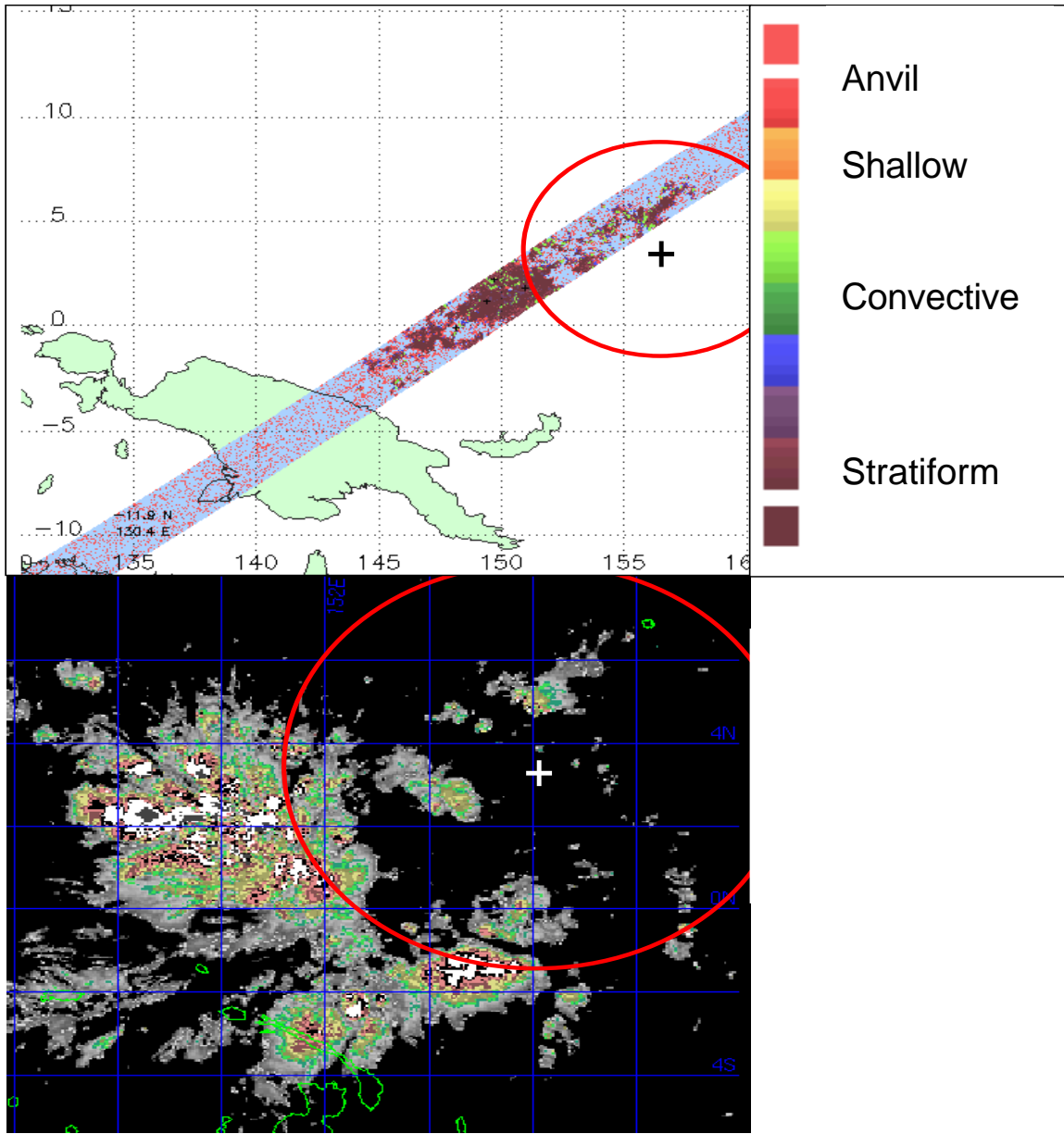


Figure 87. Two panel plot of TRMM PR pass (top), valid 4 July 2024Z and MTSAT IR image (bottom) with a BD enhancement, valid 2030Z. The TRMM image depicts 2A25 rain type. Purple colors are stratiform precipitation, green pixels are convective precipitation, orange is shallow convective precipitation, and red is anvil precipitation. The light blue coloring indicates no rain observed at that location. The dark blue and yellow pixels represent uncertain retrievals of stratiform and convective precipitation. The yellow line on the IR image represents the approximate center of the TRMM PR pass. The plus signs indicate the approximate position of the GFS FNL derived sweet spot and the red circles indicate the 5° radius circles used as an approximation of the wave pouch.

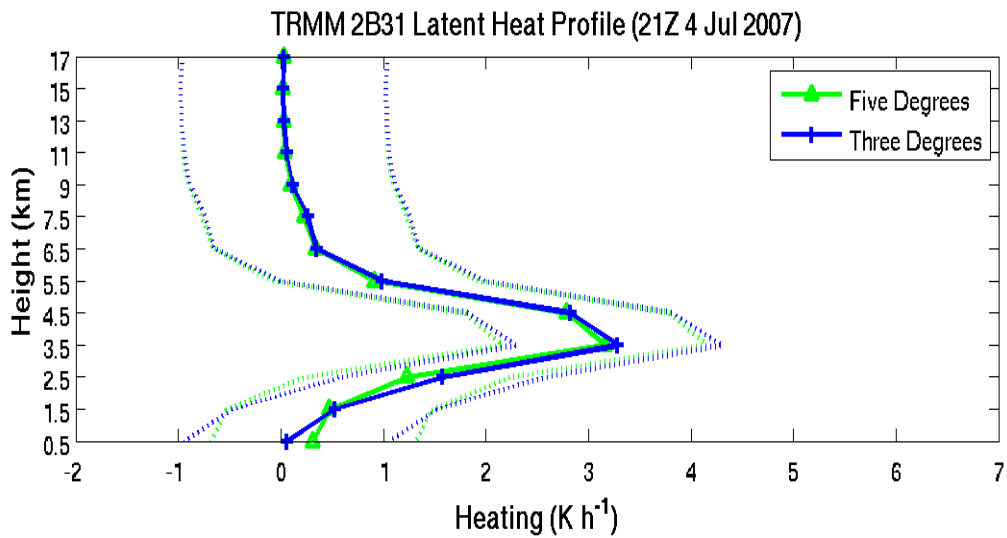


Figure 88. TRMM 2B31 retrieved latent heating profiles for the 2024Z 4 July pass through the wave pouch of the pre-Man-yi disturbance. The plot depicts average heating per pixel within the 3° (blue) and 5° (green) radii. The dotted lines represent the error bounds of the retrievals.

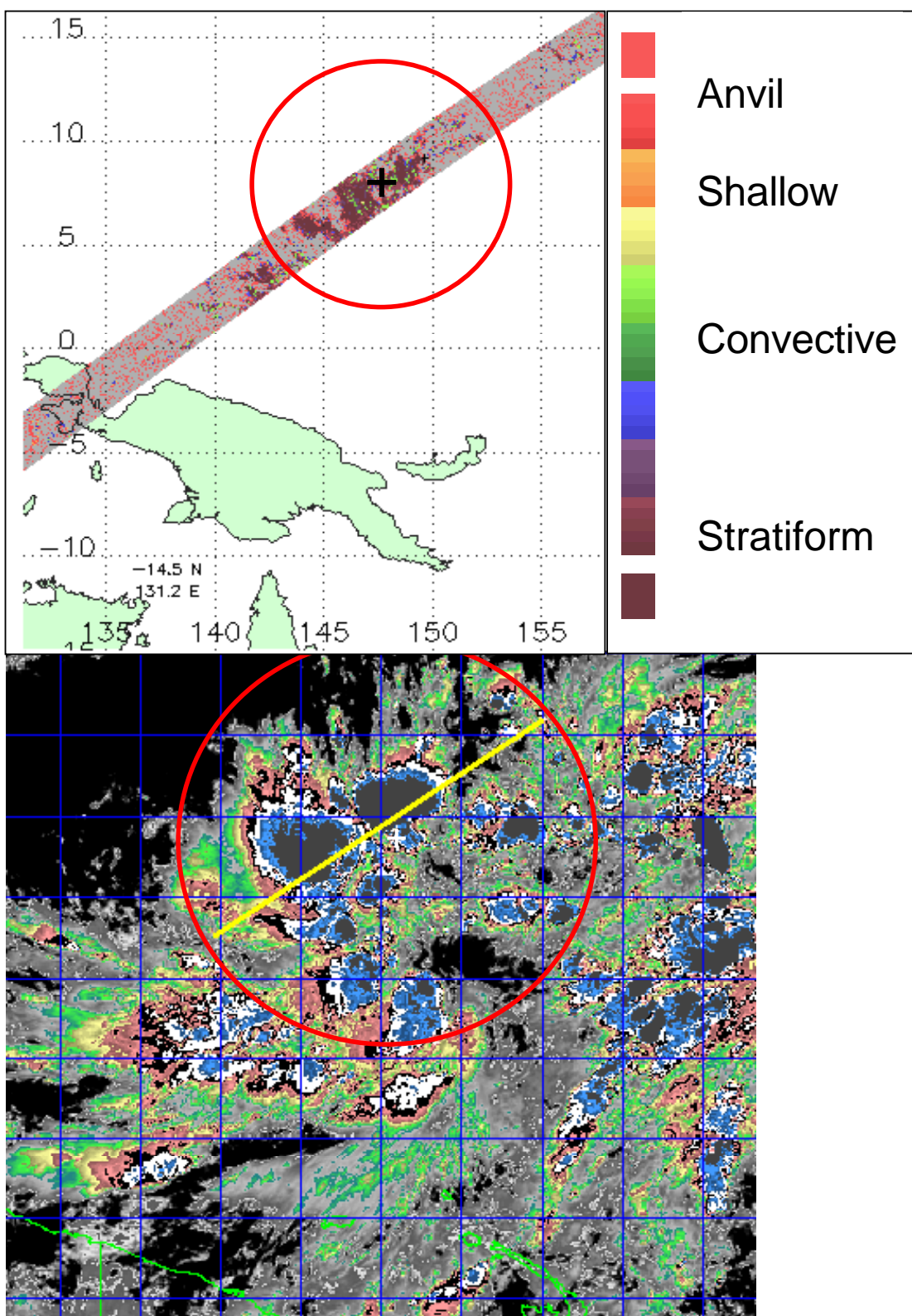


Figure 89. As in Figure 87, except valid 21Z 6 July (TRMM) and 2130Z (MTSAT IR).

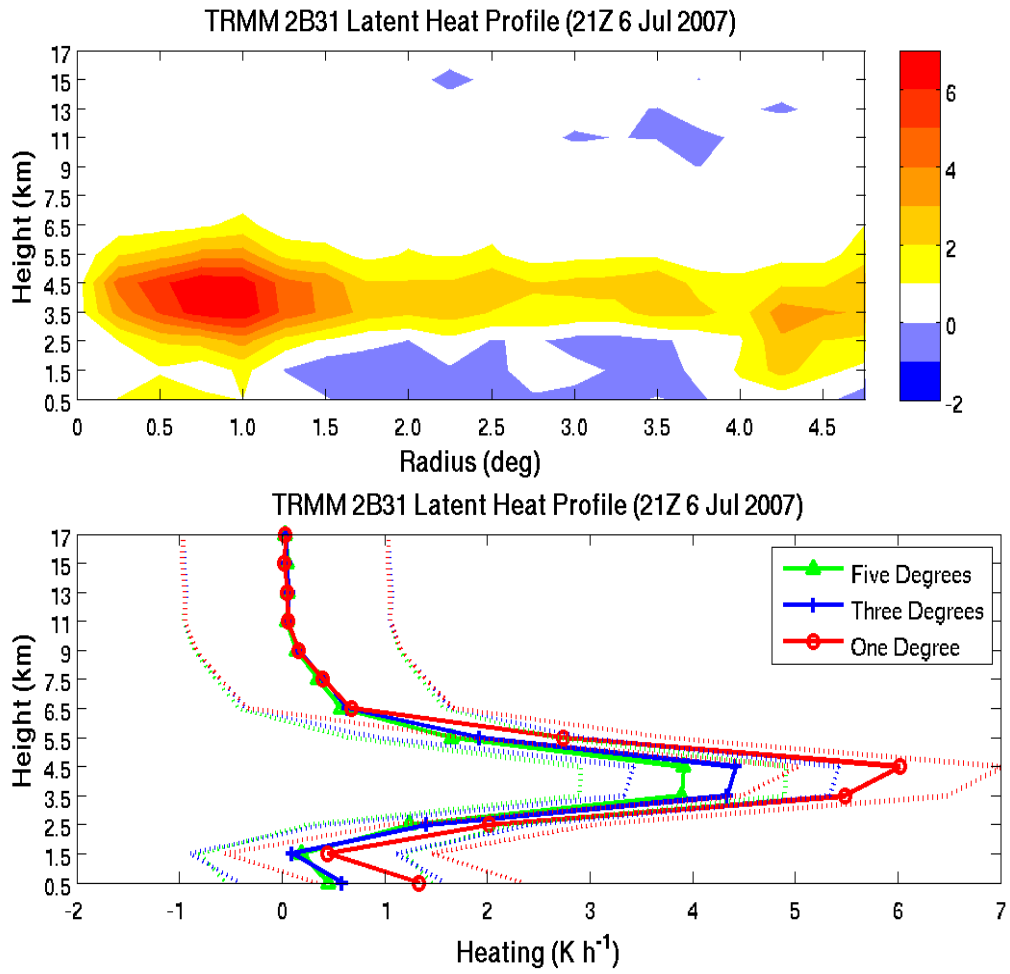


Figure 90. TRMM 2B31 retrieved latent heating profiles for the 21Z 6 July pass through the wave pouch of the pre-Man-yi disturbance. Both plots are average heating per pixel ($^{\circ}\text{K h}^{-1}$). The top is a radial height cross-section of heating and the bottom is latent heating per pixel within the 1° (red), 3° (blue), and 5° (green) radii. The dotted lines represent the error bounds of the retrievals.

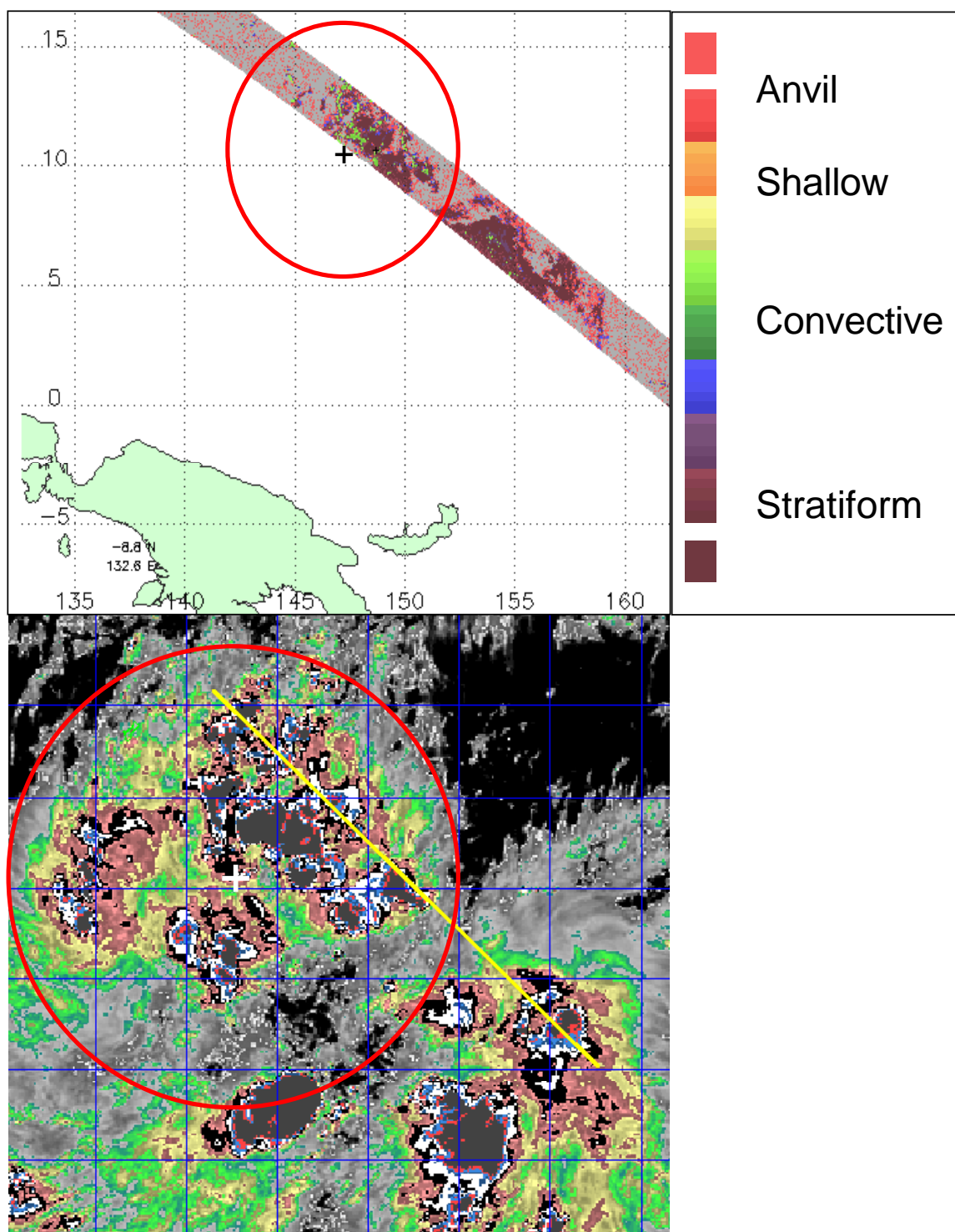


Figure 91. As in Figure 87, except valid 06Z 7 July (TRMM) and 0630Z (MTSAT IR).

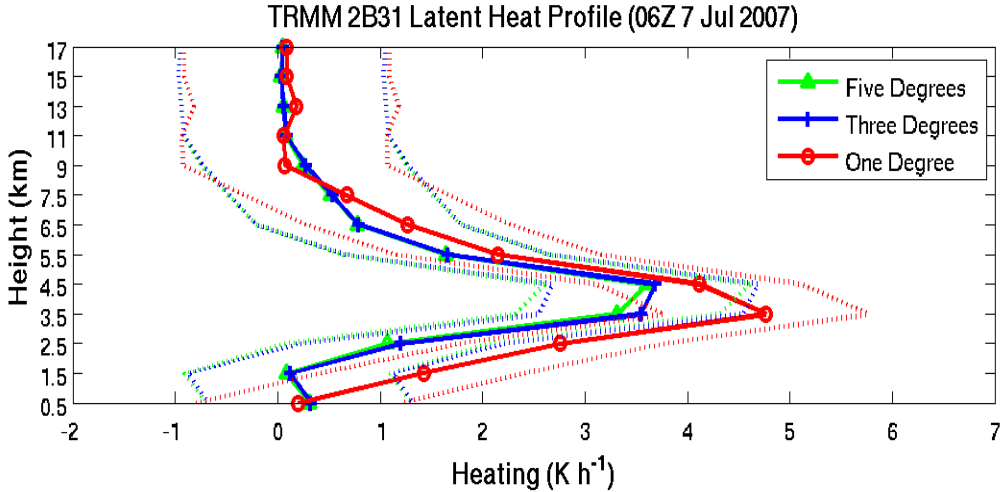


Figure 92. As in Figure 90, except valid 06Z 7 July. The red line indicates heating within the 1° radius.

These data suggest that the convective latent heating profiles within the wave pouch as hypothesized in DMW09 are observed in nature within the pre-Man-yi disturbance, especially at the inner radii of the wave pouch. Three of the four profiles show some evidence of a stratiform heating profile (i.e., cooling in the lower troposphere) in the outer radii. These cooling rates are likely underestimated due to the known biases in the latent heating algorithm (discussed in Appendix B). The latent heating maximum centered around 4 km in the vertical is fairly consistent with the convective profile of Johnson (1984). However, due to the unequal sampling of the wave pouch, robust conclusions cannot be drawn. These data are presented to demonstrate the potential of using TRMM PR data in real-world analysis.

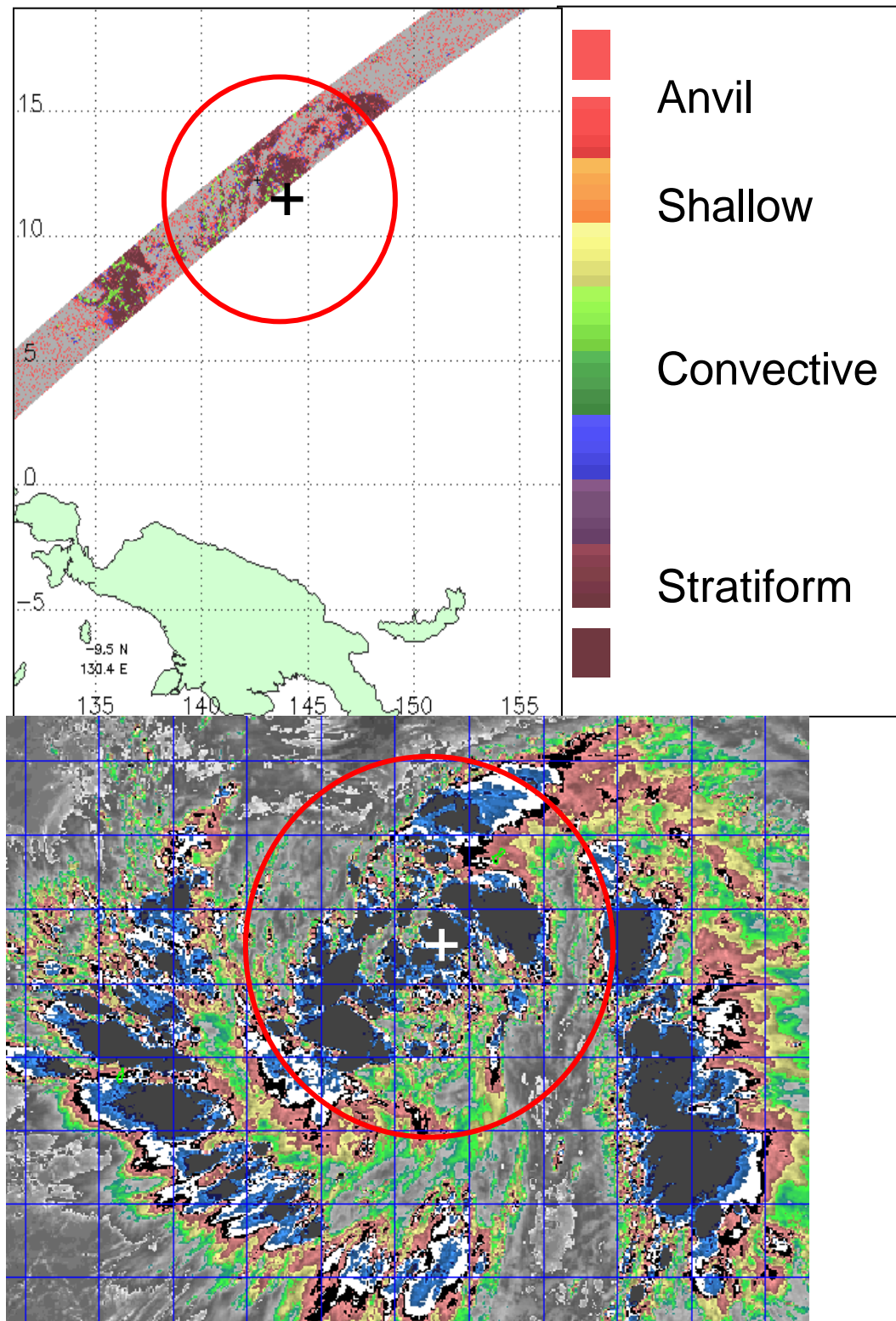


Figure 93. As in Figure 87, except valid 20Z 8 July (TRMM) and 2030Z (MTSAT IR).

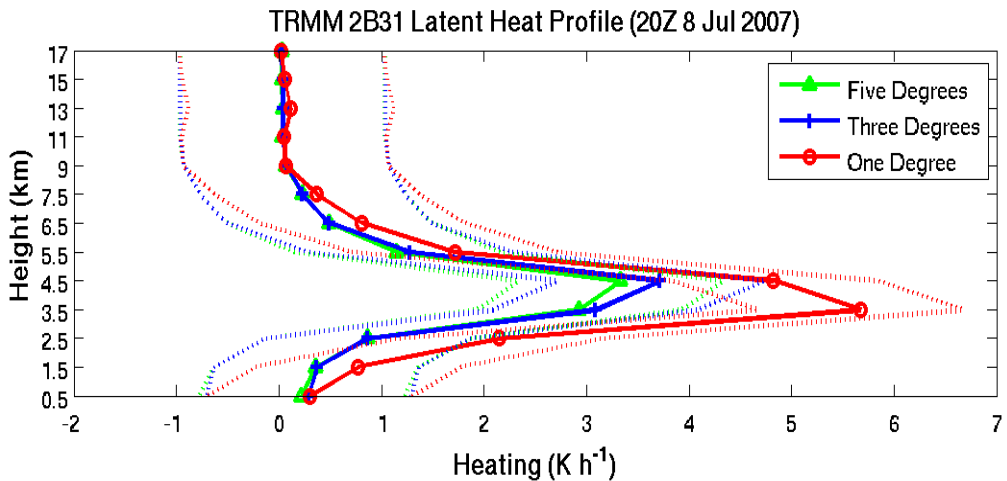


Figure 94. As in Figure 90, except valid 20Z 8 July.

To compliment the above analysis, plots of the percent coverage of each precipitation type for the four TRMM PR passes discussed above are presented in Figure 95. The trend of these observations indicates that stratiform and anvil precipitation is the dominant contributors to the areal coverage of precipitation and that shallow convection covers the least amount of area (consistent with Appendix B). Additionally, stratiform coverage increases closer to the sweet spot and anvil coverage decreases. One of the key arguments presented in DMW09 is that the areal coverage of convective precipitation increases *at the expense of* stratiform precipitation near the sweet spot as genesis nears. On 6 July, the TRMM PR observes a large decrease in stratiform coverage within 0.5° of the sweet spot. This is not accompanied by an increase in convective coverage, but rather a large increase in areal coverage of anvil type precipitation. On 7 August, there is a steady decrease in areal coverage of stratiform precipitation from 1.25° – 0.25° . This is accompanied by a corresponding increase in the convective coverage. At the same time, within 0.5° of the sweet spot, the stratiform coverage decreases rapidly. This is accompanied by an increase in anvil type precipitation. These results are not entirely unexpected as stratiform and anvil coverage are shown to be the leading contributors to areal coverage of precipitation within the pouch of a developing easterly wave (Appendix B). Additionally, maxima in stratiform type precipitation typically corresponded with minima in Anvil type precipitation and vice versa (Appendix B). On 8 August there is a

decrease in the stratiform coverage within 1.5° of the sweet spot. This is accompanied by an increase in anvil type precipitation between 1.5° – 1.25° . However, closer to the sweet spot (1.25° – 0.75°) the convective coverage increases at the expense of the stratiform coverage. While these data are limited in temporal and spatial coverage, these initial findings appear to show examples of an increase in convective type precipitation at the expense of stratiform type precipitation (DMW09) in the Typhoon Man-yi case. However, the limited temporal and spatial coverage of the TRMM satellite precludes definitive conclusions from being made.

C. DISCUSSION

Four TRMM PR overpasses on 4–8 July intersect the pre-Man-yi disturbance and are analyzed to examine the distribution of precipitation and latent heating within Typhoon Man-yi’s wave pouch. While a small, non-robust sample size, these data demonstrate the potential application of TRMM observations for analysis of developing tropical cyclones. These passes show instances of the areal coverage of convection increasing at the expense of stratiform precipitation coverage near the sweet spot (DMW09 H2). Additionally, these observations show evidence of a convective type heating profile within 1° , 3° , and 5° , radii of the sweet spot during all passes. These vertical profiles exhibit heating throughout the depth of the troposphere and a heating maximum in the lower troposphere centered from 3.5–4.5 km. Although there are areas of stratiform heating observed within the pouch, especially at the outer radii, the total heating at each time interval is dominated by the convective signal. Although a very small non-robust sample, these findings are consistent with DMW09’s hypotheses on the precipitation distribution within the critical layer of a developing easterly wave and support the notion that “bottom-up” development potentially led to the formation of Typhoon Man-yi on the sub-synoptic scales.

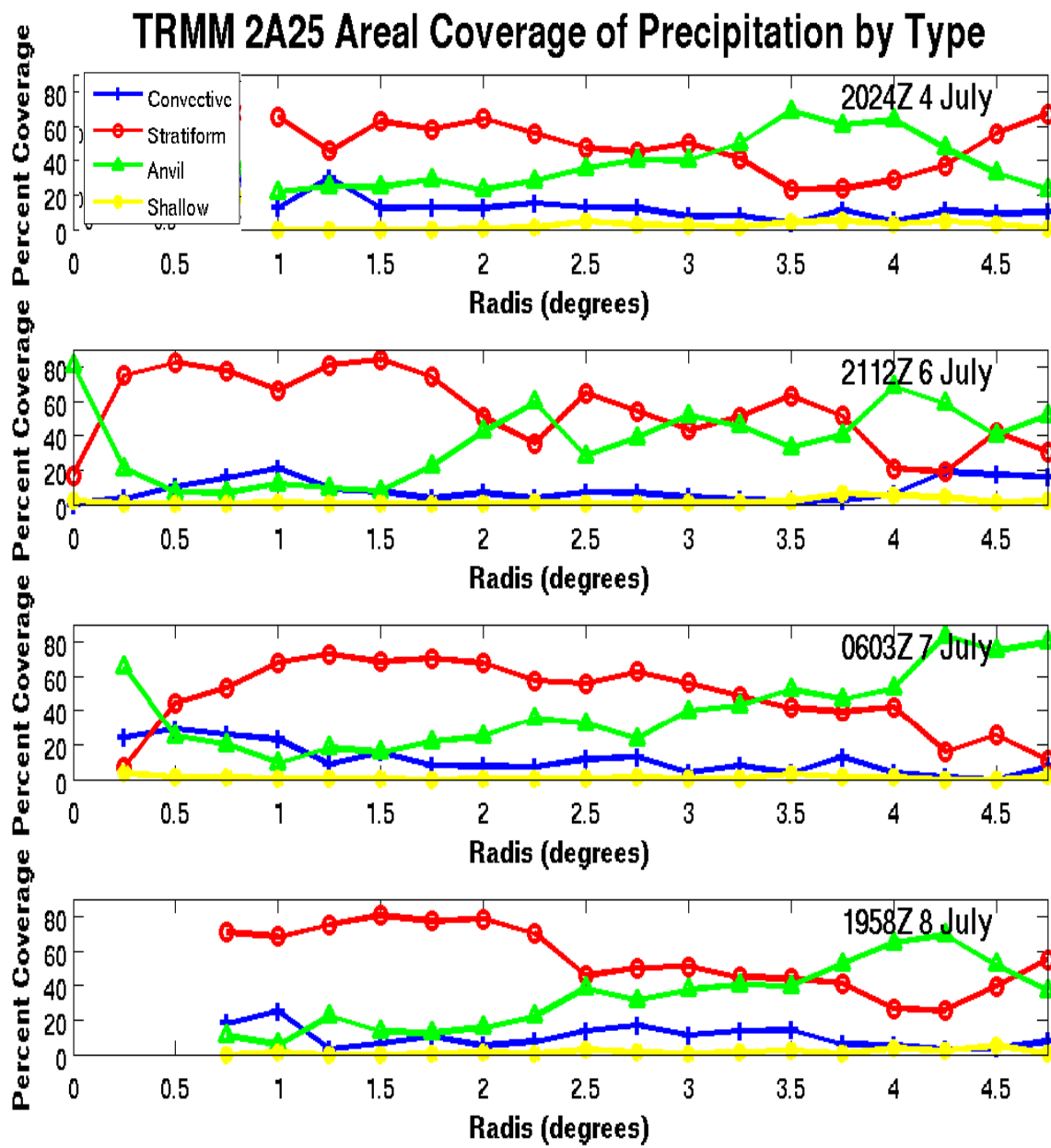


Figure 95. Percent contribution of each precipitation type to total precipitation coverage from the TRMM PR for the four passes used in this study. The blue line is convective coverage, the red is stratiform coverage, the green is anvil coverage, and the yellow is shallow convective coverage.

LIST OF REFERENCES

Andrews, D. G., J. R. Holton, and C. B. Leovy, 1987: *Middle Atmosphere Dynamics*. Academic Press, Orlando, FL, USA, 489.

AMS Statement, 2007: Hurricane forecasting in the United States, *Bull. Amer. Meteorol. Soc.*, **88**, 950–951.

Bessafi, M., and M. C. Wheeler, 2006: Modulation of South Indian Ocean tropical cyclones by the Madden–Julian oscillation and convectively coupled equatorial waves. *Mon. Wea. Rev.*, **134**, 638–656.

Betts, A., and M. Miller, 1986: A new convective adjustment scheme. Part I: Observational and theoretical basis. *Q. J. R. Meteorol. Soc.*, **112**, 1306–1335.

Bister, M., and K. A. Emanuel, 1997: The genesis of Hurricane Guillermo: TEXMEX analyses and a modeling study. *Mon. Wea. Rev.*, **125**, 2662–2682.

Braun, S. A., M. T. Montgomery, K. J. Mallen, and P. D. Reasor, 2010: Simulation and interpretation of the genesis of tropical storm GERT (2005) as part of the NASA tropical cloud systems, *J. Atmos. Sci.*, in Press.

Bracken, W. E., and L. F. Bosart, 2000: The role of synoptic-scale flow during tropical cyclogenesis over the North Atlantic Ocean. *Mon. Wea. Rev.*, **128**, 353–376.

Briegel, L. M., and W. M. Frank, 1997: Large-scale influences on tropical cyclogenesis in the western North Pacific. *Mon. Wea. Rev.*, **125**, 1397–1413.

Carr III, L. E., and R. L. Elsberry, 1995: Monsoonal interactions leading to sudden tropical cyclone track changes. *Mon. Wea. Rev.*, **123**, 265–290.

Challa, M., and R. L. Pfeffer, 1980: Effects of eddy fluxes of angular momentum on model hurricane development. *J. Atmos. Sci.*, **37**, 1603–1618.

Challa, M., and R. L. Pfeffer, 1990: Formation of Atlantic hurricanes from cloud clusters and depressions. *J. Atmos. Sci.*, **47**, 909–927.

Chang, C. P., V. F. Morris, and J. M. Wallace, 1970: A statistical study of easterly waves in the western Pacific: July–December 1964. *J. Atmos. Sci.*, **27**, 195–201.

Chen, T. C., S. Y. Wang, M. C. Yen, and A. J. Clark, 2008: Are tropical cyclones less effectively formed by easterly waves in the western North Pacific than in the North Atlantic? *Mon. Wea. Rev.*, **136**, 4527–4540.

Cheung, K. K. W., and R. L. Elsberry, 2002: Tropical Cyclone Formations over the Western North Pacific in the Navy Operational Global Atmospheric Prediction System Forecasts. *Wea. Forecasting*, **17**, 800–820.

Deleon, R. P., 2008: The role of subtropical intrusion in the development of Typhoon Usagi (5W) 2007. MS thesis, Naval Postgraduate School, Monterey, CA, 118.

Dickinson, M., and J. Molinari, 2002: Mixed Rossby–gravity waves and western Pacific tropical cyclogenesis. Part I: Synoptic evolution. *J. Atmos. Sci.*, **59**, 2183–2196.

Digital Typhoon, cited 2010: Digital Typhoon [Retrieved 2/1/2008 from: <http://agora.ex.nii.ac.jp/digital-typhoon/index.html.en>]

Dunkerton, T. J., M. T. Montgomery, and Z. Wang, 2009: Tropical cyclogenesis in a tropical wave critical layer: easterly waves. *Atmospheric Chemistry and Physics*, **9**, 5587–5646.

Elsberry, R. L., and P. A. Harr, 2008: Tropical Cyclone Structure (TCS08) field experiment science basis, observational platforms, and strategy. *Asia-Pacific Journal of Atmospheric Sciences*, **44**, 209–231.

Elsberry, R. L., 2009: Tropical meteorology class notes. Dept. of Meteor., Naval Postgraduate School, Monterey, CA.

Emanuel, K. A., 2005: Divine Wind: The History and Science of Hurricanes. Oxford University Press, New York, NY, USA, 285.

Ferreira, R. N., and W. H. Schubert, 1997: Barotropic aspects of ITCZ breakdown. *J. Atmos. Sci.*, **54**, 261–285.

Frank, N. L., 1970: Atlantic tropical systems of 1969. *Mon. Wea. Rev.*, **98**, 307–314.

Frank, W. M., and P. E. Roundy, 2006: The role of tropical waves in tropical cyclogenesis. *Mon. Wea. Rev.*, **134**, 2397–2417.

Fu, B., T. Li, M. S. Peng, and F. Weng, 2007: Analysis of tropical cyclogenesis in the western North Pacific for 2000 and 2001. *Wea. Forecasting*, **22**, 763–780.

Glickman, T. S., 2000: *Glossary of Meteorology*. American Meteorological Society Boston, MA, USA, 850.

Gray, W. M., 1968: Global view of the origin of tropical disturbances and storms. *Mon. Wea. Rev.*, **96**, 669–700.

Gray, W. M., 1975: *Tropical cyclone genesis*. Department of Atmos. Sci. Paper No. 323, Colorado State University, Fort Collins, CO, 121.

Gray, W., 1998: The formation of tropical cyclones. *Meteorology and Atmospheric Physics*, **67**, 37–69.

Gruber, A., 1974: The wavenumber–frequency spectra of satellite–measured brightness in the Tropics. *J. Atmos. Sci.*, **31**, 1675–1680.

Harr, P. A., and R. L. Elsberry, 1991: Tropical cyclone track characteristics as a function of large-scale circulation anomalies. *Mon. Wea. Rev.*, **119**, 1448–1468.

Harr, P. A., and R. L. Elsberry, 1995: Large-scale circulation variability over the tropical western North Pacific. Part I: Spatial patterns and tropical cyclone characteristics. *Mon. Wea. Rev.*, **123**, 1225–1246.

Harr, P. A., R. L. Elsberry, and J. C. L. Chan, 1996: Transformation of a large monsoon depression to a tropical storm during TCM–93. *Mon. Wea. Rev.*, **124**, 2625–2643.

Hendricks, E. A., M. T. Montgomery, and C. A. Davis, 2004: The role of “vortical” hot towers in the formation of tropical cyclone Diana (1984). *J. Atmos. Sci.*, **61**, 1209–1232.

Holland, G. J., 1983: Angular momentum transports in tropical cyclone. *Q. J. R. Meteorol. Soc.*, **109**, 187–210.

Holland, G. J., 1995.: Scale interaction in the western Pacific monsoon. *Meteorology and Atmospheric Physics*, **56**, 57–79.

Holton, J. R., 1992: *An Introduction to Dynamic Meteorology, Third Edition*. Academic Press, Inc., San Diego, CA, USA 511.

Hong, S. Y., and J. O. J. Lim, 2006: The WRF single–moment 6–class microphysics scheme (WSM6). *Journal of the Korean Meteorological Society*, **42**, 129–151.

Houze Jr, R. A., 1982: Cloud clusters and large-scale vertical motions in the tropics. *J. Meteor. Soc. Japan*, **60**, 396–410.

Houze Jr., R. A., 1989: Observed structure of mesoscale convective systems and implications for large-scale heating. *Q. J. R. Meteorol. Soc.*, **115**, 425–461.

Houze Jr, R. A., 1997: Stratiform precipitation in regions of convection: a meteorological paradox? *Bull. Amer. Meteorol. Soc.*, **78**, 2179–2196.

Houze Jr, R. A., W. C. Lee, and M. M. Bell, 2009: Convective contributions to the genesis of Hurricane Ophelia (2005). *Mon. Wea. Rev.*, **137**, 2778–2800.

Janjić, Z. I., 1994: The step–mountain eta coordinate model: Further developments of the convection, viscous sublayer, and turbulence closure schemes. *Mon. Wea. Rev.*, **122**, 927–945.

Johnson, R. H., 1984: Partitioning tropical heat and moisture budgets into cumulus and mesoscale components: Implications for cumulus parameterization. *Mon. Wea. Rev.*, **112**, 1590–1601.

Kain, J. S., and J. M. Fritsch, 1990: A one-dimensional entraining/detraining plume model and its application in convective parameterization. *J. Atmos. Sci.*, **47**, 2784–2802.

Kain, J., 1993: Convective parameterization for mesoscale models: The Kain–Fritsch scheme. *The Representation of Cumulus Convection in Numerical Models, Meteor. Monogr.*, **46**, 165–170.

Karyampudi, V. M., and H. F. Pierce, 2002: Synoptic-scale influence of the Saharan Air Layer on tropical cyclogenesis over the eastern Atlantic. *Mon. Wea. Rev.*, **130**, 3100–3128.

Kiladis, G. N., G. A. Meehl, and K. M. Weickmann, 1994: Large-scale circulation associated with westerly wind bursts and deep convection over the western equatorial Pacific. *J. Geophys. Res.*, **99**, 18,527–18,544.

Kiladis, G. N., and M. C. Wheeler, 1995: Horizontal and vertical structure of observed tropospheric equatorial Rossby waves. *J. Geophys. Res.*, **100**, 22,981–22,997.

Kiladis, G. N., M. C. Wheeler, P. T. Haertel, K. H. Straub, and P. E. Roundy, 2009: Convectively coupled equatorial waves. *Rev. Geophys.*, **47**, RG2003, doi:10.1029/2008RG000266.

Kummerow, C. D., W. Barnes, T. Kozu, J. Shiue, and J. Simpson, 1998: The tropical rainfall measuring mission (TRMM) sensor package. *J. Atmos. Ocean. Technol.*, **15**, 809–817.

Lander, M. A., 1994: Description of a monsoon gyre and its effects on the tropical cyclones in the western North Pacific during August 1991. *Wea. Forecasting*, **9**, 640–654.

Lee, C. S., K. K. W. Cheung, J. S. N. Hui, and R. L. Elsberry, 2006: Mesoscale features associated with tropical cyclone formation in the western North Pacific, *Mon. Wea. Rev.*, **136**, 2006–2022.

Leipper, D., and D. Volgenau: Hurricane heat potential of the Gulf of Mexico. *J. Phys. Oceanogr.*, **2**, 218–224, 1972.

Lonfat, M., F. D. Marks Jr, and S. S. Chen, 2004: Precipitation distribution in tropical cyclones using the Tropical Rainfall Measuring Mission (TRMM) microwave imager: A global perspective, *Mon. Wea. Rev.*, **132**, 1645–1660.

Mapes, B. E., and R. A. Houze Jr, 1995: Diabatic divergence profiles in western Pacific mesoscale convective systems. *J. Atmos. Sci.*, **52**, 1807–1828.

Matsuno, T., 1966: Quasi-geostrophic motions in the equatorial area. *J. Meteor. Soc. Japan*, **44**, 25–43.

Molinari, J., 2004: Paradigms of tropical cyclogenesis, *Bull. Amer. Meteor. Soc.*, **85**, 662–663.

Molinari, J., K. Lombardo, and D. Vollaro, 2007: Tropical cyclogenesis within an equatorial rossby wave packet. *J. Atmos. Sci.*, **64**, 1301–1317.

Montgomery, M. T., and J. Enagonio, 1998: Tropical cyclogenesis via convectively forced vortex Rossby waves in a three-dimensional quasigeostrophic model. *J. Atmos. Sci.*, **55**, 3176–3207.

Montgomery, M. T., M. E. Nicholls, T. A. Cram, and A. B. Saunders, 2006: A vortical hot tower route to tropical cyclogenesis. *J. Atmos. Sci.*, **63**, 355–386.

Montgomery, M. T., Z. Wang, and T. J. Dunkerton, 2010a: Intermediate and high resolution numerical simulations of the transition of a tropical wave critical layer to a tropical depression. *Atmospheric Chemistry and Physics*, Accepted.

Montgomery, M. T., L. L. Lussier III, R. W. Moore, and Z. Wang, 2010b: The genesis of Typhoon Nuri as observed during the Tropical Cyclone Structure 2008 (TCS-08) field experiment. Part I: The role of the easterly wave critical layer. *Atmospheric Chemistry and Physics*, In Press.

National Hurricane Center (NHC), cited 2010: [Retrieved 5/2/2010 from: <http://www.nhc.noaa.gov/aboutgloss.shtml>].

Neumann, C. J., 1993: Global overview. Global Guide to Tropical Cyclone Forecasting. World Meteor. Org, 1–1.56.

Nguyen, V. S., R. K. Smith, and M. T. Montgomery, 2008: Tropical cyclone intensification and predictability in three dimensions. *Quart. J. Roy. Meteor. Soc.*, **134**, 563–582.

Nolan, D. S., 2007: What is the trigger for tropical cyclogenesis. *Aust. Meteor. Mag.*, **56**, 241–266.

Numaguti, A., 1995: Characteristics of 4-to-20-day-period disturbances observed in the equatorial Pacific during the TOGA COARE IOP. *J. Meteor. Soc. Japan*, **73**, 353–377.

Olson, W. S., C. D. Kummerow, Y. Hong, and W.-K. Tao, 1999: Atmospheric latent heating distributions in the Tropics derived from satellite passive microwave radiometer measurements, *J. Appl. Meteorol.*, **38**, 633–664.

Olson, W. S., C. D. Kummerow, S. Yang, G. W. Petty, W.-K. Tao, T. L. Bell, S. A. Braun, Y. Wang, S. E. Lang, D. E. Johnson, and C. Chiu, 2006: Precipitation and latent heating distributions from satellite passive microwave radiometry. Part I: Improved method and uncertainties, *J. Appl. Meteorol. and Climatol.*, **45**, 702–720.

Ooyama, K. V., 1982: Conceptual evolution of the theory and modeling of the tropical cyclone. *J. Meteor. Soc. Japan*, **60**, 369–379.

Park, M.-S., R. L. Elsberry, and M. M. Bell, 2010: Latent heating rate profiles at different tropical cyclone stages during 2008 Tropical Cyclone Structure experiment: Comparison of ELDORA and TRMM PR retrievals. 29th Conference on Hurricanes and Tropical Meteorology, Tucson, AZ, Amer. Meteorol. Soc. [Retrieved 5/29/2010 from: http://ams.confex.com/ams/29Hurricanes/techprogram/programexpanded_608.htm].

Raymond, D. J., C. Lopez-Carrillo, and L. Lopez Cavazos, 1998: Case-studies of developing east Pacific easterly waves. *Q. J. R. Meteor. Soc.*, **124**, 2005–2034.

Raymond, D. J., and C. Lopez-Carrillo, 2010: The vorticity budget of developing Typhoon Nuri (2008). *Atmospheric Chemistry and Physics Discussion*, Submitted.

Reed, R. J., and E. E. Recker, 1971: Structure and properties of synoptic-scale wave disturbances in the equatorial western Pacific. *J. Atmos. Sci.*, **28**, 1117–1133.

Reed, R. J., D. C. Norquist, and E. E. Recker, 1977: The structure and properties of African wave disturbances as observed during Phase III of GATE. *Mon. Wea. Rev.*, **105**, 317–333.

Reasor, P. D., M. T. Montgomery, and L. F. Bosart, 2005: Mesoscale observations of the genesis of Hurricane Dolly (1996). *J. Atmos. Sci.*, **62**, 3151–3171.

Ritchie, E. A., and G. J. Holland, 1997: Scale interactions during the formation of Typhoon Irving. *Mon. Wea. Rev.*, **125**, 1377–1396.

Ritchie, E. A., and G. J. Holland, 1999: Large-scale patterns associated with tropical cyclogenesis in the western Pacific. *Mon. Wea. Rev.*, **127**, 2027–2043.

Riehl, H, 1955: *Tropical Meteorology*. McGraw–Hill Press, New York, NY, USA, 392.

Rodgers, E. B., and R. F. Adler, 1981: Tropical cyclone rainfall characteristics as determined from a satellite passive microwave radiometer, *Mon. Wea. Rev.*, **109**, 506–521.

Sadler, J. C., 1976: A role of the tropical upper tropospheric trough in early season typhoon development. *Mon. Wea. Rev.*, **104**, 1266–1278.

Sadler, J. C., 1978: Mid-season typhoon development and intensity changes and the tropical upper tropospheric trough. *Mon. Wea. Rev.*, **106**, 1137–1152.

Schumacher, C., and R. A. Houze Jr, 2003: Stratiform rain in the Tropics as seen by the TRMM precipitation radar. *J. Clim.*, **16**, 1739–1756.

Schumacher, C., and R. A. Houze, Jr. 2006. Stratiform precipitation production over sub-Saharan Africa and the tropical East Atlantic as observed by TRMM. *Quart. J. Roy. Meteor. Soc.* **132**, 2235–2255.

Serra, Y. L., G. N. Kiladis, and M. F. Cronin, 2008: Horizontal and Vertical Structure of Easterly Waves in the Pacific ITCZ. *J. Atmos. Sci.*, **65**, 1266–1284.

Shige, S., Y. N. Takayabu, W.–K. Tao, and C.–L. Shie, 2007: Spectral Retrieval of Latent Heating Profiles from TRMM PR Data. Part II: Algorithm Improvement and Heating Estimates over Tropical Ocean Regions. *J. Appl. Meteorol. and Climatol.* **46**, 1098–1124.

Takayabu, Y. N., and T. Nitta, 1993: 3–5 day period disturbances coupled with convection over the tropical Pacific Ocean. *J. Meteor. Soc. Japan*, **71**, 221–245.

Tao, W.–K., J. Simpson, C. H. Sui, B. Ferrier, S. Lang, J. Scala, M. D. Chou, and K. Pickering, 1993: Heating, Moisture, and Water Budgets of Tropical and Midlatitude Squall Lines: Comparisons and Sensitivity to Longwave Radiation, *J. Atmos. Sci.*, **50**, 673–690.

Tao W.–K., S. Lang, J. Simpson, W. S. Olson, D. Johnson, B. Ferrier, C. D. Kummerow, and R. F. Adler, 2000: Vertical profiles of latent heat release and their retrieval in TOGA COARE convective systems using a cloud resolving model, SSM/I and radar data. *J. Meteor. Soc. Japan*, **78**, 333–355.

Tao, W.-K., S. Lang, W. S. Olson, R. Meneghini, S. Yang, J. Simpson, C. D. Kummerow, E. A. Smith, and J. Halverson, 2001: Retrieved vertical profiles of latent heat release using TRMM rainfall products for February 1998. *J. Appl. Meteor.*, **40**, 957–982.

Tao, W.-K., E. A. Smith, R. F. Alder, Z. S. Haddad, A. Y. Hou, T. Iguchi, R. Kakar, T. N. Krishnamurti, C. D. Kummerow, S. Lang, R. Meneghini, K. Nakamura, T. Nakazawa, K. Okamoto, W. S. Olson, S. Satoh, S. Shige, J. Simpson, Y. Takayabu, G. J. Tripoli, and S. Yang, 2006: Retrieval of latent heating from TRMM measurements. *Bull. Amer. Meteorol. Soc.*, **87**, 1555–1572,

TRMM, cited 2009: Tropical Rainfall Measurement Mission Readme. [Retrieved 3/15/2009 from: http://disc.sci.gsfc.nasa.gov/precipitation/documentation/TRMM_README].

Wang, C., and G. Magnusdottir, 2006: The ITCZ in the central and eastern Pacific on synoptic time scales. *Mon. Wea. Rev.*, **134**, 1405–1421.

Wang, H., and W. M. Frank, 1999: Two modes of tropical cyclo-genesis: An idealized simulation. Preprints, 23d Conf. on Hurricanes and Tropical Meteorology, Dallas, TX, Amer. Meteor. Soc., 923–924.

Wang, Z., M. T. Montgomery, and T. J. Dunkerton, 2009: A dynamically-based method for forecasting tropical cyclogenesis location in the Atlantic sector using global model products. *Geophys. Res. Lett.*, **36**, L03801.

Wang, Z., M. T. Montgomery, and T. J. Dunkerton, 2010a: Genesis of pre-hurricane Felix (2007) Part I: The role of the easterly wave critical layer. *J. Atmos. Sci.*, In Press.

Wang, Z., M. T. Montgomery, and T. J. Dunkerton, 2010b: Genesis of pre-hurricane Felix (2007) Part II: Warm core formation, precipitation evolution and predictability. *J. Atmos. Sci.*, In Press.

Wheeler, M. C., and G. N. Kiladis, 1999: Convectively coupled equatorial waves: Analysis of clouds and temperature in the wavenumber–frequency domain. *J. Atmos. Sci.*, **56**, 374–399.

Wheeler, M. C., G. N. Kiladis, and P. J. Webster, 2000: Large-scale dynamical fields associated with convectively–coupled equatorial waves. *J. Atmos. Sci.*, **57**, 613–640.

Yang, G. Y., B. Hoskins, and J. Slingo, 2007: Convectively coupled equatorial waves. Part I: Horizontal and vertical structures. *J. Atmos. Sci.*, **64**, 3406–3423.

Yang, S., W. S. Olson, Y. J. J. Wang, T. L. Bell, E. A. Smith, and C. D. Kummerow, 2006: Precipitation and Latent Heating Distributions from Satellite Passive Microwave Radiometry. Part II: Evaluation of Estimates Using Independent Data. *J. Appl. Meteorol. and Climatol.*, **45**, 721–739.

Yanai, M., S. Esbensen, and J. H. Chu, 1973: Determination of bulk properties of tropical cloud clusters from large-scale heat and moisture budgets, *J. Atmos. Sci.*, **30**, 611–627.

Zangvil, A., 1975: Temporal and spatial behavior of large-scale disturbances in tropical cloudiness deduced from satellite brightness data. *Mon. Wea. Rev.*, **103**, 904–920.

Zuluaga, M. D., C. D. Hoyos, and P. J. Webster, 2010: Spatial and Temporal Distribution of Latent Heating in the South Asian Monsoon Region. *J. Climate*, In Press.

THIS PAGE INTENTIONALLY LEFT BLANK

INITIAL DISTRIBUTION LIST

1. Defense Technical Information Center
Ft. Belvoir, Virginia
2. Dudley Knox Library
Naval Postgraduate School
Monterey, California
3. Professor Michael Montgomery
Naval Postgraduate School
Monterey, California
4. Professor Patrick Harr
Naval Postgraduate School
Monterey, California
5. Professor Francis Giraldo
Naval Postgraduate School
Monterey, California
6. Professor Richard Moore
Naval Postgraduate School
Monterey, California
7. Professor Zhuo Wang
University of Illinois
Champaign, Illinois
8. Doctor Tim Dunkerton
Northwest Research Associates
Bellevue, Washington
9. Major Louis Lussier
Airborne Laser Program Office
Kirtland AFB, New Mexico